POLITECNICO DI MILANO
DEPARTMENT OF ENERGY
DOCTORAL PROGRAMME IN ENERGY AND NUCLEAR SCIENCE AND TECHNOLOGY

LARGE EDDY SIMULATION FOR COMPLEX INDUSTRIAL FLOWS

Doctoral Dissertation of:
Paolo Lampitella

Advisor:
Prof. Emanuela Colombo

Tutor:
Prof. Fabio Inzoli

The Chair of the Doctoral Program:
Prof. Carlo Enrico Bottani

February 2014 – XXV Cycle

"If you want a new idea
read an old book."
Anonymous

" 'Herr Hiemenz, is the flow steady now?'
He answered very sadly, 'It always oscillates.' "
Theodore von Kármán

$1 + 2 + 3 + 4 + \cdots = -\frac{1}{12}$
Leonhard Euler

Acknowledgements

I express my deepest and sincere gratitude to my supervisors, Prof. Fabio Inzoli and Prof. Emanuela Colombo, for the incredible opportunity they gave me to begin and complete this doctoral course. Their competence in the most diverse fields and problem solving attitude is something i could never stop learning from.

The experimental and computational activities related to the swirled flow combustor test case have benefited of enormous support from Prof. Fabio Cozzi, at the Department of Energy of Politecnico di Milano, and Dr. Raffaele Ponzini, at the Consorzio Interuniversitario Lombardo per l'Elaborazione Automatica (CILEA). The computational resources provided by the CILEA consortium, under the auspices of Regione Lombardia and the LISA initiative, and those provided for the LESinItaly project, by the Consorzio interuniversitario per le Applicazioni di Supercalcolo Per Universitá e Ricerca (CASPUR), are both gratefully acknowledged.

I will always be indebted to Prof. Filippo Maria Denaro, from the Second University of Naples. He never allowed me to set on lower standards and his guidance, especially in LES, has always been inestimable. This thesis work would have not been possible without him.

The friends at the CFDLAB of the Politecnico di Milano have all been invaluable during my stay in Milan: Claudio, Gael, Marco and Riccardo. Besides the fun, the food and the ping-pong, my work too has benefited of all their support. I especially thank Gael for sharing our darkest nerditude.

Last but not least, i thank my wife Nica. Her extraordinary patience has reached unprecedented levels during these doctoral years.

Abstract

THE object of this thesis is the Large Eddy Simulation (LES) of turbulent flows, its theoretical and practical development toward complex industrial flows requiring unstructured flow solvers and its specific application to flows of different complexities.

In a broad sense, LES deals with approximations of the dynamical system described by the Navier-Stokes equations (NSE), the approximation being in the use of a lower number of degrees of freedom (i.e., the number of grid cells and time steps used in a computation) than those strictly required for a correct full numerical simulation of the flow (i.e., DNS). In LES literature, the reduction in the number of degrees of freedom is usually introduced by formally applying a spatial low-pass convolution filter to the NSE. This filter is aimed at separating the large turbulent scales, which in LES are directly represented on a grid and simulated, from the small or sub-grid scales (SGS), which in LES are only modeled, i.e., by a SGS model. The rational basis for this approach and, as a matter of fact, for LES as a whole, stems from the classical Kolmogorov picture of the turbulent energy cascade. The large scales are the most energetic, anisotropic and the most dependent from the boundary conditions. Small scales, in contrast, are much less energetic, more isotropic and universal, hence they should be relatively easy to be modeled.

However, nowadays, it is fully recognized that the actual dynamical system effectively represented by the numerical simulation is different from the formally filtered NSE in several aspects. First and foremost, the effective scale separation between resolved and modeled scales is usually different from the theoretical one which, in most cases, is not even present in practice. As a consequence, the overall scale separation is actually determined by the computational grid, the numerical scheme and, possibly, the SGS model too. This, in turn, introduces uncertainty in the computation as both the resolved and the modeled scales are not precisely characterized and the SGS models, which are developed in such incorrect framework, are also required to represent a not well specified range of scales. A second important aspect concerns the specific form of the equations used for the simulation which, despite the issues described above, is still usually based on the formally filtered NSE. This approach either introduces additional

modeling errors, known as commutation errors, or requires specific numerical strategies and numerical methods with higher accuracy. These problems, which might appear secondary or abstract, are in fact fundamental. Indeed, the overall LES approach can be essentially reduced to the interaction between a scarcely resolved, numerically affected, range of scales near the cut-off of the grid, and a SGS model, which should represent the interactions of such scales with the missing ones. Whenever this interaction is misrepresented, the outcome of the simulation is strongly affected. Moreover, this picture is even more critical when considered in the framework of unstructured flow solvers, usually adopted in practical engineering applications. Indeed, the hypotheses required to fit the formal LES picture are seldom, if ever, satisfied and the higher numerical accuracy required to overcome this limit is not usually available or practical.

Despite its high resolution requirements, LES is now feasible for small-medium sized industrial applications and is explicitly required whenever the flow presents strong unsteadiness or interactions among different spatial scales. As a consequence, in order to further develop LES for complex industrial applications, it is of paramount importance to overcome its present deficiencies and limitations. In the present work, this objective is pursued by first reformulating the LES problem in a new, consistent, theoretical framework. In particular, the classical LES route described above, in which model filtered equations are used as representative of a numerical approach, is definitely abandoned. Instead, the new proposed framework is defined by equations which are an exact representation of a given numerical method, independently from any filter concept. In particular, this framework is more general than the classical one as it exactly represents most of the known numerical approaches: finite differences, finite/spectral element methods and finite volumes (FV), structured and unstructured. As such, it is particularly suitable as theoretical framework for the development of LES in complex applications using unstructured flow solvers of any type. Moreover, as a side-product of the present LES reformulation, relevant differences arise at the level of the SGS terms which need modeling and their underlying algebraic relations, also known as Germano Identities. These differences are such that important reductions in the computational costs of some classical SGS models are introduced and more complex modeling options can be explored with relative ease.

This last aspect, in particular, is further developed in the thesis trough the application of the proposed framework to the FV method. As a result of this application, a new SGS model is developed, which is intended to recover part of the energy lost by the numerically affected scales of the flow, while remaining stable on general unstructured grids.

The flexibility and suitability of the proposed LES approach and SGS model are then demonstrated by their implementation in a general purpose unstructured FV solver and the application to flows of increasing complexity. A particular attention is first devoted to the turbulent channel flow, because of its relevance as LES benchmark and the availability of solutions with different codes and SGS models. More specifically, the comparison is made with the codes participating the LESinItaly database, ranging from pseudo-spectral to finite difference ones, including several commercial and open-source FV codes. The comparison not only shows the relevance of the proposed SGS modeling strategy, which outperform all the reference LES solutions, but also evidences a striking similarity of LES results among very different codes. This similarity is further

investigated and possible causes are highlighted, leading to a better interpretation of common results found in literature.

Finally, more complex flows are considered. These include: turbulent pipe flows computed with unstructured grids at different Reynolds numbers; the flow and heat transfer in a matrix of wall-mounted cubes; the cold, swirling, flow in a lab-scale industrial combustor. In all the cases, the proposed SGS model is compared with the available DNS/experimental data and with more classical SGS modeling strategies using multiple grid resolutions. The results of these additional tests show that the proposed SGS model is, at worst, as accurate as the classical SGS models, while retaining its stability and lower computational costs. However, for the lower resolutions typical of industrial applications, the effects of the new SGS model are more evident and lead to a better prediction of the flow statistics.

Contents

List of Figures

List of Tables

CHAPTER 1

Introduction

Among the several physical phenomena governing the events on earth and influencing our daily life, the flow of fluids is one of the most important as it affects almost all the relevant physical fields. From planetary scale climate patterns, like El Niño, and mesoscale convective systems, like tropical cyclones, to energy conversion in the most diverse power plants and devices, like internal combustion engines; from the aerodynamics of cars, airplanes and trains to the blood flow in the cardiovascular system; all these physical mechanisms, or processes, involve a certain degree of interaction with a fluid in some kind of motion. As such, it comes at no surprise that fluid mechanics, the study of fluids in equilibrium or motion, can be dated back to the Classical era (250 B.C. circa) and the two books work of Archimedes, *On Floating Bodies*.

In its modern form, fluid mechanics, like every other branch of the classical mechanics, can accurately describe fluids and their motion by a set of partial differential equations (PDE)[1] governing the relations between the momentum changes of fluid parcels and the forces generating them. However, very differently from other branches of classical mechanics, the analysis of the fluid motions is challenged by the inherent non-linearity of the process, which determines, for nearly every flow, the possibility to exist in two different states: laminar or turbulent. Laminar flows are characterized by a regular pattern and time behavior for all the flow variables, usually allowing a complete mathematical description. Turbulent flows, in contrast, exhibit a chaotic and seemingly random behavior, characterized by strong three-dimensionality, unsteadiness and fluctuations over a wide range of spatial and temporal scales. It is due to Reynolds (1883), after his well known experiment, the recognition that, for incompressible, isothermal flows, the behavior of the flow depends on a single non-dimensional parameter, now

[1] Under the continuum hypothesis and supplemented by proper initial and boundary conditions.

known as *Reynolds number*:

$$Re = \frac{\rho U L}{\mu} \tag{1.1}$$

where ρ and μ are the density and dynamic viscosity of the fluid while U and L are, respectively, a characteristic velocity and length scale for the flow. When the Reynolds number is below a specific, flow dependent, value the flow is laminar and exhibits a regular pattern and time behavior; if the Reynolds number is above the specific value then the flow starts to exhibit an irregular pattern (transitional phase) and, for even higher values, eventually becomes fully turbulent. The Reynolds number is, actually, a measure of the relative magnitude of convective (nonlinear) and viscous (linear) effects; when Re is high the former dominate the latter and the flow behaves chaotically, with a strong dependence on the initial and boundary conditions due to the nonlinearity. It is still due to Reynolds (1895) the recognition that turbulent flows are more suitably described in terms of statistical means and moments which, however, cannot provide a full mathematical description of the flow.

From the engineering point of view, turbulent flows are ubiquitous while laminar ones are the exceptions; also, turbulent flows are characterized by increased mixing and dissipation, which are important in nearly all the applications (e.g., combustion, pollution dispersal, internal and external aerodynamics). As a consequence, their description and understanding is of paramount importance, not only from the physical point of view but also from a purely technical perspective. Nonetheless, still today, the non-linearity of the problem challenges our advancements in the field, which remain very limited.

This is especially true in relation to the inherent multi-scale nature of turbulent flows. Indeed, in any given flow, large scale structures[2] can be generated by interaction of the mean flow with the boundary conditions (e.g., the geometrical details of the flow domain), by instability of the mean flow itself or by any suitable external forcing. For sufficiently high Re numbers, these structures are subjected to non-linear interactions but essentially unaffected by the viscosity of the fluid; thus, by vortex stretching, these structures break down into smaller structures. The non linear process acts on the smaller structures as well, breaking them into even smaller structures, until their size is small enough for the viscosity to dissipate their motion into heat. Quoting Richardson (1922, p. 66),

> *We realize thus that: big whirls have little whirls that feed on their velocity, and little whirls have lesser whirls and so on to viscosity - in the molecular sense.*

This *energy cascade* process has been given a first quantification by Kolmogorov in 1941, now known as K41 theory[3]. The fact that it is among the few relevant theoretical results available in turbulence[4], all of which are based on dimensional analysis,

[2] Flow structures can be loosely defined as coherent spatio/temporal patterns of velocity, having definite time and length scales.

[3] K41 is based on two hypotheses also known as dissipative anomaly and scale invariance, the second of which is now known to be not exactly satisfied because of intermittency, see Frisch (1995). In the context of the present work, this discrepancy has a clear definite effect on the numerical simulation of turbulent flows. However, to the best of the author's knowledge, this has been rarely investigated (Yakhot and Sreenivasan, 2005; Yakhot and Wanderer, 2011) and has never seen any practical application. Thus, from now on, this specific flaw of K41 is not considered anymore.

[4] An additional, notable, one being the work of Oberlack (2001) on parallel shear flows.

similarity assumptions or symmetries, just reflects the difficulty to make theoretical advancements in this field. On the other hand, while experimental analysis continues to be an invaluable tool in fluid dynamic research (Kim, 2012a), it is often limited by the operational conditions of the facilities and by the restricted set of collectible data for a given experiment; more importantly, it can be hardly justified in several industrial contexts, where multiple responses to design changes are needed within specific limits of time and cost.

These motivations have led to the rapid emergence of computational fluid dynamics (CFD), not only as a research tool on its own (Kim, 2012b; Moin and Mahesh, 1998) but also as a support for industrial design. However, despite the increasing availability of computational power[5], the multi-scale feature of turbulence, as emerges from the energy cascade picture, still remains a fundamental bottleneck in CFD, both for basic research and for applied analysis in industrial design. This is easily appreciated by considering a classical result of the K41 theory:

$$\frac{L}{\eta} \approx Re^{\frac{3}{4}} \tag{1.2}$$

which expresses the ratio between the largest and smallest, dynamically active, spatial scales in a turbulent flow as a function of the large scale Reynolds number; the same number, cubed, is also a rough measure of the required number of degrees of freedom needed to discretize the flow equations in a cubical domain of side L. As, for most applications, Re ranges from few thousands up to several millions, the number of degrees of freedom required to discretize a turbulent flow then ranges, roughly, from 10^6 to 10^{14} and beyond[6]. It is thus apparent that, even with an optimal distribution of such degrees of freedom and the twofold increase in computational power expected every 18 months from the Moore's Law, high Re turbulent flow simulations are precluded for the next few decades, with such a direct, brute force, approach also known as Direct Numerical Simulation (DNS)[7].

In order to make CFD feasible at high Re numbers, the only viable route is thus to remove some turbulent scales from the computation or, more correctly, to reduce the number of represented degrees of freedom with respect to the required one. Unfortunately, because of the non-linearity (e.g., the energy cascade), a dynamic coupling exists between the different scales and, independently from how such degrees of freedom are chosen and removed, their interactions with the resolved ones have to be properly taken into account. This approach, which is also useful in basic research (Biferale, 2003) but is fundamental for industrial applications of CFD, goes under different names that, for the sake of conciseness, but not without approximation, we summarize as *turbulence modeling*. The name essentially refers to the fact that, for numerical simulations using a reduced set of degrees of freedom, and according to the method used to

[5]The ten most powerful supercomputers at November 2013, as ranked by the TOP500 list (`www.top500.org`), have peak performances ranging from 2.9 Pflop/s up to 33.9 Pflop/s. These value represent, roughly, an increase of 7 and 20 times, respectively, of the same values as reported at the beginning of the author's Ph.D. course. Unfortunately, the author's machine has remained exactly the same.

[6]Sharper estimates for wall bounded flows are provided by Choi and Moin (2012).

[7]Additional factors, of course, affect the refurbishment of DNSs performed on the top HPC machines like, for example, the need to explore additional physical effects instead of the pure increase in Reynolds number. Thus, while in 2005 the 5^{th} fastest machine available in the world was used for a DNS employing around 18 billion degrees of freedom, in 2013 the 5^{th} fastest machine, 300 times faster than its predecessor, has been used on the same DNS with only a 2.5 factor increase of the Re number and 242 billion degrees of freedom.

reduce them, a statistical model (i.e., a surrogate for the missing degrees of freedom and their interactions) has to be introduced in order to correctly predict the dynamics of the flow under investigation.

Large Eddy Simulation (LES) is among such techniques used in turbulence modeling and the main topic of the present thesis, especially in relation to industrial computations, where its relevance is rapidly growing in the recent years (Tucker and Lardeau, 2009; Bouffanais, 2010). An overview of the approaches used in the numerical simulation of turbulent flows is given in the first section of this chapter and, among them, LES is first introduced and put in perspective in the second section. After this overview, the purpose and outline of the thesis are presented in the third section. Finally, the novel contributions of this work are briefly summarized in the fourth section.

1.1 Numerical simulation of turbulent flows

As emerged in the previous section, the key issue in the numerical simulation of turbulent flows, for all but the most trivial cases, is the simultaneous presence of a wide range of dynamically active spatial and temporal scales, all of which have to be represented in a numerically accurate way. Despite the practical limit due to the availability of sufficient computational power[8], DNS has nonetheless being strongly developed in the years, for simple geometries (Orszag and Patterson, 1972; Rogallo, 1981; Kim et al., 1987) as well as for more complex ones (Laizet and Lamballais, 2009; Cockburn and Shu, 1989; Wang, 2002; Liu et al., 2006; Patera, 1984) and remains a fundamental tool in research. However, for engineering applications, a conceptual limit also remains, due to the suitability of a DNS approach with respect to the answers required from the computation. It is, indeed, very common in design engineering to only require, say, mean flow rates in pipes, average heat fluxes trough surfaces or the drag and lift coefficient for a wing. While these are readily available in DNS too, it is also true that most of the costs involved in DNS are required to produce information which is then discarded, making the approach largely inadequate.

Among the turbulence modeling approaches, the one that first became established and still today is the workhorse in the engineering practice is based on the application of an averaging operator to the equations governing the motion of the fluid, the Navier-Stokes equations (NSE). More specifically, such an operator is an *operational* time average in the original view of Reynolds (1895) while, according to the modern *axiomatic* approach to probability, it is today intended as an ensemble average over an infinite set of identical experiments (Pope, 2000; Monin and Yaglom, 1971). With a slight misuse of nomenclature, such an approach leads to the so called Reynolds-Averaged Navier-Stokes (RANS) equations. The main advantage of the RANS approach is that it provides, as main dependent variables, the mean values as required in the engineering practice and, in doing so, it also avoids the description of any other physical flow scale. Which means that the resolution requirements of RANS computations are reduced to those of the mean quantities, and their possible symmetries or steadiness can be readily exploited in further reducing the computational costs. The downside in RANS is, of course, a direct consequence of the approach: every fluctuation of flow variables on every single scale has to be taken into account by the turbulence model. That is, the

[8] Memory, storage and bandwidth limitations exist as well.

turbulence model is responsible for the whole energy cascade[9]. The difficulty of the task is well clarified by the fact that modeled fluctuations include those in the wake of bluff bodies as well as those in attached boundary layers or in separation bubbles of diffusers. Because of such variability, as a matter of fact, RANS models are effectively tuned (by modifying adjustable parameters) to perform well in specific applications.

Between DNS and RANS, turbulence modeling also allows a full range of intermediate approaches that directly compute, instead of modeling, some scales (or degrees of freedom) and model the rest[10]. Indeed, with DNS still being unfeasible, there are, nonetheless, several specific cases for which, despite its formal correctness, the RANS approach simply does not perform well or is intrinsically inadequate. Typical examples of the first group are free shear flows, ranging from mixing layers to the wakes of bluff bodies and turbulent jets, in which the mean flow properties are influenced by most of the modeled turbulent scales. Cases from the second group are flows with instabilities, which by definition are smoothed out by the average[11], or where the deterministic evolution of the flow in a specific condition is of interest (in contrast to the average one), like in weather predictions or accident scenarios. In all such cases, the inclusion of some turbulent scales in the flow representation can mitigate the demanding task of the turbulence model and lead to better flow descriptions, while still keeping the computation feasible with respect to DNS.

LES belongs to this class of turbulence modeling approaches, its specificity being that the largest flow scales (or the related degrees of freedom) are directly resolved while the smallest ones, and their interactions with the former, are modeled. This distinguishing feature of LES and, as such, LES as a whole, is essentially motivated on the basis of the K41 theory, for which large scales carry most of the energy and are those directly affected by the geometrical features of the domain. In contrast, the small scales carry much less energy and are supposed to be independent from the geometric details of the flow, isotropic and similar among different flows. Thus, from one side, the relative low energy content of the modeled scales should make them relatively unimportant in determining the mean flow features; on the other side, their relative isotropy and similarity among different flows should also make them simple to be modeled (with respect to, say, RANS). More specifically, still according to K41, the small scales simply receive energy from the large ones, at a rate which is solely determined by the large scales, and dissipate it. Thus, a simple model capable of dissipating the exact amount of energy supplied by the large scales, should be a proper choice for LES (Ferziger and Leslie, 1979).

1.2 Large Eddy Simulation: a preliminary perspective

While the previous idealized picture of LES can be considered correct when the underlying assumptions hold, it is, nonetheless, subjected to various criticalities.

First and foremost, the separation between resolved large scales and modeled small ones and the operator determining it. It should be surprising at least, even for an LES

[9] More precisely, it is the effect of the cascade on the mean quantities.

[10] It might appear, at first, that Unsteady RANS (URANS) belongs to this category. However, this is not actually the case as, by definition, the unsteadiness tracked in URANS is not related to any turbulent scale but only to some externally imposed time scale. When the latter is missing, the significance of the results is open to debate (Sagaut, 2006). See, also, the next note.

[11] For several reasons this might not actually happen in the computational practice. Still, it has to be considered a flaw in the application of the RANS approach instead of a merit.

practitioner, to recognize that the first ever tentative formalization of such an operator is still due to Reynolds (1895), whose formalism was conceived in terms of temporal or *spatial averages*[12]. However, the spatial average formalism was soon abandoned by Reynolds because, as an average operator, it does not provide the same nice properties of the time average (Monin and Yaglom, 1971).

It is only with Leonard (1974) that the spatial averaging formalism is explicitly reintroduced and used as specific operator to obtain what, for the first time, is named "Large Eddy Simulation". In practice, Leonard identifies as large scales those produced by a weighted volume average and suggests, in order to produce an LES, to explicitly apply this weighted average to the convective terms of the equations at each time step[13]. The same procedure can also be interpreted, as indeed Leonard does, as a spatial filtering operation with the weight playing the role of the filter kernel; this immediately identify, qualitatively at least, the filter cut-off length Δ as the discriminating length scale between large resolved scales and small modeled ones[14]. Of course, for the procedure to be meaningful, Δ is required to be, somehow, bigger than the local dimension of the underlying computational grid cells, say h; at the same time, following K41, Δ is also required to be within the inertial range, that is smaller than any flow scale possibly affected by the geometry of the flow domain. Finally, under the hypotheses assumed by Leonard, the spatial average operator becomes a convolution operator and recovers most (but not all) of the desirable properties required by Reynolds; in particular, the governing equations in LES, the filtered NSE, become in many aspects similar to the URANS equations and modeling is required for the sub-grid scale (SGS) stresses, due to the application of the filter to the non-linear convective terms (a rough analogous of the Reynolds stresses arising in URANS).

However, even in 1974, the Leonard formalization was in strong contrast with the mainstream pioneering works on LES performed in the meteorological community (Smagorinsky, 1963; Lilly, 1967; Deardorff, 1970, 1971; Schumann, 1975). These were all essentially based on solving the original NSE, on a grid with spacing h, with a certain numerical method and supplementing them with a SGS model, responsible for the missing scales in the computation. Thus, not only the filtering formalism completely disappears, but the whole concept of scale separation now is linked to the grid (a la Nyquist), a typical assumption being $\Delta = h$, and the numerical method employed. In addition, more often than not, the SGS model itself is just an additional non-linear viscosity, borrowed from other fields (VonNeumann and Richtmyer, 1950), used to avoid a blow up of the simulation. It thus comes at no surprise at all that, with the development of computational methods and the diffusion of the LES approach, the difference between the original Leonard formalization and the actual LES practice has indeed become wider in the years (Reynolds, 1990; Pope, 2004). The main consequence of this is that, while most of the LES works are still today developed within the classical filtering framework, the actual practice is based on the most diverse approaches and even the basic issue of the scale separation, which determines which scales are actually solved, is not usually covered in detail.

A second important issue in LES is the underlying K41 theory, which is valid for

[12] The LES concepts introduced by Reynolds, in perspective, are quite advanced and rediscovered only more than 70 years later.

[13] The classical LES approach will be discussed at length in chapter 2. Here basic details only are introduced.

[14] In this picture, Δ is either an explicit parameter of the filter kernel or can be determined analytically, by some means, from its functional form.

homogeneous, isotropic turbulence (HIT) in the limit of infinitely high Reynolds numbers; and even in that case, it usually is an oversimplification. Indeed, the K41 view of the energy cascade is static, in the sense that the energy distribution at the different flow scales is assumed to be in equilibrium and to identically satisfy the well known $-5/3$ spectrum at each time, with energy continuously flowing toward the smallest scales at a fixed rate. However, this equilibrium assumption can be easily questioned, for example, when an external forcing exists, because the different scales differently adapt to the forcing, according to their specific time scale. Moreover, the same cascade picture is not exactly true, as the energy is also subjected to an inverse cascade process, also known as backscatter, going from the small scales to the larger ones and, in general, the two processes act at the same time. Thus, in LES, a simple dissipative model could actually not suffice to properly represent the missing scales and their interactions. Finally, the whole cascade process, assuming energy injection at the largest scales, can simply be incorrect.

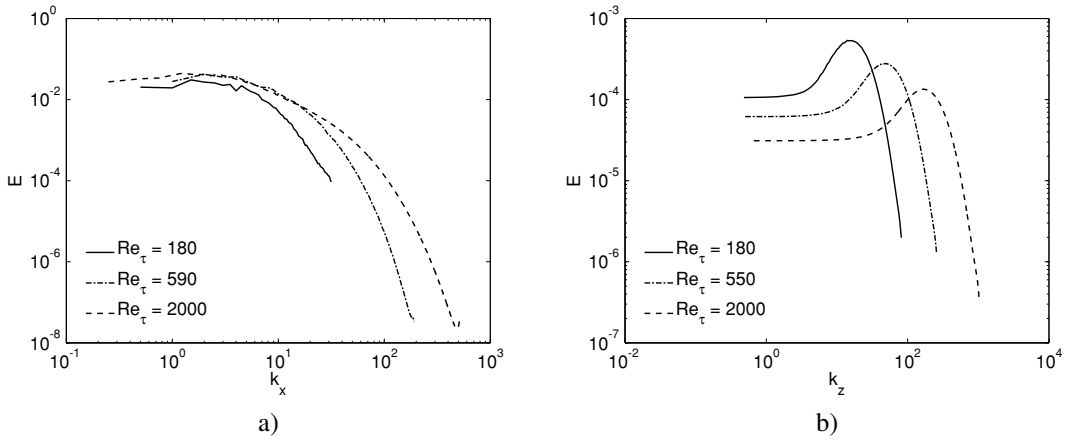

Figure 1.1: *Spectra of the wall-normal velocity component in a turbulent channel flow at different Reynolds numbers and distances from the wall, d. a) Stream-wise spectra at channel centerline, $d = H$; b) Span-wise spectra at $d \sim 5H/Re_\tau$. DNS data taken from Moser et al. (1999); Hoyas and Jiménez (2006); del Alamo and Jiménez (2003); del Alamo et al. (2004).*

An important example of this is in wall bounded flows. This is clearly shown in figure 1.1, where velocity spectra in two different regions of a turbulent channel flow are compared for different Reynolds numbers. Indeed, in the center of the channel (sub-figure a), where the influence of the walls is lower, the flow approximately behaves as in HIT and the cascade process is in rough accordance with the K41 theory; also, for sufficiently high Re numbers, an inertial range spectrum can be partly appreciated. In strong contrast, in the near wall region (sub-figure b) the energy is actually injected in the flow at the smallest scales, by vorticity production at the wall and sweeps/ejections (Brooke and Hanratty, 1993), leading to the formation of stream-wise vortices (Robinson, 1991), the overall process being largely self-sustaining besides the necessary mean shear at the wall (Jiménez and Pinelli, 1999). Of course, in this case, the energy cascade is mostly reversed. Also, these mechanisms are Re dependent and strongly anisotropic. Thus, not only a dissipative SGS model would hardly work properly but, even a more adequate model would still require, at least, a partial resolution of such mechanisms[15],

[15] By definition, a SGS model, however complex, is only based on the available information during the computation.

constraining the LES of wall-bounded flows to DNS-like scaling costs. This last issue has led, by itself, to a whole area of modeling (Piomelli and Balaras, 2002), whose efforts are devoted to the development of specific wall boundary conditions, which become fundamental for high Reynolds numbers typical of engineering applications (Fureby, 2008).

1.3 Purpose and outline of the thesis

The general purpose of the present thesis is the further development of LES toward its application in complex engineering flows. The vagueness of this statement, which is not accidental, is related to the fact that it is not possible (or anymore convenient) to develop LES without considerations on its specific numerical implementation. Actually, it is the author's opinion that LES should be a possibly exact theoretical framework for a generic numerical computation instead of, say, a possibly inexact application of a toy model within the most diverse numerical frameworks. The relevance of the correct approach for engineering applications becomes self-evident when most, if not all, of the assumptions underlying the classical LES framework (Leonard, 1974) are not verified, as is typically the case. In such circumstances, understanding the scale separation itself becomes arduous and the development of SGS models, strictly relying on it, can lead to erroneous results.

In order to achieve the proposed goal, the first necessary step, as presented in Chapter 2, is to analyze, assumption by assumption, the classical LES framework (from now on simply named as CLES) and to identify, if any, those assumptions which are limiting the applicability of CLES. This analysis will clearly point out how these are all related to the scale-separation operator, i.e., the filter, and that this has several influences on the resulting CLES framework and the related computational practice. This result also suggests, as next step, reformulating the LES problem without the unnecessary limiting assumptions. Such reformulation is performed in Chapter 3 and leads to several interesting results. Among these, the most important one is that, if properly formulated, a Genralized LES framework (from now on simply named GLES) is possible, which is applicable to most of the known LES approaches, either according to CLES or to the simple computational practice. As a matter of fact, as will be shown, it represents an exact theoretical model for a generic computational framework. A secondary aspect of such result is to show how some consolidated practices in LES are indeed wrong and unnecessarily complicated. As the intended goal of the thesis is the applicability of LES to engineering flows, a relevant part of this work is related to the finite volume (FV) method. There are several reasons for this, among which: the large flexibility of the method, including the possibility to describe both complex geometries and physics with a relatively low effort; the large availability of the method among commercial, open-source and in-house codes; the related, much larger, diffusion among CFD practitioners in the most diverse fields. As a consequence, the GLES framework is further developed, in Chapter 4, in relation to the FV method and a new SGS model is proposed. This SGS model is not simply dissipative in nature and can thus be more appropriate for a large class of flows, including wall bounded ones. It is also shown that, as GLES is a framework for a general computational approach, the proposed SGS model can be also interpreted as a modification of the basic FV discretization scheme.

It is worth emphasizing here that one of the main results from the previous two chapters is the identification of the FV method, as implemented in most available solvers, as an LES approach for which exact model equations can be written. As a consequence, the adoption of the proposed GLES framework with a FV code essentially amounts to use the code as it is and, in the present case, to the inclusion of a SGS model specifically developed for the method.

Having introduced the GLES framework and a specific SGS model for the FV method, the remaining part of the thesis is devoted to the validation of the proposed LES approach. In Chapter 5 the code adopted for the simulations, ANSYS® Fluent® 13.0, is first presented, together with the numerical settings relevant for the further developments. The choice of the code, which is certainly not immune to criticism, is essentially determined by the previously cumulated know-how on the code and the possibility to show the easiness of implementation of the proposed approach in such kind of code. Nonetheless, a specific section of the chapter is dedicated to the suitability of the code for LES, with particular emphasis on two aspects not specifically developed within this work: the numerical method and the generation of inflow boundary conditions. Finally, some implementation details related to the SGS model and the computation of the statistics in LES are also provided.

An additional aspect which is worth mentioning here is that, for the sake of generality, the whole content of the first four chapters is based on a general compressible formulation. However, all the validations and test cases are based on strictly incompressible flows. As such, the code presentation in chapter 5 is limited to the aspects relevant for this kind of flows.

The first proposed validation, presented in Chapter 6, is for the turbulent channel flow (Moser et al., 1999). Despite the strong contrast with the propositions of the thesis, and even its title, this choice is motivated by several reasons. First of all, as previously anticipated, it is a severe test case for LES and SGS models, due to its anisotropy and dependence from the resolution of the smallest scales, where the turbulence production mechanisms reside. At the same time, it is among the few, non trivial, cases not depending from initial or boundary conditions, which would further complicate the validation. Furthermore, despite its geometrical simplicity, the turbulent channel flow is representative of a general class of wall bounded flows and, more importantly, such kind of flows are usually present even in the most complex applications, either at the inflow or the outflow of the domain. Finally, it is possibly the most used benchmark for LES and allows comparisons with the most diverse codes. Indeed, part of this chapter is dedicated to the comparison of the different LES codes used within the LESinItaly group (Denaro et al., 2011; Abbà et al., 2013), an Italian collaborative framework focusing on the analysis of the performances of several LES codes. Besides providing and additional justification for the use of the code Fluent®, this comparison has evidenced several similarities among different codes and SGS models. This has motivated a deeper analysis of the LES of turbulent channel flows and the identification of possible mechanisms leading to such similarities.

The validation of the proposed SGS model is then extended to cases of increasing complexity in Chapter 7. The first proposed case is the turbulent pipe flow (Wagner et al., 2001; Wu and Moin, 2008). While having several similarities with the turbulent channel flow, the case naturally allows an unstructured discretization of the flow do-

main, it is thus well suited for a first test of the model on complex geometries. Also, the unstructured discretization for the case is found especially helpful in increasing the near-wall resolution without an excessive increase in the overall cell count for the grid, thus promoting tests also at higher Reynolds numbers. The second selected test case is the flow and heat transfer in a matrix of surface mounted cubes (Meinders and Hanjalić, 1999). While this case too shares some similarities with the channel flow case, it also introduces strong grid stretching in the flow direction and additional physics, like heat transfer, vortex shedding, flow separation and reattachment. However, very differently from the previous test cases, this flow is strongly influenced by large scale flow structures, thus allowing a test of the proposed SGS model in a case where its influence is not expected to be relevant. Finally, the SGS model developed in this thesis is validated in the case of the turbulent cold flow in a swirled combustor. The case, besides being representative of several combustion applications, has computational and physical features representative of a larger set of engineering flows, among which: regions of very scarce resolution, including toward the wall; strong grid stretching; physical inflow and outflow boundary conditions to be prescribed; complex flow physics, including separations, strong recirculation and fluid dynamic instabilities leading to the formation of large scale coherent structures. Experimental data for the comparison have been gathered with the support of the Combustion and Optical Diagnostic Group at the Department of Energy of Politecnico di Milano, both via Laser Doppler Velocimetry (LDV) and Particle Image Velocimetry (PIV).

The thesis is closed, in Chapter 8, with some conclusions drawn from the preceding tests and analyses. Possible future developments are also briefly discussed.

1.4 Novel contributions of this thesis

The novel contribution of this thesis can be summarized in the following points:

- a detailed analysis of the classical LES (CLES) framework in the more general compressible formulation and the identification of previously unnoticed inconsistencies and drawbacks of the formulation;
- the development of a general LES (GLES) framework which is an exact description for several practical LES approaches as well as for CLES;
- the further development of the GLES framework and the development of a novel SGS model for general unstructured FV codes ;
- the first application of such SGS model in cases of engineering interest by inclusion in a commercial CFD solver;
- the development of a single-pass, real time, algorithm for the parallel computation of weighted moments and co-moments, useful for the gathering of spatial/temporal statistics in LES with FV codes;
- an innovative analysis for the LES of the turbulent channel flow, with the identification of some of the mechanisms determining the prediction of mean quantities;

Finally, despite the lack of novelty, a strong personal contribution has been given to the creation of the LESinItaly database for the turbulent channel flow, which is available at `http://www.cfdlab.polimi.it/Research/Database.html`.

CHAPTER 2

The Classical LES framework

In this chapter, the basis of the classical LES (CLES) framework are reviewed. For the sake of convenience, the set of governing equations, as used in DNS, is first summarized in section 2.1. The basis of CLES are first introduced in section 2.2 and the the two main known approaches in CLES, based on implicit or explicit filtering of the equations, are first delineated in section 2.3. A detailed presentation of the two methods, including the relative SGS modeling approaches, is instead reported in Section 2.4. Finally, section 2.5 contains a resume of the main assumptions used in CLES and the consequences deriving from them. For the sake of generality, this presentation is based on the compressible form of the equations, whose main references are Garnier et al. (2009) and Wagner et al. (2007). Nonetheless, most of the concepts and details which are not specific of compressible flows are covered in greater detail by Sagaut (2006). However, it is important to stress again that the presentation given here is only representative of the basic LES approach. Several proposals for LES have emerged in the years (Boris et al., 1992; Margolin, 2009; Geurts and Holm, 2003; Guermond et al., 2004; Verstappen, 2008; Trias et al., 2010; Knaepen et al., 2005; Stolz and Adams, 1999), but most of these are better represented in the new GLES framework developed in Chapter 3, as this is actually one of the main goals of the thesis.

2.1 The Navier-Stokes equations

Under the continuum hypothesis, the conservation of mass, momentum and energy for a fluid medium are described by the Navier-Stokes equations (NSE):

$$\begin{aligned}
&\frac{\partial \rho}{\partial t} + \frac{\partial}{\partial x_j}\left(\rho u_j\right) = 0 \\
&\frac{\partial \left(\rho u_i\right)}{\partial t} + \frac{\partial}{\partial x_j}\left(\rho u_i u_j + \sigma_{ij}\right) = 0 \\
&\frac{\partial \left(\rho E\right)}{\partial t} + \frac{\partial}{\partial x_j}\left(\rho u_j E + q_j + u_i \sigma_{ij}\right) = 0
\end{aligned} \tag{2.1}$$

where the convention of summation over repeated indices hold. In equation (2.1), the independent variables t and x_i refer, respectively, to the time and spatial coordinates; u_i represents the velocity vector and ρ is the density of the fluid. The energy equation is formulated in terms of the total energy per unit mass E (Kosovic et al., 2002):

$$\rho E = \rho e + \frac{1}{2}\rho u_k u_k \tag{2.2}$$

where e is the internal energy per unit mass. Alternative formulations for the energy equation are possible (Poinsot and Veynante, 2005) and have been used in LES as well (Garnier et al., 2009; Piomelli, 1999); however, for the sake of comparison with the approach proposed in Chapter 3 and with alternative LES proposals (e.g., Stolz and Adams), the present formulation is found more suitable and thus adopted. Even though the formulation in (2.1) allows the treatment of most fluids in nearly all the conditions, for the sake of simplicity, only single-species, mono-phase, non-reactive, gaseous flows in local thermodynamic equilibrium are considered, so that an ideal gas equation of state can be assumed to hold:

$$p = \rho R T \tag{2.3}$$

where T and p are, respectively, the temperature and pressure of the fluid. $R = C_p - C_v$ is the gas constant, with C_p and C_v being the specific heats at constant pressure and volume. Under these conditions:

$$\rho e = \frac{p}{\gamma - 1} \tag{2.4}$$

with $\gamma = C_p/C_v$. Finally, it is further assumed that variations of the specific heats with the temperature can be neglected[1] (i.e., a calorically perfect gas).

[1] All these assumptions are easily removed, at least formally, without adding specific issues to the formulation, besides physical modeling ones.

The stress tensor σ_{ij} and the heat flux vector q_j are assumed to follow the Newton-Stokes-Fourier hypotheses:

$$\begin{aligned}
\sigma_{ij} &= p\delta_{ij} - 2\mu\left(S_{ij} - \frac{1}{3}S_{kk}\delta_{ij}\right) = p\delta_{ij} + \Sigma_{ij} \\
S_{ij} &= \frac{1}{2}\left(\frac{\partial u_i}{\partial x_j} + \frac{\partial u_j}{\partial x_i}\right) \\
q_j &= -\lambda\frac{\partial T}{\partial x_j}
\end{aligned} \tag{2.5}$$

where δ_{ij} is the Kronecker's delta, S_{ij} is the strain rate tensor and $\mu(T)$ and $\lambda(T)$ are the dynamic viscosity and the thermal conductivity of the fluid. According to the previous hypotheses, both depend on the temperature T only and are related trough the constant Prandtl number $Pr = C_p\mu/\lambda$.

2.2 The filtering approach to the scale separation

In the approach originally devised by Leonard (1974), the separation between the large resolved scales and the small, non resolved, ones is formally achieved by applying a spatial filtering operator[2] to the NSE (2.1). For a generic scalar field ϕ, such filtering operation, denoted by an overbar, is usually defined as::

$$\bar{\phi}\left(\mathbf{x}, t, \bar{\Delta}\right) = G * \phi(\mathbf{x}, t) = \int_{\Omega} G\left[\mathbf{x}, \boldsymbol{\xi}, \bar{\Delta}(\mathbf{x})\right]\phi(\boldsymbol{\xi}, t)\,\mathrm{d}\boldsymbol{\xi} \tag{2.6}$$

where Ω is the flow domain and G is the filter kernel which, in the most general case, has a width $\bar{\Delta}$ with an explicit dependence on the spatial coordinates[3]. The operation (2.6) is intended to be high-pass filtering in space, and leads to the following decomposition for ϕ:

$$\phi = \bar{\phi} + \phi' \tag{2.7}$$

Ideally, $\bar{\phi}$ represents the resolved, large-scale, component of ϕ and ϕ' is the unresolved SGS component. However, this sharp distinction somehow implies the presence of a computational grid or the use of a projection filter (e.g., $G * G * \phi = G * \phi$) while, in more general cases, ϕ' also has resolvable components, referred to as subfilter scales (SFS). More generally, $\bar{\phi}$ and ϕ' represents the parts of ϕ whose spatial scales are approximately larger and smaller, respectively, than the filter width $\bar{\Delta}$. Because of this

[2] LES can be also conceived in a temporal filtering framework or, more generally, in a general spatial/temporal filtering framework. As the two approaches can be generally advanced in parallel, due to the independence of spatial and temporal coordinates, and the temporal approach, in particular, is much less problematic and sufficiently developed (Pruett, 2008), the present thesis is focused on the spatial filtering approach only. Of course, both approaches are based on the rationale that filtering in space is also effective on the relative time scales and the converse.

[3] The dependence on temporal coordinates is possible as well (Leonard et al., 2007). However, it is usually needed in very specific applications, like internal combustion engines, or generally moving grids, whose use in LES is still limited by the computational costs. As such, it is not considered in the present thesis.

distinction, and because the present exposition is intended to just delineate the theoretical CLES framework, whose practical application is instead described in the following sections, the list of classical filters used in LES is deliberately omitted here. It is just worth mentioning that, for the following developments, the filter is also required to be linear and preserve the constants, two properties met by all the known theoretical and practical filters. Before applying the operator (2.6) to the NSE, it is a common, useful, practice to also introduce the Favre transformation[4] (Favre, 1983):

$$\tilde{\phi} = \frac{\overline{\rho\phi}}{\bar{\rho}} \tag{2.8}$$

Under these conventions, and without any further assumption, the filtered Navier-Stokes equations (FNSE) in the CLES framework follow:

$$\begin{aligned}
&\frac{\partial \bar{\rho}}{\partial t} + \overline{\frac{\partial}{\partial x_j}\left(\rho u_j\right)} = 0 \\
&\frac{\partial \left(\bar{\rho}\tilde{u}_i\right)}{\partial t} + \overline{\frac{\partial}{\partial x_j}\left(\rho u_i u_j + \sigma_{ij}\right)} = 0 \\
&\frac{\partial \left(\bar{\rho}\tilde{E}\right)}{\partial t} + \overline{\frac{\partial}{\partial x_j}\left(\rho u_j E + q_j + u_i \sigma_{ij}\right)} = 0 \\
&\bar{p} = \bar{\rho} R \tilde{T}
\end{aligned} \tag{2.9}$$

As presented, the set of equations (2.9) is not closed, as it provides evolution equations for filtered quantities in terms of non-filtered ones. In order to further proceed toward a closed set of equations, the main assumption *always* used in CLES is that the filter operator G commutes with the spatial derivatives operators[5] (Ghosal and Moin, 1995; Fureby and Tabor, 1997; Vasilyev, 2001):

$$G * \left[\frac{\partial}{\partial x_j}\left(\cdots\right)\right] = \frac{\partial}{\partial x_j}\left[G * \left(\cdots\right)\right] \tag{2.10}$$

whose implications will be discussed at length in the next sections. If the filter G satisfies the additional condition (2.10), the equations (2.9) then become:

$$\begin{aligned}
&\frac{\partial \bar{\rho}}{\partial t} + \frac{\partial}{\partial x_j}\left(\bar{\rho}\tilde{u}_j\right) = 0 \\
&\frac{\partial \left(\bar{\rho}\tilde{u}_i\right)}{\partial t} + \frac{\partial}{\partial x_j}\left(\bar{\rho}\widetilde{u_i u_j} + \bar{\sigma}_{ij}\right) = 0 \\
&\frac{\partial \left(\bar{\rho}\tilde{E}\right)}{\partial t} + \frac{\partial}{\partial x_j}\left(\bar{\rho}\widetilde{u_j E} + \bar{q}_j + \overline{u_i \sigma_{ij}}\right) = 0 \\
&\bar{p} = \bar{\rho} R \tilde{T}
\end{aligned} \tag{2.11}$$

[4] Again, it is interesting to know that the specific operator in (2.8) has been actually introduced by Reynolds (1895).
[5] Commutation with time derivatives, as already implied, is always verified for spatial, time-independent filters.

where computable quantities are the filtered pressure $\bar{p}$ and density $\bar{\rho}$, the Favre transformed filtered velocity components $\tilde{u}_i$ and the total energy $\tilde{E}$. It is worth noting how condition (2.10) is necessary and sufficient in order to have a closed continuity equation. Also, the equation of state is closed independently of any assumption. However, non-linearities prevent equations (2.11) from being closed yet. More specifically, three class of terms require closure:

- Filtered convective terms in the momentum and energy equations and the in the definition of the total energy, due to the non commutation between the filtering and the product.
- Filtered viscous stress tensor and heat flux vector. These are due to the fact that, from equations (2.11), Favre filtered variables $\tilde{u}_i$ and $\tilde{T}$ are known while, for constant molecular coefficients, the two terms depend on the simply filtered variables $\bar{u}_i$ and $\bar{T}$. Non-linearities due to the temperature dependence of the molecular coefficients μ and λ additionally complicate the matter.
- Filtered diffusion term $u_i\sigma_{ij}$ in the energy equation, due to a combination of the previous two.

The last step in CLES consists in arranging the different terms in (2.11) in order to obtain the final set of governing equations, to be supplemented with proper SGS models for the non closed terms. However, the arrangement of the terms also reflects the specific approach adopted in CLES and the resulting SGS modeling.

2.3 Filtering: Implicit vs. Explicit

The CLES framework, as delineated in the previous section, only represents a limited view on the subject and, in some cases, can greatly differ from the computational practice. Indeed, the basic CLES framework can be further divided in two main areas: the implicit and the explicit filtering approaches.

In the implicit filtering approach, the one already adopted before the Leonard formalization and certainly the most diffused still today, no actual filtering operation is ever invoked. Instead, it is essentially based on solving the equations (2.1) with the available spatial resolution, possibly supplementing them with a SGS model. Thus, the scale separation between large and small scales is assumed to be implicitly determined by: the grid, which for a step h can only solve spatial frequencies up to the wavenumber $k_c = \pi/h$; the numerical method, whose truncation error acts on the smallest resolved scales as an additional filter; the SGS model itself, if present, whose formulation can alter the energy fluxes toward the smallest scales, acting effectively as an additional filter (Mason and Callen, 1986; Muschinski, 1996; Magnient et al., 2001).

In contrast, the explicit filtering approach is essentially based on the approach proposed by Leonard (1974), further developed in the years (Lund, 2003; Gullbrand and Chow, 2003) up to the more recent standards (Bose et al., 2010; Singh et al., 2012). In practice, it is based on explicitly filtering the convective terms of the equations with a numerical filter which, in theory, should satisfy the hypotheses assumed in the previous section, i.e., (2.10).

In order to better understand the distinguishing features of the two approaches, and for the sake of simplicity, it is educative applying the filter G to a simpler scalar conservation law:

$$\frac{\partial \phi}{\partial t} + \nabla \cdot \mathbf{F}\left(\phi\right) = 0 \tag{2.12}$$

where $\mathbf{F}$ denotes a generic, nonlinear, flux function. Upon application of the filter, under the hypotheses of the previous section, and after a spatial discretization, equation (2.12) can be rearranged in two formally equivalent, exact forms[6] (Denaro, 2011):

$$\frac{\partial \bar{\phi}}{\partial t} + \nabla^d \cdot \mathbf{F}_M^d\left(\bar{\phi}\right) = \underbrace{\nabla \cdot \left[\mathbf{F}_M\left(\bar{\phi}\right) - \mathbf{F}\left(\phi\right)\right]}_{\text{I}} + \underbrace{\nabla \cdot \left[\mathbf{F}\left(\phi\right) - \overline{\mathbf{F}\left(\phi\right)}\right]}_{\text{II}} + \tag{2.13a}$$
$$+ \underbrace{\nabla^d \cdot \left[\mathbf{F}_M^d\left(\bar{\phi}\right) - \mathbf{F}_M\left(\bar{\phi}\right)\right] + \left[\nabla^d - \nabla\right] \cdot \mathbf{F}_M\left(\bar{\phi}\right)}_{\text{III}}$$

$$\frac{\partial \bar{\phi}}{\partial t} + \nabla^d \cdot \overline{\mathbf{F}_M^d\left(\bar{\phi}\right)}^d = \underbrace{\nabla \cdot \overline{\left[\mathbf{F}_M\left(\bar{\phi}\right) - \mathbf{F}\left(\phi\right)\right]}^d}_{\text{I}} + \underbrace{\nabla \cdot \left[\overline{\mathbf{F}\left(\phi\right)}^d - \overline{\mathbf{F}\left(\phi\right)}\right]}_{\text{II}} \tag{2.13b}$$
$$+ \underbrace{\nabla^d \cdot \overline{\left[\mathbf{F}_M^d\left(\bar{\phi}\right) - \mathbf{F}_M\left(\bar{\phi}\right)\right]}^d + \left[\nabla^d - \nabla\right] \cdot \overline{\mathbf{F}_M\left(\bar{\phi}\right)}^d}_{\text{III}}$$

where the superscript d denotes the spatial discretization and the subscript M implies that the flux function $\mathbf{F}$ has been possibly modified with a model, to take into account the non resolvable terms. The meaning of equations (2.13) is that the terms on the left hand sides are those actually retained in actual computations, while those on the right hand side are those neglected and can be assumed to be the error in doing such approximation[7]. Here, equation (2.13a) refers to the implicit filtering approach and equation (2.13b) refers to the explicit filtering one, as can be easily understood by the presence of the additional, discretized, filter level on the left hand side.

With equations (2.13) at hand, it is possible to analyze the differences among the two approaches by looking at the respective errors on the right hand sides. Among the three groups of terms evidenced, it appears that terms I and III are shared by the two approaches, with the difference that in the explicit filtering approach they are acted upon by the discrete filter. In particular, terms I represent modeling errors, while terms III represent discretization errors. It is thus apparent that, as both these terms are mostly concentrated on the smallest resolved scales, in the explicit filtering approach they can actually be filtered out by a proper selection of the filter. In contrast, the implicit filtering approach does not allow such possibility and the consistency of the resolved equation with respect to the original one is strongly determined by the specificities of

[6] The fact that the two equations are still exact can be easily verified as, with respect to the original equation (2.12), the additional terms appearing in equations (2.13) exactly cancel each other.

[7] In practice, the approach is similar to the one used to obtain the local truncation errors of discretization schemes. The only difference here is the presence of both filtered and unfiltered continuous terms together with the numerical solution $\bar{\phi}$ that is known only at grid points. Consistency is restored by intending the numerical solution to be an interpolant for the given grid points. This topic will be further discussed in chapter 3.

the term III, which are usually unknown and different among different codes as due to the numerical method.

The key factor in the explicit filtering approach is thus the proper selection of the filter which, in order to overwhelm the contribution III, needs to have a width $\bar{\Delta}$ somehow larger than the local grid spacing, say h. In practice, the required ratio $\bar{\Delta}/h$ is a decreasing function of the accuracy of the method and, in the limit of infinite accuracy, this ratio can be unity. However, it is worth noting that, while term I is still under the filtering operation, it is not usually subjected to the same reduction with increasing filter width, as it involves the difference $\mathbf{F}_M\left(\bar{\phi}\right) - \mathbf{F}\left(\phi\right)$, which usually increases unless a perfect model is employed. In practice, in the explicit filtering approach the numerical error is filtered out but the SGS model assumes a stronger role.

The distinction among the two approaches is completed by looking at the terms II, which could be defined as consistency errors, as they do not actually influence the evolution of $\bar{\phi}$ but only its interpretation. In the explicit filtering approach this can be made null by simply assuming that the discretized filter is, indeed, the one originally wanted, so that no error arises in the implementation of the filter. Something which is not usually noted, however, is the presence of an analogous term in the implicit filtering approach, which leads to a catastrophic conclusion. Indeed, this term implies completely unknown functions only, including the filter which is unspecified, and no practical or conceptual choices can ever influence it. In practice, the filter being unspecified, the meaning of the resolved variable $\bar{\phi}$ is completely determined by terms I and III, and in turn determines the term II. The informed reader will notice how terms I and II are usually combined in the implicit filtering approach, so that the model in $\mathbf{F}_M$ is also meant to include information about the filter, somehow restoring a form of consistency; however, this does not circumvent the fact that the filter itself is determined by the numerical method (term III), so that any numerical method should have its specific SGS model, something which is in contrast with the actual practice in LES.

The dependency of the implicit filtering approach on the numerical method and the grid itself is nowadays well recognized (Ghosal, 1996; Kravchenko and Moin, 1997; Fedioun et al., 2001; Chow and Moin, 2003; Park et al., 2004; Meyers and Sagaut, 2007), as the fact that, for some specific numerical methods (e.g., finite differences), it can lead to a complete lack of connection with the original NSE[8] (Lund, 2003; Bose et al., 2010). However, despite these limitations, the approach is largely diffused and motivated by the observation that no model for the non resolvable terms can actually be more effective than directly increasing the set of resolved scales, even if corrupted by the numerical error. Also, the simplicity of the method is a key feature. Moreover, theoretical results (Park and Mahesh, 2007a) and computational evidence (Majander and Siikonen, 2002) exist which indicate that numerical errors in implicitly filtered LES might not completely overwhelm SGS model effects when considered in a posteriori tests (i.e., actual computations), especially for high Reynolds number flows.

It is informative to bring forward here that one of the main goals of this thesis is to show that, despite appearances, most of the known numerical methods can actually be put in the form (2.13b). Thus, both the explicit and the implicit filtering approaches can be described within a single framework which has, at least, a formal consistency. A key

[8] In the sense that the resulting equations could not be obtained by applying a single operator to the NSE but different ones for the different terms.

step in such derivation, somehow surprisingly, will be the elimination of the condition (2.10).

2.4 Practical CLES

Having delineated the basis of the two main approaches in CLES, this section is devoted to a full description of the two methods when applied in further manipulating equations (2.11). The implicitly filtered classical LES approach (IFCLES) is described first, as it also corresponds to the most common form of CLES. The explicitly filtered classical LES approach is described next.

2.4.1 Implicitly filtered CLES (IFCLES)

In this case, the filtered unclosed terms in equations (2.11) are replaced by their computable parts. Thus, the equations are simply discretized starting from the following continuous template:

$$\begin{aligned}
\frac{\partial \bar{\rho}}{\partial t} + \frac{\partial}{\partial x_j}\left(\bar{\rho}\tilde{u}_j\right) =& 0 \\
\frac{\partial\left(\bar{\rho}\tilde{u}_i\right)}{\partial t} + \frac{\partial}{\partial x_j}\left(\bar{\rho}\tilde{u}_i\tilde{u}_j + \tilde{\sigma}_{ij}\right) =& \frac{\partial}{\partial x_j}\underbrace{\left(\bar{\rho}\tilde{u}_i\tilde{u}_j - \bar{\rho}\widetilde{u_i u_j}\right)}_{\text{I}} + \frac{\partial}{\partial x_j}\underbrace{\left(\tilde{\sigma}_{ij} - \bar{\sigma}_{ij}\right)}_{\text{II}} \\
\frac{\partial\left(\bar{\rho}\tilde{E}\right)}{\partial t} + \frac{\partial}{\partial x_j}\left(\bar{\rho}\tilde{u}_j\tilde{E} + \tilde{q}_j + \tilde{u}_i\tilde{\sigma}_{ij}\right) =& \frac{\partial}{\partial x_j}\underbrace{\left(\bar{\rho}\tilde{u}_j\tilde{E} - \bar{\rho}\widetilde{u_j E}\right)}_{\text{III}} \\
& + \frac{\partial}{\partial x_j}\underbrace{\left(\tilde{q}_j - \bar{q}_j\right)}_{\text{IV}} + \frac{\partial}{\partial x_j}\underbrace{\left(\tilde{u}_i\tilde{\sigma}_{ij} - \overline{u_i\sigma_{ij}}\right)}_{\text{V}}
\end{aligned} \tag{2.14}$$

with:

$$\begin{aligned}
\tilde{\sigma}_{ij} &= \bar{p}\delta_{ij} - 2\tilde{\mu}\left(\tilde{S}_{ij} - \frac{1}{3}\tilde{S}_{kk}\delta_{ij}\right) = \bar{p}\delta_{ij} + \tilde{\Sigma}_{ij} \\
\tilde{S}_{ij} &= \frac{1}{2}\left(\frac{\partial\tilde{u}_i}{\partial x_j} + \frac{\partial\tilde{u}_j}{\partial x_i}\right) \\
\tilde{q}_j &= -\tilde{\lambda}\frac{\partial\tilde{T}}{\partial x_j} \\
\bar{\rho}\tilde{E} &= \frac{\bar{p}}{\gamma - 1} + \frac{1}{2}\bar{\rho}\tilde{u}_k\tilde{u}_k + \frac{1}{2}\bar{\rho}\underbrace{\left(\widetilde{u_k u_k} - \tilde{u}_k\tilde{u}_k\right)}_{\text{VI}}
\end{aligned} \tag{2.15}$$

where $\tilde{\mu}$ and $\tilde{\lambda}$ refer, respectively, to $\mu(\tilde{T})$ and $\lambda(\tilde{T})$. As the filtered nonlinear terms, listed in section 2.2, have been substituted by straight computable quantities, SGS models needs to be introduced for the unclosed terms I-VI. Notice that, when SGS models

are effectively introduced in equations (2.14), no explicit reference to the filter remains besides, possibly, the filter width $\bar{\Delta}$ in the SGS model itself. If necessary, this has to be estimated by some grid related parameter, a common choice being $\bar{\Delta} = h$ for uniform grids with step h or $\bar{\Delta} = V^{\frac{1}{3}}$ for FV codes, where V is the volume of the computational cell.

2.4.2 SGS Modeling in IFCLES

For general compressible flows, no matter what approach is used, SGS modeling is usually required for several different terms, with respect to the sole convective ones for incompressible flows, and most of these arise in the energy equation. As this thesis is not devoted to the analysis of the energy equation nor to propose SGS models for all its unclosed terms, the present discussion is, for the sake of conciseness, limited to the closure of the convective terms only, I-III-VI in equations (2.14) and (2.15). A detailed description on the modeling of the remaining terms can be found in Garnier et al. (2009); Piomelli (1999); Vreman et al. (1995a); Knight et al. (1998).

A further manipulation is usually performed, on the terms III and V, to show that:

$$\begin{aligned}
\left(\bar{\rho}\tilde{u}_j\tilde{E} - \bar{\rho}\widetilde{u_jE}\right) + \left(\tilde{u}_i\tilde{\sigma}_{ij} - \overline{u_i\sigma_{ij}}\right) = \\
\tilde{u}_j\left(\bar{\rho}\tilde{E} + \bar{p}\right) - \overline{u_j\left(\rho E + p\right)} + \left(\tilde{u}_i\tilde{\Sigma}_{ij} - \overline{u_i\Sigma_{ij}}\right) = \\
\left(\tilde{u}_j\bar{p} - \overline{u_jp}\right)\left(1 + \frac{1}{\gamma - 1}\right) + \frac{\bar{\rho}}{2}\left(\tilde{u}_j\widetilde{u_ku_k} - \widetilde{u_ju_ku_k}\right) + \left(\tilde{u}_i\tilde{\Sigma}_{ij} - \overline{u_i\Sigma_{ij}}\right) = \\
\bar{\rho}C_p\left(\tilde{u}_j\tilde{T} - \widetilde{u_jT}\right) + \frac{\bar{\rho}}{2}\left(\tilde{u}_j\tilde{u}_k\tilde{u}_k - \widetilde{u_ju_ku_k} + \tilde{u}_jVI\right) + \left(\tilde{u}_i\tilde{\Sigma}_{ij} - \overline{u_i\Sigma_{ij}}\right) =
\end{aligned} \tag{2.16}$$

where the equation of state has been used in the last step. Hence, in the present thesis, SGS modeling is limited to the SGS stresses:

$$\tau_{ij} = -\bar{\rho}\left(\widetilde{u_iu_j} - \tilde{u}_i\tilde{u}_j\right) \tag{2.17}$$

and the SGS heat flux:

$$\theta_j = -\bar{\rho}C_p\left(\widetilde{u_jT} - \tilde{u}_j\tilde{T}\right) \tag{2.18}$$

Modeling options for the SGS stresses can be divided in two major classes (Sagaut, 2006): functional and structural models. Functional models are designed to model the energy transfer mechanisms between resolved and unresolved scales, without explicitly considering the exact structure of the SGS stress tensor τ_{ij}. Structural models, in contrast, are aimed at reconstructing the SGS stress tensor τ_{ij} without explicitly considering the energy transfers between the scales. Combining the two options, with the so called mixed models, is also effective. Modeling options for the SGS heat flux are then usually devised by mimicking those for the SGS stresses.

Functional models

The basic hypothesis underlying the explicit functional modeling is that the action of the sub-grid scales on the resolved scales is essentially an energetic action, so that the balance of the energy transfers between the two scale ranges is sufficient to describe the action of the unresolved scales. Thus, in general, these models modify the equations by adding the desired dissipation or energy production effects into them. In practice, instead of τ_{ij} itself, these models are aimed at representing, in a statistical sense, the action of the subgrid dissipation term $\tau_{ij}\partial\tilde{u}_i/\partial x_j$. However, as a matter of fact, most functional models, and those considered here as well, only consider the direct energy cascade and are based on eddy viscosity/conductivity assumptions (Smagorinsky, 1963; Eidson, 1985):

$$\begin{aligned} \tau_{ij}^d &= \tau_{ij} - \frac{1}{3}\delta_{ij}\tau_{kk} = 2\bar{\rho}\nu_{sgs}\left(\tilde{S}_{ij} - \frac{1}{3}\tilde{S}_{kk}\delta_{ij}\right) \\ \theta_j &= \frac{C_p\bar{\rho}\nu_{sgs}}{Pr_{sgs}}\frac{\partial\tilde{T}}{\partial x_j} \end{aligned} \tag{2.19}$$

where ν_{sgs} is the SGS viscosity, dependent on the specific model in use, and Pr_{sgs} is the SGS Prandtl number, a constant to be specified. The isotropic part of τ_{ij}, also needed for term VI in (2.15) and (2.16), is generally neglected (Erlebacher et al., 1992), modeled according to Yoshizawa (1986) or with a dedicated transport equation (e.g., Schumann); for incompressible flows it is instead absorbed in the pressure term.

The assumptions (2.19) are just variable density extensions of those usually employed for incompressible flows, according to the fact that compressibility effects on the subgrid scales are negligible for most supersonic flows (Erlebacher et al., 1992). They can also be partly justified by looking at the resolved dissipation term in IFCLES which, according to the K41 theory, in the incompressible limit has the following inertial range estimate :

$$-\tilde{\Sigma}_{ij}\frac{\partial\tilde{u}_i}{\partial x_j} \sim \mu\left[\frac{u\left(l\right)}{l}\right]^2 \sim \mu\left(\frac{u_0}{l_0}\right)^2\left(\frac{l_0}{l}\right)^{\frac{4}{3}} = \mu\left(\frac{u_0}{l_0}\right)^2\frac{Re_0}{Re\left(l\right)} = \rho\frac{u_0^3}{l_0}\frac{1}{Re\left(l\right)} \tag{2.20}$$

where l is a generic length scale within the inertial range, with associated characteristic velocity $u(l)$[9] and Reynolds number $Re(l)$, while u_0 and l_0 are relative to the largest scales, whose characteristic Reynolds number is Re_0. It is thus apparent that, for a numerical computation whose smallest resolved scale l is within the inertial range (as LES is intended to be), the resolved dissipation term cannot equal the energy transfer rate from the large scales, as $Re(l) \sim 1$, by definition, is relative to the dissipative scales. Hence, in order to prevent the energy pile-up at the smallest resolved scales (possibly leading to the simulation blow-up), the molecular dynamic viscosity should be supplemented by a SGS viscosity of the form $\mu_{sgs} = \rho\nu_{sgs} = [\rho l^2/t(l) - \mu]$, with

[9] It is assumed here that $u\left(l\right) \sim u_0(l/l_0)^{1/3}$.

$t(l)$ the characteristic time associated to the scale l[10], so that:

$$(\mu_{sgs}+\mu)\left[\frac{u(l)}{l}\right]^2=\rho\frac{l^2}{t(l)}\left[\frac{u(l)}{l}\right]^2=\rho\frac{u(l)^2}{t(l)}\sim\rho\frac{u_0^2}{t_0}=\rho\frac{u_0^3}{l_0} \tag{2.21}$$

and the resolved dissipation can then sustain the flow of energy from the largest scales independently from l. While the inclusion of the molecular viscosity is, in theory, necessary for any finite Reynolds number, it is usually neglected and ν_{sgs} is seek in the form $l^2/t(l)$, or the equivalent one $lu(l)$[11]. By definition, the smallest resolved scale in LES is related to the filter width $\bar{\Delta}$, thus, up to a constant, $l=\bar{\Delta}$ and all the SGS models differ by the way they specify the time scale $t(l)$ or the velocity scale $u(l)$.

The simplest and most diffused SGS model is the one developed by Smagorinsky (1963), which assumes:

$$\nu_{sgs}=\left(C_s\bar{\Delta}\right)^2\sqrt{2\tilde{S}_{ij}\tilde{S}_{ij}} \tag{2.22}$$

where C_s, which is a constant usually assumed to be in the range $0.1-0.2$, can be interpreted as the ratio $l/\bar{\Delta}$ and is, instead, a flow dependent quantity (Yoshizawa, 1989). A typical example of this flaw is in the limiting behavior of the model near the walls, which provides a constant SGS viscosity instead of scaling with the cube of the distance from the wall. For this reason, the Smagorinsky model is usually supplemented with a near-wall damping function f_w, so that the final form of the model is:

$$\nu_{sgs}=\left(C_s f_w\bar{\Delta}\right)^2\sqrt{2\tilde{S}_{ij}\tilde{S}_{ij}} \tag{2.23}$$

Denoting the distance from the wall as y, typical forms of such function are:

$$f_w(y)=1-\exp\left(-yu_\tau/25\nu\right) \tag{2.24}$$

according to van Driest (1956), or:

$$f_w(y)=\sqrt{1-\exp\left[-\left(yu_\tau/25\nu\right)^3\right]} \tag{2.25}$$

in order to restore the cubic near-wall behavior for ν_{sgs}. However, usually, in unstructured codes the distance from the wall is not a directly available geometrical quantity, but is instead approximated by the means of a toy transport equation. In this case, thus, as $u_\tau=\sqrt{\tau_w/\rho}$ and the wall shear stress τ_w is not directly available, there is the need to resort to simpler formulations. For example, in Fluent®, the following option is adopted (ANS, 2010):

$$\nu_{sgs}=\left[\min\left(C_s\bar{\Delta},ky\right)\right]^2\sqrt{2\tilde{S}_{ij}\tilde{S}_{ij}} \tag{2.26}$$

[10] It is assumed here that $t(l)\sim t_0(l/l_0)^{2/3}$.

[11] In practice, the present analysis is still incorrect, because inertial range arguments are not anymore valid in the dissipative range, where the molecular viscosity becomes relevant. It turns out that a better fit is given by $\rho\nu_{sgs}=\sqrt{\rho^2l^4/t^2(l)+\mu^2}-\mu$, see Meyers and Sagaut (2006)

where $k = 0.4187$ is the von Kármán constant used in the code. In general, $\bar{\Delta}$ can also vary in space (especially near the walls) as in IFCLES it is connected to the grid, thus the overall behavior of the model might not be the expected one. The importance of the near-wall behavior of SGS models will be further investigated in Chapter 6.

In order to remove some of the limitations associated with the Smagorinsky model, an alternative route to the modification of the length scale l in the model is the modification of its time scale $t(l)$. Among the several options (Sagaut, 2006), two specific models are relevant for the present thesis[12]. One is the Vreman model (Vreman, 2004a, 2007):

$$\nu_{sgs} = c\sqrt{\frac{B_\beta}{\alpha_{ij}\alpha_{ij}}} \tag{2.27}$$

with:

$$\begin{aligned}
\alpha_{ij} &= \frac{\partial \tilde{u}_j}{\partial x_i} \\
\beta_{ij} &= \bar{\Delta}_m^2 \alpha_{mi}\alpha_{mj} \\
B_\beta &= \beta_{11}\beta_{22} - \beta_{12}^2 + \beta_{11}\beta_{33} - \beta_{13}^2 + \beta_{22}\beta_{33} - \beta_{23}^2 + \left(c_c\bar{\Delta}\partial\tilde{u}_k/\partial x_k\right)^4/c^2 \\
\bar{\Delta} &= \left(\prod_{m=1}^{3}\bar{\Delta}_m\right)^{\frac{1}{3}}
\end{aligned} \tag{2.28}$$

where $\bar{\Delta}_m$ are the filter widths in the three coordinate directions[13], $c_c = 0.1$ is a constant and $c = 2.5C_s^2$, C_s being the constant in the Smagorinsky model. The model is constructed on the basis of an algebraic classification of three-dimensional flows and, trough β_{ij}, it is connected to a formal Taylor series expansion of the SGS stresses. In practice, differently from the Smagorinsky model, the Vreman model predicts a correct null SGS viscosity for 13 classes of flows and has a linear near-wall behavior.

The second one is the σ-model proposed by Nicoud et al. (2011) using the singular values of the velocity gradient tensor, $\sigma_1 \geq \sigma_2 \geq \sigma_3 \geq 0$:

$$\nu_{sgs} = \left(C_\sigma\bar{\Delta}\right)^2 \frac{\sigma_3\left(\sigma_1 - \sigma_2\right)\left(\sigma_2 - \sigma_3\right)}{\sigma_1^2} \tag{2.29}$$

with $C_\sigma \approx 1.35$. In practice, the model has the correct cubic near-wall behavior and vanishes for two-dimensional/two-component flows as well as for pure axisymmetric or isotropic expansions/contractions.

A final model which is worth mentioning, as it is the model of choice for several developments in this thesis, is the mixed-scale model developed by Sagaut (Sagaut, 1996; Sagaut et al., 1996) starting from an original idea of Cain, Bardina et al. (1980). In practice, the SGS viscosity is based on a weighted, dimensionally correct, average

[12] The reasons are their relative ease of implementation in general unstructured codes, their relative novelty, their relevance in the LES community and, finally, their particular difference in the near wall behavior, making them suitable for further analysis.

[13] In practice, especially in IFCLES, this distinction is only useful for structured codes; otherwise $\bar{\Delta}$ is used instead.

of contributions due to the length scale l, the velocity scale $u(l)$ and the time scale $t(l)$, leading to a one-parameter family of models:

$$\nu_{sgs} = C_m \bar{\Delta}^{1+\alpha} \left(q_c^2\right)^{(1-\alpha)/2} \left(2\tilde{S}_{ij}\tilde{S}_{ij}\right)^{\alpha/2} \tag{2.30}$$

where α is a prefixed real parameter, C_m is the model constant and q_c is a velocity scale. In theory, any prescription for q_c, including a transport equation for q_c^2, is a suitable choice (as well as different time scales in place of $(2\tilde{S}_{ij}\tilde{S}_{ij})^{-1/2}$); however, in the original formulation of the model, the following option is adopted:

$$q_c^2 = \frac{1}{2}\left(\tilde{u}_j - \frac{\widehat{\bar{\rho}\tilde{u}_j}}{\hat{\bar{\rho}}}\right)\left(\tilde{u}_j - \frac{\widehat{\bar{\rho}\tilde{u}_j}}{\hat{\bar{\rho}}}\right) \tag{2.31}$$

The velocity field $\left(\tilde{u}_j - \widehat{\bar{\rho}\tilde{u}_j}/\hat{\bar{\rho}}\right)$, whose kinetic energy per unit mass is q_c^2, represents the small-scale part of the resolved velocity field $\tilde{u}_j$ and is defined through the application of a second filter, referred to as test filter, denoted by a hat and associated to the cutoff length $\hat{\Delta} > \bar{\Delta}$. It should be noted that, even if an implicit filtering approach is adopted, the test filter has to be effectively applied, with an actual numerical procedure, in order to obtain the kinetic energy content of the highest resolved part of the energy spectrum. However, the test filter is not related to the formulation (e.g., IFCLES) and does not require the commutation property (2.10). By varying the parameter α different interesting cases are obtained: the Smagorinsky model is recovered for $\alpha = 1$; the original mixed-scale formulation for $\alpha = 0.5$; a model based on Kolmogorov scaling for $\alpha = 1/3$; a model based on the SGS kinetic energy for $\alpha = 0$; the original proposal of Bardina et al. (1980), later proposed again by several authors[14], for $\alpha = -1$. The distinguishing feature of the mixed-scale model, for $\alpha \neq 1$, is its sensitivity to the energy content in the smallest resolved scales, which also makes the model suitable for transitional flows.

Before closing this section, it is worth noting how, among the functional models presented, all have assumed a spurious alignment between the eigenvectors of the SGS stress tensor τ_{ij} and those of the resolved strain rate tensor $\tilde{S}_{ij}$, which is not usually verified (Tao et al., 2002; Horiuti, 2003). Also, the Smagorinsky model is the only one using a full equilibrium assumption and being completely isotropic. The mixed-scale model, in contrast, does not rely on the equilibrium assumption for $\alpha \neq 1$, but still retains the isotropy assumption. The models of Vreman and Nicoud, in contrast, while being formally isotropic, are nonetheless sensitized to several anisotropies, the most relevant one being the near-wall behavior.

Structural models

Functional models have their commonality in the presumed knowledge of the energy transfer mechanisms between the different ranges of scales. In practice, they are based on some hypotheses about the nature of the missing scales and about their functional role in the interactions with the resolved scales. In contrast, the structural models are

[14] It is indeed known as Tsubokura model, see Tsubokura (2001); Yoshizawa et al. (1996).

explicitly designed to reconstruct the SGS tensor, regardless of its function. In fact, any attempt to reconstruct the unknown terms of the SGS tensor from the resolved velocity field necessarily requires some assumptions to justify their very reconstructability and the adherence of the reconstructed tensor to the exact one. From the practical point of view, the aim and best achievable goal of a structural model is to exactly reconstruct the energy content and the energy fluxes up to the Nyquist cutoff frequency associated with the grid. However, by definition, they are not able to reconstruct non-resolvable scales or their interaction, which still require modeling. Thus, in general, structural SGS models are used in combination with functional models, in the form of a mixed model. Still, as such reconstruction intervene on some of the smallest resolved scales as well, it can also provide qualitative information on the largest non resolved scales, the most energetic among the non resolved ones, including anisotropy and/or backscatter of energy toward the largest scales. As these mechanisms are usually absent from functional models, the use of mixed models can thus be a winning strategy in complex flows.

A point of paramount importance for structural models is the assumption that the resolved energy content and fluxes, i.e., the resolved nonlinear terms in the equations, actually need a better reconstruction. While this necessity was already proven, somehow, by Leonard (1974) for the explicit filtering approach, so that this class of models is also more correctly referred to as subfilter-scale (SFS) models, this is much less obvious for the implicit filtering one. Indeed, such reconstruction not only requires that the energy transfer toward the smallest scales has been actually affected by the filter (either implicitly or explicitly) but also that some information on such filter is actually available to properly *invert* it. As shown in section 2.3, most numerical methods have such filtering effects[15] and require a better reconstruction of the nonlinear terms but, as long as their formulation remains in the form of equation (2.13a), such reconstruction remains totally arbitrary. However, as will be shown in Chapter 3, it is actually possible to express implicit filtering approaches in the form of equation (2.13b) and, at least formally, such reconstruction becomes always well defined. It is then shown in Chapter 4 how, for the FV method, such process is particularly simple and allows the derivation of a proper form of structural SGS model.

The large number of existing structural models also complicates the matter as they could be further classified in several ways, especially appealing being the framework of the approximate deconvolution models (Layton and Rebholz, 2012). However, it is out of the scope of this work to provide an exhaustive description of all the models and classifications; furthermore, for the reasons described above, the limitations of the IFCLES framework preclude most possible choices and the limitations arising for general unstructured codes preclude some others. As a consequence, this presentation is limited to the class of structural models known as scale-similar.

The scale-similarity assumption has been first introduced in the SGS modeling by Bardina (Bardina et al., 1980, 1983) and consists in assuming that the statistical structure of the velocity field at sub-grid scales is similar to that of the velocity field at the smallest resolved scales (Meneveau and Katz, 2000). This is usually justified by the fact that these two ranges of scales are contiguous in the spectral space and, as a consequence, they have similar interactions with the largest resolved scales. This scale

[15] Notable exceptions being some spectral methods, e.g., Fourier Galerkin, if the time discretization error is negligible.

similarity hypothesis has then been further generalized (and verified in experiments), by Liu et al. (1994), to the case of two generic contiguous spectral bands. From the modeling perspective, this means that tensors constructed with the smallest resolved scales can replace tensors based on the largest non resolved scales, i.e., the SGS stress tensor.

Adopting the form proposed by Liu et al. (1994), as it is the only suitable one in the IFCLES framework, and considering mixed formulations with the contribution of a functional model, as is more common for compressible flows (Erlebacher et al., 1992), leads to the following SGS models in the IFCLES framework (Vreman et al., 1995a,b):

$$\begin{aligned}\tau_{ij} &= -\bar{\rho}\left[\left(\frac{\widehat{\bar{\rho}\tilde{u}_i\tilde{u}_j}}{\hat{\bar{\rho}}} - \frac{\widehat{\bar{\rho}\tilde{u}_i}}{\hat{\bar{\rho}}}\frac{\widehat{\bar{\rho}\tilde{u}_j}}{\hat{\bar{\rho}}}\right) - 2\nu_{sgs}\left(\tilde{S}_{ij} - \frac{1}{3}\tilde{S}_{kk}\delta_{ij}\right)\right] \\ \theta_j &= -C_p\bar{\rho}\left[\left(\frac{\widehat{\bar{\rho}\tilde{u}_j\tilde{T}}}{\hat{\bar{\rho}}} - \frac{\widehat{\bar{\rho}\tilde{u}_j}}{\hat{\bar{\rho}}}\frac{\widehat{\bar{\rho}\tilde{T}}}{\hat{\bar{\rho}}}\right) - \frac{\nu_{sgs}}{Pr_{sgs}}\frac{\partial\tilde{T}}{\partial x_j}\right]\end{aligned} \tag{2.32}$$

where, as for the mixed-scale model in the previous section, the additional filter of the model, the only one effectively and explicitly applied in this approach, is denoted by a hat and $\hat{\Delta} > \bar{\Delta}$. However, very differently from the mixed-scale model, in order for the scale similar parts in models (2.32) to be consistent, the hat filter has to satisfy the condition (2.10) and possibly be representative of the basic implicit filter level, the two things being not necessarily compatible. Indeed, no matter what hat filter is adopted, this filter level can only be arbitrary and not related to the basic filter level, denoted by a bar, which is undetermined. It is worth mentioning that, in theory, to preserve the Galilean invariance of the equations (2.14), the scale-similar part of the models (2.32) is usually employed without any multiplicative constant (Speziale, 1985), thus implicitly assuming that such models are also quantitatively correct[16]. However, what is usually unnoticed is that such quantitative and qualitative correctness is not possible, otherwise the model would be perfect. More importantly, for the Galilean invariance to hold in IFCLES, would require the hat filter to be constant in space and that terms III in equation (2.13a) also satisfy it, which is not usually the case.

Dynamic Procedure

The turning point in the historical LES development certainly coincide, in the author's opinion, with the moment Massimo Germano introduced the identity that now bears his name (Germano, 1992). Germano derived his identity by looking at the form of the equations (2.14) (in their incompressible formulation) when expressed at two filter levels: the basic one with filter width $\bar{\Delta}$ and the one obtained by further application of a test filter, again denoted by a hat, with width $\hat{\Delta} > \bar{\Delta}$[17]. If the additional test filter satisfy the exact same properties of the basic one, then the following exact identities hold between the SGS stresses and heat fluxes at the two filtering levels (expressed, for the sake of consistency, in their general compressible form (Moin et al., 1991; Salvetti

[16] Some exceptions exist, e.g., Sagaut and Grohens (1999).

[17] Notice, however, that the consecutive application of the two filters will generally have an equivalent width $\hat{\bar{\Delta}} > \hat{\Delta}$, see Vreman et al. (1997).

and Banerjee, 1995)):

$$\begin{aligned} T_{ij} - \widehat{\tau_{ij}} &= -\left(\widehat{\bar{\rho}\tilde{u}_i\tilde{u}_j} - \frac{\widehat{\bar{\rho}\tilde{u}_i}\widehat{\bar{\rho}\tilde{u}_j}}{\hat{\bar{\rho}}} \right) \equiv \mathcal{L}_{ij} \\ Q_j - \widehat{\theta_j} &= -C_p \left(\widehat{\bar{\rho}\tilde{u}_j\tilde{T}} - \frac{\widehat{\bar{\rho}\tilde{u}_j}\widehat{\bar{\rho}\tilde{T}}}{\hat{\bar{\rho}}} \right) \equiv \mathcal{K}_j \end{aligned} \tag{2.33}$$

where T_{ij} and Q_j are the SGS stress tensor and heat flux vector at the test filter scale. The identities in (2.33), in the following denoted as Classical Germano Identities (CGI), express the fact that the difference between the unknown SGS tensor at the test filter level and the unknown test filtered SGS tensor is explicitly known as a function of resolved quantities, i.e., the tensor $\mathcal{L}_{ij}$. An analogous reasoning holds for the heat fluxes and the vector $\mathcal{K}_j$.

The basic idea behind the Dynamic Procedure (Germano et al., 1991; Moin et al., 1991) is to use the exact relations (2.33) as a constraint that the used SGS models have to satisfy in order to be compliant with the algebraic structure of the SGS stresses among different filtering levels. In practice, such constraint is imposed by dynamically adjusting the model constants and satisfying the identities only in a least-squares sense. Considering again, for the sake of consistency, the procedure when applied to mixed models (Salvetti and Banerjee, 1995; Horiuti, 1997; Sarghini et al., 1999; Anderson and Meneveau, 1999), the models in (2.32) can be first formally expressed at the two filter levels as:

$$\begin{aligned} \tau_{ij} &= c_{ss}a_{ij} + c_{ev}b_{ij} \\ T_{ij} &= C_{ss}A_{ij} + C_{ev}B_{ij} \\ \\ \theta_j &= c^q_{ss}d_j + c^q_{ev}f_j \\ Q_j &= C^q_{ss}D_j + C^q_{ev}F_j \end{aligned} \tag{2.34}$$

where A_{ij} and a_{ij} are the scale-similar model parts at the test and basic filter level respectively, and similarly for D_j and d_j; B_{ij} and b_{ij} are instead the eddy-viscosity model parts, at the test and basic filter level respectively, and similarly for F_j and f_j. Notice that the model constants have been factored out, including those for scale similar terms, not previously considered in equation (2.32). In general, model constants are different among the two filter levels (distinguished by an upper or lower case C), among the eddy viscosity and scale-similar parts (distinguished by the ev and ss subscripts) and among the stresses or the heat flux equation (the latter being denoted by the superscript q). Upon substitution of the models (2.34) in the identities (2.33), these become [18]:

$$\begin{aligned} E_{ij} + C_{ss}A_{ij} + C_{ev}B_{ij} - \widehat{c_{ss}a_{ij}} - \widehat{c_{ev}b_{ij}} &= \mathcal{L}_{ij} \\ E^q_j + C^q_{ss}D_j + C^q_{ev}F_j - \widehat{c^q_{ss}d_j} - \widehat{c^q_{ev}f_j} &= \mathcal{K}_j \end{aligned} \tag{2.35}$$

[18] It is worth mentioning that the first identity is, in such case, usually limited to its anisotropic part while, for compressible flows, a separate identity with different models is used for its trace (Moin et al., 1991). As this is not explicitly required in the present compressible framework, we avoid such limitation for the sake of simplicity.

where, as a consequence of the fact of using the models instead of the true SGS terms, the error terms E_{ij} and E_j^q have been added, so that equations (2.35) still remain formally exact. In order to proceed toward the determination of the constants in the models, two additional assumptions are usually invoked: model constants are equal at the two filter levels (e.g., $C_{ss} = c_{ss}$); model constants at the basic filter level, those effectively required, can be extracted from the hat filter (i.e., their variation is slow over scales of the order $\hat{\Delta}$). With these assumptions, equations (2.35) then become:

$$\begin{aligned} E_{ij} &= \mathcal{L}_{ij} - C_{ss}\overbrace{\left(A_{ij} - \widehat{a_{ij}}\right)}^{A_{ij}^m} - C_{ev}\overbrace{\left(B_{ij} - \widehat{b_{ij}}\right)}^{B_{ij}^m} \\ E_j^q &= \mathcal{K}_j - C_{ss}^q\underbrace{\left(D_j - \widehat{d_j}\right)}_{D_j^m} - C_{ev}^q\underbrace{\left(F_j - \widehat{f_j}\right)}_{F_j^m} \end{aligned} \tag{2.36}$$

where the error terms could, in theory, also take into account the last two additional hypotheses, as well as any other approximation affecting the exact identity. In the final step of the procedure, according to Lilly (1992), the coefficients are determined as those minimizing the errors in a least squares sense, as both systems in (2.36) are overdetermined. This finally leads to the following equations:

$$\begin{aligned} \frac{\partial E_{ij}E_{ij}}{\partial C_{ss}} &= 2\left[-\left(A_{ij}^m\mathcal{L}_{ij}\right) + C_{ss}\left(A_{ij}^m A_{ij}^m\right) + C_{ev}\left(A_{ij}^m B_{ij}^m\right)\right] = 0 \\ \frac{\partial E_{ij}E_{ij}}{\partial C_{ev}} &= 2\left[-\left(B_{ij}^m\mathcal{L}_{ij}\right) + C_{ss}\left(A_{ij}^m B_{ij}^m\right) + C_{ev}\left(B_{ij}^m B_{ij}^m\right)\right] = 0 \\ \frac{\partial E_j^q E_j^q}{\partial C_{ss}^q} &= 2\left[-\left(D_j^m\mathcal{K}_j\right) + C_{ss}^q\left(D_j^m D_j^m\right) + C_{ev}^q\left(D_j^m F_j^m\right)\right] = 0 \\ \frac{\partial E_j^q E_j^q}{\partial C_{ev}^q} &= 2\left[-\left(F_j^m\mathcal{K}_j\right) + C_{ss}^q\left(D_j^m F_j^m\right) + C_{ev}^q\left(F_j^m F_j^m\right)\right] = 0 \end{aligned} \tag{2.37}$$

whose solutions are:

$$\begin{aligned} C_{ss} &= \frac{\left(B_{ij}^m B_{ij}^m\right)\left(\mathcal{L}_{rs}A_{rs}^m\right) - \left(\mathcal{L}_{ij}B_{ij}^m\right)\left(B_{rs}^m A_{rs}^m\right)}{\left(A_{ij}^m A_{ij}^m\right)\left(B_{rs}^m B_{rs}^m\right) - \left(A_{ij}^m B_{ij}^m\right)\left(A_{rs}^m B_{rs}^m\right)} \\ C_{ev} &= \frac{\left(B_{ij}^m\mathcal{L}_{ij}\right) - C_{ss}\left(A_{ij}^m B_{ij}^m\right)}{\left(B_{ij}^m B_{ij}^m\right)} \\ C_{ss}^q &= \frac{\left(F_j^m F_j^m\right)\left(\mathcal{K}_r D_r^m\right) - \left(\mathcal{K}_j F_j^m\right)\left(F_r^m D_r^m\right)}{\left(D_j^m D_j^m\right)\left(F_r^m F_r^m\right) - \left(D_j^m F_j^m\right)\left(D_r^m F_r^m\right)} \\ C_{ev}^q &= \frac{\left(F_j^m\mathcal{K}_j\right) - C_{ss}^q\left(D_j^m F_j^m\right)}{\left(F_j^m F_j^m\right)} \end{aligned} \tag{2.38}$$

The coefficients so computed, when used with the respective models, have some desirable features as well as some drawbacks. For example, with the simple Smagorinsky model, C_{ev} from equation (2.38) (computed by setting $C_{ss} = 0$) replaces C_s^2 in equation (2.22) and vanishes in laminar flows as well as it goes to 0 at walls with the cube of the distance. However, as can be appreciated by the solution in (2.38), these properties arise from the specific combination between B_{ij}^m and $\mathcal{L}_{ij}$. In the Dynamic Smagorinsky model, for example, B_{ij}^m does not scale with the distance from the wall and the properties directly derive from $\mathcal{L}_{ij}$. For different formulations, e.g., the σ-model, nothing changes besides the fact that now B_{ij}^m involves ratios and differences of very small quantities going very rapidly to 0 at the wall, thus the procedure becomes numerically ill-posed toward the wall (Baya Toda et al., 2010, 2011). Such numerical problems also affects the procedure in general as, for example, still in the Dynamic Smagorinsky model, a null denominator in C_{ev} would also imply a null nominator but, from the numerical point of view such correspondence cannot be exactly verified and the constant is subjected to high oscillations, including negative values[19]. Several cures exists for this behavior, among which averaging in homogeneous spatio/temporal directions is common when possible, or along Lagrangian trajectories when this is not the case (Meneveau et al., 1996). For unstructured codes, averaging is usually limited to the neighbor of the grid point and, often, still requires clipping of the constants between predefined limits (Nicoud et al., 2011).

2.4.3 Explicitly filtered CLES (EFCLES)

In Explicitly filtered CLES (EFCLES), following Leonard (1974) and Lund (2003), an explicit spatial filter is applied to the non-linear terms of the governing equations in order to control the spectral content of the numerical solution (Bose et al., 2010; Singh et al., 2012). The continuous template used for the discretization is then the following (Radhakrishnan and Bellan, 2012):

$$
\begin{aligned}
\frac{\partial \bar{\rho}}{\partial t} + \frac{\partial}{\partial x_j}\left(\widehat{\bar{\rho}\tilde{u}_j}\right) =& \frac{\partial}{\partial x_j}\underbrace{\left(\widehat{\bar{\rho}\tilde{u}_j} - \widehat{\rho u_j}\right)}_{\text{VII}} \\
\frac{\partial\left(\bar{\rho}\tilde{u}_i\right)}{\partial t} + \frac{\partial}{\partial x_j}\left(\widehat{\bar{\rho}\tilde{u}_i\tilde{u}_j} + \widehat{\tilde{\sigma}_{ij}}\right) =& \frac{\partial}{\partial x_j}\underbrace{\left(\widehat{\bar{\rho}\tilde{u}_i\tilde{u}_j} - \widehat{\rho u_i u_j}\right)}_{\text{I}} + \frac{\partial}{\partial x_j}\underbrace{\left(\widehat{\tilde{\sigma}_{ij}} - \widehat{\sigma_{ij}}\right)}_{\text{II}} \\
\frac{\partial\left(\bar{\rho}\tilde{E}\right)}{\partial t} + \frac{\partial}{\partial x_j}\left(\widehat{\bar{\rho}\tilde{u}_j\tilde{E}} + \widehat{\tilde{q}_j} + \widehat{\tilde{u}_i\tilde{\sigma}_{ij}}\right) =& \frac{\partial}{\partial x_j}\underbrace{\left(\widehat{\bar{\rho}\tilde{u}_j\tilde{E}} - \widehat{\rho u_j E}\right)}_{\text{III}} \\
&+ \frac{\partial}{\partial x_j}\underbrace{\left(\widehat{\tilde{q}_j} - \widehat{q_j}\right)}_{\text{IV}} + \frac{\partial}{\partial x_j}\underbrace{\left(\widehat{\tilde{u}_i\tilde{\sigma}_{ij}} - \widehat{u_i\sigma_{ij}}\right)}_{\text{V}}
\end{aligned}
\tag{2.39}
$$

[19] While this is, sometimes, interpreted as a form of backscatter, it should be noticed that backscatter is mostly uncorrelated with $\tilde{S}_{ij}$ (Horiuti, 2003) and thus such interpretation appears weak and unphysical.

with:

$$\begin{aligned}\widehat{\bar{\rho}\tilde{E}} &= \frac{\hat{\bar{p}}}{\gamma-1} + \frac{1}{2}\widehat{\bar{\rho}\tilde{u}_k\tilde{u}_k} + \frac{1}{2}\underbrace{\left(\widehat{\overline{\rho u_k u_k}} - \widehat{\bar{\rho}\tilde{u}_k\tilde{u}_k}\right)}_{\text{VI}} \\ \hat{\bar{p}} &= \widehat{\bar{\rho}R\tilde{T}}\end{aligned} \tag{2.40}$$

Here, in contrast to the current trends, but in accordance with the previous section, a hat is used again to denote the explicit filtering operation while still preserving the bar-tilde combination for the effectively resolved variables; however, as in more common formulations, here it is still intended that $\overline{(\cdots)} = \widehat{(\cdots)}$ as a result of the hat filtering itself (which, consistently with the present notation, is only implied by the formulation). Also, while usually neglected, here the explicit hat filtering has been correctly applied also to the viscous non linear terms, the continuity equation[20] and the equation of state[21] (notice, in particular, the larger hats on the resolved viscous terms). Again, it has to be stressed that the hat filter has to satisfy (2.10) in order to make the previous equations meaningful.

2.4.4 SGS Modeling in EFCLES

As a result of the different approach, different SGS terms arise in EFCLES with respect to IFCLES, the two considered in (2.17) and (2.18) being now:

$$\begin{aligned}\tau_{ij} &= -\left(\widehat{\rho u_i u_j} - \widehat{\bar{\rho}\tilde{u}_i\tilde{u}_j}\right) \\ \theta_j &= -C_p\left(\widehat{\rho u_j T} - \widehat{\bar{\rho}\tilde{u}_j\tilde{T}}\right)\end{aligned} \tag{2.41}$$

In general, these are modeled with modified forms of the SGS models used for IFCLES. For eddy viscosity/conductivity SGS models, the usual assumption is (Bose et al., 2010; Radhakrishnan and Bellan, 2012):

$$\begin{aligned}\tau_{ij}^d &= \left[2\bar{\rho}\nu_{sgs}\left(\tilde{S}_{ij} - \frac{1}{3}\tilde{S}_{kk}\delta_{ij}\right)\right]^{\wedge} \\ \theta_j &= \left[\frac{C_p\bar{\rho}\nu_{sgs}}{Pr_{sgs}}\frac{\partial\tilde{T}}{\partial x_j}\right]^{\wedge}\end{aligned} \tag{2.42}$$

where, for the sake of readability, the notation $(\cdots)^{\wedge} = \widehat{(\cdots)}$ has been used. Analogous modifications also hold for the mixed models; however, in EFCLES, as well as in IFCLES, there is no unique approach to the scale similar term, with several different proposals emerged in the years. As this in no way affects the present and following discussion, only the most relevant model present in literature is cited here (Radhakrishnan

[20] SGS modeling for the term VII is, however, usually neglected (Radhakrishnan and Bellan, 2012).

[21] Which remains closed as, now, the doubly filtered pressure appears everywhere.

and Bellan, 2012):

$$\begin{aligned}\tau_{ij} &= -\left[\bar{\rho}\left(\tilde{u}_i\tilde{u}_j - \frac{\widehat{\bar{\rho}\tilde{u}_i}}{\hat{\bar{\rho}}}\frac{\widehat{\bar{\rho}\tilde{u}_j}}{\hat{\bar{\rho}}}\right) - 2\bar{\rho}\nu_{sgs}\left(\tilde{S}_{ij} - \frac{1}{3}\tilde{S}_{kk}\delta_{ij}\right)\right]^{\wedge} \\ \theta_j &= -C_p\left[\bar{\rho}\left(\tilde{u}_j\tilde{T} - \frac{\widehat{\bar{\rho}\tilde{u}_j}}{\hat{\bar{\rho}}}\frac{\widehat{\bar{\rho}\tilde{T}}}{\hat{\bar{\rho}}}\right) - \frac{\bar{\rho}\nu_{sgs}}{Pr_{sgs}}\frac{\partial\tilde{T}}{\partial x_j}\right]^{\wedge}\end{aligned} \tag{2.43}$$

However, it is worth mentioning that, especially in the compressible case, there is a lack of sustained practice on the explicit filtering approach and no specific model is established yet definitely (see Appendix A).

Dynamic Procedure

SGS terms arising in the EFCLES approach also satisfy a different form of CGI (EFCGI):

$$\begin{aligned}T_{ij} - \breve{\tau}_{ij} &= -\left\{\left[\bar{\rho}\tilde{u}_i\tilde{u}_j - \frac{(\bar{\rho}\tilde{u}_i)^{\cup}(\bar{\rho}\tilde{u}_j)^{\cup}}{\bar{\rho}^{\cup}}\right]^{\wedge}\right\}^{\cup} \\ Q_j - \breve{\theta}_j &= -C_p\left\{\left[\bar{\rho}\tilde{u}_j\tilde{T} - \frac{(\bar{\rho}\tilde{u}_j)^{\cup}\left(\bar{\rho}\tilde{T}\right)^{\cup}}{\bar{\rho}^{\cup}}\right]^{\wedge}\right\}^{\cup}\end{aligned} \tag{2.44}$$

where the notation $(\cdots)^{\cup} = (\breve{\cdots})$ is used to express the test filtering which, in EFCLES, is generally different from the basic explicit hat filtering and such that the associated filter width $\breve{\Delta} \geq \hat{\Delta}$. As in IFCLES, the test filtering still has to satisfy condition (2.10) in order for the EFCGI to be meaningful. In the current practice, the EFCGI are then enforced trough the same dynamic procedure as used for the IFCLES.

2.5 Summary on CLES

At this point, the following facts and assumptions concerning the CLES approach can be summarized:

(i) In CLES, no matter what specific approach is used, the equations are derived under the assumption that the basic filter level commutes with spatial derivative operators. While this has been made sufficiently clear for the EFCLES approach, it has been only implied for the IFCLES one. In practice, for some numerical methods this is not possible (Lund, 2003) and the interpretation of the results cannot be connected to a filtering operation. Moreover, for the EFCLES approach, the true required commutation is between numerical filters and numerical derivative operators, which implies higher-order discretizations for both (Haselbacher and Vasilyev, 2003).

(ii) The explicit test filter applied in the dynamic procedure, as needed from the CGI/EFCGI, has to satisfy the exact same conditions of the basic filter level in

order for the procedure to be meaningful. In both cases, the assumed form of the SGS stresses is such that (2.10) is implied for the basic filter, thus it is required also for the test one.

(iii) As will be more clear in the following chapter, because of the commutation requirement (2.10), the CGI (2.33) for the momentum equation requires the filtering of two tensors (τ_{ij} and $\bar{\rho}\tilde{u}_i\tilde{u}_j$, 12 scalars in total) besides the filtering of the single variables ($\bar{\rho}$ and $\tilde{u}_i$, 4 scalars), independently from the specific SGS model used. The CGI for the main term in the energy equation requires filtering two vectors (θ_j and $\bar{\rho}\tilde{u}_j\tilde{T}$, 6 scalars in total) and an additional variable ($\tilde{T}$, 1 scalar). If scale-similarity models are considered, an additional tensor (6 scalars) and vector (3 scalars) need to be test filtered with the additional test filtering of all the variables (5 scalars)[22]. In the most complex scenario this leads to filtering 37 scalars in total. Dynamic modeling of the additional unclosed terms in the energy equation, as well as the EFCGI in the EFCLES approach, make this number higher. Even in the most simple scenario, with a dynamic Smagorinsky model (Germano et al., 1991) in the incompressible isothermal case, the IFCLES approach requires filtering 15 scalars.

(iv) Because of the commutation requirement, independently from the specific approach, the CGI/EFCGI involve test filtering of the SGS model at the basic filter level (e.g., $\hat{\tau}_{ij}$ in (2.33)). This, in turn, implies either inconsistently extracting the dynamically computed constant from the test filter (as done here) or the adoption of a consistent, but computationally even more expensive, dynamic procedure (Ghosal et al., 1995).

What thus emerges from the previous analysis is that most of the problematic aspects related to the CLES approach are uniquely due to the somewhat arbitrary will to put the governing equations under the form (2.11), possibly because of the similarity with RANS/URANS approaches, which in LES appears as particularly misleading. Indeed, in turn, this requires the fulfillment of (2.10) at all the levels of the formulation. In order to understand how limiting this is, it is useful to analyze under which conditions the requirement (2.10) can be satisfied and what are the implications. It is simple to show that, for a filter of the form $G = G\left[\mathbf{x} - \boldsymbol{\xi}, \bar{\Delta}(\mathbf{x})\right]$, the spatial commutation error has the following form (Sagaut, 2006; Fureby and Tabor, 1997):

$$\frac{\partial \bar{\phi}}{\partial x_i} - \overline{\frac{\partial \phi}{\partial x_i}} = \frac{\partial \bar{\Delta}}{\partial x_i}\left(\frac{\partial G}{\partial \bar{\Delta}} * \phi\right) + \int_{\partial\Omega} G\left[\mathbf{x} - \boldsymbol{\xi}, \bar{\Delta}(\mathbf{x})\right] \phi(\boldsymbol{\xi}, t)\, \boldsymbol{n}(\boldsymbol{\xi})\, \mathrm{d}\boldsymbol{S} \qquad (2.45)$$

The second term on the right hand side represents interactions with the domain boundary $\partial\Omega$ and, in general, can only be 0 if the filter support does not cut the domain boundary. For symmetric filters, this can only be obtained by reducing $\bar{\Delta}$ toward the boundary. But then the first term, due to spatial gradients of $\bar{\Delta}$, is certainly non null. Even if the second term in (2.45) could be made null by an asymmetric filter, in general, especially for complex flows, the filter width is likely to change in any case,

[22] These are due to the fact that the scale-similar parts, as expressed in (2.32), have to be expressed at the test filter level to build T_{ij} and Q_j in (2.33).

either to better describe the different flow features or because it is implicitly tied to the computational grid.

A third viable option, still suggested by equation (2.45), is to reduce the commutation error by adopting a filter which is of high order in $\bar{\Delta}$, i.e., $G = I + O(\bar{\Delta}^n)$, where I is the identity operator. In this case, for $\bar{\Delta}(\mathbf{x}) = \bar{\Delta}(\mathbf{x_0})f(\mathbf{x} - \mathbf{x_0})$ (Iovieno and Tordella, 2003), and assuming a null contribution from the boundary term, the commutation error around the point $\mathbf{x_0}$ can be made of order n:

$$\left(\frac{\partial\bar{\phi}}{\partial x_i} - \overline{\frac{\partial\phi}{\partial x_i}}\right) \propto \bar{\Delta}^n(\mathbf{x_0})\frac{\partial f^n}{\partial x_i} \tag{2.46}$$

Such high order commuting filters (HOCF) (Vasilyev et al., 1998; Haselbacher and Vasilyev, 2003) can then allow EFCLES making the commutation error commensurate to the numerical error[23] (Bose et al., 2010; Haselbacher and Vasilyev, 2003). However, this approach has several non trivial consequences. To understand why, it has to be recalled that the EFCLES approach, based on the filtering of the convective terms, has its roots in the 2/3 dealiasing rule for spectral methods (Rogallo, 1981; Meyers et al., 2008), roughly consisting in the elimination of 1/3 of the spectral content at the smallest scales, as affected by aliasing errors; such elimination can then be interpreted as a filter, the spectral cut-off. But, in that context, the distinction between the discretization and the explicit filtering is evanescent, due to the very specific features of the numerical method, and no explicit problem of commutation exists even for more complex applications (Pope, 2001; Hughes et al., 2000). In contrast, the application of the same approach to more general numerical methods, requiring thus a HOCF, leads to a conceptual difficulty, as the possibility to derive consistent FNSE becomes tied to a specific numerical method. More precisely, as the commuting order of HOCF increases only by adding more and more constraints on the filter moments, this seems to suggest that only a very high-order discretization would lead to consistent FNSE. Moreover, as commuting filters tend to spectral cut-off filters for increasing order of commutation, the underlying reasoning would be that only spectral cut-off filters would lead to consistent FNSE and only a spectral discretization would be amenable for a consistent LES approach.

The conceptual limit is even more evident if, besides commutation with numerical derivatives, additional conflicting constraints are required for the filter, like realizability (Vreman et al., 1994; Geurts et al., 1997; van der Bos and Geurts, 2005) or simmetry (Vreman, 2004b; Lehmkuhl et al., 2012), which are not satisfied by HOCF. Moreover, the use of a HOCF in EFCLES also implies that the SFS stresses, those ideally recoverable with a structural model, scale with the same order of the filter G (van der Bos and Geurts, 2005) and their divergence scales like the commutation error. Hence, modeling SFS with low order models (e.g., scale-similar models, as done by Singh et al. (2012)), and neglecting commutation errors, is a completely inconsistent choice. Finally, as already noted in section 2.2, the advantage of HOCF diminishes for compressible flows, as Favre filtering does not commute with spatial derivatives in any case (Garnier et al., 2009) and the additional filtering of the viscous terms is required.

[23] The estimate provided in (2.46), despite correct, is based on heuristic arguments. A rigorous derivation is provided by Vasilyev et al. (1998).

The fact that the application of a generic filter with non constant width would always lead to FNSE affected by commutation errors, might be acceptable as well. There are, indeed, approaches directly dealing with their modeling (van der Bos and Geurts, 2005; Iovieno and Tordella, 2003); nonetheless, additional complexity is certainly added to the computation and no practical applications of such methods are known to date.

More generally, however, while having the equations under the form (2.11) might certainly have its advantages, the overall approach appears overly constrictive as, in a broader sense, it really is equivalent to selecting a specific model equation and then devising the most suitable numerical procedure to fit the chosen model, not necessarily with any success. Indeed, from the analysis above, it clearly appears that spectral methods would be the only suitable choice, strongly limiting the application of LES. One of the aims of the present work is to show that devising a model equation for a numerical procedure is indeed possible, almost independently from the specific numerical approach, and leads to important simplifications.

CHAPTER 3

A Generalized LES framework

This chapter is dedicated to the presentation of a generalized LES (GLES) framework, which is intended to bypass most of the limitations encountered in the CLES framework. The works and the approaches that inspired the present framework are first presented in section 3.1, so that it is put in the correct context. Basic assumptions and definitions for the GLES framework are introduced in section 3.2, while the governing equations for GLES are presented in section 3.3. As the Germano Identities play a crucial role in LES, section 3.4 is entirely devoted to their counterparts in the GLES framework and the resulting advantages with respect to the classical ones. As the GLES framework introduces some apparent differences with respect to the CLES one, especially in the form of the SGS terms, section 3.5 presents a functional analysis of the GLES framework, introducing exact equations for resolved and unresolved kinetic energies and the functional SGS modeling options deriving from them. Finally, section 3.6 is intended to show how, in fact, the present GLES framework is an exact representation of several approaches to LES. The FV method is only briefly outlined as, being the core of the present thesis, it is better analyzed in Chapter 4.

3.1 Introduction

The main conclusion to be drawn from the analysis in the previous chapter is that the CLES approach suffers a misalignment between model LES equations (i.e., the equations effectively discretized for the computations) and real LES equations (those ideally underlying the evolution of the resolved variables). Also, it is emerged that, to a very large extent, the root of the problem can be traced back to the requirement of a filter that commutes with spatial derivatives. Such misalignment has been highlighted before (Vreman, 2004b, 2003) and alternative formulations have been proposed, which avoid

commutation errors *ab initio*, i.e., arranging the equations in a different form, while retaining the filtering formalism. The volume balance procedure developed by Schumann (1975) was the first approach in this direction; it is an implicit LES formulation based on staggered finite differences and a local volume average, which do not incur in commutation issues due to the combined discretization of the volume average and derivative operators. As a matter of fact, the method of Schumann can be considered as an implicitly filtered LES based on a FV formulation. The same approach is also used by Huang (1997). The possibility of combining explicit filtering and derivative operators to avoid commutation errors was then first analyzed by Vreman and Geurts (2002), who formulated commutation error free equations for incompressible flows in the context of an explicitly filtered FV method. In practice, they intended the filter to be a top-hat:

$$\bar{\phi} = \frac{1}{|V(\mathbf{x})|} \int_{V(\mathbf{x})} \phi(\boldsymbol{\xi}, t)\, \mathrm{d}\boldsymbol{\xi} \tag{3.1}$$

that is, a local volume average, and discretized the various filtered terms according to the classical FV formulation and the Green-Gauss theorem:

$$\overline{\frac{\partial \phi_{ij}}{\partial x_j}} = \frac{1}{V} \sum_f A_f n_j^f \phi_{ij} \tag{3.2}$$

but, differently from the classical FV method, the volume V and its faces, with area A_f and normal n_j^f, are not related to the computational cell but to the volume over which filtering is desired. In the same work, Vreman and Geurts (2002) also recognize the different nature of the resulting SGS stresses, due to the formulation (3.2), and how they lead to a dynamic procedure based on a modified Germano identity. With respect to the classical procedure (Germano et al., 1991), the dynamic procedure developed by Vreman and Geurts (2002) is cheaper and avoids the inconsistent extraction of model constants from the test filter. They also propose two basic SGS parameterizations, one being based on a simple eddy-viscosity assumption and the other on a mixed scale-similar/eddy-viscosity model. This approach is then recognized by de With and Holdø (2005) to be straightly applicable to any implicitly filtered FV solver and the modified dynamic procedure, based on a simple Smagorinsky model, is implemented in the solver Fluent®. However, both the approaches above have a serious lack in justification, as both rely on standard SGS models, straightly transferred in the new framework. Also, while Vreman and Geurts (2002) apply the treatment (3.2) to convective and pressure terms, de With and Holdø (2005) only include convective terms in their formulation of the dynamic SGS viscosity.

More detailed analyses on the approach have been provided by Denaro and coworkers (Iannelli et al., 2003; Denaro et al., 2007; Denaro and De Stefano, 2011; Denaro, 2012, 2013) with a focus on the implicitly filtered FV approach. More specifically, they are the first in explicitly recognizing that the approach in (3.2) can and need to to be applied to all the terms in the equations, including the linear ones (i.e., diffusive and pressure terms) and that SGS modeling is thus required for them as well. They also

propose the relative modification for the dynamic procedure which, with respect to the one employed by de With and Holdø (2005), includes all the necessary terms.

The GLES framework proposed here can be traced back to the class of commutation error free approaches described above. In fact, when applied to the FV framework and implemented in a solver like Fluent®, it essentially consists in the work done by de With and Holdø (2005) but taking into account all the necessary terms, as proposed by Denaro and coworkers[1]. However, the advantage and novelty of the formulation proposed here is that it goes beyond a specific discretization, like that in (3.1) and (3.2), and further generalizes the previous approaches, so that it can actually include most of the known LES approaches.

3.2 Basic definitions

A possible broader definition of LES, with respect to the one used in CLES, is the one based on the concept of "degrees of freedom": LES is any approach which, for proper initial and boundary conditions, seeks a numerical solution to NSE while not having a sufficient number of degrees of freedom to properly describe it (dynamically as well as statically). Of course, what is implicit in the definition is that the degrees of freedom retained in the simulation are sufficient to describe a significant part of the flow dynamics and that a minimum set of flow statistics can be computed with a certain accuracy[2]. Thus, in view of the following developments, to be as general as possible, it is better to avoid explicit reference to any filter operation and instead introduce a more general operator G^i:

$$\bar{\phi}\left(\mathbf{x}, t, \Delta^i\right) = G^i * \phi\left(\mathbf{x}, t\right) \tag{3.3}$$

The action of G^i on any scalar field ϕ is such that $\bar{\phi}$ is the same scalar field but deprived of its *information content* on scales smaller than, approximately, Δ^i. In contrast, the *energy content* of $\bar{\phi}$ at scales $O(\Delta^i)$, or smaller, is not necessarily negligible as G^i does not necessarily imply any smoothing. For example, as will be better shown in section 3.6, G^i could be defined as the combination of a sampling operator (Knaepen et al., 2005) and of the interpolation function underlying the successive numerical operations[3] (e.g., the classical 2^{nd} order, finite difference, central scheme implies sampling and linear interpolation). In this case, $\bar{\phi}$ retains no physical information from ϕ at scales Δ^i or smaller, but its energy content at the same scales is not negligible independently from Δ^i. Here it is assumed that sampling operators (better defined in section 3.6) always involve a successive interpolation, dependent on the specific numerical method adopted, so that the dependence on continuous spatio-temporal coordinates used in equation (3.3) can be retained without specific problems (nonetheless, from now on, it

[1] However, in contrast to previous works, the developments presented in Chapter 4 are used to devise a novel form of scale-similar SGS model

[2] Besides known limitations (Meneveau, 1994), the vagueness of this implicit statement is not accidental as, still today, there is a serious lack of objective assessment measures in LES. This is intended in the sense that, independently from the quality of the results, which is easily assessed, there is no accepted indicator that a given simulation actually is a LES.

[3] A common misconception, usually typical among FEM practitioners, is that only FEM-like approaches univocally define a functional space for the numerical solution. As will be better elucidated in section 3.6, recognizing that all the numerical methods (finite volumes, finite differences, finite elements and spectral methods) can be put in the form of a weighted residual method, and that test and trial functions can be defined on different computational grids, is the key to go beyond this misconception.

will be dropped for the sake of conciseness)[4].

The superscript $i \geq 0$ is introduced to distinguish between successive applications of operators G^i which, while not necessarily different among them, are required to satisfy $\Delta^{i+1} \geq \Delta^i$; this is not at all a constraint (and could easily be removed) but greatly simplifies the understanding of the following passages. The first application of an operator G^i will always be due to G^1 with width Δ^1, the second operator applied to any function will always be G^2 with width $\Delta^2 \geq \Delta^1$, etc. In practice, the following conventions are adopted:

$$\begin{aligned}
&G^0 * \bar{\phi}^0 = \bar{\phi}^0 = \phi \\
&G^1 * \bar{\phi}^0 = \bar{\phi}^1 = \bar{\phi} \\
&\bar{\phi}^n = G^n * \bar{\phi}^{n-1} = G^n * G^{n-1} * \ldots * G^1 * G^0 * \bar{\phi}^0 \\
&\overline{\bar{\phi}^{n-m}}^{+(m)} = \bar{\phi}^n = G^n * G^{n-1} * \ldots * G^{n-m+1} * \bar{\phi}^{n-m}
\end{aligned} \tag{3.4}$$

Thus, $G^0 = I$ is assumed to be the identity operator and, by definition, $\Delta^0 = 0$. While not explicit in the notation, the operator $\overline{(\cdots)}^{+(m)}$, and the notation $\bar{\phi}^m$ itself, always implies a very specific sequence of m operators G^i which, in the following, will always be made explicit whenever necessary. Also, note that variables like $\bar{\phi}^n$ are the result of n different applications of different operators G^i and, as a consequence, the associated smallest physical scale in the field cannot be considered to be Δ^n in general, which is only associated to the last operator applied G^n (Vreman et al., 1997). In order to introduce such difference, the smallest physical length scale associated to $\bar{\phi}^n$ is denoted by Δ_n. Besides linearity and preservation of constants, two further constraints are required for G^i. The first one is commutation with temporal derivatives:

$$G^i * \left[\frac{\partial}{\partial t}(\cdots)\right] = \frac{\partial}{\partial t}\left[G^i * (\cdots)\right] \tag{3.5}$$

in accordance with the CLES framework presented in chapter 2. While precluding some kind of applications (e.g., moving grids (Leonard et al., 2007)), (3.5) is satisfied in most of the known LES approaches and, in any case, far easier to model than the commutation error for the spatial derivatives. The second constraint required for G^i in a given computational domain Ω is the lack of interaction with its boundary $\partial\Omega$. This, in turn, either implies operators whose kernels become more and more asymmetric in the proximity of the boundary or:

$$\lim_{\mathbf{x}\to\partial\Omega} G^i = G^0 \tag{3.6}$$

In fact, there is no practical application where none of these two is satisfied. Besides the previous two constraints, no additional ones are required, hence the kernel of every operator G^i is left free to vary in space, just like its width Δ^i. Finally, in order to

[4]Using the symbol Δ in the present context might appear misleading as in general, because of the interpolation, $\bar{\phi}$ still contains energy at smaller scales. It should be clear, however, that Δ refers to the physical energy content. Scales smaller than Δ do not have any physical significance and their inclusion in the formulation is just a mathematical step.

treat variable density flows as in chapter 2, the Favre transformation is extended to the present class of operators G^i by adopting the following notation:

$$\begin{aligned}
&\tilde{\phi}^n = \frac{\overline{\rho\phi}^n}{\bar{\rho}^n} \\
&\bar{\rho}^n\tilde{\phi}^n = \overline{\rho\phi}^n = \overline{\overline{\rho\phi}^{n-1}}^{+(1)} = \overline{\bar{\rho}^{n-1}\tilde{\phi}^{n-1}}^{+(1)} = \cdots = \overline{\bar{\rho}^{n-m}\tilde{\phi}^{n-m}}^{+(m)}
\end{aligned} \tag{3.7}$$

In the following, the variables $\bar{\rho}^n$, $\bar{p}^n$ and the remaining $\tilde{\phi}^n$ are assumed to be the resolved variables, those actually available during a computation.

3.3 Governing equations

With the definitions introduced in the previous section, governing equations for the GLES framework can be derived, as in CLES, by a formal application of operators G^i to the basic NSE. However, differently from CLES, here n such operators are applied in sequence, leading to:

$$\begin{aligned}
&\frac{\partial\bar{\rho}^n}{\partial t} + \overline{\frac{\partial}{\partial x_j}\left(\rho u_j\right)}^n = 0 \\
&\frac{\partial\left(\bar{\rho}^n\tilde{u}_i^n\right)}{\partial t} + \overline{\frac{\partial}{\partial x_j}\left(\rho u_i u_j + \sigma_{ij}\right)}^n = 0 \\
&\frac{\partial\left(\bar{\rho}^n\tilde{E}^n\right)}{\partial t} + \overline{\frac{\partial}{\partial x_j}\left(\rho u_j E + q_j + u_i\sigma_{ij}\right)}^n = 0 \\
&\bar{\rho}^n\tilde{E}^n = \frac{\bar{p}^n}{\gamma-1} + \frac{1}{2}\bar{\rho}^n\tilde{u}_k^n\tilde{u}_k^n + \frac{1}{2}\bar{\rho}^n\left(\widetilde{u_k u_k}^n - \tilde{u}_k^n\tilde{u}_k^n\right) \\
&\bar{p}^n = \bar{\rho}^n R\tilde{T}^n
\end{aligned} \tag{3.8}$$

This, apparently vain, tedious multi-level formulation will be shown to be helpful for several reasons. The main, most obvious, one is that not all the LES formulations are equal (e.g., IFCLES vs. EFCLES), with some explicitly requiring multiple filtering levels, in the formulation itself or in the SGS modeling (e.g., CGI), and a framework supposed to be general requires a tool to properly handle them. In practical applications, one of such levels will always be a sampling operator (usually the first or the last one) and, having included an interpolation as part of it, allows to consider equations (3.8) in their continuous form without further approximations[5]. Under the previous hypotheses, equations (3.8) are still exact evolutions equations for the $\overline{(\cdots)}^n$ level variables but, just like in CLES, require further assumptions to be closed. Here, the most trivial way is used to proceed, by simply using known variables in place of the unknown ones, which leads to the final form of the equations for the GLES framework at

[5]This, of course, has an influence on the functional spaces where solutions to GLES equations reside but, in strict mathematical terms, this is the main reason for which LES is usually applied in the first place, instead of the pure NSE.

a generic level $n \geq 0$:

$$
\begin{aligned}
&\frac{\partial \bar{\rho}^n}{\partial t} + \overline{\frac{\partial}{\partial x_j}\left(\bar{\rho}^n \tilde{u}_j^n\right)}^n = \overline{\frac{\partial}{\partial x_j}\left(\chi_j^{n-0}\right)}^n \\
&\frac{\partial\left(\bar{\rho}^n \tilde{u}_i^n\right)}{\partial t} + \overline{\frac{\partial}{\partial x_j}\left(\bar{\rho}^n \tilde{u}_i^n \tilde{u}_j^n + \tilde{\sigma}_{ij}^n\right)}^n = \overline{\frac{\partial}{\partial x_j}\left(\tau_{ij}^{n-0}\right)}^n \\
&\frac{\partial\left(\bar{\rho}^n \tilde{E}^n\right)}{\partial t} + \overline{\frac{\partial}{\partial x_j}\left(\bar{\rho}^n \tilde{u}_j^n \tilde{E}^n + \tilde{q}_j^n + \tilde{u}_i^n \tilde{\sigma}_{ij}^n\right)}^n = \overline{\frac{\partial}{\partial x_j}\left(\varepsilon_j^{n-0}\right)}^n \\
&\bar{\rho}^n \tilde{E}^n = \frac{\bar{p}^n}{\gamma - 1} + \frac{1}{2}\bar{\rho}^n \tilde{u}_k^n \tilde{u}_k^n + \alpha^n \\
&\bar{p}^n = \bar{\rho}^n R \tilde{T}^n
\end{aligned}
\tag{3.9}
$$

where:

$$
\begin{aligned}
&\tilde{\sigma}_{ij}^n = \bar{p}^n \delta_{ij} - 2\tilde{\mu}^n\left(\tilde{S}_{ij}^n - \frac{1}{3}\tilde{S}_{kk}^n \delta_{ij}\right) = \bar{p}^n \delta_{ij} + \tilde{\Sigma}_{ij}^n \\
&\tilde{S}_{ij}^n = \frac{1}{2}\left(\frac{\partial \tilde{u}_i^n}{\partial x_j} + \frac{\partial \tilde{u}_j^n}{\partial x_i}\right) \\
&\tilde{q}_j^n = -\tilde{\lambda}^n \frac{\partial \tilde{T}^n}{\partial x_j}
\end{aligned}
\tag{3.10}
$$

and $\tilde{\mu}^n = \mu(\tilde{T}^n)$, $\tilde{\lambda}^n = C_p \tilde{\mu}^n / Pr$. A first fundamental property that emerges from equations (3.9) is that, as a result of the approach, the commutation property (2.10) is not anymore necessary. The second main difference, with respect to the CLES framework, is that modeling is now required for the following SGS terms (with $m = 0$):

$$
\begin{aligned}
&\chi_j^{n-m} = -\chi_j^{m-n} = \bar{\rho}^n \tilde{u}_j^n - \bar{\rho}^m \tilde{u}_j^m \\
&\tau_{ij}^{n-m} = -\tau_{ij}^{m-n} = \left(\bar{\rho}^n \tilde{u}_i^n \tilde{u}_j^n - \bar{\rho}^m \tilde{u}_i^m \tilde{u}_j^m\right) + \left(\tilde{\sigma}_{ij}^n - \tilde{\sigma}_{ij}^m\right) \\
&\varepsilon_j^{n-m} = -\varepsilon_j^{m-n} = \left(\bar{\rho}^n \tilde{u}_j^n \tilde{E}^n - \bar{\rho}^m \tilde{u}_j^m \tilde{E}^m\right) + \left(\tilde{q}_j^n - \tilde{q}_j^m\right) + \left(\tilde{u}_i^n \tilde{\sigma}_{ij}^n - \tilde{u}_i^m \tilde{\sigma}_{ij}^m\right) \\
&\alpha^n = \frac{1}{2}\bar{\rho}^n \left(\widetilde{u_k u_k}^n - \tilde{u}_k^n \tilde{u}_k^n\right)
\end{aligned}
\tag{3.11}
$$

which, besides α^n, are different from those usually introduced in CLES, especially in the IFCLES case. In particular, SGS terms in GLES always include both linear and non-linear terms, independently from the specific approach, even for incompressible flows. The continuity equation, in general, also involves non closed terms. For modeling purposes, and following the same steps outlined in section 2.4.2, the SGS term in the energy equation can also be recast as follows:

$$
\varepsilon_j^{n-m} = \left(\bar{\rho}^n \tilde{u}_j^n \tilde{T}^n - \bar{\rho}^m \tilde{u}_j^m \tilde{T}^m\right) + \left(\tilde{q}_j^n - \tilde{q}_j^m\right) + \left(\tilde{u}_i^n \tilde{\Sigma}_{ij}^n - \tilde{u}_i^m \tilde{\Sigma}_{ij}^m\right) + \beta_j^{n-m} \tag{3.12}
$$

with:

$$\beta_j^{n-m} = -\beta_j^{m-n} = \tilde{u}_j^n \left(\frac{1}{2} \bar{\rho}^n \tilde{u}_k^n \tilde{u}_k^n + \alpha^n \right) - \tilde{u}_j^m \left(\frac{1}{2} \bar{\rho}^m \tilde{u}_k^m \tilde{u}_k^m + \alpha^m \right) \tag{3.13}$$

so that, in case, SGS modeling can be limited to the first term in equation (3.12), the SGS heat flux.

The equations presented here, as those in chapter 2, are intended for general compressible flows as well as incompressible ones. However, in both cases, especially for general purpose solvers, the actual form of the equations used for the discretization is generally different and based on a pressure equation, which allows a higher flexibility in handling both flow regimes and additional physical mechanisms. It is a matter of simple manipulations[6] to show that the following pressure equation holds in the GLES framework:

$$\overline{\frac{\partial}{\partial x_i} \frac{\partial}{\partial x_j} \left(\bar{p}^n \delta_{ij} \right)}^n = \frac{\partial^2 \bar{\rho}^n}{\partial t^2} - \overline{\frac{\partial}{\partial x_i} \frac{\partial}{\partial x_j} \left(\bar{\rho}^n \tilde{u}_i^n \tilde{u}_j^n + \tilde{\Sigma}_{ij}^n - \tau_{ij}^{n-0} \right)}^n \tag{3.14}$$

and can then be used whenever necessary. Notice that some authors (Carati et al., 2001; Winckelmans et al., 2001, 2002; Knaepen et al., 2002; De Stefano and Vasilyev, 2004) have explicitly advocated the use of equations, whose form is similar to the one proposed here, as formal LES model. However, under detailed scrutiny, their proposal can be actually seen as the application of the EFCLES formalism to the IFCLES equations and, as they still invoke the commutation property (2.10) for the implicit filter, the overall approach produces no actual difference with CLES. In fact, as will be shown in section 3.6, such commutation for the implicit filter does not hold in general.

3.4 Generalized Germano Identities

The CGI, expressed in equations (2.33) and (2.44), are exact algebraic relations between SGS terms considered at different filtering levels. As such, they obviously depend on the form of the SGS terms. It is then easy to see that, because of the different form of the SGS terms, a still more crucial difference arises in GLES, with respect to CLES, as in GLES the SGS terms satisfy the following Generalized Germano Identities (GGI):

$$\begin{aligned} \chi_j^{n-k} - \chi_j^{m-k} &= \chi_j^{n-m} \\ \tau_{ij}^{n-k} - \tau_{ij}^{m-k} &= \tau_{ij}^{n-m} \\ \varepsilon_j^{n-k} - \varepsilon_j^{m-k} &= \varepsilon_j^{n-m} \end{aligned} \tag{3.15}$$

for any (n, m, k) combination (negative values for the integers are excluded by definition). In practice, the case $k = 0$ is relevant for the use of these relations in a dynamic procedure. The primary thing to notice about such GGI is that their validity holds for

[6] Exploiting the definition of τ_{ij}^{n-0} would reveal that equation (3.14) is just the classical pressure equation acted upon by the n G^i operators.

any combination of G^i operators satisfying the hypotheses defined in section 3.2, thus they are more general than CGI in the sense that they are satisfied under much looser conditions, which in practice are always verified. The second important difference, with respect to the CGI, is that none of the tensors/vectors in (3.15) is acted upon by any of the G^i operators. This, in turn, has two major consequences. The first is that, when such GGI are used for modeling purposes, SGS model constants do not need to be arbitrarily extracted from any operator G^i. The second is that, in practice, all the terms in the equations (3.15) only involve products of variables (at the different possible levels); as a consequence, all that is required to use the GGI in a dynamic procedure are the variables at two different levels. As will be better shown in chapter 4, in the worst case scenario of a mixed model for a compressible flow, considering both the momentum and energy equation, only 12 scalars need to be explicitly filtered[7] against the 37 required in the IFCLES framework. In the simplest case of a Smagorinsky model for an incompressible flow, only 3 scalars need to be filtered, against the 15 required in the IFCLES framework. Thus, the dynamic procedure in the GLES framework is $67 - 80\%$ cheaper than the one in the IFCLES framework; with respect to the the EFCLES framework the advantage is even higher.

The only exception to the previous reasoning is for the α^i terms which, instead, still satisfy a form of CGI ($m \geq n$):

$$\alpha^m - \overline{\alpha^n}^{+(m-n)} = \frac{1}{2}\left(\overline{\bar{\rho}^n \tilde{u}_k^n \tilde{u}_k^n}^{+(m-n)} - \bar{\rho}^m \tilde{u}_k^m \tilde{u}_k^m\right) \tag{3.16}$$

Thus, in a dynamic procedure, model constants in α^n should still be arbitrarily extracted from the operator $\overline{(\cdots)}^{+(m-n)}$ and 2 additional scalars should be filtered. However, differently from the CGI, (3.16) is still valid under the more loose assumptions used in GLES.

3.5 Functional analysis

The important result from the previous sections is that, not requiring the commutation property (2.10), the GLES framework involves a different form of SGS stresses. As a consequence, a problem arises about the most suitable form of SGS models in the GLES framework, as those developed within the CLES framework are not necessarily suitable for GLES too. In practice, this matter can be analyzed by two different points of view, according to the available forms of SGS models: structural and functional.

As already noted in section 2.4.2, structural models assume that the resolved terms in the equations require a better reconstruction to be used conveniently and, to properly reconstruct them, they also require that some information on the operators affecting the resolved fields is actually available. As this would require specifying the set of G^i used in a computation, a structural analysis is postponed to chapter 4, where it is used to develop a novel form of scale-similar term for GLES applied to the FV method.

A functional analysis, in contrast, does not require such detailed information as it simply evidences the role of the SGS terms in the energy transfers between resolved and non resolved scales. In practice, such role is devised by looking at the equations

[7] In practice, as shown in section 3.6 and chapter 4, most of the times the G^i operators are still conveniently interpreted as classical filters.

for the resolved and non-resolved kinetic energies. For the present GLES framework, exact equations for the resolved kinetic energy $\tilde{q}_r^n = \bar{\rho}^n \tilde{u}_j^n \tilde{u}_j^n/2$ and the SGS kinetic energy $q_{sgs}^n = \tilde{q}_r^0 - \tilde{q}_r^n$ are derived in Appendix B. For the present analysis, however, it is sufficient to report the equation for $\tilde{q}_r^n$:

$$\begin{aligned}\frac{\partial \tilde{q}_r^n}{\partial t} =& -\frac{\partial}{\partial x_k}\left[\tilde{q}_r^n \tilde{u}_k^n + \bar{p}^n \tilde{u}_k^n + \tilde{u}_j^n\left(\tilde{\Sigma}_{jk}^n - \tau_{jk}^{n-0}\right)\right] + \bar{p}^n \frac{\partial \tilde{u}_k^n}{\partial x_k} + \tilde{\Sigma}_{jk}^n \frac{\partial \tilde{u}_j^n}{\partial x_k} \\ & -\tau_{jk}^{n-0}\frac{\partial \tilde{u}_j^n}{\partial x_k} + \tilde{u}_j^n \frac{\partial \chi_j^{n-0}}{\partial t} - \frac{\tilde{q}_r^n}{\bar{\rho}^n}\left[\frac{\partial \bar{\rho}^n}{\partial t} + \frac{\partial\left(\bar{\rho}^n \tilde{u}_k^n\right)}{\partial x_k}\right]\end{aligned} \tag{3.17}$$

and to note that, in the previous equation, the terms on the second line are those that, with an inverted sign, appear in the equation for q_{sgs}^n (see equation (B.8)). As such, these terms are then responsible for the energy transfers between resolved and non resolved scales.

Some important information can be obtained from equation (3.17). The first and most important is that, besides the last two terms, the equation exactly coincides with the analogous equation for the IFCLES approach (Sagaut, 2006). Moreover, despite being formally different, the SGS stresses also play the exact same role as in the IFCLES approach. Indeed, as in equation (2.20), the resolved dissipation term $-\tilde{\Sigma}_{jk}^n \partial \tilde{u}_j^n/\partial x_k$ is unable to completely dissipate the flux of energy from the largest scales, and the term $\tau_{jk}^{n-0}\partial \tilde{u}_j^n/\partial x_k$ should compensate for it. Hence, in practice, from the functional point of view, the SGS models introduced for the IFCLES framework are suitable choices for τ_{ij}^{n-0} too.

However, as noted above, two additional terms appear in equation (3.17), which do not have a counterpart in any CLES formulation. Before proceeding, it is important to anticipate that the first two terms, $-\tau_{jk}^{n-0}\partial \tilde{u}_j^n/\partial x_k$ and $\tilde{u}_j^n \partial \chi_j^{n-0}/\partial t$, refer, respectively, to the modeling and commutation in the momentum equation. An analogous decomposition could have been chosen for the last term but, as a matter of fact, in the continuity equation the two aspects are necessarily linked and no modeling issue exists if the operators G^i commute with the spatial derivatives. This is highlighted by the fact that the term in square brackets has the form of the continuity equation which holds for commuting filters (see equation (2.11)). Nonetheless, in case commutation does not hold, this term can also be rewritten as:

$$\begin{aligned}-\frac{\tilde{q}_r^n}{\bar{\rho}^n}\left[\frac{\partial \bar{\rho}^n}{\partial t} + \frac{\partial\left(\bar{\rho}^n \tilde{u}_k^n\right)}{\partial x_k}\right] &= -\frac{\tilde{q}_r^n}{\bar{\rho}^n}\left[\frac{\partial \chi_k^{n-0}}{\partial x_k} + \frac{\partial\left(\bar{\rho}^n - \rho\right)}{\partial t}\right] \\ &= -\frac{\tilde{q}_r^n}{\bar{\rho}^n}\overline{\frac{\partial \chi_k^{n-0}}{\partial x_k}}^n - \frac{\tilde{q}_r^n}{\bar{\rho}^n}\left[\frac{\partial\left(\bar{\rho}^n \tilde{u}_k^n\right)}{\partial x_k} - \overline{\frac{\partial\left(\bar{\rho}^n \tilde{u}_k^n\right)}{\partial x_k}}^n\right]\end{aligned} \tag{3.18}$$

Hence, the SGS model for the continuity equation, if any, affects the energy balance like any other mass source, redistributing the energy on the available resolved mass per unit volume. The fact that the term $\tilde{u}_j^n \partial \chi_j^{n-0}/\partial t$ represents the effects of the commutation is not directly demonstrable. However some heuristic arguments can be used to support this assertion. First of all, when commutation is assumed to hold, the form of

the equations is formally unchanged and the term disappears[8]. A second argument is that, by using the following decomposition:

$$\tilde{u}_j^n \frac{\partial \chi_j^{n-0}}{\partial t} = \tilde{u}_j^n \frac{\partial}{\partial t}\left[\sum_{i=0}^{n-1}\left(\bar{\rho}^{i+1}\tilde{u}_j^{i+1} - \bar{\rho}^i \tilde{u}_j^i\right)\right] = -\sum_{i=0}^{n-1} \tilde{u}_j^n \frac{\partial \chi_j^{i-(i+1)}}{\partial t} \tag{3.19}$$

the term could be interpreted as a flux of energy from the level n toward the smallest ones. However, if the different bands $\overline{(\cdots)}^{i-(i+1)}$ can be associated to the elements of an orthonormal basis for $L^2(\Omega)$ then, by the Parseval's theorem, this term has a null contribution on the overall resolved kinetic energy in the domain Ω[9]. The interpretation of the G^i as projectors into such orthonormal basis does not imply, in general, the commutation property[10] (Vreman, 2004b) but, at least conceptually, such a global expansion necessarily implies, for each band, a unique length scale Δ^i over all the domain Ω (which, in a general sense, is a condition for commutation to hold).

In conclusion, the main result of the present functional analysis is that models for the SGS stresses devised for the CLES framework would play the exact same role in GLES and, in both cases, the model is needed to counteract the lack of dissipation from the resolved terms. The role of the SGS model in the continuity equation, if any, is to remove/add energy from the resolved scales at a rate proportional to the relative effect of mass addition/removal in the continuity equation. Additional terms appearing in equation (3.17) seem to be related to the non commutation of the operators G^i with spatial derivatives, as they disappear when commutation holds. However, their interpretation is relatively unimportant as they do not describe the effect of additional SGS terms and cannot be affected by specific modeling options besides the specification of the operators G^i.

3.6 Practical relevance of GLES

The analysis and the developments from the previous sections allow to state that exact generalized LES equations can be written, which do not require limiting or impractical assumptions on the scale separation operators G^i. Such equations retain a physical significance as the formal role of the SGS terms is analogous to that found in classical LES formulations; still, the form of the SGS stresses and fluxes is different and leads to different Germano Identities with some favorable properties in terms of the related Dynamic Procedure.

Having established the previous points, what remain to be defined is the practical relevance of the proposed GLES framework, how can it be effectively applied in practical computations. It is the purpose of the present section to show that, as a matter of fact, most of the known LES approaches can be fit into this form or could be without specific problems. Considering the works of Vreman and Denaro, cited in the introduction of this chapter, and those cited in the following, it is noteworthy how most of the inconsistencies related to the CLES formulation have been somehow recognized

[8] In fact, the term does not disappear as, instead, it assumes a form that cancels terms in τ_{ij}^{n-0} and repristinates the original form of the equations for the IFCLES approach.

[9] The correctness of this assertion is strictly valid only for bases whose orthogonality condition does not involves weights.

[10] A notable exception being the Fourier modes.

in specific numerical settings but never related to a general theoretical framework, as proposed here[11].

3.6.1 Explicitly filtered GLES

It is very easy to see that the GLES framework is straightly applicable to the explicit filtering approach. In this case the operators G^i are actual filters and, for all the practical purposes, a single filter level needs to be considered (i.e., $n = 1$). In fact, the only case for which the explicit filtering approach actually follows the GLES proposal is, to the best of the author's knowledge, the Approximate Deconvolution Modeling (ADM) proposed by Stolz and Adams (1999), which in some cases is presented with the full filtering approach (Garnier et al., 2009; Stolz et al., 2001a) as in GLES. Nonetheless, the application of the GLES approach would be always straightforward as it would just require filtering all the terms after the application of the discrete spatial derivative operators. Also, it is the only consistent approach for general, non-commuting, filters.

A slight difficulty might arise in the case of implicit treatment of some terms in the equations, like the viscous terms or the discretization of the pressure equation (3.14). However, as is usually the case for higher order discretizations, a possible solution is to adopt a deferred correction approach (Khosla and Rubin, 1974), with unfiltered terms treated implicitly and the relative correction treated explicitly. In practice, for constant density flows, the explicit filtering of the pressure equation is unnecessary, and can be avoided. In contrast, it is strictly necessary for variable density flows. An even more elegant solution, however, would be the recognition that ADM is also consistently done by appropriately filtering the solution at each time step (Mathew et al., 2003), and to use the exact same approach in GLES.

Finally, is worth emphasizing how the interpretation of the explicit filtering approach performed according to the GLES framework is not different from the one in the EFCLES one. Indeed, by applying the method to a simple scalar conservation law, following the same approach used in section 2.3, the following equation is obtained:

$$\begin{aligned}\frac{\partial\bar{\phi}}{\partial t}+\overline{\nabla^d\cdot\mathbf{F}_M^d\left(\bar{\phi}\right)}^d=&\underbrace{\overline{\nabla\cdot\left[\mathbf{F}_M\left(\bar{\phi}\right)-\mathbf{F}\left(\phi\right)\right]}^d}_{\text{I}}+\underbrace{\left[\overline{\nabla\cdot\mathbf{F}\left(\phi\right)}^d-\overline{\nabla\cdot\mathbf{F}\left(\phi\right)}\right]}_{\text{II}}\\&+\underbrace{\overline{\nabla^d\cdot\left[\mathbf{F}_M^d\left(\bar{\phi}\right)-\mathbf{F}_M\left(\bar{\phi}\right)\right]}^d+\overline{\left[\nabla^d-\nabla\right]\cdot\mathbf{F}_M\left(\bar{\phi}\right)}^d}_{\text{III}}\end{aligned}\tag{3.20}$$

which has the exact same terms appearing in equation (2.13b). However, in equation (3.20) the discrete filter acts on the discrete derivatives as well, thus leading to a possible better removal of the error.

3.6.2 Implicitly filtered LES with finite differences

While not directly relevant for the present thesis, IFCLES based on finite differences certainly has an important role, at least in the academic practice. It is thus interesting to highlight how the present framework can be readily applied to this approach too.

[11] The only exceptions to this are, in fact, the EFCLES and the IFCLES based on finite differences, which still remain related to the original Leonard formalization.

A concept which is extremely useful in formalizing the discretization of continuous equations on a discrete computational grid, especially for LES, is the sampling operator introduced by Debliquy (Debliquy et al., 2004; Knaepen et al., 2005; Fauconnier et al., 2007). Such operator, in practice, acts as a projector between the continuous, physical domain Ω and its discrete counterpart $\Omega^{\Delta^i} = \{\mathbf{x}_1, \mathbf{x}_2, \ldots, \mathbf{x}_{N^i}\}$, described as a collection of N^i points $\mathbf{x}_j \in \Omega$. The superscript Δ^i serves the purpose to remind the discrete nature of the object and, more generally, indicates the typical length scale associated with it but, in no way it means that such length is constant in space. Following the presentation of the GLES framework, a general sequence of n discrete domains (in the following simply denoted as grids) Ω^{Δ^i} is considered here; however, as for GLES, such sequence cannot be arbitrary, but has to satisfy the constraints $\Omega^{\Delta^i} \subseteq \Omega^{\Delta^{i-1}}$ and $N^i \leq N^{i-1}$.

With such definitions, the sampling operator $\mathcal{S}^{\Delta^i}$ can be more precisely defined as the operator that, for any function $\phi(\mathbf{x})$ with $\mathbf{x} \in \Omega$ returns $\phi^{\Delta^i}(\mathbf{x}_j) = \phi(\mathbf{x}_j) \forall \mathbf{x}_j \in \Omega^{\Delta^i}$. In practice, for any function, the sampling operator $\mathcal{S}^{\Delta^i}$ returns the exact same value on the grid Ω^{Δ^i}:

$$\phi^{\Delta^i} = \mathcal{S}^{\Delta^i} * \phi \tag{3.21}$$

Due to the above definitions, $\mathcal{S}^{\Delta^i}$ satisfies the following properties:

$$\begin{aligned} &\phi^{\Delta^i} = \mathcal{S}^{\Delta^i} * \phi = \mathcal{S}^{\Delta^i} * \mathcal{S}^{\Delta^i} * \phi \\ &\mathcal{S}^{\Delta^i} * (\phi\psi) = \left(\mathcal{S}^{\Delta^i} * \phi\right)\left(\mathcal{S}^{\Delta^i} * \psi\right) = \phi^{\Delta^i}\psi^{\Delta^i} \end{aligned} \tag{3.22}$$

hence, it is idempotent and commutes with the product operation. Also, due to the embedding of the grids Ω^{Δ^i}:

$$\phi^{\Delta^i} = \mathcal{S}^{\Delta^i} * \phi = \mathcal{S}^{\Delta^i} * \phi^{\Delta^j} = \mathcal{C}^{\Delta^i,\Delta^j} * \phi^{\Delta^j} = \mathcal{C}^{\Delta^i,\Delta^j} * \mathcal{S}^{\Delta^j} * \phi \quad \forall j \leq i \tag{3.23}$$

where the additional coarsening operator $\mathcal{C}^{\Delta^i,\Delta^j}$ has been introduced. In order to finalize the description of the finite difference approach, it is still necessary to introduce the effect of the discretization. In practice, two possible ways exists. One consists in recognizing the fact that continuous derivative operators cannot interact with sampled values of a function and, as done in equation (3.20), to introduce discrete counterparts of continuous operators (e.g., ∇^d in place of ∇) and treat their difference as an error. This was the preferred choice in later works on the sampling formalism (Knaepen et al., 2005; Fauconnier et al., 2007). However, an additional possibility consists in embedding within the sampling operators also an interpolation, as originally proposed by Debliquy et al. (2004). The way to intend this interpolation is such that, when a continuous derivative operator is applied to a sampled function, it exactly returns the value which would have been obtained by applying the underlying discrete approximation on the available discrete values. In general, such interpolants might be more complex than expected (see Debliquy et al. (2004) for some practical examples), in order to fit all the required constraints on all the discrete operators, but in most practical cases such interpolants exist, whcih is all that is required here. Thus, roughly speaking, the sampling operator $\mathcal{S}^{\Delta^i}$ defines the grid and the underlying numerical discretization as a whole.

The important thing to notice about the sampling operators defined above is that, by themselves, they do not lead to any closure problem due to the presence of non linear terms, however complex they might be[12]. In contrast, they do not commute with continuous spatial derivatives, the relative commutation error being actually the truncation error of the underlying numerical scheme[13]:

$$\frac{\partial \phi^{\Delta^i}}{\partial x_i} - \mathcal{S}^{\Delta^i} * \frac{\partial \phi}{\partial x_i} = L.T.E. \tag{3.24}$$

Thus, when applied to the NSE, sampling operators still leads to the rise of non closed terms which need modeling, but these are only due to the numerical errors. In practice, the relevance of such errors is strictly dependent on the underlying interpolation and the resolution capabilities of the given grid with respect to the continuous function they act upon. For DNS applications such combination is selected to have an error which, in some norm, can be considered negligible. In contrast, in LES based on sampling operators the grid is by definition such that, independently from the specific numerical method, such approximation is not possible and a model is necessary.

At this point, it is straightforward to show that when a generic finite difference method is applied to the NSE on the grid Ω^{Δ^k}, the exact form of the resulting equations is the following:

$$\frac{\partial \left(\rho^{\Delta^k} u_i^{\Delta^k}\right)}{\partial t} + \mathcal{S}^{\Delta^k} * \frac{\partial}{\partial x_j}\left(\rho^{\Delta^k} u_i^{\Delta^k} u_j^{\Delta^k} + \sigma_{ij}^{\Delta^k}\right) = \mathcal{S}^{\Delta^k} * \frac{\partial}{\partial x_j}\left(\tau_{ij}^{\Delta^k}\right) \tag{3.25}$$

where, for the sake of conciseness, the discussion is limited to the sole momentum equation and, besides the specific differences due to the operator $\mathcal{S}^{\Delta^i}$, $\sigma_{ij}^{\Delta^k}$ is defined as the analogous term in equation (3.10). Of course, unless it is specifically modeled, the error $\tau_{ij}^{\Delta^k}$ in equation (3.25):

$$\tau_{ij}^{\Delta^k} = \left(\rho^{\Delta^k} u_i^{\Delta^k} u_j^{\Delta^k} + \sigma_{ij}^{\Delta^k}\right) - (\rho u_i u_j + \sigma_{ij}) \tag{3.26}$$

is not really present in actual computations. It is worth mentioning that the formulation actually proposed by Debliquy et al. is different from the one proposed here, as it is based on the error definition used in equation (3.24), which would seem more natural. However, within the present sampling formalism, the following identity holds in the sampling points:

$$\frac{\partial \phi^{\Delta^k}}{\partial x_i} - \mathcal{S}^{\Delta^k} * \frac{\partial \phi}{\partial x_i} = \mathcal{S}^{\Delta^k} * \frac{\partial \phi^{\Delta^k}}{\partial x_i} - \mathcal{S}^{\Delta^k} * \frac{\partial \phi}{\partial x_i} = \mathcal{S}^{\Delta^k} * \frac{\partial}{\partial x_i}\left(\phi^{\Delta^k} - \phi\right) \tag{3.27}$$

hence restoring the complete correspondence among the two formulations. The fact that equation (3.25) exactly fits the one in the proposed GLES framework should be

[12] As long as the evaluation is limited to the sampling points.

[13] An analogous extension could be provided for the time discretization.

already self-evident by looking at the equations (3.9), even when a series of n sampling operators are considered in series. Such correspondence, of course, also includes Germano Identities of the form:

$$\tau_{ij}^{\Delta^m} - \tau_{ij}^{\Delta^n} = \left(\rho^{\Delta^m} u_i^{\Delta^m} u_j^{\Delta^m} + \sigma_{ij}^{\Delta^m}\right) - \left(\rho^{\Delta^n} u_i^{\Delta^n} u_j^{\Delta^n} + \sigma_{ij}^{\Delta^n}\right) \tag{3.28}$$

Again, the form of such identity seems to not correspond to the one originally devised by Debliquy et al. which, in a simplified notation, could be written as:

$$\begin{aligned} &\left(\frac{\partial \phi^{\Delta^m}}{\partial x_i} - \mathcal{S}^{\Delta^m} * \frac{\partial \phi}{\partial x_i}\right) - \mathcal{C}^{\Delta^m,\Delta^n}\left(\frac{\partial \phi^{\Delta^n}}{\partial x_i} - \mathcal{S}^{\Delta^n} * \frac{\partial \phi}{\partial x_i}\right) = \\ &= \frac{\partial \phi^{\Delta^m}}{\partial x_i} - \mathcal{C}^{\Delta^m,\Delta^n}\frac{\partial \phi^{\Delta^n}}{\partial x_i} \end{aligned} \tag{3.29}$$

However, invoking again the identity in (3.27) and the properties of the coarsening operator in (3.23), it becomes:

$$\begin{aligned} &\mathcal{S}^{\Delta^m} * \frac{\partial}{\partial x_i}\left(\phi^{\Delta^m} - \phi\right) - \mathcal{S}^{\Delta^m} * \frac{\partial}{\partial x_i}\left(\phi^{\Delta^n} - \phi\right) = \\ &= \mathcal{S}^{\Delta^m} * \frac{\partial}{\partial x_i}\left(\phi^{\Delta^m} - \phi^{\Delta^n}\right) \end{aligned} \tag{3.30}$$

from which the present form of Germano Identities easily follows:

$$\left(\phi^{\Delta^m} - \phi\right) - \left(\phi^{\Delta^n} - \phi\right) = \left(\phi^{\Delta^m} - \phi^{\Delta^n}\right) \tag{3.31}$$

In practice, the whole difference among the two approaches is only a matter of interpretation of the error: it can be seen as due to the replacement of continuous derivative operators with discrete ones or, as in the present GLES approach, due to an incorrect interpolation of the underlying function. However, no matter what the interpretation is, the two approaches are exactly equivalent. Notably, different interpretations of the error lead to different forms of Germano Identities, with the form (3.31) arising in GLES being much less cumbersome than the classical one (3.29)[14]. Of course, explicit filtering (as described in the previous section) and sampling can be merged in a single GLES formulation with two levels, and nothing would change besides the interpretation of the operators, which shows the power of the approach.

3.6.3 Implicitly filtered LES with the method of weighted residuals

Notably, the most straightforward interpretation of a numerical method as a formal LES approach can be obtained by its interpretation within the weighted residuals method (Finlayson and Scriven, 1966; Finlayson, 1972). Such interpretation is not new (Hughes

[14]Notice that, when equation (3.29) is used in a dynamic procedure, the models replacing the terms in parentheses need to be in the form of the divergence of a term, for compatibility with the governing equations. As a consequence, the model constant is acted upon by the derivative operators and, while not requiring the extraction from any test filter, its computation requires the resolution of a differential problem. The overall procedure is, indeed, very similar to the one proposed by Morinishi and Vasilyev (2002).

et al., 2000; Pope, 2001; Oberai and Wanderer, 2005a), as already noted is its connection with the FV formulation (Vreman, 2004b), however it is discussed here to highlight that it exactly fits the proposed GLES framework in general. Without the intent to be complete or detailed, in the weighted residuals method, the solution u, in the domain Ω, for a generic scalar differential problem:

$$\mathbb{L}(u) = 0 \tag{3.32}$$

subject to proper initial and boundary conditions, is assumed to be representable in the form:

$$u_d^N(\mathbf{x}, t) = \sum_{i=1}^{N} \hat{u}_i(t)\, \Phi_i(\mathbf{x}) \tag{3.33}$$

where the Φ_i are trial functions used for the expansion and the $\hat{u}_i$ are N unknown coefficients to be determined. The way such coefficients are determined is by substitution of the expansion (3.33) in the original equation (3.32) and by applying the following restrictions on the resulting residual (Karniadakis and Sherwin, 1999):

$$\int_\Omega v_j(\mathbf{x})\, \mathbb{L}\left(u_d^N\right) d\mathbf{x} = 0 \qquad j = 1, 2, \ldots, N \tag{3.34}$$

where the v_j are called test or weight functions. In practice, this approach can lead to several different methods, according to the specific choice of the functions v_j and Φ_i. The first consideration emerging from equations (3.32–3.34) is that, in the present form, they already represent an LES formalism. Indeed, independently from the specific definition of v_j, it is possible to define the projector $\mathcal{P}^N$ so that (Vreman, 2004b):

$$\begin{aligned}
\mathcal{P}^N * u(\mathbf{x}, t) &= \sum_{i=1}^{N} \hat{u}_i(t)\, \Phi_i(\mathbf{x}) \\
&= \sum_{i=1}^{N} \Phi_i(\mathbf{x}) \int_\Omega v_i(\boldsymbol{\xi})\, u(\boldsymbol{\xi}, t)\, d\boldsymbol{\xi} \\
&= \int_\Omega \left[\sum_{i=1}^{N} v_i(\boldsymbol{\xi})\, \Phi_i(\mathbf{x}) \right] u(\boldsymbol{\xi}, t)\, d\boldsymbol{\xi} \\
&= \int_\Omega G^N(\mathbf{x}, \boldsymbol{\xi})\, u(\boldsymbol{\xi}, t)\, d\boldsymbol{\xi} = u_d^N(\mathbf{x}, t)
\end{aligned} \tag{3.35}$$

Also, as equation (3.34) holds for each j, it is easy to see that this implies also the following relation:

$$\int_\Omega G^N(\mathbf{x}, \boldsymbol{\xi})\, \mathbb{L}\left(u_d^N\right) d\boldsymbol{\xi} = \mathcal{P}^N * \mathbb{L}\left(u_d^N\right) = 0 \tag{3.36}$$

Thus, not only the solution (3.33) is in the form of a filtered function, but the equations themselves are discretized in the form (3.36), which is analogous to the one used in the GLES framework. In particular, it should be noted that no commutation is assumed between $\mathcal{P}^N$ and $\mathbb{L}$ as they are discretized together. What, instead, is explicitly missing from equation (3.36) is any explicit reference to the subgrid scales, as it is assumed that the number N of degrees of freedom in u_d^N is sufficient to completely resolve all the dynamically active scales. However, by definition, this is not the case in LES and one should instead consider the following form (Pope, 2001; Oberai and Wanderer, 2005a):

$$\mathcal{P}^N * \mathbb{L}\left(\mathcal{P}^N * u\right) + \mathcal{P}^N * \left[\mathbb{L}\left(u\right) - \mathbb{L}\left(\mathcal{P}^N * u\right)\right] = 0 \tag{3.37}$$

It is interesting to note that, as for GLES, even linear operators formally contribute to the definition of the SGS term in (3.37) and, in particular, the ideal SGS model is defined as:

$$\mathcal{P}^N * \mathbb{M}\left(\mathcal{P}^N * u\right) = \mathcal{P}^N * \left[\mathbb{L}\left(u\right) - \mathbb{L}\left(\mathcal{P}^N * u\right)\right] \tag{3.38}$$

Such relation can be used to derive a variational Germano Identity (Oberai and Wanderer, 2005a) by considering that, in general, it holds also for a projection $\mathcal{P}^M$ with $M < N$:

$$\mathcal{P}^M * \mathbb{M}\left(\mathcal{P}^M * u\right) = \mathcal{P}^M * \left[\mathbb{L}\left(u\right) - \mathbb{L}\left(\mathcal{P}^M * u\right)\right] \tag{3.39}$$

However, in the present case $\mathcal{P}^M * \mathcal{P}^N = \mathcal{P}^M$, and the application of $\mathcal{P}^M$ to equation (3.38) leads to:

$$\mathcal{P}^M * \mathbb{M}\left(\mathcal{P}^N * u\right) = \mathcal{P}^M * \left[\mathbb{L}\left(u\right) - \mathbb{L}\left(\mathcal{P}^N * u\right)\right] \tag{3.40}$$

Thus, subtracting equation (3.40) from equation (3.39), finally gives the variational Germano Identity:

$$\mathcal{P}^M * \mathbb{M}\left(\mathcal{P}^M * u\right) - \mathcal{P}^M * \mathbb{M}\left(\mathcal{P}^N * u\right) = \mathcal{P}^M * \left[\mathbb{L}\left(\mathcal{P}^N * u\right) - \mathbb{L}\left(\mathcal{P}^M * u\right)\right] \tag{3.41}$$

where should be noted that $\mathcal{P}^M * u$ is actually obtained as $\mathcal{P}^M * (\mathcal{P}^N * u)$. In practice, this is exactly the same identity which arises in the GLES framework, with the only difference that here the projection $\mathcal{P}^M$ has been retained in the identity. This approach, as suggested by Oberai and Wanderer (2005a), is in line with the variational formulation and, at the same time, with the approach of Morinishi and Vasilyev (2002), both leading to a vectorial level identity for the momentum equations in LES, with the model constants acted upon by differential operators. It is worth noting that this is actually also the nature of the GGI in the GLES framework but, in the author's opinion, this only masks the true local algebraic nature of such identities and, as a byproduct, extremely complicates the nature of the resulting dynamic procedure. As such, the

form (3.15) is considered here as fully valid and, in this variational formulation, it corresponds to[15]:

$$\mathbb{M}\left(\mathcal{P}^M * u\right) - \mathbb{M}\left(\mathcal{P}^N * u\right) = \mathbb{L}\left(\mathcal{P}^N * u\right) - \mathbb{L}\left(\mathcal{P}^M * u\right) \tag{3.42}$$

A final point which is worth noting is how, for different choices of v_j, different numerical methods and LES approaches are obtained. A first possible choice is to define $v_j(\mathbf{x}) = \delta(\mathbf{x}-\mathbf{x}_j)$, where the $\mathbf{x}_j$ define a set of discrete locations. Such approach, known as collocation method, leads to the following definition for u_d^N:

$$\begin{aligned}
\mathcal{P}^N * u\left(\mathbf{x},t\right) &= \sum_{i=1}^{N} \Phi_i\left(\mathbf{x}\right) \int_\Omega v_i\left(\boldsymbol{\xi}\right) u\left(\boldsymbol{\xi},t\right) d\boldsymbol{\xi} \\
&= \sum_{i=1}^{N} \Phi_i\left(\mathbf{x}\right) \int_\Omega \delta\left(\boldsymbol{\xi}-\boldsymbol{\xi}_i\right) u\left(\boldsymbol{\xi},t\right) d\boldsymbol{\xi} \\
&= \sum_{i=1}^{N} u\left(\mathbf{x}_i,t\right) \Phi_i\left(\mathbf{x}\right)
\end{aligned} \tag{3.43}$$

Thus the projector $\mathcal{P}^N$ becomes the sampling operator defined in the previous section and the functions Φ_i assume the role of shape functions, clarifying and supporting the way interpolation has been embedded in the present definition of sampling operators. However, the choice on Φ_i still can be almost arbitrary and, according to the number of points included in each shape function, it determines the specific numerical method, ranging from basic finite differences to full spectral collocation methods.

A second possible option for v_j is the one which defines Galerkin methods, which are based on $v_j(\mathbf{x}) = \Phi_j\left(\mathbf{x}\right)$. In this case u_d^N is defined as follows:

$$\begin{aligned}
\mathcal{P}^N * u\left(\mathbf{x},t\right) &= \sum_{i=1}^{N} \Phi_i\left(\mathbf{x}\right) \int_\Omega v_i\left(\boldsymbol{\xi}\right) u\left(\boldsymbol{\xi},t\right) d\boldsymbol{\xi} \\
&= \sum_{i=1}^{N} \Phi_i\left(\mathbf{x}\right) \int_\Omega \Phi_i\left(\boldsymbol{\xi}\right) u\left(\boldsymbol{\xi},t\right) d\boldsymbol{\xi} \\
&= \sum_{i=1}^{N} \hat{u}_i\left(t\right) \Phi_i\left(\mathbf{x}\right)
\end{aligned} \tag{3.44}$$

and the projection is not anymore in space but in spectral bands defined by the functions $\Phi_i\left(\mathbf{x}\right)$. As a consequence, the coefficients $\hat{u}_i(t)$ are not associated to local values of the function but to its energy content in the specific spectral band.

Another possible option for v_j, which will be the main topic for the rest of the thesis, is the one leading to the definition of the FV method. In this case, the domain Ω is first conveniently subdivided in a set of N non overlapping volumes Ω_j, of measure V_j.

[15] Note that this form is not exactly equivalent because of the specific notation used here. When the full expressions are introduced the equivalence can be restored.

Then, v_j is defined as the function which is unitary within the volume Ω_j and null outside it:

$$\begin{aligned}
\mathcal{P}^N * u(\mathbf{x},t) &= \sum_{i=1}^{N} \Phi_i(\mathbf{x}) \int_{\Omega} v_i(\boldsymbol{\xi})\, u(\boldsymbol{\xi},t)\, d\boldsymbol{\xi} \\
&= \sum_{i=1}^{N} \Phi_i(\mathbf{x}) \int_{\Omega_i} u(\boldsymbol{\xi},t)\, d\boldsymbol{\xi} \\
&= \sum_{i=1}^{N} \left[\frac{1}{V_i} \int_{\Omega_i} u(\boldsymbol{\xi},t)\, d\boldsymbol{\xi} \right] V_i \Phi_i(\mathbf{x}) \\
&= \sum_{i=1}^{N} \bar{u}_{FV}(\mathbf{x}_i,t)\, \Psi_i(\mathbf{x})
\end{aligned} \tag{3.45}$$

For the sake of convenience, the last line in equation (3.45) is expressed in terms of the FV variables $\bar{u}_{FV}(\mathbf{x}_i,t)$ which arbitrarily, but according to the current cell centered FV practice, are defined in the centroids $\mathbf{x}_i$ of the volumes Ω_i. From equation (3.45) clearly emerges the similarity with the sampling operator defined in (3.43). However, very differently from the sampling operator, this FV operator does not commute with the product as it is defined in terms of FV variables and not local ones. Also, notably, it is not even idempotent, as in this case one would have:

$$\begin{aligned}
\mathcal{P}^N * \mathcal{P}^N * u(\mathbf{x},t) &= \sum_{j=1}^{N} \Phi_j(\mathbf{x}) \int_{\Omega} v_j(\boldsymbol{\xi}) \left[\mathcal{P}^N * u(\boldsymbol{\xi},t) \right] d\boldsymbol{\xi} \\
&= \sum_{j=1}^{N} \Phi_j(\mathbf{x}) \int_{\Omega} v_j(\boldsymbol{\xi}) \left[\sum_{i=1}^{N} \bar{u}_{FV}(\mathbf{x}_i,t)\, \Psi_i(\boldsymbol{\xi}) \right] d\boldsymbol{\xi} \\
&= \sum_{i=1}^{N} \sum_{j=1}^{N} \bar{u}_{FV}(\mathbf{x}_i,t)\, \Phi_j(\mathbf{x}) \int_{\Omega_j} \Psi_i(\boldsymbol{\xi})\, d\boldsymbol{\xi} \\
&= \sum_{i=1}^{N} \bar{u}_{FV}(\mathbf{x}_i,t) \left[\sum_{j=1}^{N} \Psi_j(\mathbf{x}) \frac{1}{V_j} \int_{\Omega_j} \Psi_i(\boldsymbol{\xi})\, d\boldsymbol{\xi} \right]
\end{aligned} \tag{3.46}$$

but this is not usually noted in practice because only affects the shape functions and not the point values. The solution underlying a FV computation can be also interpreted as a combination of two different operators G^i, one due to the top-hat filtering as defined in equation (3.1) and the second in the sequence due to the sampling as in the previous

section. Indeed:

$$\begin{aligned} G^S * G^{TH} * u(\mathbf{x},t) =& \mathcal{P}^N * \int_\Omega G^{TH}(\mathbf{y},\boldsymbol{\xi})\, u(\boldsymbol{\xi},t)\, d\boldsymbol{\xi} \\ =& \mathcal{P}^N * \left[\frac{1}{V(\mathbf{y})}\int_{\Omega_\mathbf{y}} u(\boldsymbol{\xi},t)\, d\boldsymbol{\xi}\right] \\ =& \sum_{i=1}^N \Psi_i(\mathbf{x}) \int_\Omega v_i(\mathbf{y}) \left[\frac{1}{V(\mathbf{y})}\int_{\Omega_\mathbf{y}} u(\boldsymbol{\xi},t)\, d\boldsymbol{\xi}\right] d\mathbf{y} \\ =& \sum_{i=1}^N \Psi_i(\mathbf{x}) \int_\Omega \delta(\mathbf{y}-\mathbf{x}_i) \left[\frac{1}{V(\mathbf{y})}\int_{\Omega_\mathbf{y}} u(\boldsymbol{\xi},t)\, d\boldsymbol{\xi}\right] d\mathbf{y} \\ =& \sum_{i=1}^N \Psi_i(\mathbf{x}) \left[\frac{1}{V(\mathbf{x}_i)}\int_{\Omega_{\mathbf{x}_i}} u(\boldsymbol{\xi},t)\, d\boldsymbol{\xi}\right] \\ =& \sum_{i=1}^N \bar{u}_{FV}(\mathbf{x}_i,t)\, \Psi_i(\mathbf{x}) \end{aligned} \tag{3.47}$$

where $\Omega_\mathbf{y}$ is the volume, around the point $\mathbf{y}$, within which the top-hat kernel G^{TH} is non null and $\Omega_{\mathbf{x}_i}$ is such volume for the specific point $\mathbf{x}_i$. Notice, also, that the order of the two operators G^S and G^{TH} is important and cannot be inverted. Again, the multilevel GLES formalism shows all its power in handling such situation without any specific modification. The analysis of the FV method will be further advanced in the next chapter, where the knowledge of the specific form of the projection operator underlying the method will be used to develop a proper form of scale-similar SGS model.

CHAPTER 4

Application of the GLES framework to the FV method

In this chapter, the knowledge on the basic operator underlying the FV method is used, within the GLES framework, to develop a new scale-similar SGS model for LES performed with the FV method. In section 4.1 the basis of the FV method is briefly summarized and the underlying FV operator further analyzed. As a result of this analysis and with additional results derived in Appendix C and D, in section 4.2 low order approximations are obtained for the terms defining the SGS stresses (3.11) in the GLES framework. In section 4.3, structural modeling options are analyzed in terms of their applicability to the FV method and of the resulting accuracy with respect to the analysis at the previous section. A simple form of scale similar term emerges as possible candidate structural model, whose details are described in section 4.4 together with its implementation as a dynamic two parameter mixed model. In section 4.5 the proposed scale-similar term and the relative dynamic procedure are further analyzed from the numerical point of view in a simplified 1D linear framework, providing some guidance in the setting of the overall dynamic procedure. Finally, the inclusion of the scale similar model in the pressure equation is discussed in section 4.6. The chapter is closed with two sections that, while not specific of the FV approach, have benefited from the prior introduction of the proposed scale-similar model. The first, section 4.7, is a comparison of the GLES framework with the ADM approach of Stolz and Adams (1999). The second, section 4.8, contains some comments on the Galilean invariance of the proposed GLES framework.

4.1 A further analysis of the FV operator

The analysis in section 3.6.3, and in particular the form (3.34) of the discretized equations, has made clear that the FV method is a straight application of the GLES framework. The discussion in section 3.1, equation (3.2) in particular, should have also clarified how the actual discretization is performed and how it actually implies a combined discretization of both filtering and derivative operators. Thus, it is not of interest here to further specify these aspects, which nonetheless are highlighted again in the next chapter. Instead, to further proceed in the application of the GLES framework to the FV method, it is interesting to further analyze the form of the FV operator presented in section 3.6.3, which is proposed again below:

$$\begin{aligned} G^{FV} * u = G^{S} * G^{TH} * u &= \sum_{i=1}^{N} \left[\frac{1}{V_i} \int_{\Omega_i} u\left(\boldsymbol{\xi}, t\right) d\boldsymbol{\xi} \right] \Psi_i\left(\mathbf{x}\right) \\ &= \sum_{i=1}^{N} \bar{u}_{FV}\left(\mathbf{x}_i, t\right) \Psi_i\left(\mathbf{x}\right) \end{aligned} \tag{4.1}$$

Also, it is worth remembering that SGS terms in the FV method have the form (3.11) outlined for the GLES framework, that in the FV parlance amounts to a difference between solved and unsolved fluxes. Equation (4.1) contains all the necessary information to build a structural model for such terms, which is the purpose of the present chapter. However, the qualitative features of the two operators appearing in it, the sampling operator and the top-hat filter, are quite different. The first is idempotent and commutes with the product but not the derivative operators, the second is not idempotent and does not commute with the product or, in general, with the derivative operators. Both are connected to the intrinsic limited resolution of the grid, trough N and the non overlapping feature of the volumes Ω_i, but the top-hat filter itself does not imply any loss of resolution and, in theory, is fully invertible[1]. In contrast, the effects due to the sampling are not in practice invertible, but only diminishable trough a better selection of shape functions (i.e., a more accurate numerical method).

In practice, among the two operators, it appears that it is the top-hat filter that mostly determines the solution, while the sampling effect, nonetheless present, is only related to the numerical accuracy of the discretization. This can be appreciated by the fact that, if one would somehow invert the FV operator from equation (4.1), in order to have a better approximation of the original function u, then would inevitably solve equations of the form:

$$\frac{1}{V_i} \int_{\Omega_i} u\left(\boldsymbol{\xi}, t\right) d\boldsymbol{\xi} = \bar{u}_{FV}\left(\mathbf{x}_i, t\right) \qquad i = 1, 2, \ldots, N \tag{4.2}$$

while different, more accurate, choices for the Ψ_i could always be made a posteriori. The fact that the two problems are separable, and that sampling is treatable only in numerical terms, can also be appreciated by the Germano Identities (3.15). Indeed,

[1] In practice, especially for the top-hat filter, such operation is ill-posed and only approximate inversions are possible.

given a model that is optimal in terms of reconstruction of the top-hat effect, say τ_{ij}^{TH}, then the optimal model for the overall FV operator, τ_{ij}^{FV} can be built as:

$$\tau_{ij}^{FV} = \tau_{ij}^{TH} + \tau_{ij}^{FV-TH} \tag{4.3}$$

where the last term is not generally computable as it involves a stress tensor built by sampling a continuous top-hat solution, which is not available. However, the interesting thing from the practical point of view is that this term is, by definition of sampling, exactly null in all the N sampling points where it is actually needed. Hence, again, the top-hat filter is all that matter from the SGS modeling point of view, and sampling effects can always be treated a posteriori by simply improving the numerical accuracy. It should be mentioned that an alternative point of view exists, according to which the choice of the shape functions can be made also with a modeling purpose in mind, both functional and structural. Such approach (Boris et al., 1992; Fureby, 2008), which is known as Monotone Integrated Large Eddy Simulation (MILES) or, somehow misleadingly, as Implicit LES (ILES)[2], will not be discussed again but, as one of the numerical schemes implemented in Fluent® belongs to this group, some examples of this approach will be given in chapters 6 and7.

According to the previous discussion, it is then assumed from now on, but just for SGS modeling purposes, that the FV approach is consistent with a top-hat filter alone. The sampling, in contrast, is not further developed as it only concerns numerical aspects that do not directly affect LES as such. Of course, numerical aspects are important in LES as well and will be discussed whenever necessary, especially in chapter 5, but not in relation to the modeling of the sampling operator.

4.2 Structural analysis of the SGS stresses in GLES

The possibility to exclude the sampling operator from the definition of FV operators is extremely important because the remaining top-hat operator is amenable of further developments with extreme ease. In particular, it is possible to further analyze the tensor τ_{ij}^{n-m} and, by suitable hypotheses, to extend the analysis to the true SGS tensor τ_{ij}^{n-0}.

It is first worth recalling that the present definition of the unique operator G affecting the governing equations in the FV approach is:

$$G * \phi = \frac{1}{V_i} \int_{\Omega_i} \phi\left(\boldsymbol{\xi}, t\right) d\boldsymbol{\xi} = \bar{\phi}_{FV}\left(\mathbf{x}_i, t\right) \tag{4.4}$$

It is shown in Appendix C that, under suitable assumptions, the effect that a sequence of $n-m$ such operators has on a resolved variable at level m can be approximated by:

$$\bar{\phi}^n = \bar{\phi}^m + \Delta_{n,m}^2 M_k \frac{\partial^2 \bar{\phi}^m}{\partial x_k^2} + O\left(\Delta_{n,m}^4\right) \qquad \Delta_{n,m}^2 = \sum_{j=1}^{n-m} \left(\Delta^{m+j}\right)^2 \tag{4.5}$$

[2]Notice that the implicitness here is not related to filtering operations but to the SGS modeling, which is implicit in the numerical method.

where Δ^{m+j} represents the cubic root of the volume V associated to the j^{th} operator G that, in the sequence, acts on $\bar{\phi}^m$. With such relation at hand, it is further shown in Appendix D that, within the same order of approximation, and considering the viscosity as constant, the term τ_{ij}^{n-m}, which is reported here for clarity:

$$\begin{aligned}\tau_{ij}^{n-m} = &\overbrace{\left(\bar{\rho}^n\tilde{u}_i^n\tilde{u}_j^n - \bar{\rho}^m\tilde{u}_i^m\tilde{u}_j^m\right)}^{\text{I}} + \overbrace{\left(\bar{p}^n - \bar{p}^m\right)}^{\text{II}}\delta_{ij} \\ &-2\mu\overbrace{\left(\tilde{S}_{ij}^n - \tilde{S}_{ij}^m\right)}^{\text{III}} + \frac{2\mu}{3}\delta_{ij}\overbrace{\left(\tilde{S}_{qq}^n - \tilde{S}_{qq}^m\right)}^{\text{IV}}\end{aligned} \tag{4.6}$$

can be approximated as follows:

$$\begin{aligned}\tau_{ij}^{n-m} = &\underbrace{\Delta_{n,m}^2 M_k\left(\frac{\partial^2\bar{\rho}^m\tilde{u}_i^m\tilde{u}_j^m}{\partial x_k^2} - 2\bar{\rho}^m\frac{\partial\tilde{u}_i^m}{\partial x_k}\frac{\partial\tilde{u}_j^m}{\partial x_k}\right)}_{\text{I}} + \delta_{ij}\underbrace{\Delta_{n,m}^2 M_k\frac{\partial^2\bar{p}^m}{\partial x_k^2}}_{\text{II}} \\ &\underbrace{-\mu\left[\frac{\partial}{\partial x_j}\left(\Delta_{n,m}^2 M_k\frac{\partial^2\tilde{u}_i^m}{\partial x_k^2}\right) + \frac{\partial}{\partial x_i}\left(\Delta_{n,m}^2 M_k\frac{\partial^2\tilde{u}_j^m}{\partial x_k^2}\right)\right]}_{\text{III}} \\ &\underbrace{-\mu\left[\frac{\partial}{\partial x_j}\left(\frac{2\Delta_{n,m}^2 M_k}{\bar{\rho}^m}\frac{\partial\bar{\rho}^m}{\partial x_k}\frac{\partial\tilde{u}_i^m}{\partial x_k}\right) + \frac{\partial}{\partial x_i}\left(\frac{2\Delta_{n,m}^2 M_k}{\bar{\rho}^m}\frac{\partial\bar{\rho}^m}{\partial x_k}\frac{\partial\tilde{u}_j^m}{\partial x_k}\right)\right]}_{\text{III}} \\ &+\frac{2\mu}{3}\delta_{ij}\underbrace{\frac{\partial}{\partial x_q}\left(\Delta_{n,m}^2 M_k\frac{\partial^2\tilde{u}_q^m}{\partial x_k^2} + \frac{2\Delta_{n,m}^2 M_k}{\bar{\rho}^m}\frac{\partial\bar{\rho}^m}{\partial x_k}\frac{\partial\tilde{u}_q^m}{\partial x_k}\right)}_{\text{IV}} + O\left(\Delta_{n,m}^4\right)\end{aligned} \tag{4.7}$$

The final step to take, in order to arrive at an usable expression for the SGS stress tensor, is to note that, still within an approximation of order $\Delta_{n,m}^4$, and for sufficiently smooth variations[3] of $\Delta_{n,m}$, equation (4.5) can be invoked again and the relation above remains equally valid if m level variables are substituted with the n level ones. This remarkable fact allows thus to write τ_{ij}^{n-m} as a function of n level variables only, independently from m, which can then be assumed to be 0. In practice, the resulting expression can then be considered a low order model for τ_{ij}^{n-0}. In doing these steps, however, it should be noted that the validity of the approach is not independent from the difference in scale between Δ^m and Δ^n, as higher order derivatives at level m might not be negligible in general.

While equation (4.7) will be used, in the next section, as a reference for the development of a structural SGS model, it is proposed here to instead highlight the complexity of the SGS stresses arising in GLES, something which has not been possible with the simple functional analysis developed in section 3.5. In particular, similar approximations arising in the CLES framework (Vreman et al., 1996; Clark et al., 1979) simply

[3] In practice, as for the validity of equation (4.5), it is required that local variations of all the implied Δ^j have continuous second derivatives.

amount to the second term in I, also known as Clark model. Heuristically, these additional terms not arising in CLES could again be interpreted as due to the commutation of the filter with the spatial derivatives (or the lack of).

4.3 Structural modeling options in the FV method

Before turning the attention to the development of a structural SGS model for LES with the FV method, it is useful to stress again the suitability of such option when using this specific implicitly filtered approach. Indeed, it has been shown that the FV method is based on two operators, the sampling and the top-hat filter. The former has been shown to be non influential from the modeling point of view, the latter instead affects all the terms, especially the non linear ones (as it does not commute with the product), and is fully known. As the uniquely important filter (from the modeling point of view) is known and, as shown in the following, invertible, it is then assumed here that such inversion is necessary and meaningful as in any other explicit filtering approach.

Notice, also, that this is largely independent from the numerical approach, even if some correcting terms might be of the same order of the numerical error or higher. Indeed, the two act in a very different manner. Thus, inverting some effects cannot be established, a priori, to be vain by only considering leading order arguments. For example, a physically sound anti-dissipative mechanism could act in a way which is different from any possible truncation error effect. Also, leading order arguments are likely to be unimportant in LES as, more often than not, the resolved fields have low regularity and higher order derivatives might not be negligible. It is thus in this spirit that the structural modeling option is considered in the FV method.

In order to proceed in the construction of a structural SGS model for τ_{ij}^{n-0}, the only thing that remains to be determined is the best way to use the available information. More specifically, this information amounts to equation (4.2) that, from now on, is the reference for the FV operator, and equation (4.7), which will give additional insight. Among the aspects affecting this choice, some are especially relevant for the application in general purpose solvers and will be considered in detail: ease of implementation, computational cost, possible limitations in the applicability, consistency of the overall procedure.

In total, there are three possible approaches to build a structural SGS model, based respectively on the reconstruction of the missing scales, the use of a differential model or the use of a scale-similar model. All of them are analyzed in the following in terms of suitability for a general purpose solver.

4.3.1 Models based on reconstruction

A possible approach in constructing a structural SGS model is based on directly using equation (4.2) to approximately invert the top-hat filter in it. In practice, this is done by using a truncated Taylor series development for the unknown ϕ around the centroid of the volume Ω_i.

Following the same approach described in Appendix C, for a second order recon-

struction, leads to the following differential problem for ϕ in each point $\mathbf{x}_i$:

$$\begin{aligned}\bar{\phi}_{FV}\left(\mathbf{x}_i,t\right)=\phi\left(\mathbf{x}_i,t\right)+V_i^{\frac{2}{3}}\left[M_{200}\frac{\partial^2\phi}{\partial x^2}+M_{020}\frac{\partial^2\phi}{\partial y^2}+M_{002}\frac{\partial^2\phi}{\partial z^2}\right]\Bigg|_{\mathbf{x}_i}\\ +V_i^{\frac{2}{3}}\left[M_{110}\frac{\partial^2\phi}{\partial x\partial y}+M_{101}\frac{\partial^2\phi}{\partial x\partial z}+M_{011}\frac{\partial^2\phi}{\partial y\partial z}\right]\Bigg|_{\mathbf{x}_i}\end{aligned} \tag{4.8}$$

where the moments M_{qrs} are computable from equation (C.4) and $\bar{\phi}_{FV}\left(\mathbf{x}_i,t\right)$ is the known filtered variable in the cell center. Once the differential equation (4.8) is solved for all the approximate unfiltered functions $\phi\left(\mathbf{x}_i,t\right)$, they can be used in τ_{ij}^{n-0} in place of the true unfiltered ones[4]. However, such approach has several drawbacks as: the low second order approximation still requires solving an implicit second order PDE for each necessary variable (up to six per each time step), reconstructions beyond the second order would even require non available boundary conditions and operators whose discretization is cumbersome, if not impossible, in general unstructured FV solvers. Besides this, one could also argue that it is not possible to advance such a reconstruction beyond the order of the discretized differential operators[5]. Thus, this approach would have several disadvantages in a practical implementation.

A second possible approach to invert the filter in equation (4.2) is based on the Van Cittert deconvolution method (Stolz and Adams, 1999). In this approach, the inverse of a generic operator G is expressed as:

$$G^{-1}=\left[I-\left(I-G\right)\right]^{-1}=\sum_{n=0}^{\infty}\left(I-G\right)^n=\sum_{n=0}^{\infty}\sum_{k=0}^{n}\frac{\left(-1\right)^k n!}{k!\left(n-k\right)!}G^k \tag{4.9}$$

where $I=G^0$ is the identity operator and G^k stands for k consecutive applications of the operator G. The series is convergent if $\|I-G\|<1$ but, in practice, it is arrested at low finite values, e.g., $n=5$. The approximate unfiltered variables are then reconstructed as:

$$\phi=\bar{\phi}_{FV}+\left(\bar{\phi}_{FV}-G*\bar{\phi}_{FV}\right)+\left(\bar{\phi}_{FV}-2G*\bar{\phi}_{FV}+G*G*\bar{\phi}_{FV}\right)+\cdots \tag{4.10}$$

This method is, in theory, applicable to the full FV operator G^{FV}, including its sampling component as, from equation (3.46):

$$G^{FV}*G^{FV}*\phi=\sum_{i=1}^{N}\Psi_i\left(\mathbf{x}\right)\left[\sum_{j=1}^{N}\bar{\phi}_{FV}\left(\mathbf{x}_j,t\right)\frac{1}{V_i}\int_{\Omega_i}\Psi_j\left(\boldsymbol{\xi}\right)d\boldsymbol{\xi}\right] \tag{4.11}$$

thus, the point values of the doubly filtered FV variables $\bar{\bar{\phi}}_{FV}\left(\mathbf{x}_i,t\right)$ can be obtained

[4]To correctly reconstruct the SGS stresses a similar treatment is required for the pressure, the density and the three momentum components.

[5]Notice that this objection is different from the one at the beginning of this section. Here is the reconstruction itself which is considered and the consistency of its discretization.

as:

$$\bar{\bar{\phi}}_{FV}\left(\mathbf{x}_i, t\right) = \sum_{j=1}^{N} \bar{\phi}_{FV}\left(\mathbf{x}_j, t\right) \frac{1}{V_i} \int_{\Omega_i} \Psi_j\left(\boldsymbol{\xi}\right) d\boldsymbol{\xi} \tag{4.12}$$

In practice, however, the method is limited by the effective knowledge of the shape functions, which can be partial or inaccurate. For example, the typical knowledge in the FV method is limited to the point values $\bar{\phi}_{FV}\left(\mathbf{x}_i, t\right)$ and the local gradients, which means that the operation (4.12) returns the identity $\bar{\bar{\phi}}_{FV}\left(\mathbf{x}_i, t\right) = \bar{\phi}_{FV}\left(\mathbf{x}_i, t\right)$. But even including a more accurate information, the integration of arbitrary shape functions on arbitrary polyhedral cells, typical of FV applications, is far from trivial, even if it is only needed once and could be performed as a preprocessing step.

A final reconstruction option that deserves some attention is based on equation (4.8). Indeed, within an accuracy of $V_i^{\frac{2}{3}}$, it can be straightly inverted to give:

$$\phi\left(\mathbf{x}_i, t\right) = \bar{\phi}_{FV}\left(\mathbf{x}_i, t\right) - \mathcal{M}_{ij} \frac{\partial}{\partial x_i} \left(\frac{\partial \bar{\phi}_{FV}}{\partial x_j} \right) \Bigg|_{\mathbf{x}_i} \tag{4.13}$$

with:

$$\mathcal{M}_{ij} = \frac{V_i^{\frac{2}{3}}}{2} \begin{bmatrix} 2M_{200} & M_{110} & M_{101} \\ M_{110} & 2M_{020} & M_{011} \\ M_{101} & M_{011} & 2M_{002} \end{bmatrix} \tag{4.14}$$

which is an explicit relation and only requires the computation of the moments M_{qrs} and the implementation of a second order differential operator. For this reason, this option has been preliminarily considered in this work. However, its practical implementation in a general purpose FV solver resulted to be not straightforward as second order operators are not directly available and their implementation could be not exactly cost effective. Indeed, not only each of the six independent terms requires a summation over neighbor cells, which means six summations for each of the five variables needed to reconstruct τ_{ij}^{n-0}. But, also, for each variable the cell-centered gradient is also required, which means the computation of four gradient terms not usually available. A temperature dependent viscosity would then make the cost even higher. Finally, the computation of the moments M_{qrs} for general polyhedral cells requires additional storage and a dedicated routine. For these reasons, while certainly applicable, this route has been abandoned.

4.3.2 Differential model

Following Clark et al. (1979), and many others, a structural model for the FV method could be based on the approximation (4.7) which, for the present purpose, would be

written as:

$$\begin{aligned}\tau_{ij}^{n-0} \approx & \Delta_{n,0}^2 M_k \left(\frac{\partial^2 \bar{\rho}^n \tilde{u}_i^n \tilde{u}_j^n}{\partial x_k^2} - 2\bar{\rho}^n \frac{\partial \tilde{u}_i^n}{\partial x_k} \frac{\partial \tilde{u}_j^n}{\partial x_k} \right) + \delta_{ij} \Delta_{n,0}^2 M_k \frac{\partial^2 \bar{p}^n}{\partial x_k^2} \\ & -\mu \left[\frac{\partial}{\partial x_j} \left(\Delta_{n,0}^2 M_k \frac{\partial^2 \tilde{u}_i^n}{\partial x_k^2} \right) + \frac{\partial}{\partial x_i} \left(\Delta_{n,0}^2 M_k \frac{\partial^2 \tilde{u}_j^n}{\partial x_k^2} \right) \right] \\ & -\mu \left[\frac{\partial}{\partial x_j} \left(\frac{2\Delta_{n,0}^2 M_k}{\bar{\rho}^n} \frac{\partial \bar{\rho}^n}{\partial x_k} \frac{\partial \tilde{u}_i^n}{\partial x_k} \right) + \frac{\partial}{\partial x_i} \left(\frac{2\Delta_{n,0}^2 M_k}{\bar{\rho}^n} \frac{\partial \bar{\rho}^n}{\partial x_k} \frac{\partial \tilde{u}_j^n}{\partial x_k} \right) \right] \\ & +\frac{2\mu}{3} \delta_{ij} \frac{\partial}{\partial x_q} \left(\Delta_{n,0}^2 M_k \frac{\partial^2 \tilde{u}_q^n}{\partial x_k^2} + \frac{2\Delta_{n,0}^2 M_k}{\bar{\rho}^n} \frac{\partial \bar{\rho}^n}{\partial x_k} \frac{\partial \tilde{u}_q^n}{\partial x_k} \right)\end{aligned} \tag{4.15}$$

However, this option is reported here just for the sake of completeness as, while still being an approximation, its implementation cost would be far higher than the one related to the more accurate and simple approach based on equation (4.13). Also, the implementation of the second order differential terms while retaining the overall second order accuracy would be practically impossible with the basic numerical tools available in general purpose solvers.

4.3.3 Scale-similar model

The only remaining option for a structural model and, in fact, the one used in the present work, is the use of a scale similar model. Besides the true reasons that have motivated this choice, to be discussed in the following, this is also, to the best of the author's knowledge, the only approach which has been already used in the GLES framework applied to the FV method[6]. Indeed, in their explicitly filtered FV approach, Vreman and Geurts (2002) suggest[7]:

$$\tau_{ij}^{n-0} \approx \bar{\rho}^{n+1} \tilde{u}_i^{n+1} \tilde{u}_j^{n+1} - \bar{\rho}^n \tilde{u}_i^n \tilde{u}_j^n \tag{4.16}$$

thus neglecting the effect of the pressure and viscous terms. As the approach is explicit, the filter used on the n level variables, to provide those at the level $n+1$, is the same basic filter which determines the n level variables themselves. The full scale-similar approximation[8], including pressure and viscous terms, has been instead proposed by Denaro (2012):

$$\tau_{ij}^{n-0} \approx \tau_{ij}^{m-n} \tag{4.17}$$

with $m = n+1$. In practice, as the method is based on the implicit approach (i.e., a straightforward FV method), variables at the level m are obtained from those at the level n (i.e., the resolved variables) by the means of equation (4.12), thus integrating the exact shape functions of the underlying numerical method. However, this was practically possible due to the use of a fully structured in-house code.

[6] Notice, however, that none of these models has been originally presented in the GLES framework nor with a compressible formulation. For the sake of clarity, however, they are reported here using the general GLES form.

[7] In practice they use a mixed model with an eddy viscosity based on the Smagorinsky model.

[8] Within a dynamic, two parameters, mixed model.

Besides merits and demerits of these two proposals, which will be better clarified in the following, the scale-similar formulation has clear computational advantages with respect to the previous ones. Indeed, for a basic scale-similar model of the form (4.17), the required operations amount to filtering five variables and, because of the inclusion of viscous terms, computing the gradient of the three filtered velocity components (those at the basic n level being readily available). A similar, but even more interesting, advantage arises when the use of a dynamic procedure is considered. Indeed, in this case τ_{ij}^{m-n} should be computed in any case (see section 3.4) and the overall additional costs of a dynamic, two parameters, mixed model would still be those described above, but just related to the additional test filter level $r = m + 1$ and the computation of the tensor τ_{ij}^{r-m}. For such a dynamic procedure with a mixed model, the use of a second test filter might become troublesome (Anderson and Meneveau, 1999) and a differential model might be better suited; nonetheless, a priori tests performed by Chumakov (2006) have shown that, especially for LES with low resolution, scale-similar models are clearly superior with respect to differential approximations.

For these reasons, the scale-similar approach has been chosen as the only viable option for a structural model to be implemented in a general purpose FV solver. However, because of the inherent difficulty of implementing the filtering as in the previous cases, a different formulation has been developed, as described below.

4.3.4 Present proposal: a modified scale-similar term

The key aspect of any scale-similar model is the filter, or general operator, that is applied to the resolved variables to obtain tensors of the form (4.17). The approach proposed by Denaro (2012) is fully consistent with the general GLES framework applied to the FV method, does not neglect any term and uses the unique exact form for the filter which is consistent with the FV method:

$$\bar{\phi}^{n+1}(\mathbf{x}_i, t) = \sum_{j=1}^{N} \bar{\phi}^{n}(\mathbf{x}_j, t) \frac{1}{V_i} \int_{\Omega_i} \Psi_j(\boldsymbol{\xi})\, d\boldsymbol{\xi} \tag{4.18}$$

However, extending such approach to general purpose FV solvers is far from trivial and, in most cases, the available information is such that the filter (4.18) produces an identity. In order to circumvent such limit, here it is proposed to use a different form of filter, which is more easily adaptable to any unstructured grid. This is achievable if, instead of the volume Ω_i of the given cell, an extended volume Ω_i^*, with measure V_i^*, is considered for the filter. In this case, even considering a constant shape function Ψ_j on the volume Ω_j would produce a meaningful filtering formula:

$$\bar{\phi}^{n+1}(\mathbf{x}_i, t) = \sum_{j=1}^{N} \bar{\phi}^{n}(\mathbf{x}_j, t) \frac{1}{V_i^*} \int_{\Omega_i^*} \Psi_j(\boldsymbol{\xi})\, d\boldsymbol{\xi} = \frac{\sum_{j=1}^{N_b} \bar{\phi}^{n}(\mathbf{x}_j, t)\, V_j}{\sum_{j=1}^{N_b} V_j} \tag{4.19}$$

where the summation is intended over a set of N_b neighbor cells for the given cell i; in practice, a volume weighted average as also proposed by Griman et al. (2010). While this filter essentially looses the connection with the sampling part of the FV method, this could be approximately restored by not considering all the cells in the volume Ω_i^*,

but only alternating layers of cells. However, extending the approach beyond the first layer of neighbor cells (in this case would simply amount to exclude the cell i from the sum) becomes impractical and such approach is thus not considered, also because it has been shown that sampling is not relevant for modeling purposes.

With the filter (4.19) at hand, the last issue that needs to be addressed is the resulting accuracy that would be obtained by using it in producing a scale-similar model of the form τ_{ij}^{m-n}. This analysis can be performed by recurring, again, at the hypotheses introduced in section 4.2. Namely, that the action of the top-hat filter underlying the FV operator and that of the discrete filter (4.19) are both representable as ($m > n$):

$$\bar{\phi}^m = \bar{\phi}^n + \Delta_{m,n}^2 M_k \frac{\partial^2 \bar{\phi}^n}{\partial x_k^2} + O\left(\Delta_{m,n}^4\right) \qquad \Delta_{m,n}^2 = \sum_{j=1}^{m-n} \left(\Delta^{n+j}\right)^2 \tag{4.20}$$

Neglecting, for the moment, the implications of such assumption, one can then analyze the resulting scale-similar term τ_{ij}^{m-n} and compare it with the true SGS stress tensor τ_{ij}^{n-0}. This is easily done as, from section 4.3.2, emerges that:

$$\tau_{ij}^{n-0} = \overbrace{\Delta_{n,0}^2 f\left(\bar{\rho}^n, \tilde{u}_i^n, \tilde{u}_j^n\right)}^{\text{Constant } \Delta_{n,0}^2 \text{ part}} + \overbrace{h\left(\bar{\rho}^n, \tilde{u}_j^n\right) \frac{\partial \Delta_{n,0}^2}{\partial x_i} + h\left(\bar{\rho}^n, \tilde{u}_i^n\right) \frac{\partial \Delta_{n,0}^2}{\partial x_j}}^{\text{Viscous variable } \Delta_{n,0}^2 \text{ part}} + O\left(\Delta_{n,0}^4\right) \tag{4.21}$$

where the first term represents all the terms with constant $\Delta_{n,0}^2$, while the second and third term represent the variable $\Delta_{n,0}^2$ part, which is only due to the viscous terms. Both functional forms, f and h, are easily obtained from equation (4.15) thus, for the sake of conciseness, they are not reported here. From equation (4.7), a similar analysis performed for the scale-similar term produces instead ($m > n$):

$$\tau_{ij}^{m-n} = \overbrace{\Delta_{m,n}^2 f\left(\bar{\rho}^n, \tilde{u}_i^n, \tilde{u}_j^n\right)}^{\text{Constant } \Delta_{m,n}^2 \text{ part}} + \overbrace{h\left(\bar{\rho}^n, \tilde{u}_j^n\right) \frac{\partial \Delta_{m,n}^2}{\partial x_i} + h\left(\bar{\rho}^n, \tilde{u}_i^n\right) \frac{\partial \Delta_{m,n}^2}{\partial x_j}}^{\text{Viscous variable } \Delta_{m,n}^2 \text{ part}} + O\left(\Delta_{m,n}^4\right) \tag{4.22}$$

where, notably, f and h maintain the same functional form as in (4.21), but the order of the scaling is now $\Delta_{m,n}^2$, instead of $\Delta_{n,0}^2$. This notable fact implies that, despite all, only zero order terms would be well predicted. Unfortunately, the form of the SGS stresses in GLES is such that zero order terms are exactly null, hence a model of the form τ_{ij}^{m-n} is largely useless. It is worth mentioning, however, that this is explicitly due to the enlarged filter (4.19), while in the work of Vreman and Geurts (2002) and in the work of Denaro (2012) the two factors, $\Delta_{m,n}^2$ and $\Delta_{n,0}^2$, are exactly the same and no consistency error arises.

In order to restore, at least, a partial accuracy, the novel approach proposed here is

based on the following estimate:

$$\begin{aligned}\frac{\Delta_{n,0}^2}{\Delta_{m,n}^2}\tau_{ij}^{m-n} - \tau_{ij}^{n-0} =& \Delta_{n,0}^2 \left[h\left(\bar{\rho}^n, \tilde{u}_i^n\right)\beta_j + h\left(\bar{\rho}^n, \tilde{u}_j^n\right)\beta_i\right] \\ &+ O\left(\Delta_{n,0}^2\Delta_{m,n}^2\right) + O\left(\Delta_{n,0}^4\right)\end{aligned} \tag{4.23}$$

where:

$$\beta_i = \frac{1}{\Delta_{m,n}^2}\frac{\partial\Delta_{m,n}^2}{\partial x_i} - \frac{1}{\Delta_{n,0}^2}\frac{\partial\Delta_{n,0}^2}{\partial x_i} = \frac{\partial}{\partial x_i}\left(\ln\Delta_{m,n}^2 - \ln\Delta_{n,0}^2\right) = \frac{\partial}{\partial x_i}\left[\ln\left(\frac{\Delta_{m,n}^2}{\Delta_{n,0}^2}\right)\right] \tag{4.24}$$

From which follows that a scale-similar model of the form $(\Delta_{n,0}^2/\Delta_{m,n}^2)\tau_{ij}^{m-n}$ would approximate with $O(\Delta_{n,0}^2\Delta_{m,n}^2)$ accuracy the convective and pressure part of τ_{ij}^{n-0} as well as its viscous part at constant $\Delta_{n,0}^2$. If, in addition, the ratio $(\Delta_{m,n}^2/\Delta_{n,0}^2)$ is constant in space, the same accuracy would be restored for the whole SGS stress tensor. This form of structural model is the one proposed here for the use in general unstructured FV solvers and further investigated, in the form proposed in the next section, in the remaining part of the thesis. Note that similar arguments have been proposed before by Pruett (1997); Pruett et al. (2001), even if in a completely different context. Also, it seems relevant to note that the procedure developed by Iovieno and Tordella (2003) to deal with commutation errors in the CLES framework has strong similarities with the SGS model proposed above, as in fact both provide a similarity contribution for all the terms in the equations, including linear ones, and both have scaling factors depending on the filter width. However, while the overall accuracy is also the same and determined by similar Taylor series arguments, the specific arrangement of the terms adopted in the former work is different, as it reflects the underlying CLES approach and the specific error term modeled, which is the one reported in equation (2.45).

Before closing this section, it is also worth highlighting under which conditions the previous analysis can be considered valid. A first remarkable fact is that the previous analysis is actually independent from the specific approximation (4.20). That is, as long as it holds for all the filtering levels involved, the resulting functional forms f and h will be the same for the two tensors and will multiply the same leading order term of the approximation. In practice, multiplying τ_{ij}^{m-n} by $(\Delta_{n,0}^2/\Delta_{m,n}^2)^{k/2}$ will always cancel the order k error term. This also means that a variable viscosity and the mixed terms in equation (4.20), two effects which have been neglected in the analysis, are automatically taken into account. Thus, the effectively necessary conditions for the previous analysis to hold are that the filter (4.19) preserves, in passing from Ω_i to Ω_i^*, both the centroid (to avoid spurious first order terms in τ_{ij}^{m-n}) and the second order moments of the filtering volume (to have the same functional forms f and h for both τ_{ij}^{m-n} and τ_{ij}^{n-0}). Notice that, in general, this is not difficult to achieve as the only additional effective requirement for the filter is that its weights remain positive to be still representative of neighbor volumes. Their effective magnitude can indeed be quite arbitrary and still represent an ideal enlarged volume, not necessarily corresponding to the volume of a given set of cells but just given fractions of their single volumes.

4.4 A dynamic mixed SGS model for GLES with the FV method

The filter proposed in (4.19) could be easily adapted to preserve the two basic constraints required by the analysis at the previous section. Indeed, with methods similar to those developed by Sagaut and Grohens (1999), Haselbacher and Vasilyev (2003) or Marsden et al. (2002), the volume weights could be easily set to preserve any specific constraint. However, for how easy it can be, this approach would still require the computation of the matrix $\mathcal{M}_{ij}$ in (4.14) and the storage of nine weights per cell. This approximately amounts to 150% the storage of a compressible solver and 225% for an incompressible one[9]. Also, the computation of the weights can be cumbersome for general polyhedral cells[10] (Lien and Kajiya, 1984; Dobrovolskis, 1996; Jasak, 1996).

For these reasons and to keep, in general, the approach as simple as possible, the filter actually used in this work is not based on any correction and simply uses formula (4.19) over a set of neighbor cells, with the weights being exactly the volumes of the cells. Nonetheless, to overcome possible deficiencies of this approach, the model is implemented with a variable coefficient C_{ss} trough a dynamic procedure. A heuristic justification for this can be found in the fact that a possible error in the filter moments, if equal for all the moments, can be compensated by a unique constant[11]. Also, while an error in the centroid of the filter is hardly compensated by a multiplicative constant, such error should be less frequent in general as the computational stencils of the filter tend to be symmetrical in most cases. Moreover, for a filter centroid still being within the original cell, one could also argue that, having assumed constant shape functions, no error would arise. In practice, to also compensate the lack of dissipation typically associated to scale-similar models, the overall SGS model proposed is a dynamic, two parameters, mixed model with a scale-similar term as proposed in the previous section and an eddy-viscosity part based on the mixed scale model (see section 2.4.2).

Hence, for resolved variables at level n, a first test filter at level $m > n$ and a secondary test filter at level $r > m$, the proposed parameterization for the SGS stresses at the basic (n) and test (m) filter levels reads:

$$\begin{aligned}
\tau_{ij}^{n-0} =& C_{ev} 2\bar{\rho}^{n} \left|\tilde{S}^{n}\right|^{\alpha} \left(k_{SGS}^{n-m}\right)^{\frac{1-\alpha}{2}} \Delta_{n,0}^{1+\alpha} \left(\tilde{S}_{ij}^{n} - \frac{1}{3}\tilde{S}_{gg}^{n}\delta_{ij}\right) + C_{ss}\left(\frac{\Delta_{n,0}}{\Delta_{m,n}}\right)^{2} \tau_{ij}^{m-n} \\
\tau_{ij}^{m-0} =& C_{ev} 2\bar{\rho}^{m} \left|\tilde{S}^{m}\right|^{\alpha} \left(k_{SGS}^{m-r}\right)^{\frac{1-\alpha}{2}} \Delta_{m,0}^{1+\alpha} \left(\tilde{S}_{ij}^{m} - \frac{1}{3}\tilde{S}_{gg}^{m}\delta_{ij}\right) + C_{ss}\left(\frac{\Delta_{m,0}}{\Delta_{r,m}}\right)^{2} \tau_{ij}^{r-m}
\end{aligned} \tag{4.25}$$

[9] These, somehow, pessimistic estimates do not take into account the storage required for the geometric information.

[10] Nonetheless, a method for such computation has been developed as part of this thesis, as shown in chapter 5.

[11] Notice that this is a typical situation for a fully structured uniform grid, where the enlarged filter gives moments which differ from the original ones by a common factor. See next section.

where C_{ev} and C_{ss} are the constants to be computed dynamically and:

$$\begin{aligned} k_{SGS}^{n-m} &= \frac{1}{2}\left(\tilde{u}_j^n - \tilde{u}_j^m\right)\left(\tilde{u}_j^n - \tilde{u}_j^m\right) \\ k_{SGS}^{m-r} &= \frac{1}{2}\left(\tilde{u}_j^m - \tilde{u}_j^r\right)\left(\tilde{u}_j^m - \tilde{u}_j^r\right) \\ \left|\tilde{S}^n\right| &= \sqrt{2\tilde{S}_{ij}^n \tilde{S}_{ij}^n} \\ \left|\tilde{S}^m\right| &= \sqrt{2\tilde{S}_{ij}^m \tilde{S}_{ij}^m} \end{aligned} \tag{4.26}$$

In the numerical tests performed in chapters 6 and 7, different filter stencils and parameters α are used so, for the moment, these are left unspecified. The only thing to notice is that, for practical reasons, the filter to obtain the level r variables is simply based on further $r - m$ applications of the filter used to obtain the level m variables, which might lead to a slight inconsistency with respect to the parameterization at the level n. Finally, it is worth mentioning that, in the practical implementation of the model, the level n variables always refer to the variables actually resolved in the solver. The levels m and r are instead always obtained from a single application of the test filter ($r = m + 1 = n + 2$). Again, it is assumed here that the dynamic procedure, as illustrated below, can provide a cure for any possible inconsistency among the filtering procedures at the different levels.

Besides the different proposal for the scale-similar term and the use of the GGI reported in (3.15), the present dynamic procedure follows the classical approach described in section 2.4.2. Expressing the relations (4.25) in compact form as:

$$\begin{aligned} \tau_{ij}^{n-0} &= C_{ev} A_{ij}^n + C_{ss} B_{ij}^n \\ \tau_{ij}^{m-0} &= C_{ev} A_{ij}^m + C_{ss} B_{ij}^m \end{aligned} \tag{4.27}$$

the constants in the model are computed by the same least-squares error minimization, leading to:

$$\begin{aligned} C_{ss} &= \frac{A_{ij}A_{ij}L_{rs}B_{rs} - L_{ij}A_{ij}A_{rs}B_{rs}}{A_{ij}A_{ij}B_{rs}B_{rs} - A_{ij}B_{ij}A_{rs}B_{rs}} \\ C_{ev} &= \frac{L_{ij}A_{ij} - C_{ss}A_{ij}B_{ij}}{A_{ij}A_{ij}} \end{aligned} \tag{4.28}$$

with $A_{ij} = A_{ij}^m - A_{ij}^n$, $B_{ij} = B_{ij}^m - B_{ij}^n$ and $L_{ij} = \tau_{ij}^{m-n}$. By comparison with the analogous relations (2.38) in the IFCLES approach, it can be appreciated the lack of filtered tensors in the present dynamic procedure, from which results the saving in computational costs described in section 3.4.

As a matter of fact, the dynamic procedure as implemented above still is an approximate procedure to enforce an algebraic equality in a least squares sense. As such, it comes at no surprise that the resulting coefficients are affected by the same problematic behavior appearing in the CLES approach: both constants can become negative, which is physically unacceptable, can assume large values and show very rapid fluctuations.

In order to prevent instabilities in the computation, the strategy adopted here is based on a simple clipping procedure. In particular, the following limits are adopted:

$$\begin{aligned} &0 \leq C_{ss} \leq 2 \\ &0 \leq C_{ev} \leq C_q^{1-\alpha} C_s^{2\alpha} \end{aligned} \tag{4.29}$$

with $C_q = 0.2$ and $C_s = 0.18$. The limit on the eddy viscosity constant is simply the theoretical value of the constant as emerges from analyses in HIT with spectral cut-off filters (Sagaut, 2006). While this might appear strongly limited, it should be mentioned that such values are higher than those usually employed with the respective static models (Yoshizawa et al., 2000) and in line with the most advanced theoretical studies available (Meldi et al., 2011; Meyers and Sagaut, 2006), that for the Smagorinsky model coefficient predict $C_s \leq 0.18$ as satisfied even under the most extreme events. Thus, using larger values appears as largely unphysical. For what concerns the scale-similar constant C_{ss}, the chosen maximum value has been determined by the auxiliary analysis proposed in the next section and by the following heuristic argument. For the present test filter applied on a uniform structured grid with only nearest neighbors cells in the stencil, the ratio $\Delta_{n,0}^2/\Delta_{m,n}^2$ in the model is about 0.27 and the maximum value $C_{ss} = 2$ leads to an overall model coefficient which is in line with that proposed by Liu et al. (1994) for a similar model. Of course, different choices are possible and a sensitivity exists on these parameters but, nonetheless, these values have been found optimal for most of the present applications.

Despite the straightforward applicability of the present modeling strategy also for the energy equation or, at least, the SGS heat flux, this route has not been followed in the present thesis. Instead, modeling in the energy equation has been formulated on the basis of a simple constant SGS Prandtl number, leading to:

$$\varepsilon_j^{n-0} \approx \left(\bar{\rho}^n \tilde{u}_j^n \tilde{T}^n - \rho u_j T \right) \approx \frac{2 C_p \bar{\rho}^n}{Pr_{sgs}} C_{ev} \left| \tilde{S}^n \right|^{\alpha} \left(k_{SGS}^{n-m} \right)^{\frac{1-\alpha}{2}} \Delta_{n,0}^{1+\alpha} \frac{\partial \tilde{T}^n}{\partial x_j} \tag{4.30}$$

The main reason for this choice is that, having included a structural model in the momentum equation should already represent an enhancement in the transport of the energy, while the straight inclusion of a scale similar term in the energy equation might lead to unphysical unboundedness, which should be avoided. For the same reason, using an overly advanced dissipation term appears as largely useless in the present context and a constant SGS Prandtl number $Pr_{sgs} = 0.85$ is adopted in all the cases.

4.5 A numerical analysis interlude

A fact that might, maybe, pass unnoticed is that, within the FV method, the structural modeling option is always suitable, even for linear 1D equations, because the FV operator is always in place. Actually, as emerges from the considerations in the sections 3.6.2 and 3.6.3, it is indeed suitable for any numerical method, as shown by Fauconnier et al. (2007, 2008, 2009) in the finite difference case and by Oberai and Wanderer (2005b) in a more general variational formulation.

As a consequence, it becomes interesting to apply the proposed dynamic scale-similar model to a simplified 1D linear equation to further analyze it and, possibly,

correct its behavior. More specifically, such analysis is used here as a further justification for the chosen clipping limits for the C_{ss} constant. The main limitation of such analysis, of course, is due to the very different features of the underlying equation, especially the lack of three-dimensionality and nonlinear terms.

4.5.1 Model equation

In order to proceed, a simple linear 1D transport equation for a generic variable ϕ is considered in a FV formulation:

$$\frac{\partial}{\partial t}\frac{1}{V_i}\int_{\Omega_i}\phi dx + \frac{1}{V_i}\int_{\Omega_i}\frac{\partial}{\partial x}\left(U\phi - \nu\frac{\partial\phi}{\partial x}\right)dx \tag{4.31}$$

with U the constant transport velocity and ν the constant diffusivity. Even before introducing the discretization and in this simple setting, it should be apparent that equation (4.31) already introduces a closure problem, because prescribes the evolution of the FV variable $\bar{\phi}$:

$$\bar{\phi} = \frac{1}{V_i}\int_{\Omega_i}\phi dx \tag{4.32}$$

in terms of local values of ϕ. In particular, the closure problem can also be interpreted as due to the fact that the volume integral does not commute with the spatial derivative inside it[12]. The usual approach in the FV community is to simply neglect this fact, within a second order accurate discretization; however, it is clear that there is a discrepancy which is independent from the numerical discretization, and indeed has to be faced for higher order approximations. For this reason, it seems more appropriate to reformulate equation (4.31) as follows:

$$\frac{\partial\bar{\phi}}{\partial t} + \frac{1}{V_i}\int_{\Omega_i}\frac{\partial}{\partial x}\left(U\bar{\phi} - \nu\frac{\partial\bar{\phi}}{\partial x}\right)dx = \frac{1}{V_i}\int_{\Omega_i}\frac{\partial}{\partial x}\overbrace{\left[U\left(\bar{\phi}-\phi\right) - \nu\frac{\partial\left(\bar{\phi}-\phi\right)}{\partial x}\right]}^{\text{SGS flux } \tau}dx \tag{4.33}$$

and to interpret the term on the right hand side as a SGS flux τ which, in theory, needs to be modeled. In particular, according to the developments in the previous section, the model adopted here is:

$$\tau = C\alpha\left[U\left(\tilde{\bar{\phi}}-\bar{\phi}\right) - \nu\frac{\partial\left(\tilde{\bar{\phi}}-\bar{\phi}\right)}{\partial x}\right] = C\psi \tag{4.34}$$

[12] If such commutation is invoked, then the FV integral formulation reverts to the differential one.

where the tilde in $\tilde{\bar{\phi}}$ denotes the application of a test filter and the constant C is computed as a result of a dynamic procedure:

$$C = \frac{U\left(\bar{\phi} - \tilde{\bar{\phi}}\right) - \nu\frac{\partial\left(\bar{\phi} - \tilde{\bar{\phi}}\right)}{\partial x}}{\alpha\left[U\left(\tilde{\bar{\phi}} - \bar{\phi}\right) - \nu\frac{\partial\left(\tilde{\bar{\phi}} - \bar{\phi}\right)}{\partial x}\right] - \beta\left[U\left(\tilde{\hat{\bar{\phi}}} - \tilde{\bar{\phi}}\right) - \nu\frac{\partial\left(\tilde{\hat{\bar{\phi}}} - \tilde{\bar{\phi}}\right)}{\partial x}\right]} \tag{4.35}$$

The hat in $\hat{\tilde{\bar{\phi}}}$ denotes the application of a second test filter while, for the moment, the parameters α and β are unspecified. Notice that, in this special case, the constant C is an exact solution of the dynamic procedure based on the following Germano Identity:

$$\tau - T = U\left(\bar{\phi} - \tilde{\bar{\phi}}\right) - \nu\frac{\partial\left(\bar{\phi} - \tilde{\bar{\phi}}\right)}{\partial x} \tag{4.36}$$

where T is the SGS flux at the test filter level and is modeled with the second term in the denominator of C. At this point is then possible to introduce the spatial discretization[13].

4.5.2 Discretization

Considering a uniform grid with spacing Δx and variables $\bar{\phi}_i$ located in the centroids of the cells x_i, equation (4.33) can be put in the following equivalent form, after integration by parts:

$$\frac{\partial\bar{\phi}_i}{\partial t} + \frac{1}{\Delta x}\left(U\bar{\phi} - \nu\frac{\partial\bar{\phi}}{\partial x} - C\psi\right)\Bigg|_{i-\frac{1}{2}}^{i+\frac{1}{2}} = 0 \tag{4.37}$$

It is worth noting how, even in the form above, a closure problem seems to appear, as variables are known in the cell centers but their values are needed on the cell faces $x_{i\pm\frac{1}{2}}$. It should be clear now that this closure problem is relative to the sampling part in the FV operator, while the closure problem addressed above with τ is related to the top-hat part of the FV operator. Also, it is evident how the two problems are completely independent and manageable separately as, for example, different shape functions can now be selected for the interpolation. Here, for simplicity, linear shape functions are selected but, some inconsistencies are purposely/inevitably introduced, as almost always happens in the computational practice. For example, the face value $\bar{\phi}_{i+\frac{1}{2}}$ in the convective term is computed as follows:

$$\begin{aligned}\bar{\phi}_{i+\frac{1}{2}} =& \frac{1-\gamma}{2}\left(\bar{\phi}_i + \bar{\phi}_{i+1}\right) + \frac{\gamma}{2}\left[\left(\bar{\phi}_i + \frac{\Delta x}{2}\frac{\partial\bar{\phi}}{\partial x}\bigg|_i\right) + \left(\bar{\phi}_{i+1} - \frac{\Delta x}{2}\frac{\partial\bar{\phi}}{\partial x}\bigg|_{i+1}\right)\right] \\ =& \frac{\left(\bar{\phi}_i + \bar{\phi}_{i+1}\right)}{2} + \frac{\gamma\Delta x}{4}\left(\frac{\partial\bar{\phi}}{\partial x}\bigg|_i - \frac{\partial\bar{\phi}}{\partial x}\bigg|_{i+1}\right)\end{aligned} \tag{4.38}$$

[13]The temporal discretization is not influent for the following developments.

where the first term represents the only consistent part due to the linear shape function. The second part however, which is a typical correction used in unstructured FV codes to enhance the resolution capabilities of the scheme[14], is completely spurious and introduces the gradient in the cell center as additional unknown. In the present case, the discretization of this term according to the available options for unstructured codes always leads to:

$$\left.\frac{\partial\bar{\phi}}{\partial x}\right|_i = \frac{\left(\bar{\phi}_{i+1} - \bar{\phi}_{i-1}\right)}{2\Delta x} \tag{4.39}$$

and the resulting discretization for the full convective term becomes:

$$\bar{\phi}\Big|_{i-\frac{1}{2}}^{i+\frac{1}{2}} = \frac{\left(\bar{\phi}_{i+1} - \bar{\phi}_{i-1}\right)}{2} + \frac{\gamma}{8}\left[2\left(\bar{\phi}_{i+1} - \bar{\phi}_{i-1}\right) - \left(\bar{\phi}_{i+2} - \bar{\phi}_{i-2}\right)\right] \tag{4.40}$$

The parameter γ will be specified in the following as either 1 or 0, according to the scheme to be selected. For the diffusive term, instead, all the available options for unstructured codes lead, in this 1D case, to the following discretization:

$$\left.\frac{\partial\bar{\phi}}{\partial x}\right|_{i-\frac{1}{2}}^{i+\frac{1}{2}} = \frac{\left(\bar{\phi}_{i+1} - \bar{\phi}_i\right)}{\Delta x} - \frac{\left(\bar{\phi}_i - \bar{\phi}_{i-1}\right)}{\Delta x} = \frac{\bar{\phi}_{i+1} - 2\bar{\phi}_i + \bar{\phi}_{i-1}}{\Delta x} \tag{4.41}$$

which is fully consistent with the underlying linear shape functions. The convective part in the model for τ is also discretized in a consistent way:

$$\alpha U\left[C\left(\tilde{\bar{\phi}} - \bar{\phi}\right)\right]\Big|_{i-\frac{1}{2}}^{i+\frac{1}{2}} = \alpha U\frac{C_{i+1}\left(\tilde{\bar{\phi}}_{i+1} - \bar{\phi}_{i+1}\right) - C_{i-1}\left(\tilde{\bar{\phi}}_{i-1} - \bar{\phi}_{i-1}\right)}{2} \tag{4.42}$$

For the diffusive part, instead, two discretization methods are considered. The first, inconsistent, one follows the discretization of the convective part:

$$\alpha\nu\left[C\frac{\partial\left(\tilde{\bar{\phi}} - \bar{\phi}\right)}{\partial x}\right]\Bigg|_{i-\frac{1}{2}}^{i+\frac{1}{2}} = \alpha\nu\frac{C_{i+1}\left(\frac{\partial\tilde{\bar{\phi}}}{\partial x}\Big|_{i+1} - \frac{\partial\bar{\phi}}{\partial x}\Big|_{i+1}\right) - C_{i-1}\left(\frac{\partial\tilde{\bar{\phi}}}{\partial x}\Big|_{i-1} - \frac{\partial\bar{\phi}}{\partial x}\Big|_{i-1}\right)}{2} \tag{4.43}$$

The second option, instead, is a consistent one and follows the discretization (4.41)

[14]This scheme is, in practice, the default LES option in Fluent® and the default scheme used in this thesis. See chapter 5 for additional details.

for the original diffusive term:

$$\begin{aligned}\alpha\nu\left[C\frac{\partial\left(\tilde{\bar{\phi}}-\bar{\phi}\right)}{\partial x}\right]\Bigg|_{i-\frac{1}{2}}^{i+\frac{1}{2}} =&\alpha\nu\left[\frac{2C_iC_{i+1}}{C_i+C_{i+1}}\frac{\left(\tilde{\bar{\phi}}_{i+1}-\tilde{\bar{\phi}}_i\right)-\left(\bar{\phi}_{i+1}-\bar{\phi}_i\right)}{\Delta x}\right]\\ &-\alpha\nu\left[\frac{2C_iC_{i-1}}{C_i+C_{i-1}}\frac{\left(\tilde{\bar{\phi}}_i-\tilde{\bar{\phi}}_{i-1}\right)-\left(\bar{\phi}_i-\bar{\phi}_{i-1}\right)}{\Delta x}\right]\end{aligned} \tag{4.44}$$

where the variable coefficient C is interpolated according to the usual approach for variable viscosities. However, it should be noted, by looking at equation (4.35), that, whatever discretization is used for ψ, there will always be an inconsistency as C_i necessarily requires gradients in the cell center. Actually, this is not strictly required as here C could be instead computed on the faces themselves. While this could certainly improve the overall consistency, and similar approaches in SGS modeling have been tried for different terms (Viré and Knaepen, 2009), it should be noted that the practical relevance of such approach is certainly null for unstructured codes, as there dynamic constants are necessarily computed in the cell centers. The last required discretization is for the test filter, which defines $\tilde{\bar{\phi}}_i$ and $\hat{\tilde{\bar{\phi}}}_i$. Again, two options are available. One is based on equation (4.18), which is possible because the shape functions are known, and leads to:

$$\begin{aligned}\tilde{\bar{\phi}}_i=\frac{1}{\Delta x}\int_{x_i-\frac{\Delta x}{2}}^{x_i+\frac{\Delta x}{2}}\bar{\phi}\left(x\right)dx=&\frac{1}{\Delta x}\int_{x_i-\frac{\Delta x}{2}}^{x_i}\bar{\phi}_{i-1}+\frac{\bar{\phi}_i-\bar{\phi}_{i-1}}{\Delta x}\left(x-x_{i-1}\right)dx\\ &+\frac{1}{\Delta x}\int_{x_i}^{x_i+\frac{\Delta x}{2}}\bar{\phi}_i+\frac{\bar{\phi}_{i+1}-\bar{\phi}_i}{\Delta x}\left(x-x_i\right)dx\\ =&\frac{1}{8}\left(\bar{\phi}_{i-1}+6\bar{\phi}_i+\bar{\phi}_{i+1}\right)\end{aligned} \tag{4.45}$$

Analogously:

$$\hat{\tilde{\bar{\phi}}}_i=\frac{1}{8}\left(\tilde{\bar{\phi}}_{i-1}+6\tilde{\bar{\phi}}_i+\tilde{\bar{\phi}}_{i+1}\right)=\frac{1}{64}\left(\bar{\phi}_{i-2}+12\bar{\phi}_{i-1}+38\bar{\phi}_i+12\bar{\phi}_{i+1}+\bar{\phi}_{i+2}\right) \tag{4.46}$$

The second option is based on equation (4.19) and corresponds to the approach adopted here for the implementation of the scale-similar model:

$$\begin{aligned}\tilde{\bar{\phi}}_i=&\frac{1}{3}\left(\bar{\phi}_{i-1}+\bar{\phi}_i+\bar{\phi}_{i+1}\right)\\ \hat{\tilde{\bar{\phi}}}_i=&\frac{1}{3}\left(\tilde{\bar{\phi}}_{i-1}+\tilde{\bar{\phi}}_i+\tilde{\bar{\phi}}_{i+1}\right)=\frac{1}{9}\left(\bar{\phi}_{i-2}+2\bar{\phi}_{i-1}+3\bar{\phi}_i+2\bar{\phi}_{i+1}+\bar{\phi}_{i+2}\right)\end{aligned} \tag{4.47}$$

Notice that, the underlying second order approximations of the two filters are:

$$\begin{aligned}\frac{1}{8}\left(\bar{\phi}_{i-1}+6\bar{\phi}_i+\bar{\phi}_{i+1}\right) &= \bar{\phi}_i+\frac{2}{8}\Delta x^2\frac{\partial^2\bar{\phi}}{\partial x^2}\Big|_i \\ \frac{1}{3}\left(\bar{\phi}_{i-1}+\bar{\phi}_i+\bar{\phi}_{i+1}\right) &= \bar{\phi}_i+\frac{2}{27}\left(3\Delta x\right)^2\frac{\partial^2\bar{\phi}}{\partial x^2}\Big|_i\end{aligned} \tag{4.48}$$

thus, actually, none of the two provides the exact value $\Delta x^2/24$ for the second order moment, which can be seen as a further justification of the overall approach proposed in section 4.3. Nonetheless, it should be appreciated that the inconsistent filter, when properly scaled (by α, see below), provides a value which is much closer to the exact one. Without scaling, of course, the error is much higher[15].

It should be clear now that the parameters α and β refer, respectively, to the ratios $\Delta^2_{n,0}/\Delta^2_{m,n}$ and $\Delta^2_{m,0}/\Delta^2_{r,m}$ in (4.25). Thus, when the consistent filter (4.45) is used, they are assumed both unitary. In contrast, when the inconsistent filter (4.47) is used, they are assigned the values:

$$\begin{aligned}\alpha &= \frac{\Delta x^2}{\left(3\Delta x\right)^2}=\frac{1}{9} \\ \beta &= \frac{\Delta x^2+\left(3\Delta x\right)^2}{\left(3\Delta x\right)^2}=\frac{10}{9}\end{aligned} \tag{4.49}$$

Table 4.1: *Spatial discretization options for equation* (4.37).

	Consistent discretization	Inconsistent discretization
Convective term	(4.40), $\gamma = 0$	(4.40), $\gamma = 1$
Diffusive term	(4.41)	
Model - Convective part	(4.42)	
Model - Diffusive part	(4.44)	(4.43)
Filter	(4.45-4.46)	(4.47)
α	1	1/9
β	1	10/9

For the sake of clarity, the previous discretization options are all summarized in Table 4.1.When these are used within equation (4.37), the resulting approximation finally

[15]Following the same reasoning, it can be shown that excluding the central cell i from the filter stencil would provide an even better estimate of the filter moment, if properly scaled.

reads:

$$\begin{aligned}\frac{\partial\bar{\phi}_i}{\partial t} =& -U\frac{\left(\bar{\phi}_{i+1}-\bar{\phi}_{i-1}\right)}{2\Delta x}-\frac{U\gamma}{8\Delta x}\left[2\left(\bar{\phi}_{i+1}-\bar{\phi}_{i-1}\right)-\left(\bar{\phi}_{i+2}-\bar{\phi}_{i-2}\right)\right]\\ &+\nu\frac{\bar{\phi}_{i+1}-2\bar{\phi}_i+\bar{\phi}_{i-1}}{\Delta x^2}\\ &+\alpha U\frac{C_{i+1}\left(\tilde{\bar{\phi}}_{i+1}-\bar{\phi}_{i+1}\right)-C_{i-1}\left(\tilde{\bar{\phi}}_{i-1}-\bar{\phi}_{i-1}\right)}{2\Delta x}\\ &-\frac{\alpha\nu}{\Delta x}\left[C\frac{\partial\left(\tilde{\bar{\phi}}-\bar{\phi}\right)}{\partial x}\right]\Bigg|_{i-\frac{1}{2}}^{i+\frac{1}{2}}\end{aligned} \tag{4.50}$$

where the last term can be discretized either trough (4.43) or (4.44). It is easy to show that, in fact, both the filtering methods leads to the exact same discretization for the model terms, the only difference being a multiplicative constant that can be absorbed in the definition of the dynamic constant C_i[16]. Thus, in practice, the only difference among the two filtering methods is in the computation of C_i, independently from the discretization used for the diffusive part of the model. In particular, the consistent filtering approach, after some algebra, can be shown to imply the following dynamic constant C_i^C:

$$C_i^C=\frac{-1}{8\alpha-\beta\frac{\left(10\bar{\phi}_i-4\bar{\phi}_{i-1}-4\bar{\phi}_{i+1}-\bar{\phi}_{i-2}-\bar{\phi}_{i+2}\right)-\frac{1}{Re}\left[11\left(\bar{\phi}_{i+1}-\bar{\phi}_{i-1}\right)-4\left(\bar{\phi}_{i+2}-\bar{\phi}_{i-2}\right)-\left(\bar{\phi}_{i+3}-\bar{\phi}_{i-3}\right)\right]}{\left(2\bar{\phi}_i-\bar{\phi}_{i-1}-\bar{\phi}_{i+1}\right)-\frac{1}{Re}\left[2\left(\bar{\phi}_{i+1}-\bar{\phi}_{i-1}\right)-\left(\bar{\phi}_{i+2}-\bar{\phi}_{i-2}\right)\right]}} \tag{4.51}$$

while, for the inconsistent one, the dynamic constant C_i^I is computed as:

$$C_i^I=\frac{-1}{3\alpha-\beta\frac{\left(\bar{\phi}_{i-1}+\bar{\phi}_{i+1}-\bar{\phi}_{i-2}-\bar{\phi}_{i+2}\right)-\frac{1}{Re}\left[\left(\bar{\phi}_{i+1}-\bar{\phi}_{i-1}\right)+\left(\bar{\phi}_{i+2}-\bar{\phi}_{i-2}\right)-\left(\bar{\phi}_{i+3}-\bar{\phi}_{i-3}\right)\right]}{\left(2\bar{\phi}_i-\bar{\phi}_{i-1}-\bar{\phi}_{i+1}\right)-\frac{1}{Re}\left[2\left(\bar{\phi}_{i+1}-\bar{\phi}_{i-1}\right)-\left(\bar{\phi}_{i+2}-\bar{\phi}_{i-2}\right)\right]}} \tag{4.52}$$

and, in both cases, $Re = 2U\Delta x/\nu$. In the following, the no model formulation (both with $\gamma = 0$ and $\gamma = 1$) is compared, trough a Non linear Spectral Analysis (NSA), with two model formulations: the consistent one and the inconsistent one, both with $\gamma = 0$. In addition, the inconsistent filter formulation is also evaluated with a consistent diffusive term and/or with unitary parameters α and β.

4.5.3 Nonlinear Spectral Analysis

From the previous analysis emerges the fact that, overall, the effect of a scale-similar model in this simplified framework can be interpreted as a modification of the basic discretization schemes. Also, this interpretation is independent from the specific filtering

[16]This heuristically confirms the assumption made in section 4.4 that an error introduced by the filter can be, possibly, corrected by the dynamic procedure.

approach and from the use, or not, of a dynamic procedure for the computation of the constant C. In the former case, however, the resulting schemes are strictly nonlinear.

A possible approach to analyze such modified schemes is based on the so called Nonlinear Spectral Analysis developed by Fauconnier and Dick (2011), which is suitable for general nonlinear schemes. In particular, the analysis is aimed at determining, among other things, the modified wavenumber of a scheme by direct comparison with an exact spectral discretization, instead of determining its theoretical expression, which might be impossible for nonlinear schemes.

In practice, to this end, a set of N_r random fields with prescribed spectrum are first generated. In the present case the selected spectrum $E(k)$ is the one proposed by Pope (2000):

$$E\left(k\right) = C_0 \varepsilon^{\frac{2}{3}} k^{-\frac{5}{3}} \left\{ \frac{kL}{\left[\left(kL\right)^2 + c_L\right]^{\frac{1}{2}}} \right\}^{\frac{5}{3}+p_0} e^{-\beta\left\{\left[(k\eta)^4 + c_\eta^4\right]^{\frac{1}{4}} - c_\eta\right\}} \tag{4.53}$$

where, given the value U, a prescribed maximum spatial period L_0 and the number n of points over L_0, the parameters in the spectrum have been determined as:

$$L = \frac{L_0}{6} \qquad \eta = \frac{\Delta x}{2} = \frac{L_0}{2\left(n-1\right)} \qquad \varepsilon = \frac{U^3}{L} \qquad \nu = \left(\eta^4 \varepsilon\right)^{1/3} \tag{4.54}$$

and the remaining constants fixed at[17]: $p_0 = 2$, $C_0 = 1.5$, $\beta = 5.2$, $c_L = 6.78$ and $c_\eta = 0.4$. Each of the N_r fields f_j is then constructed by taking the inverse Fourier transform of the coefficients:

$$\hat{f}_{\pm k} = \sqrt{E\left(k\right)} e^{\pm i\theta} \tag{4.55}$$

with θ a uniform random number in the interval $[-\pi, \pi]$ and $i = \sqrt{-1}$. Finally, for a given numerical scheme and for each of these random fields f_j, the modified wavenumber $k'_j(k)$ can be built by taking the Fourier transform of the signal f_j acted upon by the scheme. For first and second order discrete derivatives the result is:

$$k'_j\left(k\right) = \mathfrak{R}\left[\frac{1}{i\hat{f}_k}\mathcal{F}\left(\frac{\delta f_j}{\delta x}\right)\right] \qquad k'_j\left(k\right) = \mathfrak{I}\left[\frac{1}{i\hat{f}_k}\mathcal{F}\left(\frac{\delta^2 f_j}{\delta x^2}\right)\right] \tag{4.56}$$

where $\mathfrak{R}$ and $\mathfrak{I}$ represent, respectively, the real and imaginary parts. As each of these functions is relative to a single, random realization, they are more meaningfully

[17] In theory, c_L and c_η should be determined by the requirements that $E(k)$ and $2\nu k^2 E(k)$ integrate, respectively, to the total kinetic energy and ε. However, for the present purposes it was not necessary and, for simplicity, high Reynolds values have been selected.

presented as means μ within $\pm 2\sigma$ bands, with:

$$\begin{aligned} \mu_{k'}(k) &= \frac{1}{N_r}\sum_{j=1}^{N_r} k'_j(k) \\ \sigma_{k'}(k) &= \sqrt{\frac{1}{N_r-1}\sum_{j=1}^{N_r}\left[k'_j(k)-\mu_{k'}(k)\right]^2} \end{aligned} \tag{4.57}$$

In the following, all the presented results are relative to $N_r = 1000$, a grid with $n = 201$ points on a period $L_0 = 2\pi$ and $U = 10$. A representative function f_j and the underlying spectrum function $E(k)$ are depicted in Figure 4.1.

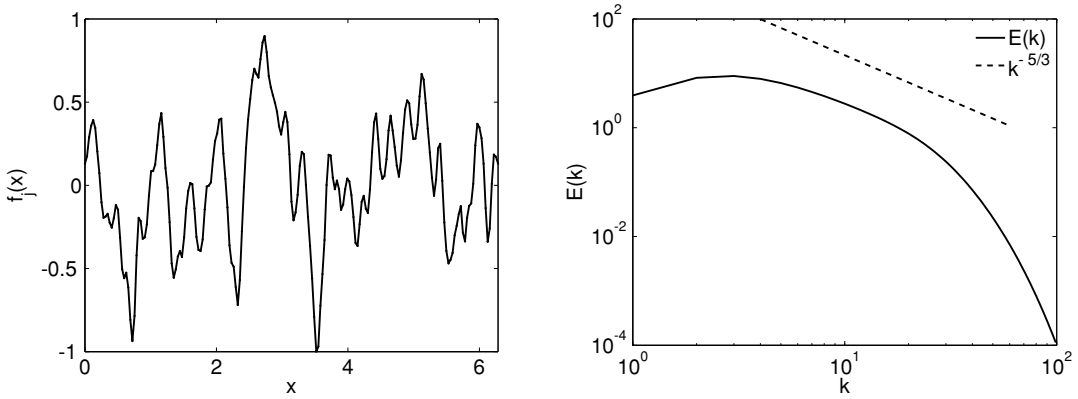

Figure 4.1: *Random function f_j (a) and its underlying spectrum (b).*

4.5.4 Results

A first interesting comparison is presented in Figure 4.2, where the effect of the parameter γ in the convective scheme is analyzed without any model for τ (i.e., $C = 0$) and compared with several alternative finite difference discretizations. It is apparent how, despite the lack of a formal accuracy improvement[18], the spectral resolution properties for $\gamma = 1$ are comparable to the ones of a 6^{th} order scheme. This effect is extremely valuable in LES as, more than the formal accuracy, for a convective scheme is important to correctly transport the turbulent structures[19].

The effect of the scale-similar model and its discretization are instead investigated in Figure 4.3, for $\gamma = 0$ and with a fixed value of the constant C. In particular, for the consistent discretization ($\alpha = 1$) the values $C^C = 1$ and $C^C = 2$ are investigated. However, for the inconsistent discretization ($\alpha = 1/9$) the constant C^I is selected so that the convective term in the model exactly fits the consistent discretization and differences can be appreciated only in the diffusive term. As emerges from the relations (4.48), such value of the constant C^I is exactly $27/8$ times the value C^C used for the

[18] On nonuniform grids the contribution of γ might even become inconsistent!

[19] Indeed, the formal accuracy of a scheme might easily break down for the scarcely resolved functions typical of LES.

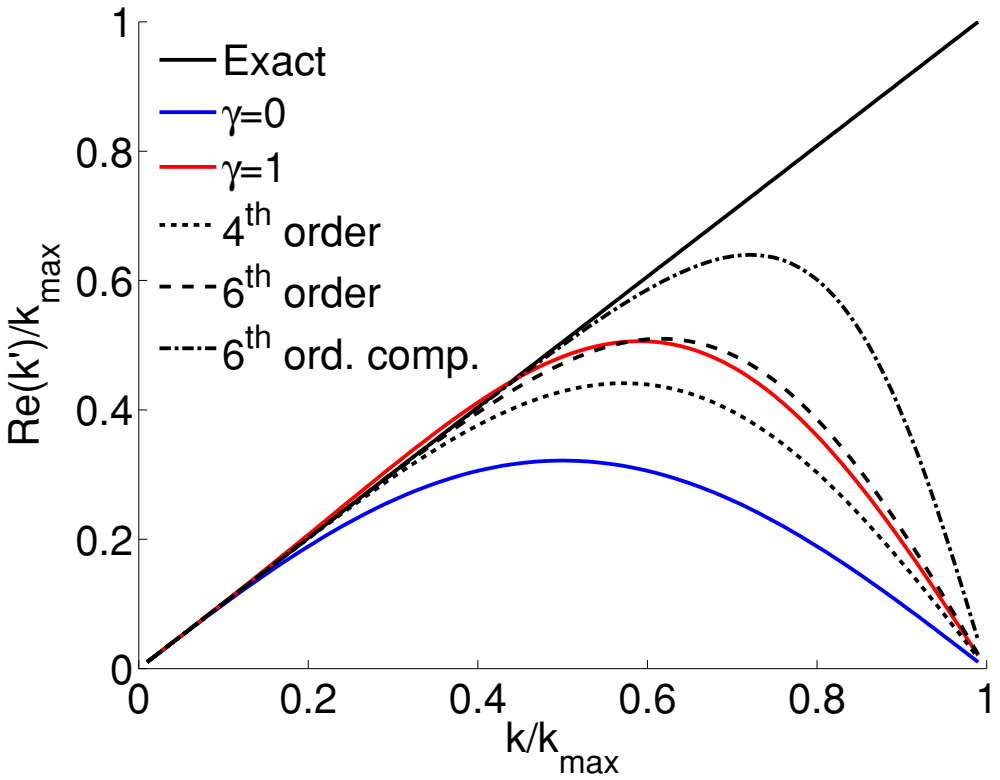

Figure 4.2: *Effect of the parameter γ in the convective scheme* (4.40).

consistent discretization. Also notice that, having a fixed value for the constant in the model, such schemes are still fully linear and 2σ bands are not necessary.

The main thing emerging from the analysis is that the convective part of the scale similar model has an effect comparable to the one due to the parameter γ[20]. In particular, a 6^{th} order-like spectral behavior is recovered for $C^C = 2$ or $C^I = 27/4 = 6.75$. A somehow unexpected effect, however, is also apparent for the diffusive term that, for the consistent discretization, already recovers a 6^{th} order-like behavior for $C^C = 1$, while a higher constant value somehow disrupts this accuracy. In contrast, an inconsistent discretization for the diffusive term does not have the same appreciable effect and, despite the favorable behavior at intermediate wavenumbers, the second order accuracy is inevitably recovered at the grid cut-off, independently from the value of the constant C^I. It is worth noting that, differently from the filter, in a general purpose solver both discretization methods are readily applicable for the diffusive term. However, according to the common practice, in this thesis the scale-similar model is implemented explicitly and, in this case, a higher effectiveness of the diffusive term would imply a more stringent stability requirement on the time step. For this reason, and because of the lower sensitivity to the value of the constant, the inconsistent discretization method is selected in this thesis for the implementation of the diffusive part of the scale-similar model. Overall, the analysis above also suggests that, despite the formal accuracy of

[20] Actually, in this simplified 1D framework, there is a full equivalence, as can be easily seen by developing the formula (4.42) and setting $C^C = 2\gamma$ or $C^I = (27/4)\gamma$. See also equation (5.49).

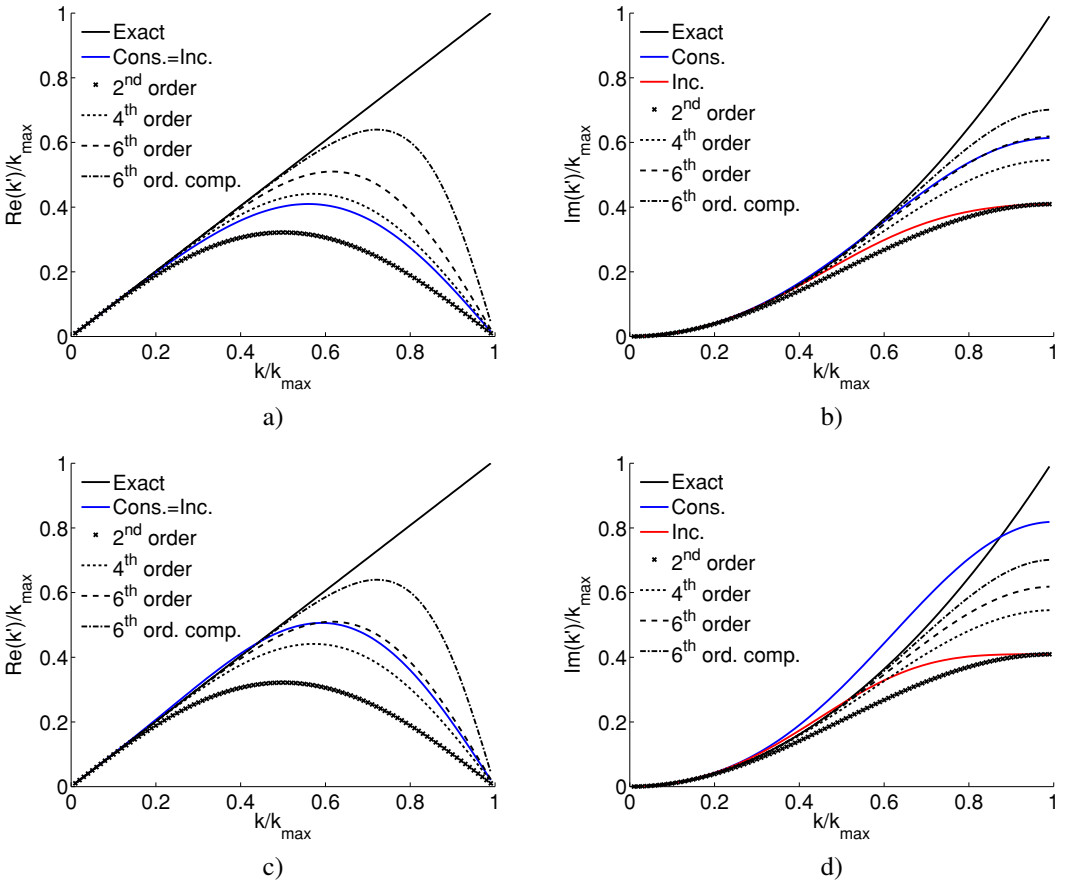

Figure 4.3: *Effect of the model constant for a consistent* (4.44) *and an inconsistent* (4.43) *discretization of the diffusive part of the model. Left: convective term. Right: diffusive term. Top:* $C^C = 1$, $C^I = 27/8$. *Bottom:* $C^C = 2$, $C^I = 27/4$.

the approximations, even in such a rigid 1D linear framework, the use of a scale-similar model is valuable for the implicitly filtered FV method and, heuristically, provides a justification for its use in 3D turbulent fields, where the model would also contribute to the resolution of additional physical effects not present in these tests.

What remains to be assessed is thus the effectiveness of the dynamic scale-similar model as effectively implementable in the code Fluent® and compare it with its consistent ideal counterpart. This comparison is thus between a fully consistent discretization with a dynamic constant C^C in the range $0 - 1$ and the fully inconsistent discretization with a dynamic constant C^I in the tentative range $0 - 27/8$, as determined from the previous static analysis. In both cases $\gamma = 0$ is assumed and both the convective and diffusive term are compared. The certainly expected result of this comparison, presented in Figure 4.4, is that the dynamic procedure cannot ameliorate the performances of the static models in this specific linear case, where the filter moment is fixed and determines the optimum value of the constant in the model, which instead is used here only as upper limit of the dynamic range. However, it is somehow surprising how the dynamic procedure for the inconsistent discretization is much less disruptive for the potential accuracy of the model, while totally annihilates it in the consistent case. Ac-

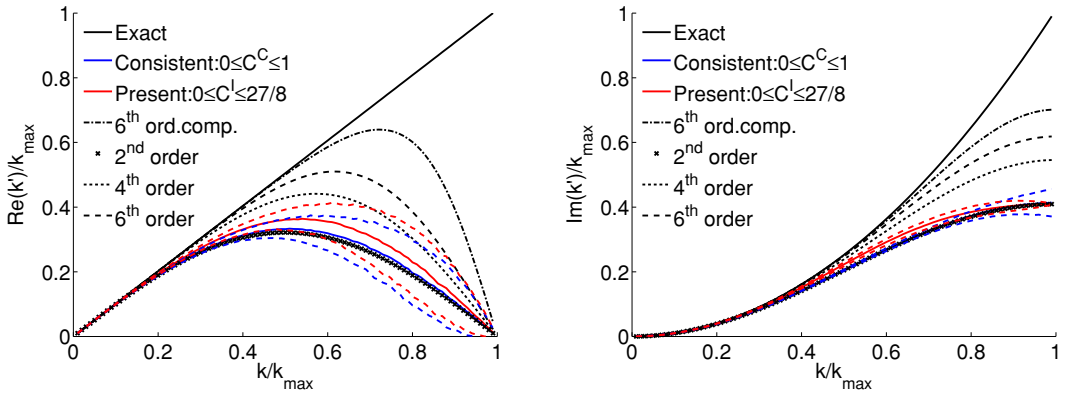

Figure 4.4: *Present dynamic scale-similar model vs. fully consistent one. (a) Convective term. (b) Diffusive term. Dashed colored lines: 2σ bands. Full colored lines: mean values.*

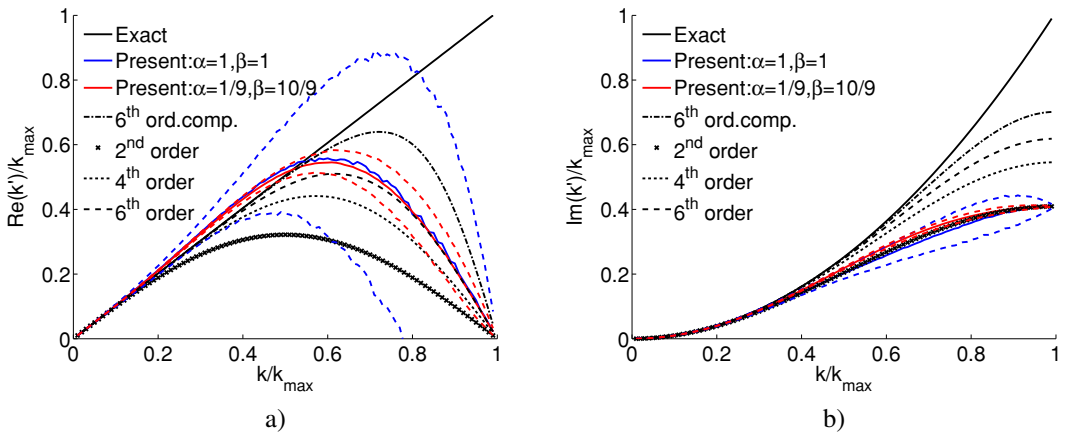

Figure 4.5: *Present dynamic scale-similar model with $\gamma = 1$ and $0 \leq C^I \leq 2$. Correct implementation ($\alpha = 1/10$, $\beta = 10/9$) vs. incorrect one ($\alpha = 1$, $\beta = 1$). (a) Convective term. (b) Diffusive term. Dashed colored lines: 2σ bands. Full colored lines: mean values.*

tually, as shown by the dashed lines, which represent the 2σ bands around the mean full lines, the dynamic procedure for the consistent model is likely to ruin even the accuracy of the basic discretization scheme.

This fact also promotes another consideration: what would be the accuracy of the present implementation of the model when coupled with $\gamma = 1$ in the convective scheme? Indeed, this is the actual default option for the convective scheme in Fluent® and the model should not promote any inaccuracy with respect to the basic scheme. In practice, for the previously investigated range $0 \leq C^I \leq 27/8$, the resulting 2σ band appears to be too wide and, after trial and error, a safer option appears to be the range $0 \leq C^I \leq 2$, which has indeed been adopted as default range in the present implementation of the dynamic scale-similar model (see equation (4.29)). For the sake of completeness, this implementation ($\alpha = 1/10$, $\beta = 10/9$) is analyzed in Figure 4.5 together with a wrong implementation, whose scaling factors are assumed unitary ($\alpha = 1$, $\beta = 1$). The figure shows that, not only the limited range $0 - 2$ is compatible with the

accuracy of the underlying scheme, but also that a wrong implementation of the model is simply unacceptable from the point of view of the accuracy due to the very wide 2σ band. In practice, for real applications of the model in 3D turbulent fields, it will be shown that such wrong behavior is likely to leave the basic discretization unaffected, but the resulting model would be totally useless.

A final note is necessary on the suitability of the dynamic procedure and its effectiveness, which here appears to be, at best, null. However, besides the differences in the resolved fields, when real 3D turbulent applications are considered, the nature of the dynamic procedure itself is completely different. Indeed, for the 1D linear case the Germano Identity is enforced exactly and this has a strong effect on the resulting scheme, as its suitability as static model does not imply the suitability within a dynamic procedure[21]. In contrast, for 3D turbulent fields, the Germano Identity is tensorial and can only be enforced in a least-squares sense. Thus, not only the enforcement has to take into account additional 3D effects, but the procedure itself should tend to promote those parts of the modeling assumption that are more likely to hold, and loosen those that do not. This, indeed, usually happens for two-parameters mixed models, whose scale-similar part is strongly promoted because of its higher correlation with the true SGS stress tensor (Anderson and Meneveau, 1999). As a consequence, in the present work, the use of the dynamic procedure in the model formulation is retained.

4.6 Effect of the model on the pressure equation

An interesting aspect of the GLES framework, which is not shared with any other LES approach, is the prescription of a SGS term, in the momentum equation, which is strictly dependent on the pressure. This difference is due to the fact that, differently from other approaches, all the linear terms contribute to the SGS stresses in GLES. For functional modeling assumptions, and from the functional perspective in general, this fact appears to be irrelevant as, in practice, the pressure term only becomes relevant for compressible flows and the overall energy balance between resolved and non resolved scales can be managed with a single eddy viscosity term. However, for structural models explicitly taking the pressure into account the situation is different. To better understand this effect, let us consider the pressure equation (3.14):

$$\overline{\frac{\partial}{\partial x_i}\frac{\partial}{\partial x_j}\left(\bar{p}^n\delta_{ij}\right)}^n = \frac{\partial^2\bar{\rho}^n}{\partial t^2} - \overline{\frac{\partial}{\partial x_i}\frac{\partial}{\partial x_j}\left[\bar{\rho}^n\tilde{u}_i^n\tilde{u}_j^n + \tilde{\Sigma}_{ij}^n - \tau_{ij}^{n-0}\right]}^n \tag{4.58}$$

and a simplified numerical framework, with the discretized pressure $\bar{p}^n_{i,j,k}$ located in the cell centers $\mathbf{x}_{i,j,k} = [x_{i,j,k}, y_{i,j,k}, z_{i,j,k}]$ of a grid with constant steps Δx, Δy, and Δz. For this setting, with second order accuracy, a straightforward discretization of the left hand side of equation (4.58) would make use of the linear shape functions for the

[21] In practice, the use of a Germano Identity, especially for scale-similar models, implies the hypotheses of scale invariance over a certain range of scales. This, of course, might not hold in general and depends from the spectrum of the underlying function.

inner derivatives, leading to:

$$\left[\overline{\frac{\partial}{\partial x_i}\frac{\partial}{\partial x_j}\left(\bar{p}^n\delta_{ij}\right)}^n\right]\Bigg|_{\mathbf{x}_{i,j,k}} \approx \nabla^2_{\Delta x}\left(\bar{p}^n\right)|_{\mathbf{x}_{i,j,k}} = \frac{\bar{p}^n_{i+1,j,k} - 2\bar{p}^n_{i,j,k} + \bar{p}^n_{i-1,j,k}}{\Delta x^2} + \frac{\bar{p}^n_{i,j+1,k} - 2\bar{p}^n_{i,j,k} + \bar{p}^n_{i,j-1,k}}{\Delta y^2} + \frac{\bar{p}^n_{i,j,k+1} - 2\bar{p}^n_{i,j,k} + \bar{p}^n_{i,j,k-1}}{\Delta z^2} \tag{4.59}$$

with the terms on the right hand side of equation (4.58) discretized with the same approach. However, this approach would result in an inconsistency as the internal gradient term should instead respect its actual discretization in the momentum equation in order for the pressure equation to be meaningful. In particular, for a cell-centered FV approach, the pressure gradient term in the momentum equation is usually discretized as:

$$\left[\overline{\frac{\partial\bar{p}^n}{\partial x_j}}^n\right]\Bigg|_{\mathbf{x}_{i,j,k}} = \frac{1}{V}\sum_f \mathbf{n}_f\bar{p}^n_f A_f \approx \frac{1}{\Delta x\Delta y\Delta z}\begin{bmatrix}\left(\bar{p}^n_{i+1,j,k} - \bar{p}^n_{i-1,j,k}\right)\Delta y\Delta z/2\\ \left(\bar{p}^n_{i,j+1,k} - \bar{p}^n_{i,j-1,k}\right)\Delta x\Delta z/2\\ \left(\bar{p}^n_{i,j,k+1} - \bar{p}^n_{i,j,k-1}\right)\Delta x\Delta y/2\end{bmatrix} \tag{4.60}$$

Thus, a consistent approach should consist in using the linear approximation on this whole gradient term:

$$\left[\overline{\frac{\partial}{\partial x_i}\overline{\frac{\partial}{\partial x_j}\left(\bar{p}^n\delta_{ij}\right)}^{n}}^n\right]\Bigg|_{\mathbf{x}_{i,j,k}} \approx \nabla^2_{2\Delta x}\left(\bar{p}^n\right)|_{\mathbf{x}_{i,j,k}} = \frac{\bar{p}^n_{i+2,j,k} - 2\bar{p}^n_{i,j,k} + \bar{p}^n_{i-2,j,k}}{4\Delta x^2} + \frac{\bar{p}^n_{i,j+2,k} - 2\bar{p}^n_{i,j,k} + \bar{p}^n_{i,j-2,k}}{4\Delta y^2} + \frac{\bar{p}^n_{i,j,k+2} - 2\bar{p}^n_{i,j,k} + \bar{p}^n_{i,j,k-2}}{4\Delta z^2} \tag{4.61}$$

and a similar discretization for all the remaining terms in the pressure equation. Hence, a first consequence of this analysis is that equation (4.58), while exact, is not really suitable for the GLES framework as not representative of the actual computational approach. Indeed, it has been derived by directly applying the G^i operators to the true pressure equation. If, instead, the GLES pressure equation is derived, consistently, from the GLES equations (3.9), the still exact result is[22]:

$$\overline{\frac{\partial}{\partial x_i}\overline{\frac{\partial}{\partial x_j}\left(\bar{p}^n\delta_{ij}\right)}^{n}}^n = \frac{\partial^2\bar{\rho}^n}{\partial t^2} - \overline{\frac{\partial}{\partial x_i}\overline{\frac{\partial}{\partial x_j}\left[\bar{\rho}^n\tilde{u}^n_i\tilde{u}^n_j + \tilde{\Sigma}^n_{ij} - \tau^{n-0}_{ij}\right]}^n}^n - \overline{\frac{\partial}{\partial x_i}\left(\frac{\partial\chi^{n-0}_i}{\partial t}\right)}^n$$

[22]The procedure, not reported here for the sake of conciseness, amounts to applying the time derivative operator to the continuity equation, the filtered divergence operator $\overline{\partial/\partial x_i(\cdots)}^n$ to the momentum equations and mixing the two.

(4.62)

and now, not surprisingly, also includes the contribution from the SGS term in the continuity equation, as one would expect. Unfortunately, equation (4.62), when implemented in co-located FV arrangements[23], has the well known drawback of producing checkerboard solutions, because of the double spacing in the discretization (4.61). However, here the pressure SGS term comes into play. Indeed, for the present scale-similar model (4.25), the differential model (4.15) or, as better explained in the next section, even a reconstruction based model as those in section 4.3.1, the pressure part in the SGS stresses τ_{ij}^{n-0} is approximated, at the lowest order, as:

$$\delta_{ij}\left(\bar{p}^n - p\right) \approx \delta_{ij}\Delta_{n,0}^2 M_k \frac{\partial^2 \bar{p}^n}{\partial x_k^2} \tag{4.63}$$

Hence, if this term is compared with the difference in the Taylor series expansions of the approximations in (4.59) and (4.61):

$$\left[\nabla_{2\Delta x}^2\left(\bar{p}^n\right) - \nabla_{\Delta x}^2\left(\bar{p}^n\right)\right]|_{\mathbf{x}_{i,j,k}} \approx \left(\frac{\Delta x^2}{4}\frac{\partial^4 \bar{p}^n}{\partial x^4} + \frac{\Delta y^2}{4}\frac{\partial^4 \bar{p}^n}{\partial y^4} + \frac{\Delta z^2}{4}\frac{\partial^4 \bar{p}^n}{\partial z^4}\right)\Bigg|_{\mathbf{x}_{i,j,k}} \tag{4.64}$$

the overall effect of the pressure SGS term appears approximately similar to that of stabilizing terms used to counteract the pressure checkerboard typical of the approach (4.62) in co-located FV methods (Ferziger and Perić, 2002):

$$\begin{aligned}\overline{\frac{\partial}{\partial x_i}\overline{\frac{\partial}{\partial x_j}\left(\delta_{ij}\Delta_{n,0}^2 M_k \frac{\partial^2 \bar{p}^n}{\partial x_k^2}\right)}^n}^n \approx & \frac{\partial^2}{\partial x_j^2}\left(\Delta_{n,0}^2 M_k \frac{\partial^2 \bar{p}^n}{\partial x_k^2}\right) \\ \propto & C\left[\nabla_{2\Delta x}^2\left(\bar{p}^n\right) - \nabla_{\Delta x}^2\left(\bar{p}^n\right)\right] + O\left(\Delta_{n,0}^2\right)\end{aligned} \tag{4.65}$$

More specifically, besides the difference in the proportionality constant C, the pressure part in the structural model also has additional terms of order $\Delta_{n,0}^2$, due to the mixed derivatives, not present in (4.64)[24]. Thus, adding the pressure term in the structural model has an overall stabilizing effect which should prevent the pressure checkerboard. For the present scale-similar model (4.25), the exact effect of this inclusion is that the pressure equation is solved for:

$$\overline{\frac{\partial}{\partial x_i}\overline{\frac{\partial}{\partial x_j}\delta_{ij}\left[\bar{p}^n + C_{ss}\frac{\Delta_{n,0}^2}{\Delta_{m,n}^2}\left(\bar{p}^n - \bar{p}^m\right)\right]}^n}^n \tag{4.66}$$

and the checkerboard is avoided due to the coupling effect of the term $\bar{p}^m$. Unfortunately, this auxiliary effect of the scale-similar pressure term can only be effective if it is discretized consistently. In particular, this means that the pressure part in the scale-similar term should be updated during the iterations for the pressure equation, in order

[23] The only ones considered here.

[24] Actually, even more terms appear if the full second order approximation (4.8) is considered. However, this difference is specifically due to the stencils (4.59) and (4.61) used for the discretization. For full, 27-points, Laplacian stencils the full correspondence is recovered.

for the final solution to be effectively representative of the discretization (4.66). While, in general, this would not be difficult to achieve with a deferred correction approach (Khosla and Rubin, 1974), the suitability of this modification should confront the fact that stabilizing terms for the pressure equation are inevitably present in general purpose solvers and cannot, in general, be removed. At the same time, for general unstructured solvers, the discretization (4.61) is also largely impractical. As a consequence, in the present thesis, structural pressure effects in the pressure equation have not been explicitly included. It is instead assumed that such role is implicitly played, with sufficient accuracy, by the stabilizing terms originally present in the discretized pressure equation. Finally, notice that a pressure treatment similar to the one resulting here from the SGS model has been proposed by several authors. For example, Dormy (1999) advocated a similar treatment for an equation of the form (4.58) in order to recover the accuracy of the correct one (4.62) while using a compact stencil for the Laplacian. An even more interesting view is furnished by Date (2003), whose reading is recommended because the pressure equation is directly envisaged in terms of a filtered correction as proposed here in (4.66), but motivated on the basis of its connection with the Stokes' hypothesis for the continuous stresses.

4.7 Connection with ADM

An additional feature of the present GLES framework, which becomes particularly evident after the introduction of a structural SGS model, is its intimate connection with the Approximate Deconvolution Modeling (ADM) approach proposed by Stolz and Adams (1999). This connection has already been mentioned, in section 3.6.1, with reference to the form of the discretized equations. However, when a structural SGS model is used, the connection is also practical, as shown in the following. The connection between ADM and CLES with differential structural models has already been shown by Stolz et al. (2001b). A similar approach is followed here but, notably, no commutation for the filter is required as the GLES framework uses the exact same equations used in ADM.

In order to proceed with the demonstration, it is just necessary to note that, after the introduction of the scale-similar part of the model in (4.25), and because of the scaling factor $C_{ss}\Delta_{n,0}^2/\Delta_{m,n}^2$ in it, the momentum equations in (3.9) become[25]:

$$\begin{aligned}
&\frac{\partial\left(\bar{\rho}^n\tilde{u}_i^n\right)}{\partial t}+\overline{\frac{\partial}{\partial x_j}\left[\frac{\left(\rho u_i\right)^*\left(\rho u_j\right)^*}{\rho^*}+\sigma_{ij}^*\right]}^n=O\left(\Delta_{n,0}^4\right)\\
&\sigma_{ij}^*=p^*\delta_{ij}-2\mu\left(S_{ij}^*-\frac{1}{3}S_{kk}^*\delta_{ij}\right)\\
&S_{ij}^*=\frac{1}{2}\left\{\frac{\partial}{\partial x_j}\left[\frac{\left(\rho u_i\right)^*}{\rho^*}\right]+\frac{\partial}{\partial x_i}\left[\frac{\left(\rho u_j\right)^*}{\rho^*}\right]\right\}
\end{aligned}\tag{4.67}$$

[25] A similar reasoning could be done for the remaining equations if a proper structural SGS model is used in them too.

where the asterisk in the superscript denotes variables of the form:

$$\phi^* = \bar{\phi}^n - C_{ss}\Delta_{n,0}^2 M_k \frac{\partial^2 \bar{\phi}^n}{\partial x_k^2} + O\left(\Delta_{n,0}^4\right) \qquad \Delta_{n,m}^2 = \sum_{j=1}^{n-m} \left(\Delta^{m+j}\right)^2 \tag{4.68}$$

and the whole equation (4.67) is a direct consequence of equations (4.7) and (4.15), their underlying hypotheses (e.g., μ =constant) and the following two relations derived in Appendix E:

$$\begin{aligned} \frac{(\rho u_i)^* (\rho u_j)^*}{\rho^*} =& \bar{\rho}^n \tilde{u}_i^n \tilde{u}_j^n - C_{ss}\Delta_{n,0}^2 M_k \left(\frac{\partial^2 \bar{\rho}^n \tilde{u}_i^n \tilde{u}_j^n}{\partial x_k^2} - 2\bar{\rho}^n \frac{\partial \tilde{u}_i^n}{\partial x_k} \frac{\partial \tilde{u}_j^n}{\partial x_k} \right) + O\left(\Delta_{n,0}^4\right) \\ \frac{(\rho u_i)^*}{\rho^*} =& \tilde{u}_i^n - C_{ss}\Delta_{n,0}^2 M_k \left(\frac{\partial^2 \tilde{u}_i^n}{\partial x_k^2} + \frac{2}{\bar{\rho}^n} \frac{\partial \bar{\rho}^n}{\partial x_k} \frac{\partial \tilde{u}_i^n}{\partial x_k} \right) + O\left(\Delta_{n,0}^4\right) \end{aligned} \tag{4.69}$$

Thus, by recognizing that (4.68) is analogous to the deconvolution/reconstruction relation (4.13), the connection between GLES and ADM becomes evident, as equations (4.67) use reconstructed fluxes to advance the filtered momentum components. In particular, for the present scale-similar model, only second order terms can be correctly reconstructed, thus the overall approximation is limited to the fourth order. In contrast, ADM is based on explicit filtering and arbitrary order reconstruction trough equation (4.9). With this connection, the dynamic procedure can then be also interpreted as a dynamic reconstruction of second order terms in a second order ADM approach.

It is worth noting that, as for the pressure term, the action of the diffusive term on the deconvolved variables in (4.69) can be interpreted as the addition of an hyper-viscosity term. However, because of the specific implementation adopted for the viscous part of the scale-similar model, the resulting effect is possibly limited (see section 4.5.4).

4.8 On the Galilean invariance in the GLES framework

Before closing this chapter, it seems appropriate to finally point out a classical criticism on the proposed arrangement of the terms in the GLES equations (3.9), which is the lack of Galilean invariance for some of the terms (Speziale, 1985). While the matter deserves some attention in terms of SGS modeling, as shown in the following, such a criticism can however be considered as highly unmotivated, for three main reasons.

The first, most important one, is that for general G^i operators, whose kernels arbitrarily vary in space, Galilean invariance is not preserved in any case, independently from the specific arrangement of the terms, because the resulting $\bar{(\cdots)}^n$ variables are not Galilean invariant themselves (Sagaut, 2006).

A less solid, but nonetheless valid, motivation is that Galilean invariance is not necessarily preserved when the equations are discretized (Bernardini et al., 2013), especially because such invariance depends from the combined discretization of the time derivative term and the convective term.

Indeed, and this brings in the third reason, the Galilean invariance for the single terms in the equations does not even hold for the pure NSE and it appears as completely

arbitrary to have such a requirement for the GLES equations (or any other form of LES equations). More specifically, in the pure NSE, the spurious term arising from the lack of invariance of the time derivative term exactly cancels an analogous spurious term arising from the convective part, leading to the full invariance of the NSE. What happens for the GLES equations is exactly the same, with the difference that the lack of Galilean invariance is common to the resolved convective term, the SGS term and the time derivative term. Their sum, however, exactly recovers the full Galilean invariance. To show this, let us consider the following coordinates transformation:

$$\begin{aligned} t^* &= t \\ x_i^* &= x_i - c_i t \end{aligned} \tag{4.70}$$

between the fixed inertial frame (x_i, t) and the one (x_i^*, t^*), moving at a constant speed c_i with respect to the fixed one, as depicted in Figure 4.6.

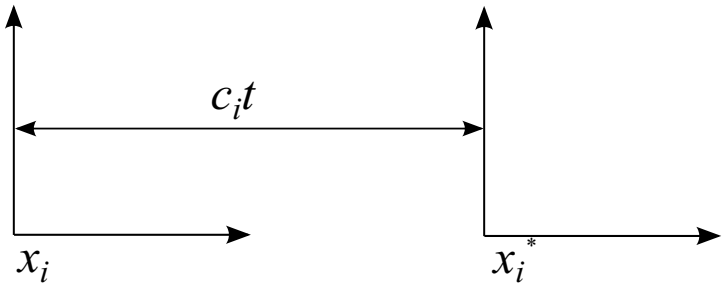

Figure 4.6: *Translation of the reference frame in a Galilean transformation.*

Under this coordinate transformation, flow variables transform as (Pope, 2000; Pruett, 2000):

$$\begin{aligned} u_i^*\left(x_i^*, t^*\right) &= u_i\left(x_i, t\right) - c_i \\ p^*\left(x_i^*, t^*\right) &= p\left(x_i, t\right) \\ \rho^*\left(x_i^*, t^*\right) &= \rho\left(x_i, t\right) \end{aligned} \tag{4.71}$$

As already stated, these transformations do not hold in LES/GLES if the operators G^i do not preserve themselves the Galilean invariance. In practice this is never the case but, for the sake of the discussion, here this is assumed to be true. In this case, after the application of n operators G^i, the relations (4.71) become:

$$\begin{aligned} \tilde{u}_i^{n*}\left(x_i^*, t^*\right) &= \tilde{u}_i^n\left(x_i, t\right) - c_i \\ \bar{p}^{n*}\left(x_i^*, t^*\right) &= \bar{p}^n\left(x_i, t\right) \\ \bar{\rho}^{n*}\left(x_i^*, t^*\right) &= \bar{\rho}^n\left(x_i, t\right) \end{aligned} \tag{4.72}$$

Moreover, independently from the operators G^i, the derivative operators transform

as:

$$\begin{aligned}\frac{\partial}{\partial t} &= \left(\frac{\partial t^*}{\partial t}\right)\frac{\partial}{\partial t^*} + \left(\frac{\partial x_i^*}{\partial t}\right)\frac{\partial}{\partial x_i^*} = \frac{\partial}{\partial t^*} - c_i\frac{\partial}{\partial x_i^*} \\ \frac{\partial}{\partial x_i} &= \left(\frac{\partial t^*}{\partial x_i}\right)\frac{\partial}{\partial t^*} + \left(\frac{\partial x_i^*}{\partial x_i}\right)\frac{\partial}{\partial x_i^*} = \frac{\partial}{\partial x_i^*}\end{aligned} \tag{4.73}$$

Thus, with reference to the momentum equation:

$$\frac{\partial\left(\bar{\rho}^n\tilde{u}_i^n\right)}{\partial t} + \overline{\frac{\partial}{\partial x_j}\left(\bar{\rho}^n\tilde{u}_i^n\tilde{u}_j^n + \bar{p}^n\delta_{ij} + \tilde{\Sigma}_{ij}^n\right)}^n = \overline{\frac{\partial}{\partial x_j}\left(\tau_{ij}^{n-0}\right)}^n \tag{4.74}$$

the pressure and diffusive terms exactly preserve the Galilean invariance:

$$\bar{p}^n\delta_{ij} + \tilde{\Sigma}_{ij}^n = \underbrace{\bar{p}^{n*}\delta_{ij} + \tilde{\Sigma}_{ij}^{n*}}_{\text{TE}} \tag{4.75}$$

In contrast, the remaining terms do not. For the time derivative term the following transformation is obtained[26]:

$$\begin{aligned}\frac{\partial\left(\bar{\rho}^n\tilde{u}_i^n\right)}{\partial t} =& \overline{\frac{\partial\left(\rho^*u_i^* + \rho^*c_i\right)}{\partial t}}^n = \overline{\frac{\partial\left(\rho^*u_i^* + \rho^*c_i\right)}{\partial t^*}}^{n*} - c_j\overline{\frac{\partial\left(\rho^*u_i^* + \rho^*c_i\right)}{\partial x_j^*}}^{n*} \\ =& \underbrace{\frac{\partial\left(\bar{\rho}^{n*}\tilde{u}_i^{n*}\right)}{\partial t^*}}_{\text{TE}} - \underbrace{c_j\overline{\frac{\partial\left(\rho^*u_i^*\right)}{\partial x_j^*}}^{n*}}_{\text{VI}} + c_i\left[\underbrace{\overline{\frac{\partial\rho^*}{\partial t^*}}^{n*}}_{\text{IV}} - \underbrace{\overline{\frac{\partial\left(\rho^*c_j\right)}{\partial x_j^*}}^{n*}}_{\text{II}}\right]\end{aligned} \tag{4.76}$$

While the convective term gives:

$$\bar{\rho}^n\tilde{u}_i^n\tilde{u}_j^n = \underbrace{\bar{\rho}^{n*}\tilde{u}_i^{n*}\tilde{u}_j^{n*}}_{\text{TE}} + \underbrace{c_ic_j\bar{\rho}^{n*}}_{\text{I}} + \bar{\rho}^{n*}\left(\underbrace{c_i\tilde{u}_j^{n*}}_{\text{III}} + \underbrace{c_j\tilde{u}_i^{n*}}_{\text{V}}\right) \tag{4.77}$$

Finally, the SGS term becomes[27]:

$$\begin{aligned}\tau_{ij}^{n-0} = \underbrace{\tau_{ij}^{n-0*}}_{\text{TE}} &+ c_ic_j\left(\underbrace{\bar{\rho}^{n*}}_{\text{I}} - \underbrace{\rho^*}_{\text{II}}\right) + c_i\left(\underbrace{\bar{\rho}^{n*}\tilde{u}_j^{n*}}_{\text{III}} - \underbrace{\rho^*u_j^*}_{\text{IV}}\right) \\ &+ c_j\left(\underbrace{\bar{\rho}^{n*}\tilde{u}_i^{n*}}_{\text{V}} - \underbrace{\rho^*u_i^*}_{\text{VI}}\right)\end{aligned} \tag{4.78}$$

[26] Notice that in equation (4.76) the G^i operators are applied after the transformation. This is exactly the same procedure used in obtaining the transformations (4.72) from those in (4.71).

[27] Again, pressure and viscous terms give no spurious contributions.

Thus, by comparison of terms with similar symbols (I-VI), one can readily observe that, after the application of the operators G^i, spurious terms cancel each other and the remaining terms (TE) return the transformed equation in the moving reference frame, which is identical to the one in the fixed frame. In particular, it is evident that, like for the pure NSE and the IFCLES approach[28], the single terms (4.76-4.78) are not Galilean invariant. However, differently from the pure NSE and from the IFCLES approach, here the SGS term is necessary in order to recover the overall Galilean invariance.

One might argue that, by definition, SGS terms should not depend on the largest resolved scales and, as a consequence, that Galilean invariance should be invoked for them. However, this interaction just reflects the non-linearity of the governing equations, which is a true physical phenomenon. The conclusion to be drawn is that, in GLES, in order to preserve Galilean invariance of the equations, specific SGS models have to be used, which is not different from what is currently done in EFCLES (Singh et al., 2012). Finally, notice that this has implications which are far from trivial because, as shown in chapter 3, the GLES framework is representative of a large fraction of numerical methods, which indeed do not preserve the Galilean invariance property a priori.

Let us now turn the attention to the specific scale-similar SGS model developed in this thesis, to see if it actually recovers the Galilean invariance property. Assuming that the test filter in the model also preserves the Galilean invariance, a straightforward computation shows that:

$$\begin{aligned} C_{ss}\frac{\Delta_{n,0}^2}{\Delta_{m,n}^2}\tau_{ij}^{m-n} =& C_{ss}\frac{\Delta_{n,0}^2}{\Delta_{m,n}^2}\tau_{ij}^{m-n*} + C_{ss}\frac{\Delta_{n,0}^2}{\Delta_{m,n}^2}\left[c_i c_j\left(\bar{\rho}^{m*}-\bar{\rho}^{n*}\right)\right] \\ &+C_{ss}\frac{\Delta_{n,0}^2}{\Delta_{m,n}^2}\left[c_i\left(\bar{\rho}^{m*}\tilde{u}_j^{m*}-\bar{\rho}^{n*}\tilde{u}_j^{n*}\right)+c_j\left(\bar{\rho}^{m*}\tilde{u}_i^{m*}-\bar{\rho}^{n*}\tilde{u}_i^{n*}\right)\right] \end{aligned} \tag{4.79}$$

Thus, by comparison with analogous terms arising in equation (4.78), the following requirement arises, for both the momentum components and the density, in order to preserve the Galilean invariance of the equations:

$$\bar{\phi}^n-\phi = C_{ss}\frac{\Delta_{n,0}^2}{\Delta_{m,n}^2}\left(\bar{\phi}^m-\bar{\phi}^n\right) \tag{4.80}$$

In practice, if the hypotheses underlying the model are satisfied, this condition is met with a fourth order accuracy. This analysis also suggests an additional interpretation of the factor $\Delta_{n,0}^2/\Delta_{m,n}^2$ in the model, that is the factor required to preserve the Galilean invariance at the largest possible order with a test filter of the form (4.19).

[28]The usually suggested form of the equations in LES is the one used in the IFCLES approach, because they share the same invariance properties of the pure NSE.

CHAPTER 5

Numerical method

A fundamental property of the GLES approach is that it is straightly applicable to any numerical method, as explained in section 3.6. As a consequence, the use of the GLES framework in a specific solver simply requires, if any, the implementation of a specific SGS model. In particular, the solver adopted in the present thesis is the unstructured, cell-centered, FV code Fluent® 13.0 and the developments in chapter 4 exactly fit its structure. This chapter describes the numerical aspects of the solver and specific implementation details related to the proposed SGS model and LES in general. Section 5.1 provides a general description of the solver and the underlying FV discretization, with particular emphasis on the connection with the GLES framework. The specific numerical schemes and procedures used in this thesis are described in section 5.2, 5.3 and 5.4, respectively for the spatial discretization, the temporal advancement and the pressure-velocity coupling. The accuracy of the solver is assessed in section 5.5, both from a theoretical point of view, with a simplified 1D linear analysis, and a posteriori, by verification with analytical solutions. Finally, implementation details are discussed in section 5.6, both in relation to the specific SGS model proposed here and the remaining aspects relevant for LES in general. As mentioned in chapter 1, the whole presentation in the previous chapters is based, for the sake of generality, on a compressible formulation. However, all the verification and validation tests, in this and the following chapters, are based on strictly incompressible flows. As a consequence, the only aspects of the code which are presented in this chapter are those relevant for incompressible flows. Nonetheless, according to the presentation in section 4.4, implementation details for the proposed SGS model are given in their full generality.

5.1 Basic discretization

The CFD solver Fluent® is based on a cell-centered, co-located FV discretization of the governing equations (ANS, 2010; Mathur and Murthy, 1997; Kim et al., 1998). As already explained in sections 3.6.3 and 4.5.1, the method consists in partitioning the fluid domain of interest in a set of non overlapping finite volumes, or cells, and discretizing the integral form of the equations for each of the volumes with the resolved, dependent variables defined in the centroids of the volumes. Analogously to section 4.5.1, the overall discretization procedure can be better illustrated by considering a generic balance equation for a scalar ϕ, written in integral form for the arbitrary cell Ω_i[1]:

$$\frac{\partial}{\partial t}\frac{1}{V_i}\int_{\Omega_i}\rho\phi dx + \frac{1}{V_i}\int_{\Omega_i}\frac{\partial}{\partial x_j}\left(\rho u_j\phi - \Gamma\frac{\partial\phi}{\partial x_j}\right)d\Omega = \frac{1}{V_i}\int_{\Omega_i}S_\phi d\Omega \tag{5.1}$$

where V_i is the cell volume, Γ is a diffusion coefficient, ρ and ρu_j are the density of the fluid and the momentum which satisfy the continuity equation for the flow and S_ϕ is a generic source term. It should be now clear that this equation is affected by a closure problem because prescribes the evolution of the FV variable $\bar{\rho}\tilde{\phi}$:

$$\bar{\rho}_i\tilde{\phi}_i = \frac{1}{V_i}\int_{\Omega_i}\rho\phi d\Omega \tag{5.2}$$

in terms of local values of ϕ, u_j, ρ and Γ. However, for the present purposes this is not influential and a model for the missing scales, if any, is assumed to be embedded in S_ϕ. Thus, equation (5.1) can be conveniently rewritten as:

$$\frac{\partial\bar{\rho}_i\tilde{\phi}_i}{\partial t} + \frac{1}{V_i}\int_{\Omega_i}\frac{\partial}{\partial x_j}\left(\bar{\rho}\tilde{u}_j\tilde{\phi} - \Gamma\frac{\partial\tilde{\phi}}{\partial x_j}\right)d\Omega = \bar{S}_{\tilde{\phi}_i} \tag{5.3}$$

where the subscript for the source term S clearly evidences its dependence from the resolved variable $\tilde{\phi}_i$, in the sense that it can only be computed from the resolved variables. Also, for the sake of simplicity, the same symbol has been retained for Γ, but it is implicitly assumed that only its computable part is effectively retained. Before proceeding with the discretization, it should be again appreciated how equation (5.3) effectively has the form of a filtered equation, the filter being the top-hat one in (5.2). Moreover, exactly as in GLES, no commutation property is invoked for the filter, otherwise the differential form of the equations would be recovered. Instead, the actual discretization used in Fluent® (and any other FV code) employs the Green-Gauss theorem to transform the equation above in the exact equivalent form below:

$$\frac{\partial\bar{\rho}_i\tilde{\phi}_i}{\partial t} + \sum_f^{N_i^f}\frac{1}{V_i}\int_{S_f}n_j^f\left(\bar{\rho}\tilde{u}_j\tilde{\phi} - \Gamma\frac{\partial\tilde{\phi}}{\partial x_j}\right)dS_f = \bar{S}_{\tilde{\phi}_i} \tag{5.4}$$

[1]The topology and the volume of the cells are assumed to be constant in time.

where the volume integral has been reduced to a sum of surface integrals over the N_i^f faces S_f of the cell Ω_i, n_j^f being the outward unit normal of such faces. Here, again, the sampling problem due to the FV filter emerges, as resolved variables are known in the cell centers but their values are required on the faces of the cells in order to advance equation (5.4) in time. It is also worth noting that, differently from the simple 1D case analyzed in section 4.5.1, an additional approximation is required here because face values should also be integrated over the single faces, which is actually equivalent to explicitly perform the top-hat filtering. In Fluent® (and most second order FV codes), the filtering operation (i.e., the surface integral) is first approximated by the midpoint rule and then the interpolation is invoked to provide the point values of the variables in the face centroids. Hence, equation (5.4) is finally approximated as:

$$\frac{\partial \bar{\rho}_i \tilde{\phi}_i}{\partial t} + \sum_f^{N_i^f} \left(\bar{\rho} \tilde{u}_j \tilde{\phi} - \Gamma \frac{\partial \tilde{\phi}}{\partial x_j} \right)_f n_j^f \frac{A_f}{V_i} = \bar{S}_{\tilde{\phi}_i} \tag{5.5}$$

where the subscript f for the terms in parenthesis means that such terms have to be interpolated to the centroid of the face f, A_f is the area of the face and n_j^f now denotes the outward unit normal in the face centroid.

It is worth mentioning that softwares for the grid generation only provide information on the nodes of the grid and, for anything different from tetrahedral grids, the information on the cell volume and the face normals and areas is somehow arbitrary. In these cases (i.e., general polyhedral cells), each cell face is first split into triangular sub-faces and a unique normal per face is obtained, n_j^f, together with the face centroid f_j^c. Then this normal, which actually includes also the face area A_f, is used in the integrals in (5.5) and to compute the volume V_i itself as:

$$V_i = \frac{1}{3} \sum_f^{N_f} n_j^f f_j^c A_f \tag{5.6}$$

so that the overall consistency is guaranteed. The final closure for equation (5.5) is achieved by selecting a proper interpolation scheme for the cell variables and their gradients. However, notice that the density and mass fluxes trough the faces are themselves solution of a similar equation obtained by setting $\tilde{\phi} = 1$ in (5.5). Thus, the final form of the discretized equation is more conveniently rewritten as:

$$\frac{\partial \bar{\rho}_i \tilde{\phi}_i}{\partial t} + \sum_f^{N_i^f} \left[\bar{m}_j^f \tilde{\phi}_f - \left(\Gamma \frac{\partial \tilde{\phi}}{\partial x_j} \right)_f \right] n_j^f \frac{A_f}{V_i} = \bar{S}_{\tilde{\phi}_i} \tag{5.7}$$

where the mass flux per unit area $\bar{m}_j^f = (\bar{\rho} \tilde{u}_j)_f$ and the density $\bar{\rho}_i$ are assumed to be known and interpolation is only required for $\tilde{\phi}$ and its diffusive flux, both described in the following section.

5.2 Numerical schemes

Formally, the selection of a shape function is all that is actually needed in a FV method to close equation (5.7). However, while this is effectively done for node centered arrangements, this approach is far from being straightforward for the cell centered ones, especially for unstructured grids. Also, for historical reasons, such direct interpolation has been avoided because of the lack of continuity for the typical inviscid early applications of the method. As a consequence, the cell centered FV practice is instead based on the so called reconstruction, for which the convective face flux is first reconstructed within the two adjacent cells of a face and the overall flux is then devised as a solution of an exact or approximate Riemann problem (Toro, 2009)[2]. In practice, even for incompressible viscous flows, where the interpolation could certainly be invoked, the reconstruction approach remains the preferred one for the convective term. While for first order accuracy one could just rest on the cell values themselves, this is generally too low for most practical applications and gradients in the cell centers are used to improve the accuracy (Blazek, 2005).

In the following subsections, the gradient methods available in Fluent® and used in this thesis are first described. Then the methods used for the convective and diffusive flux computation, which are based on such gradients, are presented. For future reference, a typical arrangement of computational cells and relative variables is reported in Figure 5.1. Notice that, unless otherwise stated, all the higher order terms involving the precomputed gradients are treated by the solver explicitly, with a deferred correction approach (Khosla and Rubin, 1974), and updated with a specific iterative cycle[3].

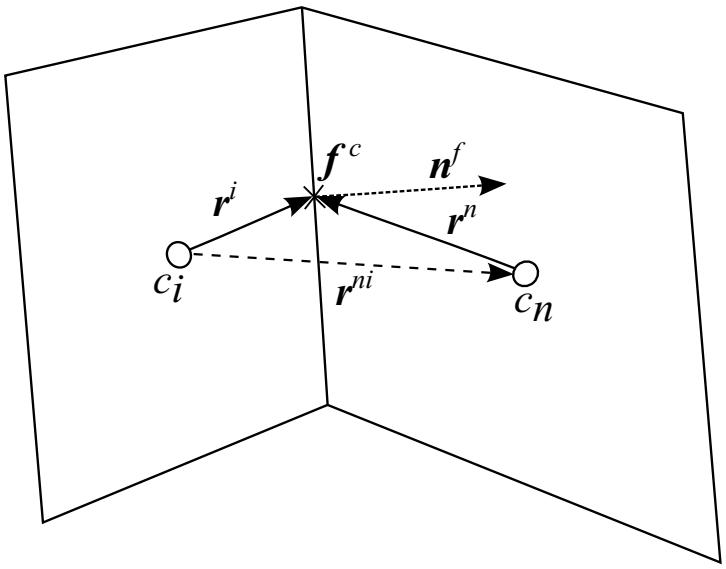

Figure 5.1: *Typical arrangement of computational cells sharing a face in a cell centered FV framework.*

[2]Notice, indeed, that the weighted residual method, on which the FV one is based, does not give a prescription for the interpolation stencil, which can be quite arbitrary and include upwind cells only.

[3]This cycle, which in some codes is also referred to as non-orthogonal correction, is intermediate between the classical inner and outer iterations.

5.2.1 Gradient computation

Two classes of gradient computation methods are available in the solver. The first one is based on the Green-Gauss theorem (Kim et al., 2003; Barth and Jespersen, 1989):

$$\int_{\Omega_i} \frac{\partial \tilde{\phi}}{\partial x_j} d\Omega = \sum_f^{N_i^f} \int_{S_f} n_j^f \tilde{\phi} dS_f \tag{5.8}$$

which is then discretized according to the same procedure described in the previous section, leading to the following value for the cell c_i:

$$\left.\overline{\frac{\partial \tilde{\phi}}{\partial x_j}}\right|_{c_i} = \sum_f^{N_i^f} \tilde{\phi}_f n_j^f \frac{A_f}{V_i} \tag{5.9}$$

Notice, in particular, how the approximation is formally resulting in a filtered gradient instead of the pure gradient[4]. The face centroid values $\tilde{\phi}_f$ required in (5.9) can be computed with alternative methods. In the present thesis the selected option is based on a simple average among the cells sharing the face f[5]:

$$\tilde{\phi}_f = \frac{\tilde{\phi}_i + \tilde{\phi}_n}{2} \tag{5.10}$$

where, for the given face f, $\tilde{\phi}_i$ and $\tilde{\phi}_n$ represent, respectively, the value of $\tilde{\phi}$ in the given cell c_i and the neighbor one c_n (see Figure 5.1). A variant of this scheme has also been considered, for the terms in the SGS model, and implemented trough a separate routine. In this case the face values are computed as a weighted volume average:

$$\tilde{\phi}_f = \frac{V_n \tilde{\phi}_i + V_i \tilde{\phi}_n}{V_i + V_n} \tag{5.11}$$

The second available option for the gradient is based on a least squares linear reconstruction of the variable $\tilde{\phi}$ (Barth, 1991). In practice, for every cell c_n surrounding the cell c_i, the following identity is assumed to be valid:

$$\tilde{\phi}_n = \tilde{\phi}_i + \left.\frac{\partial \tilde{\phi}}{\partial x_j}\right|_{c_i} r_j^{ni} \tag{5.12}$$

This yields an overdetermined system of N_i^f equations in three unknowns (i.e., the gradient components) whose coefficient matrix is purely a function of the geometry.

[4] Nonetheless, this is usually neglected in second order codes.

[5] The alternative more accurate option, which is based on a node based average from the vertexes of the face, is not used here for several reasons. The most important one is that it is unable to properly handle the doubly periodic boundary condition used here in several test cases. Also, it has limitations for general polyhedral cells and incurs in higher computational costs.

The least-squares solution of the system is based on a Gram-Schmidt orthogonalization of the coefficient matrix which can be expressed in closed form and stored in advance (Blazek, 2005), hence the overall solution cost amounts to the computation of a matrix-vector product and is comparable to the cost of the Green-Gauss method above. For this reason, and because of its better accuracy for general unstructured grids, the least-squares method is chosen as default gradient computation method in this thesis. However, is worth noting that, for fully structured uniform grids, all the methods above reduce to a classical central scheme (e.g., see equation (4.39)).

5.2.2 Convective flux

Among the several available options for the convective flux, three of them are presented here, as they are the only suitable ones for LES[6]. The default option in this thesis is the second order central scheme originally introduced by Batten et al. (1996):

$$\tilde{\phi}_f = \frac{1}{2}\left[\left(\tilde{\phi}_i + \left.\frac{\partial\tilde{\phi}}{\partial x_j}\right|_{c_i} r_j^i\right) + \left(\tilde{\phi}_n + \left.\frac{\partial\tilde{\phi}}{\partial x_j}\right|_{c_n} r_j^n\right)\right] \tag{5.13}$$

which is an obvious extension of the scheme (4.38) with $\gamma = 1$. The computational stencil of the scheme is symmetric and independent from the velocity field thus, for uniform Cartesian meshes, it is non-diffusive and well suited for LES. The scheme has indeed been used in LES by Park and Mahesh (2007b) and found especially suitable when the gradient method (5.9-5.10) is used. However, as any other linear higher order scheme, it is non-monotone and, for general grids, can alter the energy content of the flow. For this reason, two additional options are also considered. The first one is a simpler, first order accurate, central scheme:

$$\tilde{\phi}_f = \frac{\tilde{\phi}_i + \tilde{\phi}_n}{2} \tag{5.14}$$

which is obtained by deactivating the higher order terms in (5.13) and is the equivalent of the scheme (4.38) with $\gamma = 0$. Despite the low formal accuracy[7], this scheme has the merit to not alter the energy content of the flow, as the true convective term, independently from the grid (Verstappen and Veldman, 1998; Benhamadouche et al., 2002; Verstappen and Veldman, 2003; Mahesh et al., 2004; Felten and Lund, 2006; Verstappen and Van Der Velde, 2006; Verstappen, 2008). This scheme has also been used, by Rossi (2009), for the DNS of scalar transport in Fluent®, confirming its suitability for scale resolving simulations on general unstructured grids.

The second option is still based on the scheme (5.13), but modified according to a Convection Boundedness Criterion (CBC) and the Normalized Variable Diagram (NVD) (Gaskell and Lau, 1988; Leonard, 1988, 1991), both formulated in a general unstructured framework (Jasak et al., 1999). In practice, the scheme involves the following steps:

[6]The scale separation which is assumed to hold in LES is such that the energy content of the flow, even at the grid cut-off scale, is not formally negligible. As such, numerical schemes used in LES need to avoid any artificial viscosity in order to alter the resolved scales as little as possible.

[7]Which, again, has only a limited importance in LES.

- The parameters α_f and γ_f are first computed:

$$\alpha_f = 1 - \frac{S_m\left(\tilde{\phi}_n - \tilde{\phi}_i\right)}{2\left[\left(\frac{1+S_m}{2}\right)\frac{\partial\tilde{\phi}}{\partial x_j}\Big|_{c_i} + \left(\frac{S_m-1}{2}\right)\frac{\partial\tilde{\phi}}{\partial x_j}\Big|_{c_n}\right] r_j^{ni}}$$
$$\gamma_f = \frac{\alpha_f}{\beta_m} \tag{5.15}$$

  with $\beta_m = 1/10$ and $S_m = \mathrm{sign}(\bar{m}_j^f n_j^f)$.

- The face value $\tilde{\phi}_f$ is then determined as follows:

$$\tilde{\phi}_f = \begin{cases} \text{UD (5.17)} & \text{for} \quad \alpha_f \leq 0 \quad \text{or} \quad \alpha_f \geq 1 \\ \text{BLEND (5.18)} & \text{for} \quad \alpha_f > 0 \quad \text{and} \quad \alpha_f < \beta_m \\ \text{CENTRAL (5.13)} & \text{for} \quad \alpha_f \geq \beta_m \quad \text{and} \quad \alpha_f < 1 \end{cases} \tag{5.16}$$

  where CENTRAL denotes the default central scheme in (5.13), UD is the first order upwind scheme:

$$\tilde{\phi}_f = \left(\frac{1+S_m}{2}\right)\tilde{\phi}_i + \left(\frac{1-S_m}{2}\right)\tilde{\phi}_n \tag{5.17}$$

  and BLEND denotes a blending between the central scheme and a second order upwind scheme:

$$\begin{aligned} \tilde{\phi}_f = &(1-\gamma_f)\left[\left(\frac{1+S_m}{2}\right)\left(\tilde{\phi}_i + \frac{\partial\tilde{\phi}}{\partial x_j}\Big|_{c_i} r_j^i\right)\right] \\ &+ (1-\gamma_f)\left[\left(\frac{1-S_m}{2}\right)\left(\tilde{\phi}_n + \frac{\partial\tilde{\phi}}{\partial x_j}\Big|_{c_n} r_j^n\right)\right] \\ &+ \frac{\gamma_f}{2}\left[\left(\tilde{\phi}_i + \frac{\partial\tilde{\phi}}{\partial x_j}\Big|_{c_i} r_j^i\right) + \left(\tilde{\phi}_n + \frac{\partial\tilde{\phi}}{\partial x_j}\Big|_{c_n} r_j^n\right)\right] \end{aligned} \tag{5.18}$$

For reference, its representation in the NVD is reported in Figure 5.2 in terms of the normalized variable $\tilde{\phi}_f^+$:

$$\tilde{\phi}_f^+ = 1 - \frac{\left[\left(\frac{1-S_m}{2}\right)\tilde{\phi}_i + \left(\frac{1+S_m}{2}\right)\tilde{\phi}_n\right] - \tilde{\phi}_f}{2\left[\left(\frac{1+S_m}{2}\right)\frac{\partial\tilde{\phi}}{\partial x_j}\Big|_{c_i} + \left(\frac{S_m-1}{2}\right)\frac{\partial\tilde{\phi}}{\partial x_j}\Big|_{c_n}\right] r_j^{ni}} \tag{5.19}$$

For obvious reasons, this scheme will be referred to as Bounded Central Scheme. A similar scheme has been used by Grinstein et al. (2005) and found suitable for ILES when coupled with proper wall boundary conditions. As such, it is considered in the present thesis as a reference for the ILES approach, which is still completely justified within the GLES framework.

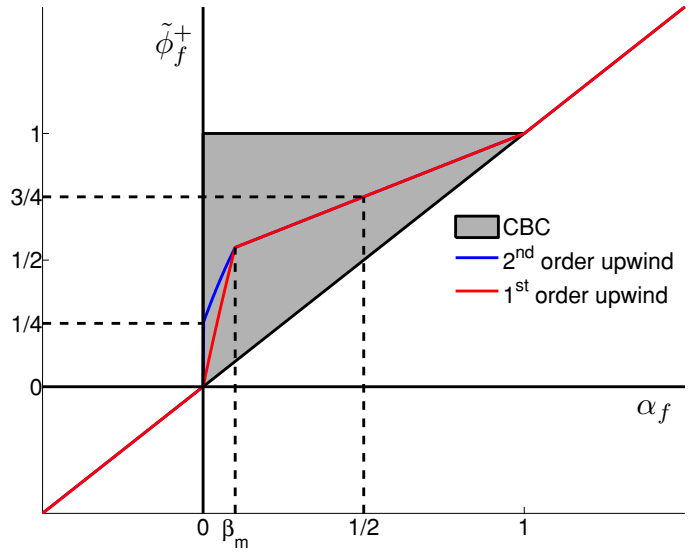

Figure 5.2: *Bounded central scheme in the NVD. Effect of the blending: second order upwind* (5.18) *vs. first order upwind (Jasak et al., 1999).*

5.2.3 Diffusive flux

As most of the unstructured FV solvers, Fluent® adopts a second order central scheme for the discretization of the diffusive flux (Mathur and Murthy, 1997; Kim et al., 1998). First, the face normal derivative is computed as:

$$n_j^f \left(\frac{\partial\tilde{\phi}}{\partial x_j}\right)_f = \left[\left(\frac{\tilde{\phi}_n - \tilde{\phi}_i}{ds^{ni}}\right)\frac{1}{n_k^f e_k^{ni}} + \left\langle\frac{\partial\tilde{\phi}}{\partial x_j}\right\rangle_f \left(n_j^f - \frac{e_j^{ni}}{n_k^f e_k^{ni}}\right)\right] \tag{5.20}$$

where:

$$\begin{aligned} ds^{ni} &= \sqrt{r_j^{ni} r_j^{ni}} \\ e_j^{ni} &= \frac{r_j^{ni}}{ds^{ni}} \\ \left\langle\frac{\partial\tilde{\phi}}{\partial x_j}\right\rangle_f &= \frac{1}{2}\left(\left.\frac{\partial\tilde{\phi}}{\partial x_j}\right|_{c_i} + \left.\frac{\partial\tilde{\phi}}{\partial x_j}\right|_{c_n}\right) \end{aligned} \tag{5.21}$$

Then the overall diffusive flux is computed as:

$$n_j^f \left(\Gamma\frac{\partial\tilde{\phi}}{\partial x_j}\right)_f = \Gamma_f n_j^f \left(\frac{\partial\tilde{\phi}}{\partial x_j}\right)_f = \frac{2\Gamma_{c_i}\Gamma_{c_n}}{\Gamma_{c_i}+\Gamma_{c_n}} n_j^f \left(\frac{\partial\tilde{\phi}}{\partial x_j}\right)_f \tag{5.22}$$

The specific choice in (5.20) avoids the checkerboard effect, caused by the exclusive use of the cell centered gradients in (5.21), and recovers the classical finite difference

approximation for the Laplacian (4.59) on uniform Cartesian meshes. In particular, among the different possible decompositions of the diffusion term (Moukalled and Darwish, 2006; Jasak, 1996), the one adopted in the code is known as over-relaxed approach and privileges the finite difference part for increasing non-orthogonality of the mesh.

5.2.4 Boundary conditions

Dirichlet or Neumann boundary conditions are treated in Fluent® as in any other code, by direct inclusion of the respective convective or diffusive flux. A particular attention is instead required for the mixed terms, i.e., convective fluxes for Neumann boundaries and diffusive fluxes for Dirichlet ones. The first case is representative of outflow boundaries, where the diffusive flux normal to the boundary is assumed null. In this case the face value for the transported variable is simply extrapolated from the interior with a first order upwind, while the overall mass flux trough the boundary is assumed constant and such that the continuity equation is satisfied.

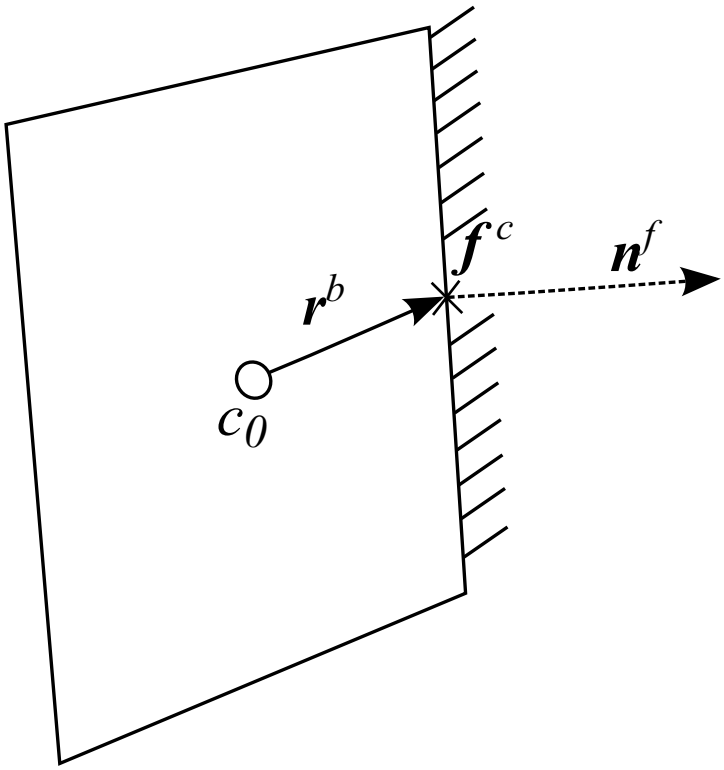

Figure 5.3: *Typical arrangement of a near-wall computational cell.*

The second case is instead more interesting as representative of walls. In the general case equation (5.20) is used directly (Mathur and Murthy, 1997) (see Figure 5.3):

$$n_j^f \Gamma_f \left(\frac{\partial \tilde{\phi}}{\partial x_j} \right)_f = \Gamma_b \left[\left(\frac{\tilde{\phi}_b - \tilde{\phi}_0}{ds^b} \right) \frac{1}{n_k^f e_k^b} + \left. \frac{\partial \tilde{\phi}}{\partial x_j} \right|_{c_0} \left(n_j^f - \frac{e_j^b}{n_k^f e_k^b} \right) \right] \tag{5.23}$$

with $\tilde{\phi}_b$ the specified Dirichlet value, Γ_b the diffusion coefficient at the boundary and

all the remaining terms simply following from their definitions in (5.21). However, it is worth highlighting that this is just a first order approximation for the diffusive flux at the boundary. Indeed, for a fully Cartesian grid, denoting by y the normal to the boundary coordinate entering the domain, equation (5.23) reduces to:

$$\Gamma_b \left(\frac{\tilde{\phi}_b - \tilde{\phi}_0}{ds^b} \right) \approx -\Gamma_b \left(\frac{\partial \tilde{\phi}}{\partial y} \right)_b - \Gamma_b \frac{ds^b}{2} \left(\frac{\partial^2 \tilde{\phi}}{\partial y^2} \right)_b + O\left[\left(ds^b \right)^2 \right] \tag{5.24}$$

While possibly negligible in most of the cases, this error might become problematic for wall boundaries in wall driven turbulent flows. Indeed, the instantaneous resolved profiles in LES are not expected to be linear in the near-wall region and the overall interaction between turbulence production at the walls and the mean flow might be impaired by the error at the wall. However, besides the numerical accuracy, the wall boundary condition in LES is important in itself. Indeed, as already mentioned in chapter 1, wall bounded flows have resolution requirements which are strictly dependent on the Reynolds number and, for sufficiently high values, become practically intractable in LES. Among the several available options, the approximate wall boundary condition used here for these cases is based on a simple wall function approach. In practice, instead of directly using equation (5.23), the wall shear stress τ_w in the momentum equations is approximated trough a blending of two terms according to Kader (1981):

$$\tilde{u}^+_{c_0} = e^B y^+ + e^{\frac{1}{B}} \frac{1}{k} \ln(E y^+) \tag{5.25}$$

where $k = 0.4187$ is the von Kármán constant used in the code, $E = 9.793$ and:

$$\tilde{u}^+_{c_0} = \frac{\tilde{u}^p_{c_0}}{\sqrt{\tau_w / \bar{\rho}}} \qquad y^+ = \frac{\bar{\rho} y \sqrt{\tau_w / \bar{\rho}}}{\mu} \qquad B = -\frac{a \left(y^+ \right)^4}{1 + b y^+} \tag{5.26}$$

with $\tilde{u}^p_{c_0}$ the wall parallel velocity in the cell adjacent to the wall, y the distance between the cell center c_0 and the wall, μ the dynamic viscosity of the fluid, $a = 0.01$ and $b = 5$. Thus, due to the non-linearity and implicitness of relation (5.25), it is used iteratively. Notice, also, that this wall-function is always active in Fluent® and recovers the linear approach in (5.23) only for well resolved boundary layers (i.e., $y^+_{c_0} < 5$). For reference, the velocity profile (5.25) is compared in Figure 5.4 with the Reichardt's wall law (Reichardt, 1951):

$$\tilde{u}^+_{c_0} = \frac{1}{k} \ln(1 + k y^+) + 7.8 \left[1 - \exp(-\frac{y^+}{11}) - \frac{y^+}{11} \exp(-\frac{y^+}{3}) \right] \tag{5.27}$$

5.3 Temporal discretization

The numerical schemes introduced in the previous section allow to rewrite the sum in equation (5.7) as a linear combination of the value $\tilde{\phi}_i$ in the integration cell c_i and those

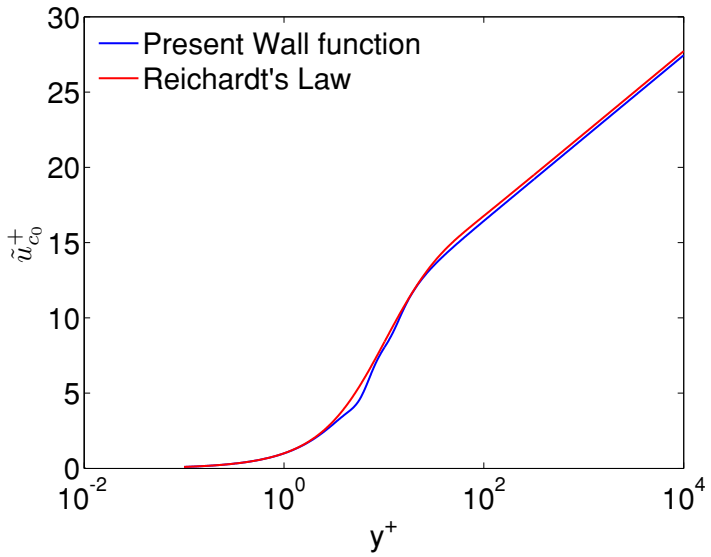

Figure 5.4: *Comparison of the wall function in Fluent® versus the Reichardt's velocity profile.*

in the neighboring cells c_n involved in the discretization of the convective and diffusive terms, $\tilde{\phi}_n$. The final step to obtain a computable model for the full equation is the discretization of the time derivative term. As for the spatial terms, LES requires a high order accuracy also for the time discretization and, for incompressible flows, the only feasible option in Fluent® is a second order backward scheme. Developed by Gear (1971) for stiff ordinary differential equations, it is the most accurate A-stable linear multi-step method which also completely dumps the highest frequencies (i.e., it is L-stable) and includes the full positive imaginary axis in its stability region. It is based on the following Taylor series expansions:

$$\begin{aligned}
\tilde{\phi}_i^m &= \tilde{\phi}_i^{m+1} - \Delta t \frac{\partial \tilde{\phi}}{\partial t}\bigg|_{c_i}^{m+1} + \frac{\Delta t^2}{2}\frac{\partial^2 \tilde{\phi}}{\partial t^2}\bigg|_{c_i}^{m+1} - \frac{\Delta t^3}{6}\frac{\partial^3 \tilde{\phi}}{\partial t^3}\bigg|_{c_i}^{m+1} + O\left(\Delta t^4\right) \\
\tilde{\phi}_i^{m-1} &= \tilde{\phi}_i^{m+1} - 2\Delta t \frac{\partial \tilde{\phi}}{\partial t}\bigg|_{c_i}^{m+1} + 2\Delta t^2\frac{\partial^2 \tilde{\phi}}{\partial t^2}\bigg|_{c_i}^{m+1} - \frac{8\Delta t^3}{6}\frac{\partial^3 \tilde{\phi}}{\partial t^3}\bigg|_{c_i}^{m+1} + O\left(\Delta t^4\right)
\end{aligned} \tag{5.28}$$

where Δt is the time step used in the computation and the superscripts are used here to momentarily denote the time levels $t^{m-1} = (m-1)\Delta t$, $t^m = m\Delta t$ and $t^{m+1} = (m+1)\Delta t$. Hence, for given values $\tilde{\phi}_i^m$ and $\tilde{\phi}_i^{m-1}$, at the current and previous time steps respectively, the time derivative at the next time level is discretized as:

$$\frac{3\tilde{\phi}_i^{m+1} - 4\tilde{\phi}_i^m + \tilde{\phi}_i^{m-1}}{2\Delta t} = \frac{\partial \tilde{\phi}}{\partial t}\bigg|_{c_i}^{m+1} - \frac{\Delta t^2}{3}\frac{\partial^3 \tilde{\phi}}{\partial t^3}\bigg|_{c_i}^{m+1} + O\left(\Delta t^3\right) \tag{5.29}$$

and, in its fully discretized form, equation (5.7) becomes:

$$\frac{3\bar{\rho}_i^{m+1}\tilde{\phi}_i^{m+1} - 4\bar{\rho}_i^{m}\tilde{\phi}_i^{m} + \bar{\rho}_i^{m-1}\tilde{\phi}_i^{m-1}}{2\Delta t} + \sum_f^{N_i^f}\left[\bar{m}_j^f\tilde{\phi}_f - \left(\Gamma\frac{\partial\tilde{\phi}}{\partial x_j}\right)_f\right] n_j^f\frac{A_f}{V_i} = \bar{S}_{\tilde{\phi}_i} \quad (5.30)$$

When the discretization methods described in the previous sections are then introduced, the equation above can be finally expressed as:

$$\underbrace{\left(\frac{3\bar{\rho}_i^{m+1}}{2\Delta t} + a_0\right)}_{a_i}\tilde{\phi}_i^{m+1} + \sum_n a_n\tilde{\phi}_n^{m+1} = \overbrace{\sum_n b_n\tilde{\phi}_n^{m+k}}^{b_i^{m+k}} + \underbrace{\frac{4\bar{\rho}_i^{m}\tilde{\phi}_i^{m} - \bar{\rho}_i^{m-1}\tilde{\phi}_i^{m-1}}{2\Delta t} + \bar{S}^*_{\tilde{\phi}_i}}_{b_i^m} \quad (5.31)$$

In particular, it should be noted that the present temporal discretization assumes a fully implicit treatment of all the terms. As a consequence, the spatial discretization terms have been split in a linear low order part treated implicitly and a possibly nonlinear part, containing higher order terms, which is treated with the deferred correction approach within sub-iterations with index k. The same treatment, if possible, is also used for the source term $\bar{S}_{\tilde{\phi}_i}$, which is split as follows:

$$\begin{aligned}\bar{S}^{m+1}_{\tilde{\phi}_i} =& \bar{S}^m_{\tilde{\phi}_i} + \left.\frac{\partial\bar{S}_{\tilde{\phi}_i}}{\partial\tilde{\phi}_i}\right|_{c_i}^m\left(\tilde{\phi}_i^{m+1} - \tilde{\phi}_i^m\right) = \left(\bar{S}^m_{\tilde{\phi}_i} - \tilde{\phi}_i^m\left.\frac{\partial\bar{S}_{\tilde{\phi}_i}}{\partial\tilde{\phi}_i}\right|_{c_i}^m\right) + \left.\frac{\partial\bar{S}_{\tilde{\phi}_i}}{\partial\tilde{\phi}_i}\right|_{c_i}^m\tilde{\phi}_i^{m+1} \\ =& \bar{S}^*_{\tilde{\phi}_i} + C\tilde{\phi}_i^{m+1}\end{aligned} \quad (5.32)$$

Thus, the coefficients a_0, a_n and b_n in (5.31) absorb all the relevant terms according to the specific discretization, including the mass flux per unit area $\bar{m}_j^f$. The final step for the time advancement of equation (5.30) is the resolution of the overall linear algebraic system:

$$a_i\tilde{\phi}_i^{m+1} + \sum_n a_n\tilde{\phi}_n^{m+1} = b_i^{m+k} + b_i^m = b_i \quad (5.33)$$

which in Fluent® is performed by a Gauss-Seidel point iteration method with an algebraic multigrid acceleration technique.

5.4 Pressure-velocity coupling

The discussion so far regarded the template linear equation (5.1). When the same reasoning is applied to the momentum and continuity equations for incompressible flows, the matter is complicated by three main factors: the equations are nonlinear and coupled, the lack of an independent equation for the pressure and the need to satisfy the

continuity constraint. Indeed, for the incompressible flows considered in this thesis, the governing equations reduce to:

$$\begin{aligned}
&\sum_{f}^{N_i^f} \bar{m}_j^f n_j^f \frac{A_f}{V_i} = \bar{S}_{\bar{\rho}} \\
&\frac{\partial \bar{\rho}\tilde{u}_i}{\partial t} + \sum_{f}^{N_i^f} \left(\bar{m}_j^f \tilde{u}_i^f + \bar{p}_f \delta_{ij} + \tilde{\Sigma}_{ij}^f \right) n_j^f \frac{A_f}{V_i} = \bar{S}_{\tilde{u}_i} \\
&\frac{\partial \bar{\rho} C_p \tilde{T}}{\partial t} + \sum_{f}^{N_i^f} \left[\bar{m}_j^f C_p \tilde{T}_f - \left(\tilde{\lambda} \frac{\partial \tilde{T}}{\partial x_j} \right)_f \right] n_j^f \frac{A_f}{V_i} = \bar{S}_{\tilde{T}}
\end{aligned} \tag{5.34}$$

where $\tilde{\Sigma}_{ij}$ is defined in (3.10) and, for clarity of notation, both $\tilde{\Sigma}_{ij}$ and $\tilde{u}_i$ now have f as superscript, but it still refers to their interpolated face values. Also, the source terms on the right hand sides in (5.34) possibly contain SGS models in addition to any explicit additional source. Coupling and non linearity among the momentum equations are due to the presence of the mass flux per unit area $\bar{m}_j^f$ and are both handled by sub-iterations, as for the deferred correction terms, hence no particular difficulty is actually introduced. However, an explicit connection between the pressure, the energy equation and the density/mass conservation is now missing and a particular attention is required to treat the equations above.

Indeed, any fluid velocity field is actually compressible to some degree and, whatever is the Mach number or the heat transfer mechanism acting on it, it is still governed by the fully compressible NSE if the continuum hypothesis holds. However, in the limit of a small Mach number in nearly isothermal cases, the flow equations become stiff, in the sense that the flow adapts to disturbances within times which are very small compared to the convective time (which leads to the approximation of a null Mach number). While, in this limit, the continuous equations remain the same, they become numerically intractable as the discretization would require a tremendous increase in the computational cost to correctly describe all the time scales present in the simulation, the most of which are not of interest. Hence, in order to overcome this difficulty, the most common approach consists in adopting a simplified version of the equations, in which the disturbance adaption time scales have been filtered out, that is the fully incompressible NSE above (i.e., their GLES counterpart), with the temperature treated as a simply transported (i.e., uncoupled) scalar. This step, while resolving the previous issue, essentially changes the nature of the equations in the two aspects mentioned above: the original conservation equation for the mass becomes a kinematic constraint on the velocity field and the pressure loses its thermodynamic role, as the link with the energy and mass equations is definitively lost due to the limit process. Moreover, an independent equation for the pressure seems lacking.

The above issues are solved by first noting that, in fact, a pressure equation can be derived and, for the GLES framework, it corresponds to equation (4.62). Then, it can be also shown that, in the new set of equations (5.34), the pressure and the continuity constraint are still linked, as the pressure now plays the role of a Lagrange multiplier,

which is used to enforce the continuity constraint on the velocity field (Ferziger and Perić, 2002).

Among the several methods available in Fluent® to deal with the aforementioned pressure-velocity coupling issues, the one adopted in this thesis is the fractional step method (FSM). The overall approach has been originally developed by Chorin (1968) and is a two step method in which a provisional pressure field is used to advance in time the momentum equations[8]. The new velocity field, which does not satisfy the continuity constraint, is then corrected with a pressure gradient term, computed after the resolution of a Poisson-like equation for the pressure. Besides the theoretical basis over which the method is built (Chorin and Marsden, 1997; Denaro, 2003), what greatly differs with respect to more common methods (e.g., SIMPLE) is that the outer iterations required to drive to zero the splitting error committed in fractioning the problem are unnecessary, because in the FSM this error is made commensurate to the time integration error.

The specific method used in Fluent® (Kim and Makarov, 2005) is based on an approximate LU factorization of the system of discretized momentum and continuity equations (5.34) (Quarteroni et al., 2000), originally introduced by Dukowicz and Dvinsky (1992) and subsequently reinterpreted by Perot (1993), but modified according to van Kan (1986) in order to preserve the second order accuracy (see also Guermond et al. (2006) for a detailed discussion on the issues concerning the pressure accuracy and the boundary conditions).

The basis of the method is best presented by expressing the momentum and the continuity equations[9] in (5.34) in the following matrix form, which is equivalent to the form in equation (5.33):

$$\begin{aligned} \underbrace{\left(\frac{1}{\Delta t}\mathbf{M}+\mathbf{B}\right)}_{\mathbf{A}}\mathbf{U}^{n+1}+\mathbf{G}\mathbf{p}^{n+1} &= \mathbf{r} \\ \mathbf{D}\mathbf{U}^{n+1} &= \mathbf{s} \end{aligned} \tag{5.35}$$

In particular, the vectors $\mathbf{U}^{n+1}$ and $\mathbf{p}^{n+1}$ represent the fully discrete, cell-centered, velocity and pressure solutions at the time level $n+1$. The matrix $\mathbf{A}$ represents the discrete operators, which are split in a diagonal mass matrix $\mathbf{M}$ relative to the time discretization and a non diagonal matrix $\mathbf{B}$ representing the spatial discretization of both convection and diffusion. The matrices $\mathbf{G}$ and $\mathbf{D}$ denote, respectively, the discrete gradient and divergence operators and, finally, the vectors $\mathbf{r}$ and $\mathbf{s}$ contain all the explicit contributions, including any possible source term or SGS model. Notice, also, that the density is assumed to be known, but not necessarily constant, and absorbed in the discretization operators. The equations (5.35) can be conveniently put in a block-matrix form including the boundary conditions, represented as an additional vector:

$$\begin{bmatrix}\mathbf{A} & \mathbf{G}\\ \mathbf{D} & \mathbf{0}\end{bmatrix}\begin{bmatrix}\mathbf{U}^{n+1}\\ \mathbf{p}^{n+1}\end{bmatrix}=\begin{bmatrix}\mathbf{r}\\ \mathbf{s}\end{bmatrix}+\begin{bmatrix}\mathbf{b}_m\\ \mathbf{b}_c\end{bmatrix} \tag{5.36}$$

[8] Different versions of the method exist, according to the way such provisional pressure field is defined.

[9] From now on the temperature is considered as a simple transported scalar whose discretization simply follows the techniques described in the previous section.

with the original discrete operators suitably modified according to the specific boundary conditions adopted. The FSM implemented in Fluent consists in an approximate LU factorization of the system (5.36). To this end, the equations are first factorized exactly:

$$\begin{bmatrix} \mathbf{A} & \mathbf{0} \\ \mathbf{D} & -\mathbf{D}\mathbf{A}^{-1}\mathbf{G} \end{bmatrix} \begin{bmatrix} \mathbf{I} & \mathbf{A}^{-1}\mathbf{G} \\ \mathbf{0} & \mathbf{I} \end{bmatrix} \begin{bmatrix} \mathbf{U}^{n+1} \\ \delta\mathbf{p} \end{bmatrix} = \begin{bmatrix} \mathbf{r} - \mathbf{G}\mathbf{p}^n \\ \mathbf{s} \end{bmatrix} + \begin{bmatrix} \mathbf{b}_m \\ \mathbf{b}_c \end{bmatrix} \tag{5.37}$$

with the pressure split in a known term from the previous time step, $\mathbf{p}^n$, and an unknown correction $\delta\mathbf{p} = \mathbf{p}^{n+1} - \mathbf{p}^n$, according to van Kan (1986). Then, the two following approximations are adopted:

$$\begin{aligned} \mathbf{A}^{-1} \approx& \Delta t \mathbf{M}^{-1} \\ \mathbf{D}\mathbf{A}^{-1}\mathbf{G} \approx& \Delta t \mathbf{D}\mathbf{M}^{-1}\mathbf{G}_s \end{aligned} \tag{5.38}$$

In particular, the first one is required in order to avoid the full inversion of $\mathbf{A}$ at each time step. As will be better clarified in the following, the second approximation represents, instead, the classical Rhie-Chow approach (Rhie, 1982; Rhie and Chow, 1983), with the original gradient operator $\mathbf{G}$ appearing in the momentum equations replaced with the operator $\mathbf{G}_s$. By further substitution of the approximations (5.38) in the equations (5.37), the overall FSM can then be split in the following sub-steps:

$$\begin{aligned} \mathbf{A}\mathbf{U}^* =& \mathbf{r} - \mathbf{G}\mathbf{p}^n + \mathbf{b}_m \\ \Delta t \mathbf{D}\mathbf{M}^{-1}\mathbf{G}_s \delta\mathbf{p} =& \mathbf{D}\mathbf{U}^* - \mathbf{s} - \mathbf{b}_c \\ \mathbf{U}^{n+1} =& \mathbf{U}^* - \Delta t \mathbf{M}^{-1}\mathbf{G}\delta\mathbf{p} \\ \mathbf{p}^{n+1} =& \mathbf{p}^n + \delta\mathbf{p} \end{aligned} \tag{5.39}$$

Hence, the procedure consists in first advancing in time the velocity field with the provisional pressure field $\mathbf{p}^n$. This yields an intermediate velocity field $\mathbf{U}^*$ that, in general, does not satisfy the continuity constraint. The second second step involves the solution of a Poisson equation for the pressure correction $\delta\mathbf{p}$. Finally, the last step involves the correction of the provisional velocity with a gradient term and the update of the pressure to the new time level. The overall error committed by the approximations (5.38) can be evaluated by considering the resulting equations in their full, non factorized, form:

$$\begin{bmatrix} \mathbf{A} & \Delta t \mathbf{A}\mathbf{M}^{-1}\mathbf{G} \\ \mathbf{D} & \Delta t \mathbf{D}\mathbf{M}^{-1}\left(\mathbf{G} - \mathbf{G}_\mathbf{s}\right) \end{bmatrix} \begin{bmatrix} \mathbf{U}^{n+1} \\ \delta\mathbf{p} \end{bmatrix} = \begin{bmatrix} \mathbf{r} - \mathbf{G}\mathbf{p}^n \\ \mathbf{s} \end{bmatrix} + \begin{bmatrix} \mathbf{b}_m \\ \mathbf{b}_c \end{bmatrix} \tag{5.40}$$

Thus, two error terms are introduced, respectively, in the momentum and the continuity equations, both dependent from the pressure correction term:

$$\begin{aligned} \Delta t \mathbf{B}\mathbf{M}^{-1}\mathbf{G}\delta\mathbf{p} \approx& \Delta t^2 \mathbf{B}\mathbf{M}^{-1}\mathbf{G}\frac{\partial \mathbf{p}}{\partial t}\bigg|^n \\ \Delta t \mathbf{D}\mathbf{M}^{-1}\left(\mathbf{G} - \mathbf{G}_\mathbf{s}\right)\delta\mathbf{p} \approx& \Delta t^2 \mathbf{D}\mathbf{M}^{-1}\left(\mathbf{G} - \mathbf{G}_\mathbf{s}\right)\frac{\partial \mathbf{p}}{\partial t}\bigg|^n \end{aligned} \tag{5.41}$$

However, while both are second order in time and consistent with the time integration error in (5.29), their nature is completely different. Indeed, the momentum error term is entirely due to the approximate factorization (i.e., the approximate inverse for $\mathbf{A}$) and, while not actually done in the present case or the FSM in general, it can be readily reduced by adding outer iterations to the cycle in (5.39), until the provisional pressure field corresponds to the pressure field at the next time step and no pressure corrections are anymore required. In contrast, the error in the continuity equation is only related to the use of a compact Laplacian stencil in the Poisson equation for the pressure and is not, in general, avoidable because the action of $\mathbf{G}_s$ produces a gradient which is not even defined in the cell centers. This error is particularly harmful because, in a single time step, introduces a direct kinetic energy source proportional to (Mahesh et al., 2004; Felten and Lund, 2006; Jofre et al., 2014):

$$-\left(\mathbf{p}^{n+1}\right)^T \Delta t^2 \mathbf{D}\mathbf{M}^{-\mathbf{1}} \left(\mathbf{G}-\mathbf{G_s}\right) \frac{\partial \mathbf{p}}{\partial t}\bigg|^n \tag{5.42}$$

which might lead to instabilities or excessive dissipation. While the scale-similar SGS model introduced in (4.25) explicitly contains a term which counteracts this issue, the selection of a proper gradient operator for the pressure, $\mathbf{G}$, is nonetheless fundamental in order to limit this spurious effect. In particular, the error (5.42) is due to the fact that the proper gradient term is only known on the faces of the grid while, in order to advance/correct the momentum equations, it is required in the cell centers (Trias et al., 2014). Hence, suitable gradient operators are based on a sort of reconstruction of the cell center gradient from the surface one. A possible approach consists in using an approximate Green-Gauss identity (Perot, 2000; Jofre et al., 2014) leading to:

$$\left.\frac{\partial \bar{p}}{\partial x_j}\right|_{c_i} = \frac{1}{V_i}\sum_f^{N_i^f}\left(\frac{\partial \bar{p}}{\partial n}\right)_f A_f r_j^i \qquad \left(\frac{\partial \bar{p}}{\partial n}\right)_f = \left(\frac{\bar{p}_n - \bar{p}_i}{ds^{ni}}\right)\frac{1}{n_k^f e_k^{ni}} \tag{5.43}$$

A similar alternative is usually adopted for body-force discretization methods. For example, Mencinger (2012) proposes using:

$$\left.\frac{\partial \bar{p}}{\partial x_j}\right|_{c_i} = \frac{1}{V_i}\sum_f^{N_i^f}\left(\frac{\partial \bar{p}}{\partial n}\right)_f \left(\frac{r_k^i r_k^{ni}}{r_q^{ni} r_q^{ni}} n_m^f r_m^{ni}\right) A_f n_j^f \tag{5.44}$$

while the discretization adopted in OpenFOAM (OpenFOAM Foundation, 2013) is based on:

$$\left.\frac{\partial \bar{p}}{\partial x_j}\right|_{c_i} = \frac{\mathcal{W}_{jm}^{-1}}{V_i}\sum_f^{N_i^f}\left(\frac{\partial \bar{p}}{\partial n}\right)_f A_f n_m^f \qquad \mathcal{W}_{jm}^{-1} = V_i\left(\sum_f^{N_i^f} A_f n_j^f n_m^f\right)^{-1} \tag{5.45}$$

A different, more elaborated, approach relies on directly minimizing the continuity error in a least squares sense. In particular, this can be done, as for the basic least-

squares gradient method (5.12), on a face per face basis (Vidović, 2009; Jofre et al., 2014), assuming for each face:

$$\left.\frac{\partial \bar{p}}{\partial x_j}\right|_{c_i} n_j^f = \left(\frac{\partial \bar{p}}{\partial n}\right)_f \qquad f = 1, 2, \ldots, N_i^f \tag{5.46}$$

or on a full cell basis (Benhamadouche et al., 2002; Mahesh et al., 2004), by minimizing:

$$\sum_f^{N_i^f} \left[\left.\frac{\partial \bar{p}}{\partial x_j}\right|_{c_i} n_j^f - \left(\frac{\partial \bar{p}}{\partial n}\right)_f\right] A_f \tag{5.47}$$

Finally, while formally different in nature, it is worth mentioning also the approaches developed by Date (1993), Deng et al. (1994) and Ashrafizadeh et al. (2009, 2012) which essentially consist in using the Green-Gauss approach (5.9) with the pressure face values determined in such a way to be consistent with the continuity preserving velocities $\mathbf{U}_c^{n+1} = \mathbf{U}^{n+1} + \Delta t \mathbf{M}^{-1}(\mathbf{G} - \mathbf{G}_s)\delta\mathbf{p}$. The Fluent® solver offers two pressure gradient schemes which are in line with those described above, the Body Force Weighted (BFW) scheme and the PRESTO (PREssure STaggering Option) scheme. Unfortunately, no specific details are available on the implementation, hence their accuracy will be assessed a posteriori in the next section.

5.5 Accuracy analysis and assessment

This section is dedicated to the accuracy analysis and assessment of the different parts of the solver which are involved in the computations presented in the next chapters. When possible, a theoretical approach is used to provide more insight; otherwise, the accuracy assessment is based on straight a posteriori tests for cases with an available analytical solution. All the tests reveal that the solver achieves the presumed second order accuracy, both in space and time. As a consequence, its use in LES can be considered feasible.

5.5.1 Gradient computation

The implementation of the dynamic mixed SGS model proposed here requires the gradient for the test filtered and doubly test filtered velocity fields. While certain implementation approaches would have allowed their direct availability in the solver, these would have also limited the applicability of the model to iterative pressure-velocity algorithms (i.e., the use of the FSM would have not been possible) because of specific solver features related to Fluent®. As a consequence, a gradient computation algorithm based on equation (5.11) has been implemented in the solver trough a separate routine. The specific choice of the algorithm, which is different from the basic least-squares approach used in the main solver, has been mostly dictated by the ease of implementation and the good balance between costs and accuracy. The accuracy of the implementation has been assessed by computing the gradient of the test function:

$$f(x, y, z) = \sin(x)\sin(y)\sin(z) \tag{5.48}$$

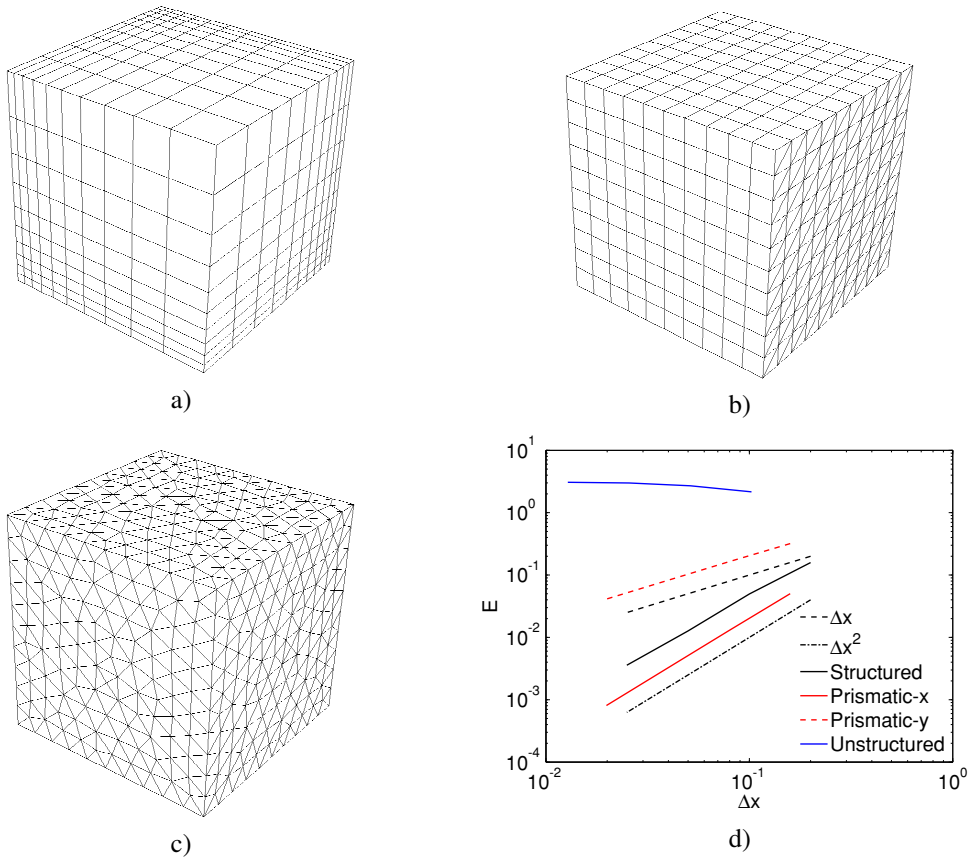

Figure 5.5: *Accuracy of the Gree-Gauss gradient computation method implemented in the code. a) Structured, non-uniform grid. b) Uniform prismatic grid. c) Unstructured tetrahedral grid. d) L^{∞} norm of the error.*

on three different grids, as depicted in Figure 5.5. These are, respectively, a fully structured non-uniform grid (sub-figure a), a uniform prismatic grid (sub-figure b) whose cells are split along a diagonal in the $y - z$ plane and a fully unstructured grid made of tetrahedrons (sub-figure c). For each grid, three successive refinements have been performed and the computed gradient has been compared with the analytical one. As results from sub-figure d, the method is second order accurate on structured non-uniform grids. For the prismatic grid, which is typical of boundary layers, the x component of the gradient (e.g., wall-normal), not affected by the split, still retains the second order accuracy while the two remaining components are clear affected and only present a first order accuracy. Finally, for the unstructured grid the method is clearly not effective and should be replaced by a more accurate one. However, for the present thesis no such grids are actually used as their suitability for LES, especially for wall bounded flows, is certainly debatable.

5.5.2 Bounded central scheme

In this section the suitability of the Bounded Central scheme (5.16) for LES is tested trough an NSA, whose results are reported in Figure 5.6 and compared with second and third order upwind schemes and an upwind biased fifth order scheme. While LES

results on the use of this scheme will be provided in the next two chapters, here it is simply evidenced that the spectral properties of the scheme are such that it barely recovers the transport and dissipative properties of a third order upwind scheme. While Park et al. (2004) have found the third order upwind scheme not particularly useful for LES, Aprovitola and Denaro (2004) have determined the opposite. Hence, according also to Grinstein et al. (2005), the scheme is retained as possible candidate for ILES.

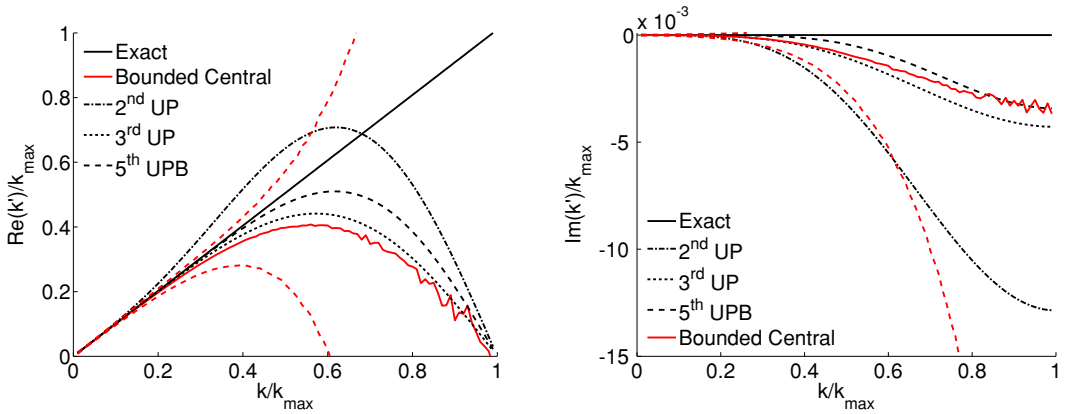

Figure 5.6: *NSA for the Bounded Central scheme. (a) Real (convective) part. (b) Imaginary (diffusive) part. Dashed colored lines: 2σ bands. Full colored lines: mean value.*

5.5.3 Simplified analysis of the time advancement

In order to analyze the combined features of the temporal and spatial discretization, it is possible to extend the simplified 1D linear analysis presented in section 4.5 to the fully discretized equation (5.30) and compare the resulting amplification factor of the scheme with the exact one of the underlying model equation (4.31) in its differential form. To this end, a uniform grid with spacing Δx is considered again, with $\bar{\phi}_i^n$ denoting the solution in the centroid of the cell i at the time level $t^n = n\Delta t$. When the temporal discretization (5.29) is inserted in the FV equation (4.50), the resulting fully discretized equation is:

$$\begin{aligned}\frac{3\bar{\phi}_i^{n+1} - 4\bar{\phi}_i^n + \bar{\phi}_i^{n-1}}{2\Delta t} = &-U\frac{\left(\bar{\phi}_{i+1}^{n+1} - \bar{\phi}_{i-1}^{n+1}\right)}{2\Delta x} + \nu\frac{\bar{\phi}_{i+1}^{n+1} - 2\bar{\phi}_i^{n+1} + \bar{\phi}_{i-1}^{n+1}}{\Delta x^2} \\ &-\frac{U\gamma}{2}\left[\frac{\left(\bar{\phi}_{i+1}^{n+1} - \bar{\phi}_{i-1}^{n+1}\right)}{2\Delta x} - \frac{\left(\bar{\phi}_{i+2}^{n+1} - \bar{\phi}_{i-2}^{n+1}\right)}{4\Delta x}\right] \\ &-\frac{2UM_c}{3}\left[\frac{\left(\bar{\phi}_{i+1}^{n} - \bar{\phi}_{i-1}^{n}\right)}{2\Delta x} - \frac{\left(\bar{\phi}_{i+2}^{n} - \bar{\phi}_{i-2}^{n}\right)}{4\Delta x}\right] \\ &-\frac{M_c\nu}{\Delta x}\left[\frac{\partial\left(\tilde{\bar{\phi}} - \bar{\phi}\right)}{\partial x}\right]\Bigg|_{i-\frac{1}{2}}^{i+\frac{1}{2}}\end{aligned} \tag{5.49}$$

where $M_c = \alpha C$ denotes the overall constant in the scale-similar model, which is

considered fixed with $\alpha = 1/9$, and the diffusive part of the model will be analyzed with both the inconsistent discretization (4.43):

$$\left[\frac{\partial\left(\tilde{\bar{\phi}}-\bar{\phi}\right)}{\partial x}\right]\Bigg|_{i-\frac{1}{2}}^{i+\frac{1}{2}} = -\frac{1}{12}\left(\frac{\bar{\phi}_{i+1}^n - 2\bar{\phi}_i^n + \bar{\phi}_{i-1}^n}{\Delta x}\right) - \frac{8}{12}\left(\frac{\bar{\phi}_{i+2}^n - 2\bar{\phi}_i^n + \bar{\phi}_{i-2}^n}{4\Delta x}\right) + \frac{9}{12}\left(\frac{\bar{\phi}_{i+3}^n - 2\bar{\phi}_i^n + \bar{\phi}_{i-3}^n}{9\Delta x}\right) \tag{5.50}$$

and the consistent one (4.44):

$$\left[\frac{\partial\left(\tilde{\bar{\phi}}-\bar{\phi}\right)}{\partial x}\right]\Bigg|_{i-\frac{1}{2}}^{i+\frac{1}{2}} = -\frac{4}{3}\left(\frac{\bar{\phi}_{i+1}^n - 2\bar{\phi}_i^n + \bar{\phi}_{i-1}^n}{\Delta x}\right) + \frac{4}{3}\left(\frac{\bar{\phi}_{i+2}^n - 2\bar{\phi}_i^n + \bar{\phi}_{i-2}^n}{4\Delta x}\right) \tag{5.51}$$

According to the so called Von Neumann analysis (Crank and Nicolson, 1947), if the boundary conditions for the above equation are periodic, the solution at each time step can be expanded in a discrete Fourier series (due to the limited set of nodes in which the solution is available) and, since the equation is linear, a single harmonic of the series can be substituted in the equation (5.49) to study the effect of the numerical method on the time evolution of a generic Fourier coefficient of the series. In practice, it is assumed:

$$\bar{\phi}_{i+r}^{n+s} = C_k^{n+s} e^{jk(x_i + r\Delta x)} \tag{5.52}$$

where C_k^{n+s} is the Fourier coefficient associated to the wave number k at the time level $t^{n+s} = (n+s)\Delta t$ and $j = \sqrt{-1}$. After the substitution of (5.52) into (5.49), the simplification of the common factor e^{jkx_i} and the introduction of the amplification factor $G = C_k^{n+1}/C_k^n = C_k^n/C_k^{n-1}$, equation (5.49) reduces to:

$$G^2 \overbrace{\left[3 - \frac{4\sigma}{Re}(\cos\theta - 1) + j\sigma\sin\theta\,(2 + \gamma - \gamma\cos\theta)\right]}^{a+jb} + G\underbrace{\left[-4 - \frac{M_c\sigma}{3Re}h(\theta) + j\frac{4M_c\sigma}{3}\sin\theta\,(1-\cos\theta)\right]}_{c+jd} + 1 = 0 \tag{5.53}$$

where $\sigma = U\Delta t/\Delta x$ is the Courant number, $Re = U\Delta x/\nu$, $\theta = k\Delta x$ and the function $h(\theta)$ is defined as:

$$\begin{aligned} h(\theta) &= 2(\cos 2\theta - 1) - \cos 3\theta + \cos\theta \quad \text{for} \quad (5.50) \\ h(\theta) &= 4\left[3(\cos\theta - 1) - \cos 2\theta + \cos\theta\right] \quad \text{for} \quad (5.51) \end{aligned} \tag{5.54}$$

Equation (5.53) has two complex solutions for G, which are given by:

$$G = \frac{-(c+jd)(a-jb) \pm (a-jb)\sqrt{(c+jd)^2 - 4(a+jb)}}{2(a^2+b^2)} \tag{5.55}$$

but only the one with the positive sign is of interest here and has to be compared with the exact amplification factor G^{ex}:

$$G^{ex} = e^{-\sigma\theta^2/Re} e^{-j\sigma\theta} \tag{5.56}$$

Three Courant numbers $\sigma = 0.1$, 0.5, 1 and three Reynolds numbers $Re = 100$, 500, 1000 are used for the comparison, selected according to the typical values found in the numerical simulations presented in the next chapters. In general, a cell Reynolds number $Re = 100$ can be considered typical of near wall zones while the higher values can be considered typical of free stream cells. In contrast, as will be soon clear, only the Courant number $\sigma = 0.1$ can be considered suitable for LES with the present time integration scheme and the higher values are only considered for reference. A first result of the analysis, which however is not presented, is that for such high Reynolds numbers the discretization of the diffusive part in the scale-similar model is not appreciable, hence the results presented here are relative to the inconsistent discretization (5.50) only, which is also the one used for the actual SGS model implementation. The behavior of the real part of the numerical amplification factor as a function of the Courant number and the model constant M_c is presented in Figure 5.7 for $Re = 100$ and $Re = 500$ and in Figure 5.8 for $Re = 1000$. The viscosity ν is assumed equal to the exact molecular viscosity ν_{ex} in all but three cases: Figure 5.7 (a-b) and Figure 5.8 (a), where the effect of a SGS eddy viscosity is mimicked by using $\nu = 2\nu_{ex}$ for the $Re = 100$ case and $\nu = 11\nu_{ex}$ for the two remaining higher Reynolds cases.

The analysis of the scheme without model ($M_c = 0$) clearly reveals that, independently from the Reynolds number, increasing the Courant number above 0.1 produces a bottleneck effect in the spectrum, for which intermediate spatial frequencies appear strongly damped with respect to higher and lower ones. A similar effect can also be observed when, at fixed Courant $\sigma = 0.1$, the Reynolds number is increased, but it is much less evident and practically disappears for higher Courant numbers. The effect of the Courant number is also evident for the imaginary part of the amplification factor, depicted in Figure 5.9, as a unitary Courant number appears to completely remove the advantage provided by the gamma scheme or the scale-similar model.

What is more important, however, is the emerged behavior of the scale-similar model, which actually seems to counteract the bottleneck effect cited above, at least for low/intermediate Courant numbers. More specifically, two effects are worth noting. The first one is that for the $Re = 100$ case the model constant can, and should, have values up to 2 without sensibly altering the stability ($G < 1$ should be preserved), while the higher Reynolds cases already show more serious stability issues for a model constant equal to 1. The second effect to note is that for $\sigma = 0.1$ and $\nu = \nu_{ex}$ the scale-similar model does not appear as particularly helpful, but just compromises an otherwise optimal behavior. However, if the effect of an additional eddy viscosity is

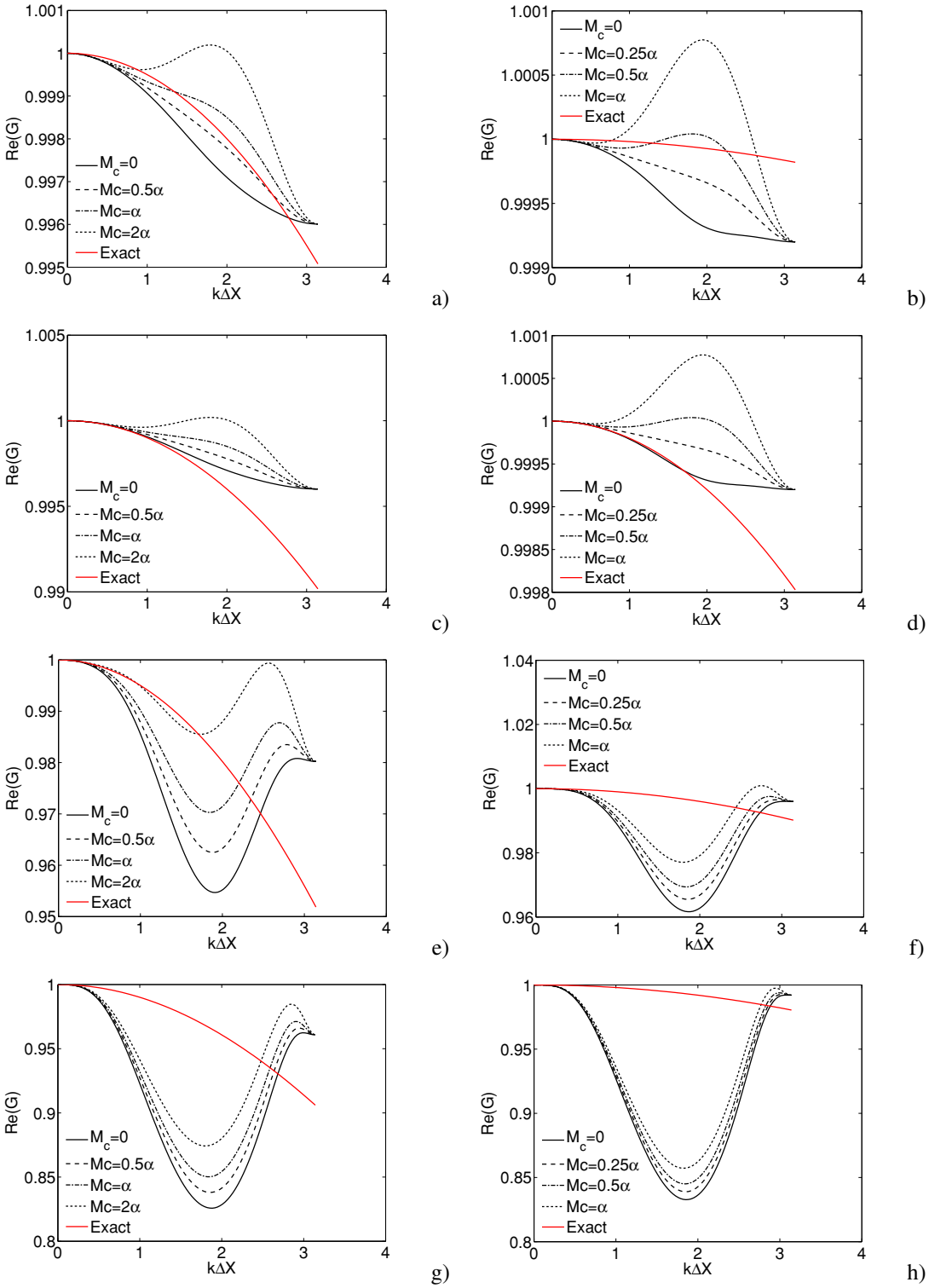

Figure 5.7: *Comparison between numerical and exact amplification factors. Left:* $Re = 100$. *Right:* $Re = 500$. *a)* $\sigma = 0.1$, $\nu = 2\nu_{ex}$. *b)* $\sigma = 0.1$, $\nu = 11\nu_{ex}$. *c-d)* $\sigma = 0.1$, $\nu = \nu_{ex}$. *e-f)* $\sigma = 0.5$, $\nu = \nu_{ex}$. *g-h)* $\sigma = 1$, $\nu = \nu_{ex}$.

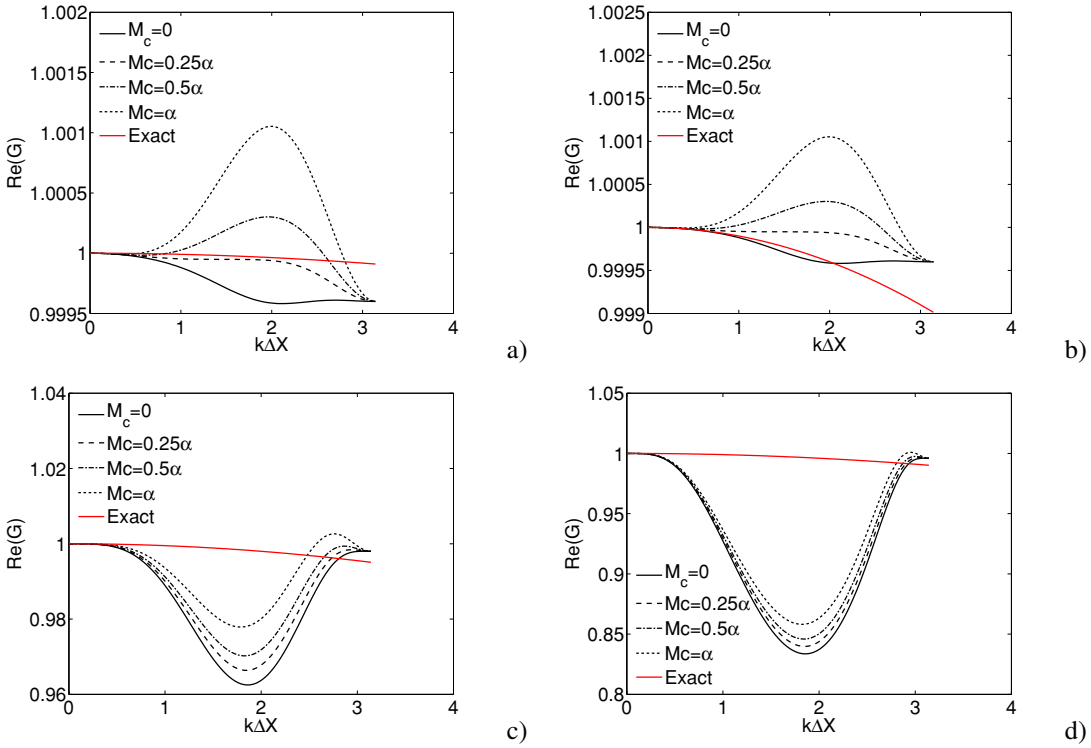

Figure 5.8: *Comparison between numerical and exact amplification factors at* $Re = 1000$. *a)* $\sigma = 0.1$, $\nu = 11\nu_{ex}$. *b)* $\sigma = 0.1$, $\nu = \nu_{ex}$. *c)* $\sigma = 0.5$, $\nu = \nu_{ex}$. *d)* $\sigma = 1$, $\nu = \nu_{ex}$.

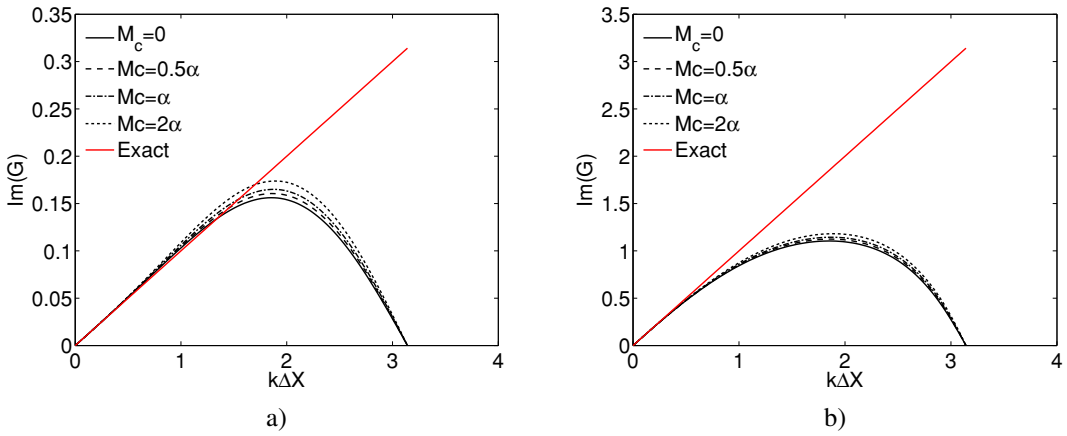

Figure 5.9: *Effect of the Courant number* σ *on the imaginary part of the amplification factor at* $Re = 100$. *a)* $\sigma = 0.1$. *b)* $\sigma = 1$.

considered, the reasoning is reversed, as now the scale-similar model becomes fundamental in order to restore a more accurate spectral behavior. Overall, while this analysis should not be considered conclusive, the effect of the scale similar term can be considered beneficial and the selected range for the dynamic constant, $0 \leq C \leq 2$, appears as representative of the most practical cases. Also, despite the low formal accuracy of the model, its effects are net. The effective stability of the model will be instead assessed a posteriori in the actual numerical simulations presented in the next chapters.

5.5.4 2D Taylor-Green test case

In order to test the overall solver accuracy, both in space and time, the 2D Taylor solution (Taylor, 1923) is considered as benchmark problem:

$$\begin{aligned} u(x,y,t) &= -\cos(m\pi x)\sin(m\pi y)\, e^{-2m^2\pi^2\mu t/\rho} \\ v(x,y,t) &= \sin(m\pi x)\cos(m\pi y)\, e^{-2m^2\pi^2\mu t/\rho} \\ p(x,y,t) &= -\frac{1}{4}\left[\cos(2m\pi x)+\cos(2m\pi y)\right] e^{-4m^2\pi^2\mu t/\rho} \end{aligned} \tag{5.57}$$

where μ and ρ denote the dynamic viscosity and the density of the fluid, x and y denote the spatial coordinates, $t \geq 0$ is the physical time and $m > 0$ is any positive integer. Despite its simplicity, this test case allows the investigation of several parameters with relative ease. In particular, here the analysis is focused on the ratio $\sigma = \Delta x/\Delta t$ (which is representative of the Courant number), the Reynolds number $Re = \rho/\mu$ and the resolution parameter m. All the simulations are performed with a structured uniform grid on a square domain with linear dimensions $L_x = L_y = 2$ and periodic boundary conditions in both the spatial directions. The error is evaluated by sampling, at a given time T, the continuous exact solution (5.57) in the finite set of points where the numerical solution is defined (i.e., the cell centers) and by taking the L^∞ norm of the difference between the numerical solution vector and the exact sampled solution. In all the cases the least-squares gradient computation method (5.12) is adopted[10].

The effect of the ratio σ is analyzed in Figures 5.10 and 5.11, for $m = 1$ and $Re = 1$, by varying, respectively, the pressure discretization scheme and the convection scheme. The analysis is limited to the values $\sigma = 0.1$ and $\sigma = 0.5$ as, consistently with the results of the previous section, higher values completely destroy the overall accuracy. In particular, in Figure 5.10 three different pressure discretization methods are analyzed: the PRESTO, the BFW (see 5.4 for both) and a standard second order (2ND) central scheme (5.13) based on the Green-Gauss formula (5.9). For all the cases, the results clearly indicate that the solver achieve the expected second order accuracy for the velocity and the first order accuracy for the pressure. Indeed, it should be noted that the first of the two approximations in (5.38) is such that the pressure correction in the adopted FSM can only be first order accurate in time, no matter what boundary conditions are used on the pressure.

The comparison performed in Figure 5.11 is instead meant to analyze the possibility to use a symmetry preserving scheme, as advocated by several authors in order to avoid any net kinetic energy effect due to the convection scheme (Verstappen and Veldman, 1998; Benhamadouche et al., 2002; Verstappen and Veldman, 2003; Mahesh et al., 2004; Felten and Lund, 2006; Verstappen and Van Der Velde, 2006; Verstappen, 2008; Rossi, 2009; Jofre et al., 2014; Trias et al., 2014). In order to do so, two options are available in the solver: disabling the reconstruction of higher order terms (DisRec) or setting to 0 the blending between high and low order schemes (HOB). While one would expect that both options obtain the exact same effect, no specific information is

[10] In order to correctly perform the tests on this specific case, three solver details are of paramount importance: the selection of a proper gradient scheme, in order to avoid inconsistencies at the corners of the domain; the double initialization of the solution at the first two time steps, in order to avoid the inconsistency introduced by the first order Euler scheme used on the first time step; the setting of the reference pressure $p = 0$ in a proper point, according to the exact solution (5.57).

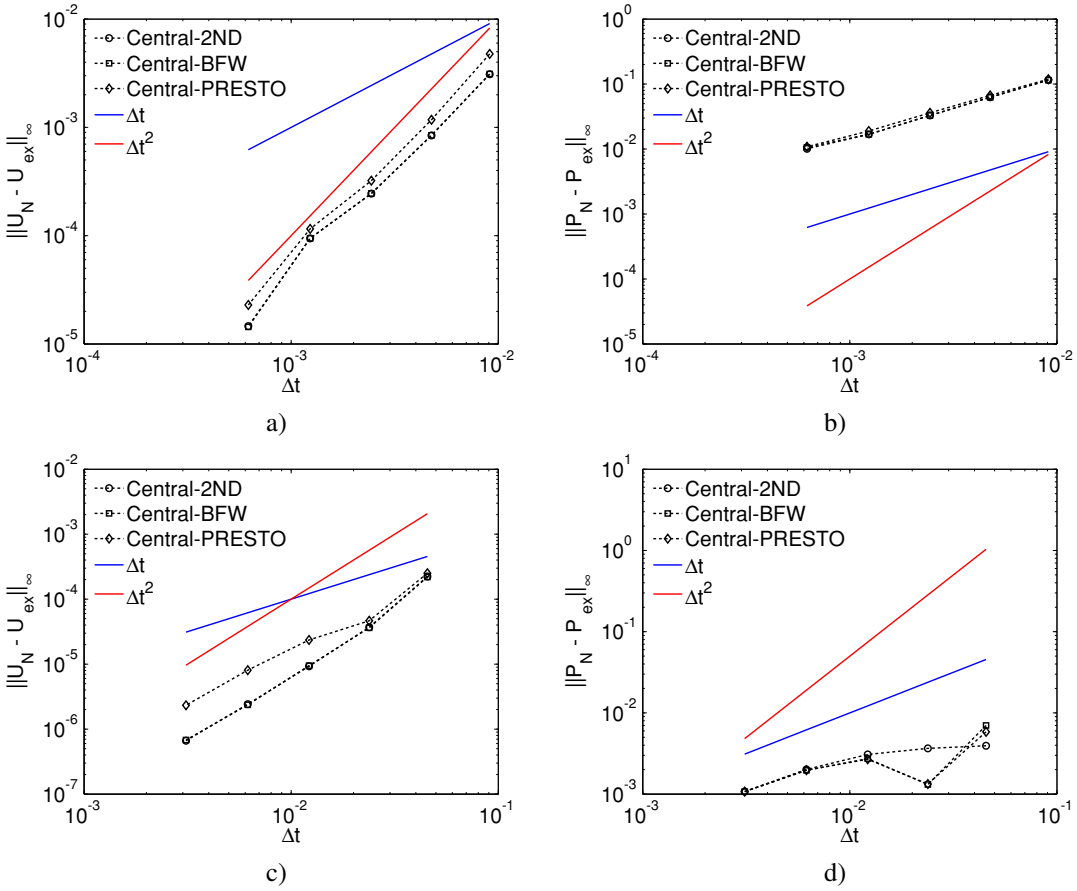

Figure 5.10: *Courant number effect on the solution of the Taylor problem for different pressure discretizations and the central scheme at* $Re = 1$*. Top:* $\sigma = 0.1$*. Bottom:* $\sigma = 0.5$*. Left: Velocity error. Right: Pressure error.*

available on how and which term is effectively disabled in the equations, hence both are tested. The results, which are presented for the PRESTO scheme only[11], indicate that disabling the reconstruction (DisRec) effectively retains the second order accuracy for the velocity field, hence it is a suitable alternative. Notice, however, that some spurious effects appear on the pressure accuracy, which might not be preserved.

The effect of the Reynolds number is investigated in Figure 5.12, with $\sigma = 0.1$, for the basic Central-PRESTO discretization. For both the cases, $Re = 100$ and $Re = 10000$, the velocity accuracy remains second order, even if for the higher Reynolds case it is not explicitly evident for the range of time steps considered in the analysis. What is more interesting, however, is the fact that, for a sufficiently high Reynolds number, the pressure achieves a full second order accuracy, which seems in contradiction with previous results and statements. However, such contradiction is only apparent as, for this specific flow, the pressure gradient exactly balance the convective terms, while the viscous terms only determine the time variations. This, in turn, means that for high Reynolds numbers the approximation (5.38) adopted in the FSM is still first order accurate but, due to the low influence of the diffusive terms, the dominant error is due

[11] The two other schemes give exactly the same results.

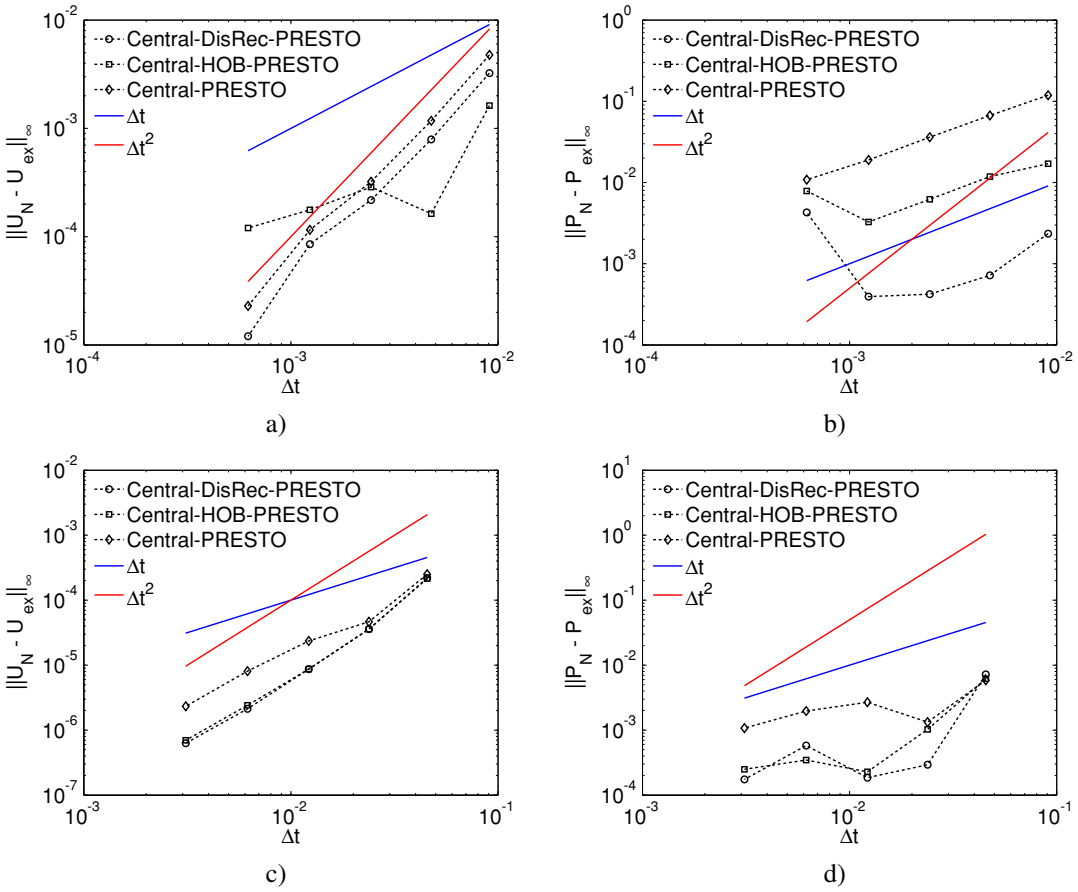

Figure 5.11: *Courant number effect on the solution of the Taylor problem for different centered discretizations and the PRESTO scheme at* $Re = 1$. *Top:* $\sigma = 0.1$. *Bottom:* $\sigma = 0.5$. *Left: Velocity error. Right: Pressure error.*

to the convective terms and reverts to second order to satisfy the balance. This effect is particularly evident when comparing the results for the two Reynolds numbers. For the lower one the second order range is still limited but a change in slope is discernible. For the higher one, instead, the range is much wider and full second order accuracy is achieved. Obviously, extending the range of time steps toward smaller values would have revealed the true first order accuracy for the pressure. Finally, notice that similar results are also obtained with the Dis-Rec option (not shown), the only difference being that the full second order accuracy for the pressure is already achieved for the $Re = 100$ case.

The final test performed is on the influence of the resolution parameter m, which in literature appears to be seldom, if ever, tested. However, as for the test on the Reynolds number, this is certainly important for solvers which are intended to be used in LES. Indeed, the velocity fields typically resolved in LES never have the smoothness and the resolution which are associated with $m = 1$. In particular, for $m = 1$, the grids used in the previous tests provided from 22 to 642 cells per wavelength of the velocity solution and the half of these values for the pressure, which are far from common, even in DNS. Obviously, the overall analysis becomes increasingly meaningless for

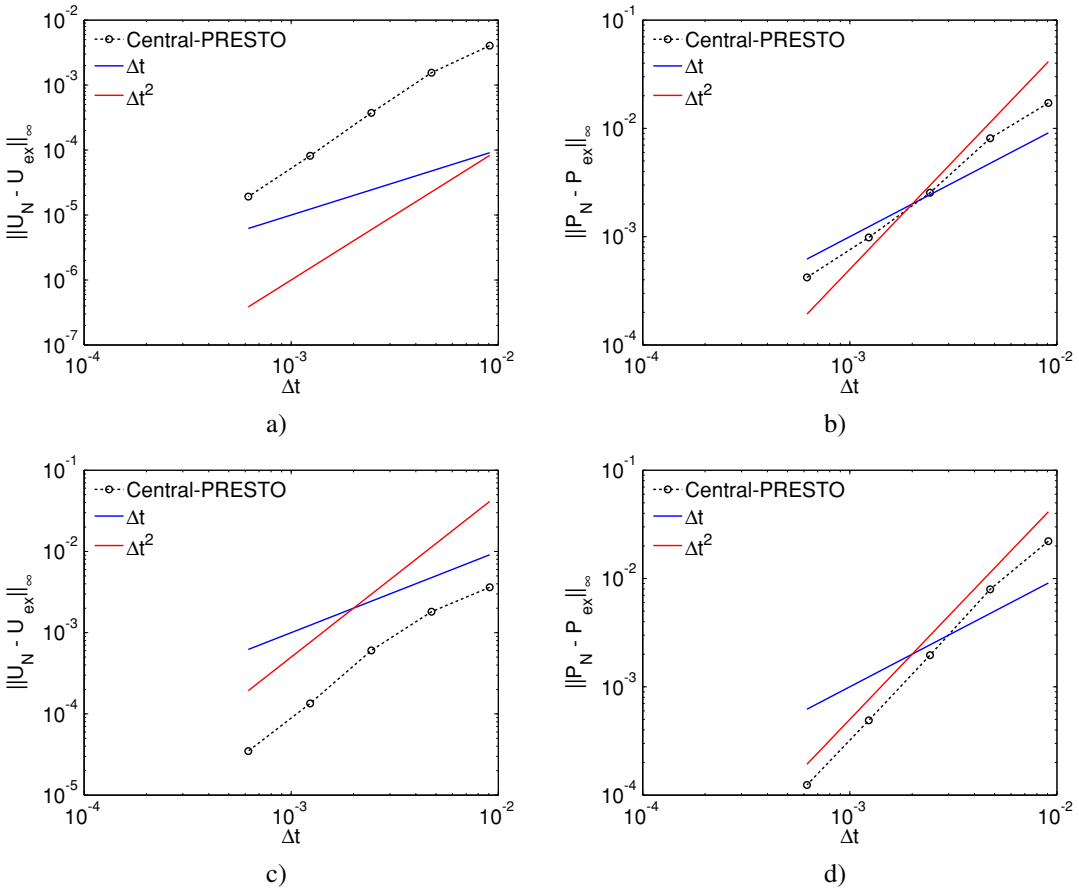

Figure 5.12: *Reynolds number effect on the solution of the Taylor problem with* $\sigma = 0.1$. *Top:* $Re = 100$. *Bottom:* $Re = 10000$. *Left: Velocity error. Right: Pressure error.*

increasing values of m as higher order error terms might not be negligible at very scarce resolutions. Nonetheless, while the order of accuracy is not anymore a meaningful error measure, the consistency of the numerical schemes should not be impaired by the scarce resolution and an error reduction with the grid and time steps is still expected. Formally, this test should have been done on a fixed grid, to keep the number of cells per wavelength fixed. However, as the Courant number has been determined as a strongly limiting factor, the test presented here is still performed at $Re = 1$ with a fixed ratio $\sigma = 0.1$. Hence, in practice, it can be also considered as an extension of the results in Figure 5.10 (a-b) toward very coarse grids.

In particular, three different values are considered for m: 2, 5 and 10. This values determine, respectively, the following resolution ranges for the velocity on the adopted grids: $11-321$, $4.4-128.4$ and $2.2-64.2$ cells per wavelength. Those for the pressure are instead the half of the previous values, thus accuracy cannot certainly be invoked but, nonetheless, consistency and stability of the scheme can be assessed.

The results are presented in Figure 5.13 and, somehow surprisingly, still show that the velocity is approximately second order accurate, even for $m = 10$. However, the results for the intermediate value $m = 5$, especially for the pressure, clearly evidence that this might be a limit value, the results for $m = 10$ being purely fortuitous. Nonethe-

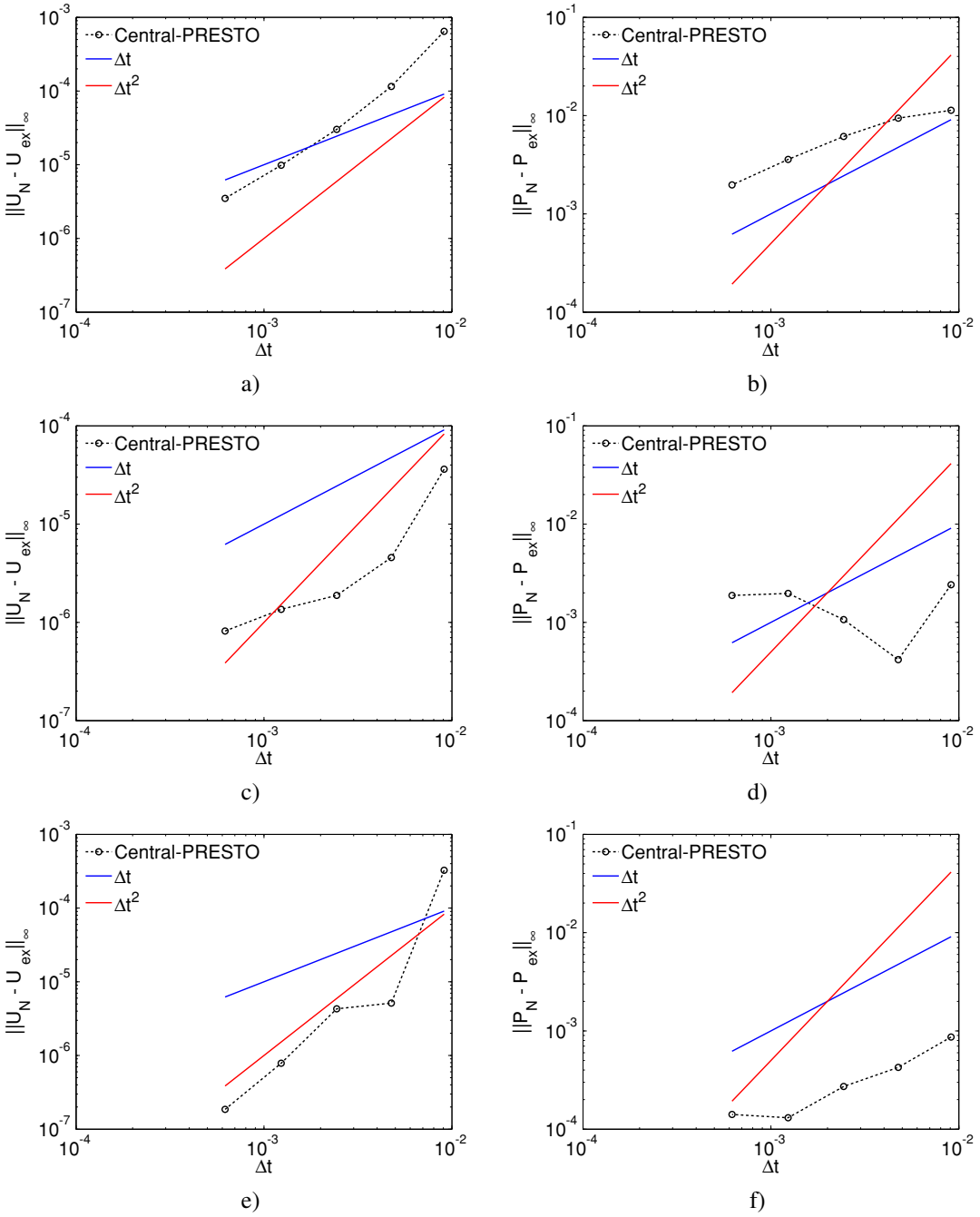

Figure 5.13: *Effect of the resolution parameter m on the solution of the Taylor problem with $\sigma = 0.1$ and $Re = 1$. Top: $m = 2$. Center: $m = 5$. Bottom: $m = 10$. Left: Velocity error. Right: Pressure error.*

less, the stability of the scheme has not been impaired by the simulations. Finally, it is worth mentioning that similar results have been obtained with the Dis-Rec option (not shown), the main difference being in the lack of a clear error reduction for the pressure for all the three values of m.

5.5.5 Laminar channel flow

The final test presented in this section is relative to the classical Poiseuille flow between two parallel flat plates. The flow is driven by a constant longitudinal pressure gradient $\Delta P/L$, which produces the unique steady velocity component $u(y)$:

$$u\left(y\right) = -\frac{2H^2}{\mu}\frac{\Delta P}{L}\left[\left(\frac{y}{2H}\right) - \left(\frac{y}{2H}\right)^2\right] \tag{5.58}$$

where μ is the viscosity of the fluid and y is the wall-normal direction, along which the plates are separated by a distance $2H$. This particular test is performed to assess the influence of the first order boundary conditions at walls on grids which are representative of actual LES applications, as shown in the next chapter. In particular, the simulations are performed on two sets of grids: one with a uniform cells distribution in wall normal direction and the second one with a cosine stretching law:

$$y_j = H\left\{1 - cos\left[\frac{(j-1)\pi}{N_y}\right]\right\} \quad j = 1, 2, ..., N_y + 1 \tag{5.59}$$

where y_j is the j^{th} grid node wall-normal coordinate and N_y, the number of computational cells in the y direction, is varied among the grids to obtain different wall-normal resolutions.

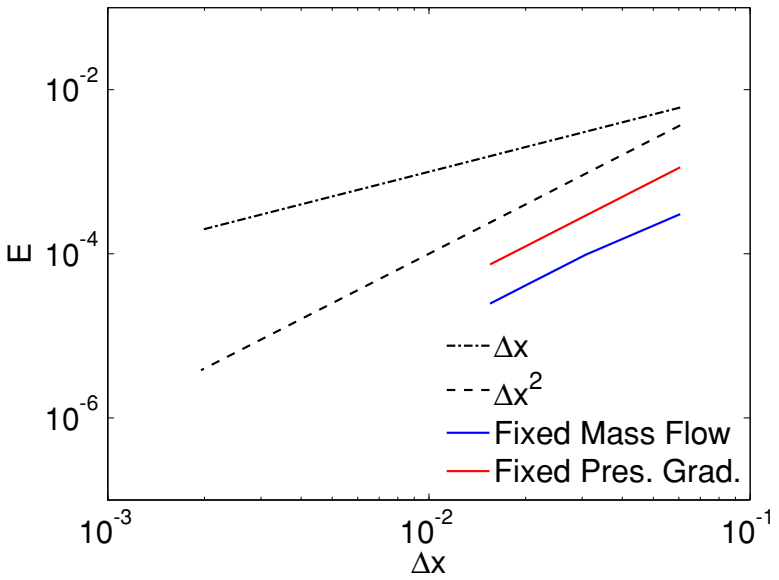

Figure 5.14: *Reduction of the L^∞ norm of the error on the stretched grid for the laminar channel flow test case.*

Fully three-dimensional computations are performed, with periodic boundary conditions along the wall-parallel directions and the overall flow driven by either fixing the pressure gradient or the overall mass flux. The computations are steady, in order to avoid additional time discretization effects, and the pressure velocity coupling is based

on a standard SIMPLEC method (Van Doormaal and Raithby, 1984). The remaining numerical settings are the default Central-PRESTO discretization and a least-squares method for the gradient computation. As shown in Figure 5.14, with both flow conditions a full second order accuracy is achieved on the stretched grid and a similar accuracy is also achieved on the uniform grid for Ny between 33 and 129 (not shown). While this seems to invalidate the discussion in 5.2.4, this is not actually the case. Indeed, as shown in Figure 5.15, the error distributions on the two grids are very different and, for the uniform grid, two error peaks are also present at the first cells near the walls[12].

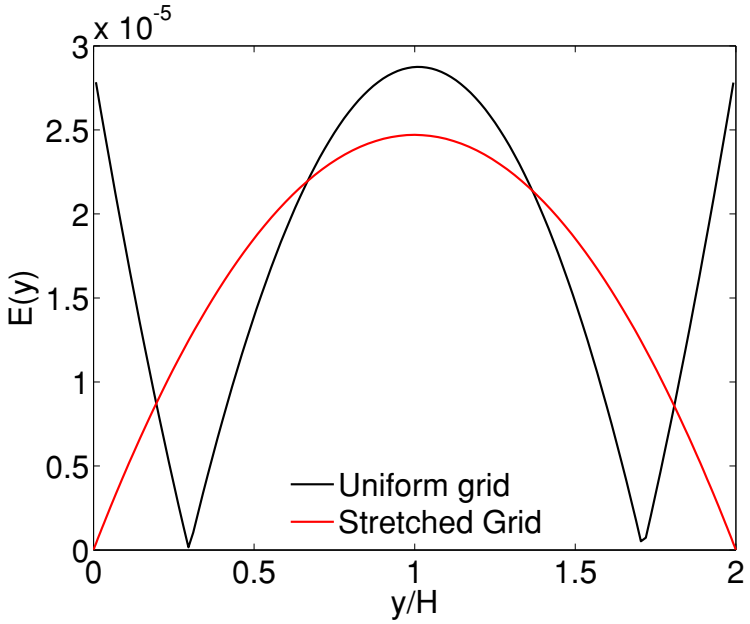

Figure 5.15: *Error distribution for the laminar channel flow test case with* $Ny = 129$ *and fixed mass flow rate.*

What thus happens is that, for the non-uniform grid, the near-wall grid spacing is always much smaller than the maximum grid spacing in the center of the channel and the error at the wall is negligible. In contrast, for the uniform grid, while the first order error at the wall would be expected to emerge, it actually doesn't because, with the grid refinement, the velocity in the near-wal cells also decreases with the first power of the grid step and the overall spatial error remains second order. While this seems to suggest that the overall error actually is of second order, this is really not the case and the observed behavior simply reflects the fact that, for this particular test, there is no way to refine the grid without moving the effective point which is affected by the first order error term. Of course, when the error is evaluated for the wall shear stress the first order accuracy clearly emerges. In conclusion, while not readily apparent, the first order error at the wall is certainly present, but its magnitude can be controlled with an appropriate refinement of the grid.

[12]Notice that, for the fixed pressure gradient case, the wall peaks are also the only error peaks present on the uniform grid.

5.6 Implementation details

Before closing this chapter it is necessary to introduce some details regarding both the default LES implementation in Fluent® and the implementation of the scale-similar model proposed here, as well as some details regarding additional LES aspects which are usually overlooked.

5.6.1 Default LES implementation

It should be now clear that, as a FV code, Fluent® is perfectly suited for GLES. From the practical point of view, the code being of the implicitly filtered type, differences only arise at the SGS model level and just for two specific points in particular: the form of the GI, which is that in (3.15), and the possible forms of structural models, which are described in section 4.3. Finally, both these two points usually imply also the definition of a proper test filter[13], which should be implemented according to equation (4.18). However, this is seldom done in practice and formula (4.19) is more typically adopted. For understandable reasons, Fluent® has no structural models implemented, hence its default LES implementation is strictly defined by the test filter and the dynamic procedure/GI used to compute model constants.

Unfortunately, despite the fact that the applicability of present GLES framework to Fluent® is known since the work of de With and Holdø (2005), the dynamic procedure implemented in the code is based on the CGI as presented in (2.33) (Kim, 2004). In particular, the test filter is in the form of equation (4.19), but does not involve the central cell and the stencil is limited to first neighbor cells only. Also, the Smagorinsky model is the only algebraic model available for the dynamic procedure[14] and will be used as a reference for the dynamic procedure proposed here.

5.6.2 SGS model

The full implementation of the proposed dynamic mixed SGS model has required the development of three specific numerical aspects: a gradient computation algorithm, already described and tested in the previous section; a filtering routine, due to the lack of user-access to the default one implemented in the solver; an implementation strategy for the whole model.

The filtering routine, which is required by both the proposed dynamic procedure and the specific eddy-viscosity and scale-similar models used in it, has been designed following equation (4.19) and such that it is already suitable for general compressible flows. In particular, it is based on a two step procedure which is executed at each time step and by each processor separately. In the first step the filtering stencil is created for each cell trough the following procedure[15]:

[13] See Chester et al. (2001) for an alternative dynamic procedure without test filter.

[14] Additional SGS model options available in the solver are the WALE model of Nicoud and Ducros (1999) and the Dynamic subgrid Kinetic Energy Model (DKEM) developed by Kim and Menon (1997). However, none of the two is further considered in this thesis.

[15] A relevant alternative would have been the pre-computation and storage of the filtering stencils. However, this would have required additional memory locations and the implementation of a dedicated data structure. In contrast, the computational burden of performing such procedure at each time step is generally limited and preserves the flexibility which would be required, for example, near shocks or other moving discontinuities typical of variable density flows.

- Insertion of the cell in the stencil vector and its initialization as "Most Recently Added Group of Cells" (MRAGC), trough a couple of integers denoting the start and end positions of this group in the stencil vector.
- N_L inner loops (m_loop) over the MRAGC (N_L identifying the number of cell layers in the filter stencil). In each loop, the following sub-steps are performed:
  - For each cell i in MRAGC an inner loop over its faces (f_loop) is performed.
  - For each face, the adjacent cell j is added to the stencil if: the stencil is not full yet, the cell is not already into the stencil, the cell is a fluid cell and effectively belongs to the current parallel partition.
  - After the last cell in MRAGC has been visited, update MRAGC with the newly added cells and go to the next m_loop.
- If necessary, remove from the stencil the cells having less than a certain number of neighbors in the stencil (compactness criterion).

Which, while not being particularly designed to achieve high performances, has the merit to be flexible enough to perform tests on the filter stencil independently from the filter itself. After the stencil creation, for each cell the filter (4.19) is applied only once to the resolved variables ($\bar{\rho}^n$, $\bar{\rho}^n\tilde{u}_i^n$, $\bar{p}^n$ and, if needed, $\bar{\rho}^n\tilde{T}^n$ and $\bar{\rho}^n\tilde{u}_j^n\tilde{u}_j^n$) and the filtered variables are then exchanged among contiguous parallel domain partitions. This overall procedure is applied $m+1$ times and the results of the last two applications are finally stored in memory together with the required gradient components, computed with the newly implemented routine. The default setting used in this thesis is $m = 1$ and $N_L = 1$, without satisfying any compactness criterion, hence the overall procedure consists, for each cell, in four loops over neighbor cells (two for the stencil creation and two for the effective filtering). However, in some cases with unstructured grids, using a larger filter width has been found fundamental in order to correctly remove the high frequency component from the computed solution. While both increasing m or N_L would have produced the desired effect, increasing the value of N_L has been found more suitable for two reasons. First, while having an higher serial cost then increasing m, its parallel performances are superior as no extra communication costs are involved. Second, as the overall procedure is only applied $m + 1$ times, for practical reasons, increasing m to obtain a larger filter width would introduce an inconsistency between the last two filter levels. Hence, this last option has been finally discarded.

For what concerns the implementation strategy of the whole model for τ_{ij}^{n-0}, its two components have been split. For the eddy-viscosity part, naturally handled by the solver trough a dedicated routine, no specific effort has been required for its implementation and the dynamically computed viscosity is simply passed to the solver. The scale-similar part, instead, has been implemented as an additional source term following the classical FV integration rule:

$$\overline{\frac{\partial}{\partial x_j}\left(\tau_{ij}^{n-0}\right)}^{n} = \frac{1}{V_i}\int_{\Omega_i}\frac{\partial}{\partial x_j}\left(\tau_{ij}^{n-0}\right)d\Omega = \sum_{f}^{N_i^f}\left(\tau_{ij}^{n-0}\right)_f n_j^f\frac{A_f}{V_i} \tag{5.60}$$

with $(\tau_{ij}^{n-0})_f$ interpolated according to (5.11), whose cost is an additional loop over the cell's nearest neighbors[16]. Finally, it's worth mentioning that, on physical boundaries, no contribution from the scale-similar term is considered in (5.60). In contrast, for the computation of the gradient of the filtered variables, the resolved variables are used at the boundaries.

5.6.3 Inflow boundary conditions

Because of the very specific range of scales involved in a simulation, the specification of proper boundary conditions is as important in LES as the use of proper numerical methods and SGS models. Indeed, for a given computational domain, two specific ranges of scales can be identified. One is relative to the so called super-grid scales (SPGS), which are larger or comparable to the domain size and, in practice, determine the mean flow entering/leaving the domain (Grinstein, 2006, 2009). Such scales require modeling as the SGS ones, by proper specification of the domain boundaries and by suitable mean flow specifications, both on the physical and the numerical side. The second range of scales which can be identified is the one relative to the effectively resolved scales in the domain, ranging from domain size scales down to the smallest scales allowed by the computational grid and the specific LES approach adopted. Not only the two ranges usually interact but, for a given domain, both need to be specified on the boundaries and both determine the specific flow realization. In practice, besides wall boundaries (where boundary conditions are, formally, trivial), these issues have implications for inflow and outflow boundaries. SPGS modeling and outflows are not specifically treated in this section but further discussed in chapter 7 with a practical example. Inflow boundary conditions are discussed in the following.

The problem of specifying proper inflow boundary conditions in LES is usually split in two sub-problems. One relative to the specification of the mean flow profiles at inlet and one to the specification of the remaining scales down to the grid resolution. Despite few exceptions (see Sagaut et al. (2004)), this is usually limited to the velocity components and consists in assuming for the velocity on the boundary:

$$\tilde{u}_i\left(x_j,t\right) = U_i\left(x_j,t\right) + u_i'\left(x_j,t\right) \tag{5.61}$$

where U_i is the mean velocity and u_i' the relative fluctuation. The specification of U_i is not usually an issue as it is based on the results of preliminary or concurrent RANS/URANS computations or determined by analytical/empirical profiles (e.g., (5.27)). Still, this component is certainly important and has to be specified with care. The difficulties in specifying u_i' can instead be traced back to three main factors. The first, most important, one is that u_i' represents almost all the scales actually present in the incoming flow while U_i only represents few of the largest ones. Hence, in terms of physical information, u_i' is more rich and flow determining. The second factor is due to the fact that the information contained in u_i' is representative of: the whole energy cascade up to the grid cut-off and the scale reduction process in it; the coherent structures and their spatial-temporal correlations; any possible anisotropy or lack of homogeneity. Hence, in practice, u_i' actually contains most of the dynamics of the full NSE. Finally, u_i' also

[16]Notice that the face based data structure typical of FV solvers is not usually available to the user. As a consequence, the source term is implemented on a per cell basis.

needs to be compatible with the actual discrete dynamical system simulated in the domain, which means that it has to be compatible with both the overall numerical method and the computational grid. As a consequence, most of the known methods specify u_i' only approximately, trough some stochastic process which is further enforced to satisfy specific flow constraints.

Among the several possible approaches (Tabor and Baba-Ahmadi, 2010), two methods are available in Fluent®: the Spectral Synthesizer (SS) (Smirnov et al., 2001) and the Vortex Method (VM) (Sergent, 2002; Mathey et al., 2003, 2006). Specific details on these two methods can be found in the relative references and in (Viaro et al., 2012). Here only some common features are recalled. In particular, both methods require the specification, at the inflow boundary, of turbulence related velocity and length scales, at least, or the full Reynolds stress tensor. Which means that, in general, a precursor RANS simulation is required. As spatial and temporal correlations are enforced artificially trough an approximate procedure and, possibly, an incorrect RANS specification, such methods also require an adaptation region between the inflow boundary and the spatial location where the numerically sustainable flow dynamics is restored. Finally, the specific implementation used in Fluent® is such that: for the SS the spectral energy distribution of the fluctuations is strictly Gaussian[17] while for the VM it almost completely lacks a viscous range. These features are such that the VM recovers the numerically sustainable flow dynamics only about 10 hydraulic diameters downstream the inlet plane. For the current implementation of the SS instead no such recovery is generally possible and the fluctuations are almost always dissipated, leading to a full laminarization of the flow and a completely incorrect computation (Viaro et al., 2012).

Besides the specific implementation details, the necessity for an adaptation region is a well known issue of all the stochastic inflow generation methods. Indeed, despite the lack of physical correlations among the prescribed scales, an even more important deficiency of such methods is that the prescribed velocity fluctuations are not adapted to the current discretization method and grid resolution, which cannot be reasonably considered in the procedure. Also, from the conceptual point of view, the dependence of such methods on RANS simulations is not only a limit in itself but also mines the reliability of the LES results as most RANS models have serious deficiencies even for flows as simple as those in square ducts. In this case, there would be the embarrassing situation of a turbulence modeling approach, LES, designed to overcome the RANS limits, which instead relies on it for the inflow specification.

An alternative to stochastic inflow specification methods is based on the mapping of velocity fields from concurrent simulations or databases. In these methods an auxiliary computation, targeted toward the required inflow condition, is performed in parallel or in advance with the same numerical parameters used in the main computation and with specific boundary conditions. Once the auxiliary flow has reached the target condition for the inflow, its velocity field is sampled on a representative plane and either used directly as inflow in the main domain or stored over a sufficiently long time and used subsequently. Such method has the advantage that no adaptation regions are required and the resulting inflow is always the best possible prescription. Also, no additional RANS computations are involved and the whole computation relies on LES features only. However, this approach has been usually disregarded because considered costly,

[17] This behavior has been modified recently (Huang et al., 2010; Castro and Paz, 2013).

due to the required storage or the parallel auxiliary computation, and impractical for general purpose solvers.

While not specifically designed for any of the test cases analyzed in the next chapters, a part of this thesis has been also dedicated to the implementation of such a mapping procedure in the Fluent® solver. This was not only motivated by the effective lack of a consistent inflow method in the code, but also by the fact that, in contrast to the common beliefs, such a method is easily manageable in a general purpose solver and can actually be competitive with the alternative stochastic methods, if not the only available option in some specific cases. Such implementation is briefly described in the following while the test on its implementation is best presented in chapter 7.

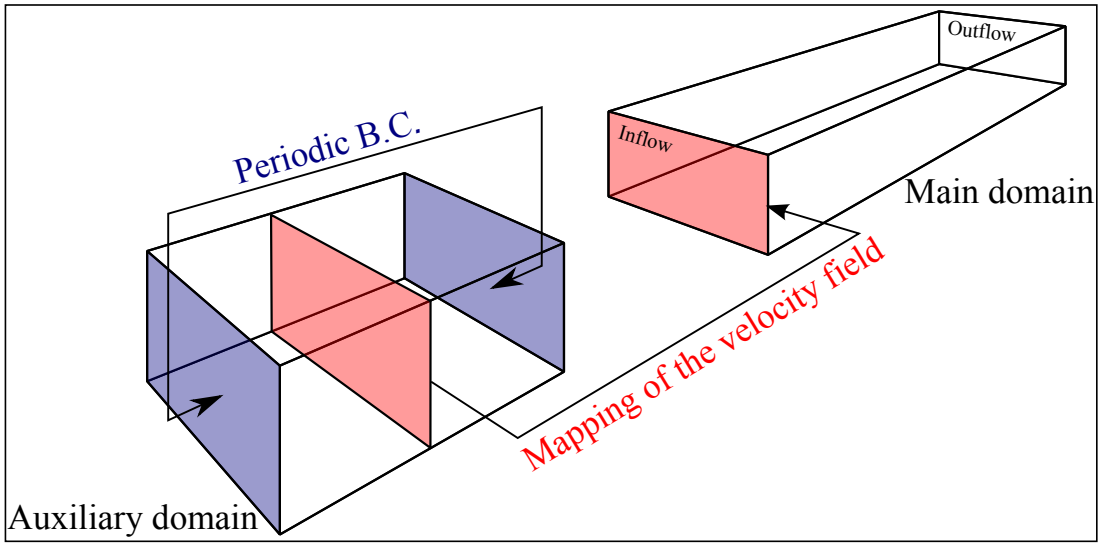

Figure 5.16: *Sketch of the mapping procedure.*

A sketch of the general approach followed in the implementation of the mapping procedure is presented in Figure 5.16. In practice the method consists in having, parallel to the main computational domain, also an auxiliary domain. While the simulation in the main domain is set up as would be done normally, the one in the auxiliary domain is performed on a smaller domain with periodic boundary conditions, but with the same grid resolution and numerics used in the main domain. In practice, the flow in the auxiliary domain is set up in order to reach equilibrium conditions, representative of the required inflow, trough the application of a specific volume forcing.

Notice that, with respect to the total domain size, the auxiliary domain is usually a small fraction and, most of the times, it is smaller than the development region needed by stochastic methods. Also, it is worth stressing that a good practice in LES requires that building block flows are tested in advance, in order to assess the required spatial resolution and numerical setting for the flow at hand. Hence, in general, the fully developed flow in the auxiliary domain should be available in advance, with the correct numerical setting, and ready to be inserted in the computation next to the main computational domain. Finally, it is also worth mentioning that a current trend for general purpose solvers is to have the mapping plane within the main domain itself, invoking a sort of simplification in the overall setting (Baba-Ahmadi and Tabor, 2009; Tabor and Baba-Ahmadi, 2010). Here, as clearly evidenced by Figure 5.16, this approach is not

followed for several reasons. The first is that, as explained before, having a separate auxiliary domain promotes the good practice of computing building block flows in advance. The second is that a mapping plane in the main domain introduces a dynamic coupling with the inflow plane which, most of the times, requires spatial separations among the two which are much larger than those required by stochastic methods, nullifying any advantage of the approach. Finally, having a separate auxiliary domain allows more flexibility in several aspects: the forcing of the flow; the use of nominally different flow conditions with a scaling (Schlüter et al., 2004), which still provides better results than pure stochastic methods (Keating et al., 2004); the use of the method only for portions of the overall inlet section.

With both the main and auxiliary computations in place and correctly set up, the mapping procedure implemented in the code follows the steps described below (see Lampitella et al. (2012) for more details):

- First pre-processing step: all the parallel processes hosting cell faces on the mapped or inflow boundaries transfer their information to the master process.
- Second pre-processing step: the master process determines the logical connections among the faces/processes by a brute force search method and the Rodrigues' rotation formula (Rodrigues, 1840). This information is stored in a four column matrix of integers, whose i^{th} row has the following structure:

$$IN_i^P \quad IN_i^f \quad MAP_i^P \quad MAP_i^f \quad \text{for} \quad i = 1, 2, \ldots, N \tag{5.62}$$

  indicating, for each of the N faces on the inflow boundary, the hosting process (IN_i^P), the local face index (IN_i^f), the process hosting the corresponding face on the mapped section (MAP_i^P) and the local index of this face (MAP_i^f). This relational matrix is then transferred back to all the processes, which make it local by eliminating rows not involving them.
- At run time, for each time step, each process performs a loop over its own relational matrix and performs one of the following operations according to the specific case (all the communications are non-blocking):
  - The process hosts both the mapped and inflow faces. The required fields (e.g., velocity components, density, etc.) are simply stored in a dedicated memory location.
  - The process hosts a face on the mapped section. The required fields are sent to the process hosting the corresponding face on the inlet.
  - The process hosts a face on the inlet section. The required fields are received from the process hosting the corresponding face on the mapped section and stored in a dedicated memory location.
- At run time, for each time step, a classical routine for the implementation of boundary conditions is used together with the information stored at the previous step. This, in particular, may involve any required consideration on incoming/outcoming waves, according to the needs. As this routine is separate from the one

above and called after it, the non-blocking communication paradigm has no specific effects and full synchronization is always in place.

In practice, the main limitation of the algorithm is in the fact that both the mapped and inlet boundaries need to have the exact same distribution of cell faces and this is not allowed to change during the computation. It is also worth noting that all the preprocessing steps are done only once in advance and the relational matrix stored in memory. Hence, the overall cost of the algorithm is simply related to the communication between the usually low number of processes hosting the involved couples of faces. Tests on different hardware architectures, as well as with different CPU loadings, and a random domain partitioning have shown that, for fixed total number of cells, the above procedure reduces the overall cost per time step between the 23% and the 12% with respect to the VM, with an average cost saving around the 18%.

The interesting fact about these numbers is that, from the computational point of view, the inflow specification method is blocking for the overall time advancement, no matter how small the inlet face is. As a consequence, the savings above approximately allows investing the 18% of the total computational cells in the auxiliary domain while keeping the same costs of the VM. At the same time, the VM would still need an adaptation region, hence requiring an overall greater number of cells and greater costs. The effectiveness of the present implementation will be assessed in chapter 7 on two specific test cases.

5.6.4 Flow statistics

An LES aspect which is often overlooked, or simply neglected, is the computation of flow statistics. Indeed, an LES computation is strictly three-dimensional and unsteady and, to produce the usually required mean flow quantities, the instantaneous quantities need to be averaged in time and/or spatial directions along which the flow is homogeneous. However, for its own nature, LES can, and is usually required to, give additional statistical information on the flow, like spatial and temporal spectral energy distributions, second or higher order moments, etc.

A first issue which is encountered in computing such first or higher order statistical quantities is that, formally, the LES solution, independently from the specific approach, is not equivalent to a DNS solution but, as demonstrated in section 3.6, almost always responds to the GLES equations (3.9). As a consequence, even a mean velocity profile does not exactly correspond, in theory, to the mean profile which is ideally looked for. Higher order statistics are also subjected to additional subtle limitations (Sagaut, 2006) and, even considering SGS models in their reconstructions, might not always lead to the correct statistics, depending on the specific SGS model in use (Knaepen et al., 2002; Winckelmans et al., 2002).

Here a different approach is followed, which in practice consists in computing straight LES statistics and considering them as representative of the real flow. While certainly incorrect, this is motivated by different reasons. The first one is that any possible approach to compute the statistics is always acting a posteriori, as a post-processing step; hence the matter is not related to the actual computation as to the correct interpretation of the results. The second one is that different SGS models or LES codes would generally require different reconstruction procedures, making the analysis work

extremely elaborate and impractical for a general purpose solver. Also, SGS models are usually devised as only statistically correct, which means that their inclusion in the flow statistics is not justified as it is not justified in RANS/URANS. Nonetheless, for the present GLES framework applied to the FV method and the scale-similar model developed in this thesis, an easy approach to such approximate reconstruction exists, which consists in using equation (4.80):

$$\phi^* = \bar{\phi}^n + C_{ss}\frac{\Delta^2_{n,0}}{\Delta^2_{m,n}}\left(\bar{\phi}^n - \bar{\phi}^m\right) \tag{5.63}$$

Hence, instead of computing the statistics from the resolved variables $\bar{\phi}^n$, it is possible to compute them from the enhanced field ϕ^*, which is consistent with both the Galilean invariance of the equations and the FV filter affecting them. As stated above, such approach is not generally used here, but an example of the differences arising due to its use is given in the next chapter.

A second issue related to the computation of the flow statistics is in the actual algorithmic implementation. Indeed, the one adopted in Fluent®, as well as in more advanced research codes (Nek5000, 2013), is based on running time integrals. In particular, for any two given variables, ϕ and ψ, the following quantities are stored in Fluent®:

$$\begin{aligned}
&\langle\phi\rangle^{t-t_0} = \int_{t_0}^{t}\phi dt = \sum_{i=1}^{N}\phi^i\Delta t_i \quad \langle\psi\rangle^{t-t_0} = \int_{t_0}^{t}\psi dt = \sum_{i=1}^{N}\psi^i\Delta t_i \\
&\left\langle\phi^2\right\rangle^{t-t_0} = \int_{t_0}^{t}\phi^2 dt = \sum_{i=1}^{N}\left(\phi^i\right)^2\Delta t_i \quad \left\langle\psi^2\right\rangle^{t-t_0} = \int_{t_0}^{t}\psi^2 dt = \sum_{i=1}^{N}\left(\psi^i\right)^2\Delta t_i \\
&\langle\phi\psi\rangle^{t-t_0} = \int_{t_0}^{t}\phi\psi dt = \sum_{i=1}^{N}\phi^i\psi^i\Delta t_i
\end{aligned} \tag{5.64}$$

with Δt_i denoting the N time steps covering the time interval $t - t_0$ used for the average and ϕ^i and ψ^i the values of the variables at such time steps. Then, variance and covariance are computed as follows:

$$\begin{aligned}
\left\langle\left(\phi - \langle\phi\rangle\right)^2\right\rangle &= \frac{\left\langle\phi^2\right\rangle^{t-t_0}}{t-t_0} - \frac{\left(\langle\phi\rangle^{t-t_0}\right)^2}{\left(t-t_0\right)^2} \\
\left\langle\left(\phi - \langle\phi\rangle\right)\left(\psi - \langle\psi\rangle\right)\right\rangle &= \frac{\langle\phi\psi\rangle^{t-t_0}}{t-t_0} - \frac{\langle\phi\rangle^{t-t_0}\langle\psi\rangle^{t-t_0}}{\left(t-t_0\right)^2}
\end{aligned} \tag{5.65}$$

Besides the lack of a tool for statistical moments and co-moments of order higher than two, this approach is a numerical nightmare as, not only serious cancellation errors can occur, for example, in the subtractions in (5.65), but the stored variables in (5.64) can grow in time without bounds! Hence, the accuracy on the variance and co-variance can be lost even before the cancellation error occurs. These problems are well known and reported as simple introductory examples in numerical analysis books,

e.g., Higham (2002, p. 11) and Hammarling (2005, p. 46). It could be argued that, with the double-precision floating-point format, these issues have low relevance, if any. However, as shown, for example, by Chan et al. (1983), the previous algorithm for the computation of the variance has a relative error with an upper bound given by:

$$e_r = Nk^2u \quad k = \sqrt{1 + N\frac{\langle\phi\rangle_{ex}^2}{\left\langle\left(\phi - \langle\phi\rangle\right)^2\right\rangle_{ex}}} \tag{5.66}$$

where the subscript ex denotes the exact value, N is the number of collected samples, u is the arithmetic precision (e.g., around 10^{-15}-10^{-17} for double precision) and k represents the condition number of the sample with respect to the variance computation. Hence, the error grows like uN^2 and, as it is not uncommon for the ratio under the square root to be approximately $10^3 - 10^4$, in the worst case scenario the error would grow as $10^{-11}N^2$. As a consequence, for $N \approx 10^5$, which is not uncommon in LES, the relative error bound would be 0.1; as soon as N reaches $3 \cdot 10^5$, the relative error bound is approximately 100%. Even arguing that these are only upper bounds and that some multiplicative constant lower than one might be present, the result can still be non catastrophic but simply inaccurate. A typical case where this would happen is in the realization of anisotropy maps for the resolved Reynolds stresses (Banerjee et al., 2007). In this case the resolved Reynolds stress tensor is made anisotropic and the local anisotropy is classified according to the eigenvalues of the anisotropy tensor, whose components have specific upper and lower bounds. In this case, even small errors in the computation of the statistics might make the resolved stresses not realizable and completely useless in this kind of analysis.

In order to overcome such difficulties, and for additional reasons that will become clear soon, a dedicated routine for the single-pass computation of the flow statistics has been developed. Previous works in this area can be dated back to Weldford (1962), which first developed a stable and accurate recurrence formula for the computation of the mean, the variance and covariance, and general, arbitrary order, univariate moments. In particular, Weldford's formulas are suited for single samples updating the previously computed statistics. Chan et al. (1979) have extended the formulas for the mean, the variance and the covariance to the case when they have to be updated from already computed values over populations with the most diverse cardinality; Terriberry (2008) additionally extended the work to the computation of third and fourth order univariate moments. Finally, Pébay (2008) extended the previous works to the computation of arbitrary order univariate central moments. While certainly reliable and robust, all these methods still suffer a lack of flexibility, as not directly applicable to general computations with variable time steps, which is instead possible with the formulas in (5.64-5.65). Also, in anticipation of alternative applications, they would also be inapplicable for spatial statistics, as for a FV method the local variables should be weighted by the local cell volume V_i. To the best of the author's knowledge, much less work has been done in this area. Indeed, an update formula for the weighted variance has been developed by West (1979) and further generalized by Chan et al. (1979) into a pair-wise algorithm to handle data sets of different cardinalities[18].

[18]The work of Choi and Sweetman (2010) is a notable exception which, nonetheless, employs a different approach based on computed PDFs, hence it looses the generality of an exact integration formula.

The formulation proposed here is intended as a generalization of the previous works to the case of arbitrary order, univariate or multivariate, central moments. In particular, given the two sets of N samples $\phi^1, \phi^2, \ldots, \phi^N$ and $\psi^1, \psi^2, \ldots, \psi^N$, and the corresponding set of generic weights, $w_1, w_2, \ldots, w_N$, the variables which should be computed are the weighted means, $\langle\phi\rangle_w^N$ and $\langle\psi\rangle_w^M$, and the weighted, multivariate, central moment $C_{k,q}^N$:

$$\begin{aligned}
\langle\phi\rangle_w^N &= \frac{\sum_{i=1}^{N} w_i \phi^i}{\sum_{i=1}^{N} w_i} \qquad \langle\psi\rangle_w^N = \frac{\sum_{i=1}^{N} w_i \psi^i}{\sum_{i=1}^{N} w_i} \\
C_{k,q}^N &= \frac{\sum_{i=1}^{N} w_i \left(\phi^i - \langle\phi\rangle_w^N\right)^k \left(\psi^i - \langle\psi\rangle_w^N\right)^q}{\sum_{i=1}^{N} w_i}
\end{aligned} \tag{5.67}$$

for any given combination of positive integers k and q. For the sake of generality, it can be assumed that the original data samples and weights are available as two separate sets of respective cardinality M and $N - M$, with $N > M > 0$, and that weighted means and moments are available for the two sets[19]: $\langle\phi\rangle_w^M$, $\langle\phi\rangle_w^{N-M}$, $\langle\psi\rangle_w^M$, $\langle\psi\rangle_w^{N-M}$, $C_{r,s}^M$ and $C_{r,s}^{M-N}$, with $(0,0) \leq (r,s) \leq (k,q)$. Then, as shown in Appendix F, the following recurrence formulas hold:

$$\begin{aligned}
\langle\phi\rangle_w^N &= \frac{W^M}{W^N} \langle\phi\rangle_w^M + \frac{W^{N-M}}{W^N} \langle\phi\rangle_w^{N-M} \\
\langle\psi\rangle_w^N &= \frac{W^M}{W^N} \langle\psi\rangle_w^M + \frac{W^{N-M}}{W^N} \langle\psi\rangle_w^{N-M} \\
C_{k,q}^N &= \sum_{r=0}^{k} \sum_{s=0}^{q} \binom{k}{r} \binom{q}{s} \frac{\left(\langle\phi\rangle_w^{N-M} - \langle\phi\rangle_w^M\right)^r \left(\langle\psi\rangle_w^{N-M} - \langle\psi\rangle_w^M\right)^s}{\left(W^N\right)^{r+s+1}} A_{k-r,q-s}^{N,M}
\end{aligned} \tag{5.68}$$

where:

$$W^M = \sum_{i=1}^{M} w_i \quad W^{N-M} = \sum_{i=M+1}^{N} w_i \quad W^N = \sum_{i=1}^{N} w_i = W^M + W^{N-M} \tag{5.69}$$

$$A_{k-r,q-s}^{N,M} = W^{N-M} \left(W^M\right)^{r+s} C_{k-r,q-s}^{N-M} + W^M \left(-W^{N-M}\right)^{r+s} C_{k-r,q-s}^{M}$$

These formulas, besides allowing the stable, single-pass/parallel[20] computation of

[19] The relevant case of the update of time statistics is obtained for $M = 1$.

[20] The same formulas can be used with $M = 1$ to update time statistics, but also with any other combination which would then allow the computation of the statistics for distributed data sets in parallel environments.

second and higher order statistics[21], also have an additional advantage in the fact that they can be used to simplify exact integration formulas. Hence, for example, they could be used to simplify the computation of the second order moments in (4.14) by splitting an arbitrary computational cell in a sum of tetrahedrons, whose moments can be computed exactly and then combined according to the last equation in (5.68)[22].

[21] The fact that they reduces to those in the cited references can be readily verified by properly setting the weights and the integers k and q. Still, the overall error bound is also problem dependent and will certainly grow with k and q.

[22] This would be also valuable in computational geometry for the computation of the inertia tensors for objects whose spatial data are distributed among different processes.

CHAPTER 6

Turbulent channel flow

In this chapter the proposed dynamic, mixed SGS model is tested on the turbulent channel flow at $Re_\tau = 590$ and compared with the available DNS data (Moser et al., 1999) and alternative modeling options. A general description of the flow is first presented in section 6.1, together with the most relevant features regarding its LES computation. A brief description of the main computational setup used for all the tests is then given in section 6.2, while extensive tests of the SGS model are presented in section 6.3. As this test case also served as benchmark for the LESinItaly initiative (Denaro et al., 2011; Abbà et al., 2013), a comparison of the proposed model with several alternative ones is finally presented in section 6.4.

6.1 Flow description

The test case considered is the fully developed, turbulent, incompressible, isothermal flow between two infinitely extended flat plates separated by a distance $2H$. The mean flow direction is along the x axis, the wall-normal direction is represented by the y axis and the z axis represents the span-wise direction, as depicted in Figure 6.1. The velocity components in the three directions are, respectively, u, v, and w. Both the density, ρ, and the kinematic viscosity, ν, are assumed constant. The flow is statistically steady, homogeneous in the wall parallel directions and its statistics are dependent on the coordinate y only; moreover, the plane $y = H$ is a symmetry plane for all the statistics. Under these conditions, the basic equations governing the statistics in the channel are presented in the following.

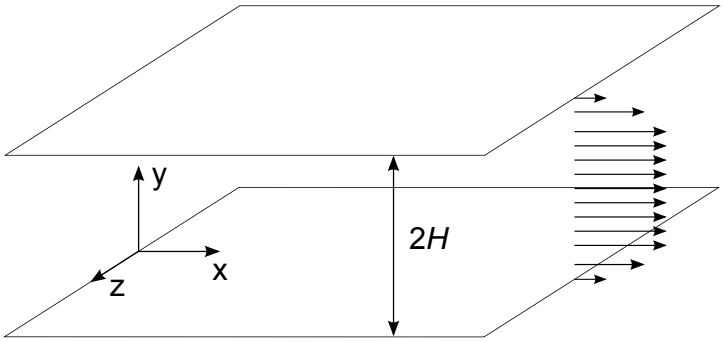

Figure 6.1: *Sketch of the channel flow.*

6.1.1 Mean momentum equations

Introducing a generic statistical average operator $\langle \cdots \rangle$ (e.g., the ensemble average or the time average), the velocity and pressure fields can be decomposed into an average part and a fluctuation, denoted by a prime:

$$\begin{aligned} u &= \langle u \rangle + u' \\ v &= \langle v \rangle + v' \\ w &= \langle w \rangle + w' \\ p &= \langle p \rangle + p' \end{aligned} \tag{6.1}$$

The usual approach in presenting this flow considers such components as relative to the fully resolved velocity and pressure fields, as in DNS. However, in order to extend the following discussion also to the general GLES case, while preserving a familiar notation, the preceding decomposition is considered applied to the resolved fields, independently from the specific resolution or LES approach adopted. With this slight misuse of notation, under the mentioned hypotheses ($\partial\langle\cdot\rangle/\partial x = 0$, $\partial\langle\cdot\rangle/\partial z = 0$, $\partial\langle\cdot\rangle/\partial t = 0$), the average momentum and continuity GLES equations for the channel flow can be written as:

$$\begin{aligned} \frac{\partial \langle v \rangle}{\partial y} &= \frac{\partial \left\langle \chi_y^{LES} \right\rangle}{\partial y} \\ \frac{1}{\rho}\frac{\partial \langle p \rangle}{\partial x} &= \frac{\partial}{\partial y}\left(\nu \frac{\partial \langle u \rangle}{\partial y} - \langle u \rangle \langle v \rangle - \langle u'v' \rangle + \left\langle \tau_{xy}^{LES} \right\rangle \right) \\ \frac{1}{\rho}\frac{\partial \langle p \rangle}{\partial y} &= \frac{\partial}{\partial y}\left(\nu \frac{\partial \langle v \rangle}{\partial y} - \langle v \rangle \langle v \rangle - \left\langle v'^2 \right\rangle + \left\langle \tau_{yy}^{LES} \right\rangle \right) \\ \frac{1}{\rho}\frac{\partial \langle p \rangle}{\partial z} &= \frac{\partial}{\partial y}\left(\nu \frac{\partial \langle w \rangle}{\partial y} - \langle w \rangle \langle v \rangle - \langle w'v' \rangle + \left\langle \tau_{wy}^{LES} \right\rangle \right) \end{aligned} \tag{6.2}$$

where the commutation between spatial and average operators has been fully exploited and the outer filter level present in GLES has been dropped, as not actually affecting the balance equations above[1]. Notice that, in the previous equations, no assumption has been made yet on the boundary conditions or the effective resolution of

[1] This can be also seen by the alternative form (B.1) for the momentum equation.

the computation. As a consequence, generic LES terms have been retained in all the equations. In particular, such terms may or not include explicit SGS models, but they always include the effect of the resolution and the resulting numerical error[2], hence they are always present unless a full DNS computation is employed. When the boundary conditions are introduced, namely, $\langle v \rangle_w = 0$ and the fact that the mean flow is along the x direction, hence it is driven only by the axial pressure gradient $\partial \langle p \rangle / \partial x$ and $\langle w \rangle = 0$, the equations (6.2) reduce to the following form:

$$
\begin{aligned}
\langle v \rangle =& \left\langle \chi_y^{LES} \right\rangle - \left\langle \chi_y^{LES} \right\rangle_w \\
\frac{1}{\rho} \frac{\partial \langle p \rangle}{\partial x} =& \frac{\partial}{\partial y} \left[\nu \frac{\partial \langle u \rangle}{\partial y} - \langle u'v' \rangle + \left\langle \tau_{xy}^{LES} \right\rangle \overbrace{- \langle u \rangle \langle v \rangle}^{\phi_x} \right] \\
0 =& \frac{\partial}{\partial y} \left[-\frac{\langle p \rangle}{\rho} - \left\langle v'^2 \right\rangle + \left\langle \tau_{yy}^{LES} \right\rangle + \overbrace{\nu \frac{\partial \langle v \rangle}{\partial y} - \langle v \rangle^2}^{\phi_y} \right] \\
0 =& \frac{\partial}{\partial y} \left(- \langle w'v' \rangle + \left\langle \tau_{wy}^{LES} \right\rangle \right)
\end{aligned}
\tag{6.3}
$$

At this point, a few comments are in order. First, it has been implicitly assumed that only an explicit pressure gradient can generate a mean flow in a certain direction and not any component of $\langle \tau^{LES} \rangle$, which is usually the case. As a consequence, the z momentum equation reduces to the fact that the stress $\langle w'v' \rangle$, if present, is only due to $\langle \tau_{wy}^{LES} \rangle$. As these are usually negligible for the present arrangement, the z momentum equation will not be further considered in the following. The second, more important, thing to note is that, differently from the classical DNS case (Pope, 2000, p. 266), $\langle v \rangle$ cannot be considered null anymore. This would only happen for a commuting filter/G operator and for mass fluxes which are consistent with the actual momentum components. As none of these conditions is usually satisfied, it is shown in the sections 3.3 and 5.4 respectively that both these effects can be accounted for by the mass source $\langle \chi_y^{LES} \rangle$. In case, any explicit SGS model for the continuity equation would also be contained in it, exactly as for $\langle \tau^{LES} \rangle$. This fact has probably an even more important effect, as a non null vertical velocity component $\langle v \rangle$ implies the presence of spurious terms in both the x and y momentum equations, ϕ_x and ϕ_y, which are similar to the effect of a wall transpiration velocity. From now on, for the sake of conciseness, they will both be included in the $\langle \tau^{LES} \rangle$ terms in the respective equations. However, it should be noted that ϕ_x appears as particularly harmful, it being directly proportional to the mean velocity in the channel. Omitting, from now on, also the relation for $\langle v \rangle$, the average GLES equations for the channel flow are then reduced to the two momentum

[2]It is assumed here that the GLES framework is applied in its implicit filtering form.

equations:

$$\begin{aligned}\frac{1}{\rho}\frac{\partial\langle p\rangle}{\partial x} =& \frac{\partial}{\partial y}\left(\nu\frac{\partial\langle u\rangle}{\partial y} - \langle u'v'\rangle + \left\langle\tau_{xy}^{M}\right\rangle\right)\\ 0 =& \frac{\partial}{\partial y}\left(-\frac{\langle p\rangle}{\rho} - \left\langle v'^{2}\right\rangle + \left\langle\tau_{yy}^{M}\right\rangle\right)\end{aligned} \tag{6.4}$$

where the superscript M for the LES related terms denotes the fact that the respective ϕ contributions have been added to them. These equations can be further simplified by first integrating the y momentum equation along y, which yields:

$$\frac{\langle p\rangle}{\rho} + \left\langle v'^{2}\right\rangle - \left\langle\tau_{yy}^{M}\right\rangle = \frac{p_w^M(x)}{\rho} \tag{6.5}$$

Hence, the sum of the three terms on the left side, which is constant in y, can only be a function of x. Notice that, besides the density, such a function is usually identified with the pressure at the wall, which is also true in this case. However, it has to be stressed that this specific value appears to be a function of $\langle\tau_{yy}^{M}\rangle$, which in general might not be null at walls, thus motivating the use of the superscript M in $p_w^M(x)$. In any case, as neither $\langle v'^2\rangle$ or $\langle\tau_{yy}^{M}\rangle$ can depend on x, the relation (6.5) implies that:

$$\frac{\partial\langle p\rangle}{\partial x} = \frac{\partial p_w^M(x)}{\partial x} \tag{6.6}$$

Hence the driving axial pressure gradient is not a function of y. This fact can be finally used to integrate the x momentum equation, which reduces to:

$$\frac{1}{\rho}\frac{\partial p_w^M(x)}{\partial x} = \frac{\partial}{\partial y}\left(\nu\frac{\partial\langle u\rangle}{\partial y} - \langle u'v'\rangle + \left\langle\tau_{xy}^{M}\right\rangle\right) \tag{6.7}$$

As the term in parentheses is only a function of y and $p_w^M(x)$ is only a function of x, then the two sides of the equation (6.7) are both constant and the above relation implies the well known total linear stress variation along the channel height:

$$\nu\frac{\partial\langle u\rangle}{\partial y} - \langle u'v'\rangle + \left\langle\tau_{xy}^{M}\right\rangle = \frac{\tau_w}{\rho}(1 - y/H) \tag{6.8}$$

where τ_w is the wall shear stress. However, even considering $\langle\tau_{xy}^{M}\rangle$ null at the walls, equation (5.24) implies that, for the Fluent® code, the effective stress entering the balance is:

$$\tau_w \approx \rho\nu\left.\frac{\partial\langle u\rangle}{\partial y}\right|_w + \rho\nu\frac{\Delta y}{4}\left.\frac{\partial^2\langle u\rangle}{\partial y^2}\right|_w + O\left(\Delta y^2\right) \tag{6.9}$$

where Δy is the width of the first layer of cells next to the walls and, as for the flow, it has been assumed that the grid is symmetric with respect to the plane $y = H$. To

understand the effect of such error, the second derivative above can be estimated from the equation (6.8):

$$\frac{\partial^2 \langle u \rangle}{\partial y^2} = -\frac{\tau_w}{\rho \nu H} + \frac{1}{\nu}\frac{\partial \langle u'v' \rangle}{\partial y} - \frac{1}{\nu}\frac{\partial \left\langle \tau_{xy}^{LES} \right\rangle}{\partial y} - \frac{1}{\nu}\frac{\partial \phi_x}{\partial y} \tag{6.10}$$

In order to evaluate (6.10) at the wall, it is safe to assume that both $\langle u'v' \rangle$ and the numerical error in $\langle \tau_{xy}^{LES} \rangle$ vanish sufficiently fast toward the walls that they do not give any contribution[3]. Moreover, in case of no-slip boundary conditions, the contribution due to ϕ_x is also null. However, SGS models which do not vanish at walls sufficiently fast would give a net contribution, finally leading to:

$$\left.\frac{\partial^2 \langle u \rangle}{\partial y^2}\right|_w = -\frac{\tau_w}{\rho \nu H} - 2\left.\frac{\partial \langle \nu_{sgs}/\nu \rangle}{\partial y}\right|_w \left.\frac{\partial \langle u \rangle}{\partial y}\right|_w \tag{6.11}$$

where it has been assumed $\langle \tau_{xy}^{LES} \rangle \approx 2\langle \nu_{sgs} \rangle \partial \langle u \rangle / \partial y$ and that $\langle \nu_{sgs} \rangle$ is null at the wall, but not its derivative. Hence, from (6.9) and (6.11) follows that:

$$\tau_w \approx \rho \nu \left.\frac{\partial \langle u \rangle}{\partial y}\right|_w \frac{\left(1 - \frac{\Delta y}{2}\left.\frac{\partial \langle \nu_{sgs}/\nu \rangle}{\partial y}\right|_w\right)}{\left(1 + \frac{\Delta y}{4H}\right)} \tag{6.12}$$

Considering that any finite value for the SGS viscosity in the first cell near the wall, c_w, would, in fact, imply a finite derivative at the wall, the previous equation can also be arranged as follows:

$$\tau_w \approx \rho \nu \left.\frac{\partial \langle u \rangle}{\partial y}\right|_w \frac{\left(1 - \langle \nu_{sgs}/\nu \rangle|_{c_w}\right)}{\left(1 + \frac{\Delta y}{4H}\right)} \tag{6.13}$$

As a consequence, the overall balance in the channel is altered by a first order term. Finally, from the equations (6.6), (6.7) and (6.8), follows that the driving pressure gradient is balanced by:

$$\frac{\partial \langle p \rangle}{\partial x} = -\frac{\tau_w}{H} \tag{6.14}$$

The overall set of equations derived up to now can be more conveniently rewritten by noting that the overall stream-wise momentum balance is determined solely by the imposed external pressure gradient and the wall shear stress τ_w. It is then plausible that ν and τ_w are the most relevant parameters for a proper nondimensionalization. These, in particular, lead to the definition of the viscous, or friction, velocity and length scales:

$$\begin{aligned} u_\tau &= \sqrt{\frac{\tau_w}{\rho}} = \sqrt{-\frac{H}{\rho}\frac{\partial \langle p \rangle}{\partial x}} \\ \delta^+ &= \frac{\nu}{u_\tau} \end{aligned} \tag{6.15}$$

[3] A limiting wall behavior proportional to $(y - y_w)^2$ is sufficient, but the numerical error is expected to depend on higher order derivatives of $\langle uv \rangle$, hence its near-wall behavior might not respect this constraint.

also known as wall units. Notice that, for simulations where the pressure gradient is fixed and used as flow driving mechanism, as assumed here, the definition of these scales is always well posed. Indeed, any possible term which could give a net contribution at the wall, hence altering the definition of τ_w, is always balanced by the given pressure gradient, as demonstrated above for the error at the wall in (6.9) and (6.13). The use of these scales leads to the following nondimensional quantities:

$$\begin{aligned} u^+ =& \frac{\langle u \rangle}{u_\tau} \\ \frac{y}{H} =& \left(\frac{y}{\delta^+}\right)\left(\frac{\delta^+}{H}\right) = \left(\frac{y u_\tau}{\nu}\right)\left(\frac{\nu}{u_\tau H}\right) = \frac{y^+}{Re_\tau} \end{aligned} \tag{6.16}$$

where u^+ and y^+ are the mean velocity and the wall-normal coordinate expressed in wall units and Re_τ is the friction Reynolds number. Then, the nondimensional momentum equations are obtained dividing (6.5) and (6.8) by u_τ^2:

$$\begin{aligned} p^+ + \left\langle v'^2 \right\rangle^+ - \left\langle \tau_{yy}^M \right\rangle^+ =& p_w^+ \\ \frac{\partial u^+}{\partial y^+} - \left\langle u'v' \right\rangle^+ + \left\langle \tau_{xy}^M \right\rangle^+ =& 1 - \frac{y^+}{Re_\tau} \end{aligned} \tag{6.17}$$

Finally, the above nondimensionalization can be used to easily determine the pressure gradient required to sustain a flow at a given friction Reynolds number:

$$\frac{\partial \langle p \rangle}{\partial x} = -\frac{\tau_w}{H} = -\frac{\rho u_\tau^2}{H} = -\frac{\rho}{H}\left(\frac{\nu Re_\tau}{H}\right)^2 = -\frac{\rho \nu^2 Re_\tau^2}{H^3} \tag{6.18}$$

6.1.2 Bulk velocity

When a simulation is performed with a fixed pressure gradient, a relevant flow parameter as the mean bulk velocity U_b:

$$U_b = \frac{1}{2H}\int_0^{2H} \langle u \rangle \, dy \tag{6.19}$$

is not fixed but it is an outcome of the simulation. It is then interesting to understand what are the physical and numerical effects determining it. A first preliminary insight can be obtained integrating by parts the definition above:

$$U_b = \left[\frac{y \langle u \rangle}{2H}\right]_0^{2H} - \frac{1}{2H}\int_0^{2H} y \frac{\partial \langle u \rangle}{\partial y} dy = -\frac{1}{2H}\int_0^{2H} y \frac{\partial \langle u \rangle}{\partial y} dy \tag{6.20}$$

and then adding $(1/2)\partial\langle u \rangle/\partial y$ to the integrand, upon consideration of the no-slip boundary conditions:

$$U_b = \frac{1}{2}\int_0^{2H} \left(1 - \frac{y}{H}\right) \frac{\partial \langle u \rangle}{\partial y} dy \tag{6.21}$$

Thus, the equation above reveals that the overall mass flux in the channel is determined by $\partial\langle u\rangle/\partial y$, and how it is balanced by the remaining terms in equation (6.8). Moreover, the weighting factor in parentheses and the general behavior for the velocity profile, suggest that it is the near-wall zone that mostly influence its value, as would be expected by the fact that the driving pressure gradient is balanced by the wall shear stress. In contrast, the zone far from the wall, in the channel center, determines the difference between the centerline velocity $U_c = \langle u\rangle_{y=H}$ and U_b. Indeed, by symmetry:

$$U_b = \int_0^H \left(1 - \frac{y}{H}\right) \frac{\partial \langle u\rangle}{\partial y} dy = U_c - \frac{1}{H}\int_0^H y \frac{\partial \langle u\rangle}{\partial y} dy \tag{6.22}$$

In order to effectively understand the effect of the various terms on U_b, it is useful to insert $\partial\langle u\rangle/\partial y$, as derived by equation (6.8), in (6.21):

$$U_b = \frac{1}{2}\int_0^{2H} \left(1 - \frac{y}{H}\right) \left[\frac{\tau_w}{\rho\nu}\left(1 - \frac{y}{H}\right) - \frac{1}{\nu}\left(-\langle u'v'\rangle + \left\langle \tau_{xy}^M \right\rangle\right)\right] dy \tag{6.23}$$

Which, upon integration of the linear term, becomes:

$$U_b = \frac{\tau_w H}{3\rho\nu} - \frac{1}{2\nu}\int_0^{2H} \left(1 - \frac{y}{H}\right)\left(-\langle u'v'\rangle + \left\langle \tau_{xy}^M \right\rangle\right) dy \tag{6.24}$$

a relation equivalent to the one derived by Fukagata et al. (2002) and Gomez et al. (2009), here extended to consider the generic effects due to the scarce resolution typical of LES. In particular, the first term is the laminar contribution (Pope, 2000, p. 268) and, as shown in the previous paragraph, can be affected by the way the wall shear stress τ_w is computed at walls and, consequently, by the adopted SGS model (e.g., (6.10)). Still, its overall contribution is fixed by the pressure gradient (e.g., (6.14)) and cannot be affected by any LES related issue. The second term represents instead the turbulent contribution, due to the combined effect of the general resolution capabilities, the numerical error and any possible SGS model employed. It is useful to express this term in parentheses by the symbol $\langle u'v'\rangle_{LES}$, denoting an equivalent tangential stress:

$$-\langle u'v'\rangle_{LES} = -\langle u'v'\rangle + \left\langle \tau_{xy}^{LES} \right\rangle - \langle u\rangle\langle v\rangle \tag{6.25}$$

As will be shown in the next paragraph, the response of the resolved $\langle u'v'\rangle$ to the overall LES effect is nonlinear and cannot be determined solely by the balances above. However, the common experience (see section 6.3) with low order codes suggests that the typical resolution of LES computations usually determines an under-prediction of $-\langle u'v'\rangle$ in the near wall region for simulations performed without a SGS model. As a consequence, in order to correctly predict the mean velocity in the channel, it is necessary that the SGS model in $\langle \tau_{xy}^{LES}\rangle$ is capable to overcome such deficiency by explicitly adding a balancing contribution. This contribution might itself further damp $-\langle u'v'\rangle$, but it is the combined effect that is required to overcome the original deficiency. Nonetheless, it might as well happen that the employed numerical method is capable to appropriately resolve a significant fraction of the near-wall contribution in

$-\langle u'v'\rangle$, or even over-predict it. In this case, obviously, the required role for $\langle \tau_{xy}^{LES} \rangle$ is the opposite, it has to avoid any explicit contribution near the wall or even damp a possibly overestimated $-\langle u'v'\rangle$. It will be shown in section 6.4 that such a different behavior for different codes actually exists.

An additional interesting effect is the one produced by $\phi_x = -\langle u\rangle\langle v\rangle$, which is only due to the possible errors in the continuity equation. In practice, whenever there is a spurious source of mass, the resulting effect would be an increase of $\langle v\rangle$ and, for no penetration boundary conditions at the walls, a net spurious mean velocity toward the channel center, which would further decrease the overall stresses $-\langle u'v'\rangle_{LES}$.

In the author's opinion, it is informative to highlight the analogy between LES mechanisms producing an overestimation of U_b, namely, the suppression of $-\langle u'v'\rangle_{LES}$, and the typical mechanisms used in practice to reduce the drag in actual flows. For example, riblet surfaces (Jiménez, 2004; García-Mayoral and Jiménez, 2011, 2012) confine the near-wall turbulent structures, also known as stream-wise streaks, in a way which is resemblant of the constraint given by a limited grid resolution. More direct analogies exists with the explicit suppression of the near wall stresses $-\langle u'v'\rangle$ (Iwamoto et al., 2005) or the blowing at the walls (Fukagata et al., 2002).

6.1.3 Resolved stresses

An equation for the mean resolved stresses in GLES could be derived starting from equations (B.1) and (B.6), taking their average, building an evolution equation for $\langle\bar{\rho}^n\rangle\langle\tilde{u}_i^n\rangle_F\langle\tilde{u}_j^n\rangle_F$ and subtracting the latter from the averaged (B.6). Indeed, denoting with $\langle\cdot\rangle_F$ the Favre transformed average[4], the following relation holds:

$$\frac{\partial \left\langle \bar{\rho}^n \tilde{u}_i^n \tilde{u}_j^n \right\rangle}{\partial t} = \frac{\partial \left\langle \bar{\rho}^n \right\rangle \left\langle \tilde{u}_i^n \tilde{u}_j^n \right\rangle_F}{\partial t} = \frac{\partial \left\langle \bar{\rho}^n \right\rangle \left\langle \tilde{u}_i^n \right\rangle_F \left\langle \tilde{u}_j^n \right\rangle_F}{\partial t} + \frac{\partial \left\langle \bar{\rho}^n \right\rangle \left\langle \tilde{u}_i^{n''} \tilde{u}_j^{n''} \right\rangle_F}{\partial t} \quad (6.26)$$

where:

$$\langle\bar{\rho}^n\rangle \left\langle \tilde{u}_i^{n''} \tilde{u}_j^{n''} \right\rangle_F = \langle\bar{\rho}^n\rangle \left\langle (\tilde{u}_i^n - \langle\tilde{u}_i^n\rangle_F)(\tilde{u}_j^n - \left\langle\tilde{u}_j^n\right\rangle_F) \right\rangle_F \quad (6.27)$$

is the mean resolved stress tensor. Hence, its evolution equation is the result of the subtraction of the first term in the rightmost member above from the the term in the leftmost member. However, this procedure, which is already convoluted for general compressible flows, is rendered even more complicated by the fact that additional terms appear for GLES on the last row in (B.6) and the second member in (B.1). Even considering the inclusion of such a derivation here as fruitful, which is hardly the case, the understanding of the additional terms would be hardly possible. If, instead, such additional terms are neglected, which amounts to consider commuting spatial operators only, then a strong simplification is obtained. Indeed, both equations (B.1) and (B.6) would retain the exact same form of the classical continuous equations if the trace of $-\tau_{ij}^{n-0}$ is included in the resolved pressure and its trace free part is absorbed in the

[4] Analogous to the one defined for the filter in (2.8).

viscous tensor $\tilde{\Sigma}_{ij}^n$. Hence, all the manipulations could be done in the exact same way and the terms put together could be separated back just at the end of the procedure[5].

The resulting equations can be found, for example, in Adumitroaie et al. (1999) for their general compressible version and in Launder et al. (1975) for the incompressible one. Here, none of the two is reported, for the sake of conciseness. Instead, the approximate GLES form (i.e., neglecting the non-commutation terms) for the incompressible channel flow is directly reported, by adopting the convention that the instantaneous LES/numerical terms can be decomposed as $\tau_{ij}^{LES} = \langle \tau_{ij}^{LES} \rangle + \tau_{ij}^{LES'}$ (Wu and Meyers, 2013)[6]. Limiting the discussion to the three normal stresses $\langle u'^2 \rangle$, $\langle v'^2 \rangle$, $\langle w'^2 \rangle$ and the tangential one $\langle u'v' \rangle$, the following equations are obtained[7] (Mathieu and Scott, 2000, p. 108):

$$\begin{aligned}
\frac{\partial T_{xy}}{\partial y} - \epsilon_x - \pi_y - \pi_z &= \langle u'v' \rangle \frac{\partial \langle u \rangle}{\partial y} \\
\frac{\partial T_{yy}}{\partial y} - \epsilon_y + \pi_y &= 0 \\
\frac{\partial T_{zy}}{\partial y} - \epsilon_z + \pi_z &= 0 \\
\frac{\partial R_{xy}}{\partial y} - \epsilon_{xy} + \pi_{xy} &= \left\langle v'^2 \right\rangle \frac{\partial \langle u \rangle}{\partial y}
\end{aligned} \tag{6.28}$$

Indicating, momentarily, the three velocity components and spatial coordinates as u_α and x_α (with $\alpha = x, y, z$), the transport, dissipative and pressure terms in the equations for the normal stresses above can then be written as (no summation implied over Greek indices):

$$\begin{aligned}
T_{\alpha y} &= \frac{\nu}{2} \frac{\partial \langle u_\alpha'^2 \rangle}{\partial y} - \frac{\langle u_\alpha'^2 v' \rangle}{2} + \left\langle u_\alpha' \tau_{\alpha y}^{LES'} \right\rangle - \delta_{\alpha y} \frac{\langle p' u_\alpha' \rangle}{\rho} \\
\epsilon_\alpha &= \nu \left\langle \frac{\partial u_\alpha'}{\partial x_j} \frac{\partial u_\alpha'}{\partial x_j} \right\rangle + \left\langle \tau_{\alpha j}^{LES'} \frac{\partial u_\alpha'}{\partial x_j} \right\rangle \\
\pi_\alpha &= \left\langle \frac{p'}{\rho} \left(\frac{\partial u_\alpha'}{\partial x_\alpha} \right) \right\rangle
\end{aligned} \tag{6.29}$$

where $\delta_{\alpha y}$ is the Kronecker's delta symbol. The analogous terms in the equation for

[5] With the warning of not invoking specific properties for $\bar{p}^n$ or $\tilde{\Sigma}_{ij}^n$, besides the symmetry and the null trace property for the latter.

[6] The effects due to a non null vertical mean velocity are, for the sake of consistency with the present approach, excluded from the treatment.

[7] These are the only components which, nominally, are different from zero. However, a non null vertical velocity might induce couplings with other components. Again, these are not considered in the following.

the resolved tangential stress are instead given by:

$$\begin{aligned} R_{xy} =& \nu \frac{\partial \langle u'v' \rangle}{\partial y} - \langle u'v'^2 \rangle + \left\langle u' \tau_{yy}^{LES'} \right\rangle + \left\langle v' \tau_{xy}^{LES'} \right\rangle - \frac{\langle p'u' \rangle}{\rho} \\ \epsilon_{xy} =& 2\nu \left\langle \frac{\partial u'}{\partial x_j} \frac{\partial v'}{\partial x_j} \right\rangle + \left\langle \tau_{xj}^{LES'} \frac{\partial v'}{\partial x_j} \right\rangle + \left\langle \tau_{yj}^{LES'} \frac{\partial u'}{\partial x_j} \right\rangle \\ \pi_{xy} =& \left\langle \frac{p'}{\rho} \left(\frac{\partial u'}{\partial y} + \frac{\partial v'}{\partial x} \right) \right\rangle \end{aligned} \tag{6.30}$$

Some important details emerge from the equations above which are worth noting. First and foremost, only the equations for $\langle u'^2 \rangle$ and $\langle u'v' \rangle$ are effectively coupled with the mean momentum equations, trough the respective source terms on the right hand sides of the equations (6.28). The equations for the wall normal and span-wise fluctuations, $\langle v'^2 \rangle$ and $\langle w'^2 \rangle$, are instead formally uncoupled from the mean equations and their only direct source is the pressure redistribution trough π_y and π_z[8]. Hence, in practice, the energy enters the stream-wise fluctuations from the mean stream-wise momentum equation and is then redistributed to the remaining normal stresses. In parallel, the tangential stress $\langle u'v' \rangle$ is modulated by a source term depending from both the wall normal and the stream-wise momentum equations. Here, however, there is a direct feedback mechanism at play[9] as an increase in the mean velocity derivative would produce an increase in the resolved tangential stress[10], which would then reduce the mean velocity derivative.

Further insight on these two source terms can be gained by rearranging them trough the momentum equations. More specifically, for the $\langle u'^2 \rangle$ source term:

$$\begin{aligned} \langle u'v' \rangle \frac{\partial \langle u \rangle}{\partial y} =& \left(\langle u'v' \rangle - \left\langle \tau_{xy}^{LES} \right\rangle \right) \frac{\partial \langle u \rangle}{\partial y} + \left\langle \tau_{xy}^{LES} \right\rangle \frac{\partial \langle u \rangle}{\partial y} \\ =& \frac{1}{\nu} \left(\left\langle \tau_{xy}^{LES} \right\rangle - \langle u'v' \rangle \right) \left[\left(\left\langle \tau_{xy}^{LES} \right\rangle - \langle u'v' \rangle \right) - \frac{\tau_w}{\rho} \left(1 - \frac{y}{H} \right) \right] \\ &+ \left\langle \tau_{xy}^{LES} \right\rangle \frac{\partial \langle u \rangle}{\partial y} \end{aligned} \tag{6.31}$$

Or, by using the definition (6.25) with $\langle v \rangle = 0$ and the viscous units:

$$\langle u'v' \rangle^+ \frac{\partial u^+}{\partial y^+} = \left\langle \tau_{xy}^{LES} \right\rangle^+ \frac{\partial u^+}{\partial y^+} - \langle u'v' \rangle_{LES}^+ \left[- \langle u'v' \rangle_{LES}^+ - \left(1 - \frac{y^+}{Re_\tau} \right) \right] \tag{6.32}$$

Analogously, for the $\langle u'v' \rangle$ source term:

$$\left\langle v'^2 \right\rangle^+ \frac{\partial u^+}{\partial y^+} = \left\langle \tau_{yy}^{LES} \right\rangle^+ \frac{\partial u^+}{\partial y^+} - \left(p_w^+ - p^+ \right) \left[- \langle u'v' \rangle_{LES}^+ - \left(1 - \frac{y^+}{Re_\tau} \right) \right] \tag{6.33}$$

[8] It is assumed here that $\pi_x + \pi_y + \pi_z = 0$. This is not anymore the case when a divergence error is present.

[9] Obviously, additional couplings among the equations exist.

[10] Note that the source term has a sign which is congruent with the sign of $\langle u'v' \rangle$, hence it really produces an enhancement of the resolved stress.

Hence, the source for the stream-wise normal stress is actually composed by an LES dissipation term (e.g., for $\langle \tau_{xy}^{LES} \rangle^+ \propto \partial u^+ / \partial y^+$), which would decrease it, and a pseudo-production term PP^+ (the remaining part in (6.32)), which instead transfers the energy from the mean momentum equation. The interesting feature of PP^+, however, is that it is bounded with respect to $\langle u'v' \rangle^+_{LES}$ and the envelope of the absolute maximum achievable values[11] is given by $PP^+_{ENV} = (1 - y^+/Re_\tau)^2/4$. However, this is not the actual value of the maximum, which is instead given by (Laadhari, 2002):

$$PP^+_{MAX} = \left(\frac{\partial u^+}{\partial y^+} \right)^2 \left(1 + \frac{1}{Re_\tau \frac{\partial^2 u^+}{\partial y^{+2}}} \right) \tag{6.34}$$

and is achieved at the position where:

$$- \langle u'v' \rangle^+_{LES} = \frac{\partial u^+}{\partial y^+} \left(1 + \frac{1}{Re_\tau \frac{\partial^2 u^+}{\partial y^{+2}}} \right) \tag{6.35}$$

Hence, more than the actual maximum value of the pseudo-production, is its location that is mostly determined by the specific LES approach. The source term for the tangential stress, while having the same structure of the former one, has the second term which is instead modulated by the pressure decay from its wall value. Also, the effect of the SGS model is not anymore clearly dissipative. The pressure influence is such that the faster is its decay from the wall the higher is the resulting enhancement for the tangential stress. For an eddy viscosity SGS model the first term also has, approximately, a positive effect if the mean vertical velocity increases toward the channel center, thus counteracting the negative effect appearing in (6.25). However, the present analysis is formally valid for null vertical velocities only and such conclusion is only partial.

The major difference among these two sources is that, obviously, only the one appearing in the stream-wise stress equation is an actual source of energy drained from the mean flow, while the other one is just a feedback mechanism acting as modulation and no actual energy flux is involved in its role. This can be also appreciated by adding together the first three equations in (6.28), which gives the equation for the mean resolved turbulent kinetic energy $\langle k \rangle$:

$$\frac{\partial T_y}{\partial y} = \epsilon + \langle u'v' \rangle \frac{\partial \langle u \rangle}{\partial y} \tag{6.36}$$

with:

$$\begin{aligned} T_y &= \sum_\alpha T_{\alpha y} = \frac{\nu}{2} \frac{\partial \langle k \rangle}{\partial y} - \frac{\langle kv' \rangle}{2} + \left\langle u'_j \tau_{jy}^{LES\prime} \right\rangle - \frac{\langle p'v' \rangle}{\rho} \\ \epsilon &= \sum_\alpha \epsilon_\alpha = \nu \left\langle \frac{\partial u'_i}{\partial x_j} \frac{\partial u'_i}{\partial x_j} \right\rangle + \left\langle \tau_{ij}^{LES\prime} \frac{\partial u'_i}{\partial x_j} \right\rangle \end{aligned} \tag{6.37}$$

[11] The term is actually negative.

And comparing such equation with the one for the mean resolved kinetic energy, obtained multiplying the mean stream-wise momentum equation[12] in (6.4) by $\langle u \rangle$:

$$\frac{\partial \langle T \rangle}{\partial y} = \frac{\langle u \rangle}{\rho} \frac{\partial \langle p \rangle}{\partial x} - \langle u'v' \rangle \frac{\partial \langle u \rangle}{\partial y} + \left\langle \tau_{xy}^{LES} \right\rangle \frac{\partial \langle u \rangle}{\partial y} + \nu \left(\frac{\partial \langle u \rangle}{\partial y} \right)^2 \tag{6.38}$$

with:

$$\langle T \rangle = \frac{\nu}{2} \frac{\partial \langle u \rangle^2}{\partial y} - \langle u \rangle \langle u'v' \rangle + \langle u \rangle \left\langle \tau_{xy}^{LES} \right\rangle \tag{6.39}$$

The first term on the right side of equation (6.38) represents the net energy injection by the driving pressure gradient, while the third and the last member represent, respectively, the dissipation due to the LES model/numerics and the viscous dissipation, both of which formally disappear from the overall energy balance. In contrast, the term $\langle u'v' \rangle \partial \langle u \rangle / \partial y$ appears with switched sign in equation (6.36) and represents the only possible energy flux for the stream-wise normal stress. As a consequence it is also the only energy source for all the normal stresses.

It is worth closing this section by noting that equations (6.36) and (6.38) allow a further understanding of the dependence of the mean bulk velocity U_b from the overall simulation details. Indeed, integrating both equations between $y = 0$ and $y = 2H$, and assuming that both $\langle T \rangle$ and T_y vanish at the walls, the following result is obtained (Eyink, 2008; Mathieu and Scott, 2000, p. 110):

$$-\frac{1}{\rho} \frac{\partial \langle p \rangle}{\partial x} U_b = \frac{1}{2H} \int_0^{2H} \epsilon + \left\langle \tau_{xy}^{LES} \right\rangle \frac{\partial \langle u \rangle}{\partial y} + \nu \left(\frac{\partial \langle u \rangle}{\partial y} \right)^2 dy \tag{6.40}$$

which reflects the fact that, for a given pressure gradient, the resulting bulk flow velocity is adjusted in order to sustain the overall dissipation in the simulation, which is due to the viscous contribution (both mean and fluctuating) and the LES contribution, including both numerical and SGS modeling effects. Thus, as explained before, in order to correctly predict U_b, the suitability of a given SGS model is strictly dependent from the numerical details of the code. Whenever the numerical details are such that the overall dissipation is underestimated, the SGS model is required to overcome this deficiency by adding a further dissipation (i.e., an eddy viscosity model). On the contrary, whenever a given code already overestimates the dissipation, the SGS model is required to counteract this action by an anti-diffusive effect. However, is worth noting that such under/overestimations are likely to depend strongly from the details of the velocity profile at the walls, where the mean velocity gradient is higher. This, in turn, implies that a SGS model whose effect is stronger than required near the walls (e.g., a limiting behavior different from y^3) might sufficiently dump the mean velocity gradient (according to the overall linear variation of the stresses) that the resulting bulk velocity is instead underestimated. A final, alternative view on the bulk flow prediction is provided by comparison with the work of Eyink (2008), which interprets the turbulent channel flow as a cross-stream flux of span-wise vorticity. Hence, an overestimation of U_b can be also seen as due to some effect blocking this flux of vorticity.

[12] Again, for consistency in the derivation, $\langle v \rangle = 0$ is assumed here.

6.2 Computational setup

In the present thesis the turbulent channel flow is simulated for $Re_\tau = 590$ and the results compared with the available DNS data (Moser et al., 1999). According to the fully developed condition and the flow homogeneity in the wall parallel directions, all the computations have been performed in a computational box of extension $L_x \times 2H \times L_z$ with periodic boundary conditions along the x and z directions and no-slip conditions at the walls. In order to avoid SPGS modeling issues (see section 5.6.3), the box dimension are selected according to the reference DNS, $L_x = 2\pi H$ and $L_z = \pi H$, so that any difference with respect to a full DNS is due to the lack of the smallest scales, their modeling and the specific details of the scale separation operator, which in the present case is the FV one, but possibly corrupted by the relatively low numerical fidelity of the solver (i.e., the sampling operator). The flow is driven by a constant pressure gradient that is determined according to equation (6.18) and, for all the simulations reported here, the flow parameters are set up in order to obtain a resulting friction velocity $u_\tau = 1m/s$. Fully structured computational grids are used in all the simulations, with constant stream-wise and span-wise spacings, Δx and Δz, and a stretched nodes distribution in the wall normal direction. Except for one case, all the grids adopt a cosine stretching law:

$$y_j = H\left\{1 - cos\left[\frac{(j-1)\pi}{N_y}\right]\right\} \quad j = 1, 2, ..., N_y + 1 \tag{6.41}$$

where y_j is the j^{th} grid node wall-normal coordinate and N_y is the number of computational cells in the y direction. This is also selected for the LESinItaly comparisons (see section 6.4) and is thus the default one. In order to analyze grids more similar to the ones used in the computational practice, an additional hyperbolic tangent stretching is also considered:

$$y_j = H + H\frac{\tanh\left\{\gamma\left[\frac{2(j-1)}{N_y} - 1\right]\right\}}{\tanh\gamma} \quad j = 1, 2, ..., N_y + 1 \tag{6.42}$$

The overall set of used computational grids, with their labels and main parameters are summarized in Table 6.1 in terms of viscous units, with the only grid employing the hyperbolic stretching denoted by the label CT. In Table 6.1, the number of cells in the x and z directions are denoted, respectively, by N_x and N_z and the computational parameters for the reference DNS (Moser et al., 1999) are also reported.

The basic numerical settings for all the computations are those described in chapter 5, namely, a pure second order central scheme for the convective terms, the PRESTO discretization for the pressure gradient, a least-squares approach for the gradient computation and the implicit second order time advancement scheme with the fractional step method for the pressure-velocity coupling. Alternatively, tests will be performed with the bounded central scheme or the symmetry preserving scheme (SYM) by disabling the reconstruction of higher order terms.

Besides the proposed dynamic mixed SGS model (DM), whose specific settings will be described case by case, alternative SGS modeling options are also considered

Table 6.1: *Grid parameters for the channel flow simulations.*

ID	N_x	N_z	N_y	Δ_x^+	Δ_z^+	$\Delta_{y_{min}}^+$	$\Delta_{y_{max}}^+$
DNS	384	384	257	9.7	4.8	0.04	7.2
C	64	64	33	57.92	28.96	1.34	56.15
CT	40	40	59	92.68	46.34	0.4	66.11
F	64	64	99	57.92	28.96	0.15	18.72
CZ	64	40	99	57.92	46.34	1.34	56.15
FZ	64	128	99	57.92	14.48	0.15	18.72

Table 6.2: *SGS models for the channel flow simulations.*

ID	Type	Formulation	Reference eq.	Damping	Model constants
DM	Mixed	Dynamic	(4.25)-(4.26)-(4.28)	Implicit	(4.29)
DS	Eddy viscosity	Dynamic	(2.22)-(2.23)-(2.38)	Implicit	$0 \leq C_s \leq 0.23$
NM	No model				
SM	Eddy viscosity	Static	(2.22)-(2.23)	(2.26)	$C_s = 0.1$
SMVD	Eddy viscosity	Static	(2.22)-(2.23)	(2.24)	$C_s = 0.13$
SVD	Eddy viscosity	Static	(2.22)-(2.29)	Implicit	$C_\sigma = 1.35$
VR	Eddy viscosity	Static	(2.22)-(2.27)-(2.28)	Implicit	$c = 0.07225$

for comparison. These are all summarized in Table 6.2 for clarity, with reference to the relative equations for more details. For the DM model, different tests are performed which, besides the grid and the convection scheme influence, investigate: the formulation for the eddy viscosity part, by changing the parameter α; the influence of the delta ratio scaling $(\Delta_{n,0}^2/\Delta_{m,n}^2)$, by purposely disabling it; the influence of the test filter stencil extension; the smoothing of the dynamic constants; the rotational and Galilean invariance of the model; the influence of the reconstruction procedure (5.63) in the computed statistics. In all the cases, the reference model formulation (DM) employs the delta ratio scaling with $\alpha = 0$, $m = 1$, the filter stencil involving first neighbor cells only and no smoothing of the constants, which are clipped in the ranges (4.29). Also, no reconstruction is used to compute the flow statistics.

All the computations are performed with a constant time step $\Delta t^+ = \Delta t u_\tau^2/\nu = 0.1$, which roughly ensures a maximum Courant number with the same value. Preliminary tests with higher time step values confirmed the theoretical predictions in section 5.5.3 and the numerical results in section 5.5.4, always leading to anomalous results with clear spectral bottleneck effects. As a consequence no specific tests are reported here for the time step.

For the flow initialization, a single reference NM case has been initialized on the coarse grid C by superimposing random fluctuations to the Reichardt's velocity profile (5.27). This computation has been advanced in time until the instantaneous, domain averaged, resolved kinetic energy reached a statistically steady state. This preliminary

flow field has then been used to further initialize all the remaining cases (using interpolation when necessary) and further advancing them until the new statistically steady state was reached.

For this specific test case the flow statistics are not computed by the means of the algorithm presented in section 5.6.4, but by gathering full domain flow samples at selected time intervals and applying a standard two pass algorithm[13]. In particular, mean quantities are computed as:

$$\langle\phi\rangle(y) = \sum_{i=0}^{N_s-1} \frac{1}{N_s L_x L_z} \int_0^{L_x} \int_0^{L_z} \phi(x, y, z, in\Delta t + t_0)\, dzdx \tag{6.43}$$

where ϕ is a generic variable to be averaged, t_0 is the time at which the first sample is taken, $N_s = 60$ is the number of samples used here for all the average operations and $n = 3000$ has been selected in order to have flow samples which are sufficiently separated in time to be statistically independent. The resulting sampling time and the separation time among different samples are respectively $T = 30.6H/u_\tau$ and $\Delta T = 0.51H/u_\tau$. Root mean squared (RMS) fluctuations are then computed in a second pass as $\phi_{RMS} = \sqrt{\langle(\phi - \langle\phi\rangle)^2\rangle}$. Finally, as the flow is homogeneous in the two wall-parallel directions, spatial spectral energy distributions are also presented and computed as:

$$\begin{aligned} E_{\phi\phi}(y, k_x) &= \sum_{i=0}^{N_s-1} \frac{1}{N_s L_z} \int_0^{L_z} \mathcal{F}_x\left[\phi(x, y, z, in\Delta t + t_0), k_x\right] dz \\ E_{\phi\phi}(y, k_z) &= \sum_{i=0}^{N_s-1} \frac{1}{N_s L_x} \int_0^{L_x} \mathcal{F}_z\left[\phi(x, y, z, in\Delta t + t_0), k_z\right] dx \end{aligned} \tag{6.44}$$

where $\mathcal{F}_x$ and $\mathcal{F}_z$, which denote the Fourier transform in the x and z directions, have been computed by a Fast Fourier Transform (FFT) algorithm. The integrals in both (6.43) and (6.44) are approximated with a trapezoidal integration method which, for the present grids and boundary conditions, reduces to a simple arithmetic average when the relative interval length, L_x or L_z, is included in the operation.

6.3 Numerical tests

The numerical results presented in the following are expressed in nondimensional viscous units (6.16). The only exception to this is for the wavenumbers $k_x = 2\pi n_x/L_x$ and $k_z = 2\pi n_z/L_z$ used in the spectral results, whose dimensions are m^{-1}. Unless otherwise stated, the grid F is used for all the computations (see Table 6.1) and the spectral results are relative to the location $y = H$.

6.3.1 Basic solver capabilities

Before addressing SGS modeling issues, it is worth to first investigate the basic resolution capabilities of the solver, in order to select the most suitable numerical settings

[13] In order to extract spatial informations which, otherwise, would not be available.

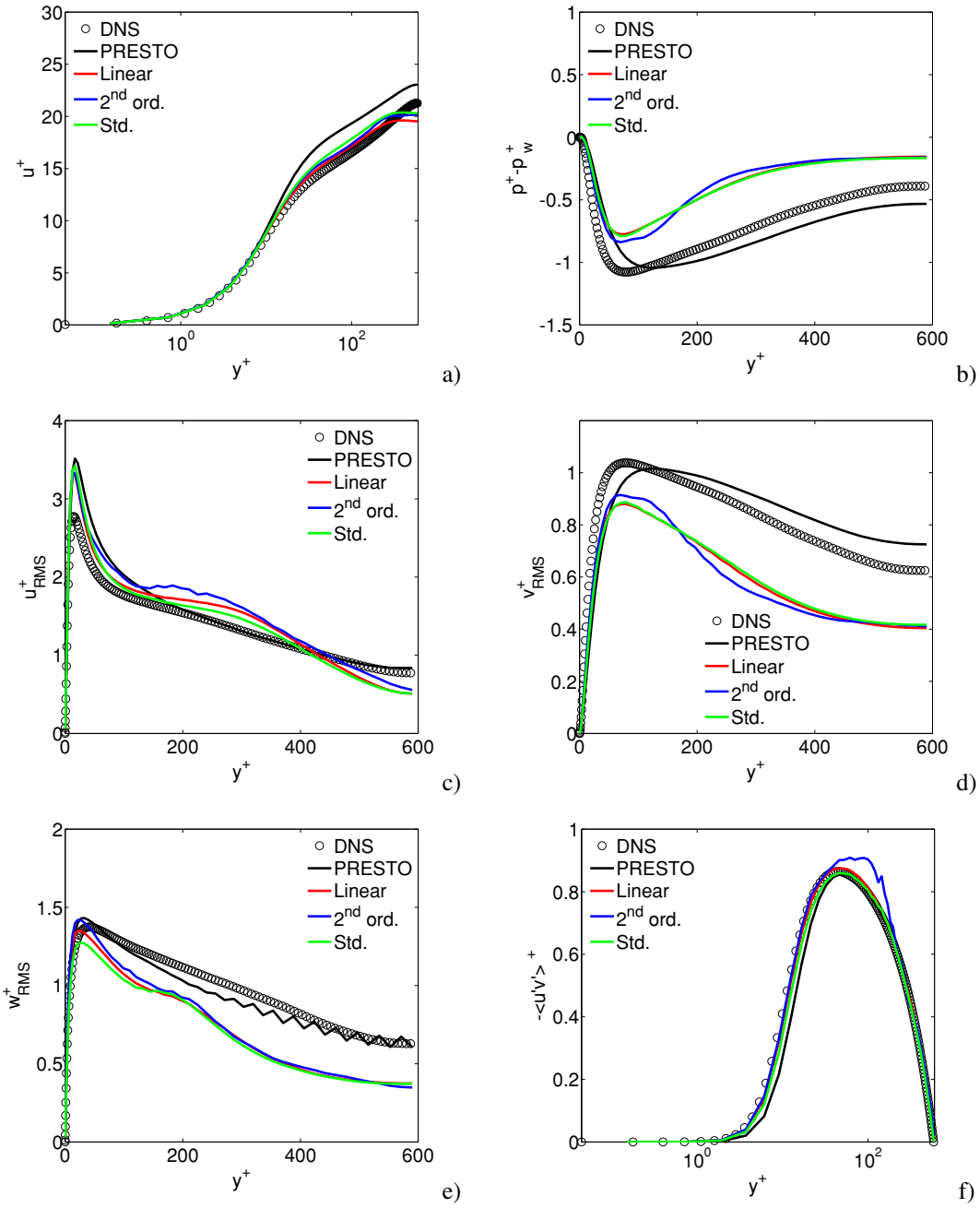

Figure 6.2: *Mean and RMS quantities for the channel flow with different pressure discretization schemes. No-model simulations with central scheme.*

for all the forthcoming tests. Two aspects, in particular, are first investigated, which are related to the pressure and convective term discretization.

The effects of the pressure discretization are shown first, in Figures 6.2 and 6.3, where the main statistical quantities for the channel flow are presented for the pure central convective scheme and no model for the SGS terms. More specifically, the PRESTO discretization scheme is compared with all the available alternatives, except the BFW whose results are similar to the ones for the PRESTO. These include the

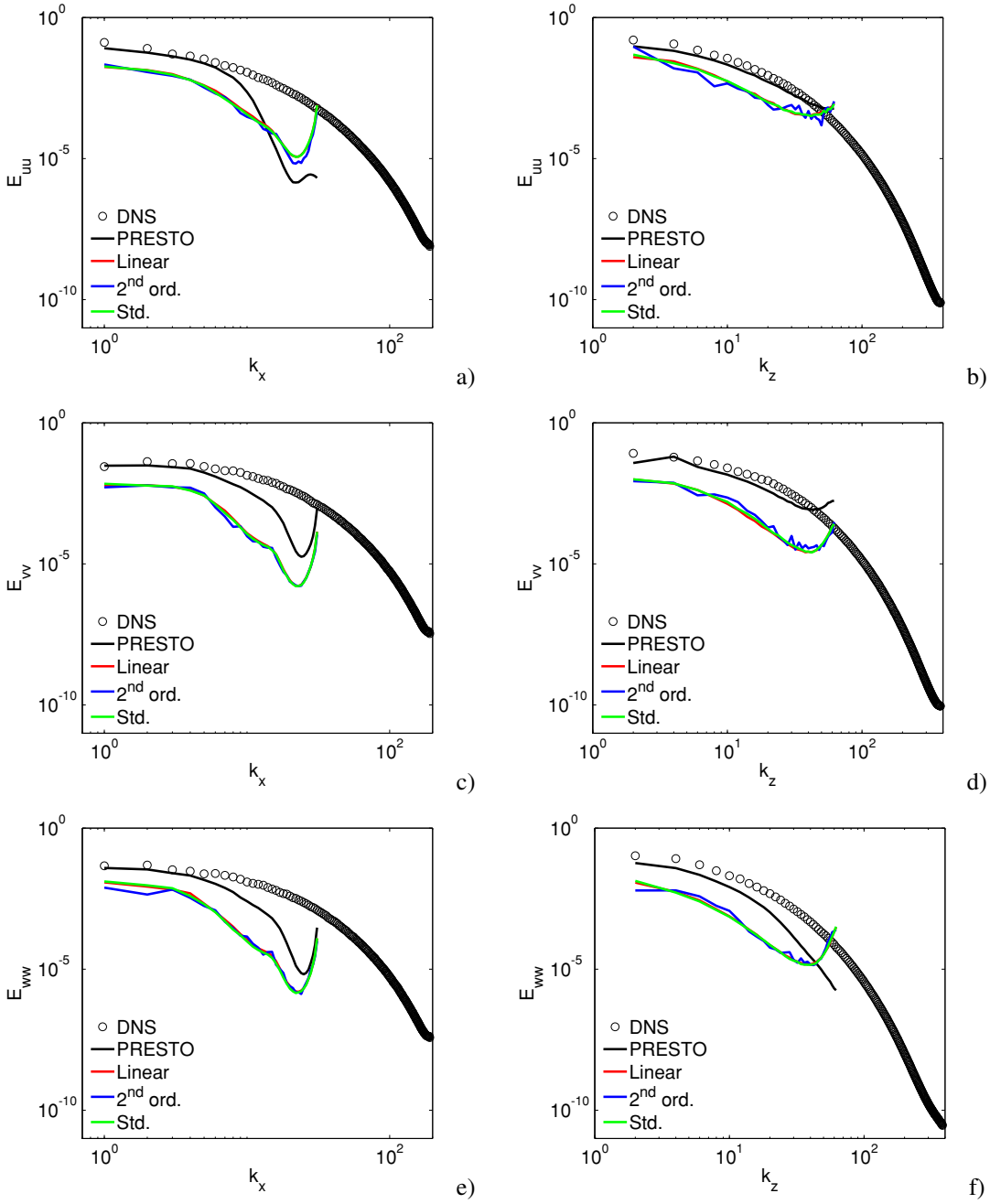

Figure 6.3: *Spectral energy distributions for the channel flow with different pressure discretization schemes. No-model simulations with central scheme.*

second order scheme (2^{nd} ord.) also analyzed in section 5.5.4, a linear scheme based on equations (5.9) and (5.10) and the standard scheme (Std.) based on equations (5.9) and interpolation trough the discrete coefficients appearing in the momentum equations (see ANS (2010) for more details.). The main outcome of this comparison is that, despite the better agreement for the mean velocity profile (subfigure 6.2a) and, consistently, for most of the resolved tangential stresses (subfigure 6.2f), all the remaining results are strongly distorted for the simulations not employing the PRESTO discretization. The

spectral energy distributions (Figure 6.3), in particular, are also inconsistent as even the energy content in the largest scales is strongly underestimated, which is in contradiction with the main assumption in LES, requiring the correct prediction of the largest flow scales.

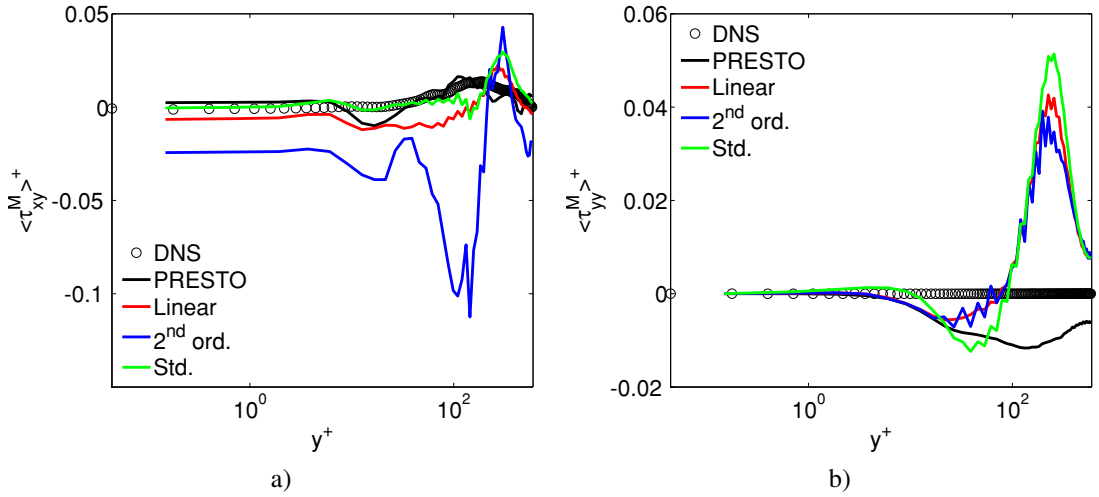

Figure 6.4: *Spurious LES effects in the momentum equations for different pressure discretizations. No-model simulations with central scheme. a) x momentum. b) y momentum.*

Several causes can be identified that, at least partially, justify these behaviors. First, the strong underestimation of the energy for all the velocity components suggests a possible effect due to a positively divergent velocity field. Indeed, as shown in equation (3.17), a spurious creation of mass represents a net negative source of kinetic energy, as the available energy is redistributed over the augmented mass of fluid. This is also coherent with the analysis presented in section 5.4 and the fact that the PRESTO scheme is designed to minimize the inconsistency with the pressure equation. A confirmation of this can be also obtained by looking at the spurious term in equation (6.17), $\langle \tau_{yy}^M \rangle^+$, which is derived by adding together the mean pressure (subfigure 6.2b) and the square of the RMS wall-normal velocity fluctuation (subfigure 6.2d). Indeed, as shown in equation (6.3), this term also contains a direct contribution due to the divergence of the mean velocity field, which is expected to be more relevant with respect to the remaining numerical part and the squared mean vertical velocity[14]. This quantity is presented in Figure 6.4b and is effectively positive in the channel center. Also, by comparison with the same quantity for the x momentum equation, $\langle \tau_{xy}^M \rangle^+$ in Figure 6.4a, it is apparent that the behavior of the PRESTO scheme, which appears to produce a negatively divergent field, is instead within the uncertainty of the statistics, as now both PRESTO and DNS results are non-null and roughly comparable. In contrast, in both equations, the effect of alternative pressure discretizations appears qualitatively strong and similar among different discretizations.

The net source of mass can also be appreciated by the mean velocity profiles in Figure 6.2a, as all the schemes producing a net positive divergence also have an abrupt change in the profile slope near the channel center. The fact that the remaining part of

[14]This quantity, which is not presented, has much higher absolute values for the alternative pressure discretizations than for the PRESTO one. Still, its square is actually negligible.

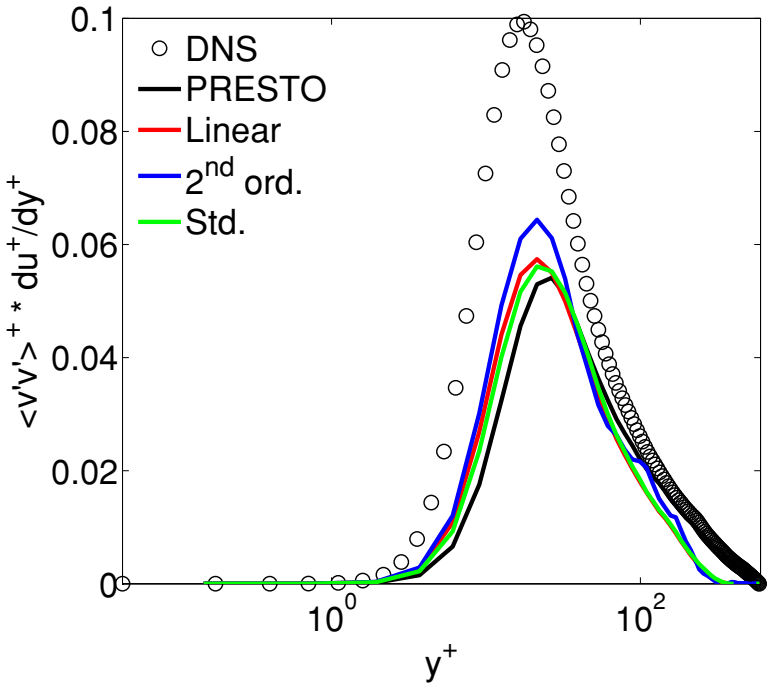

Figure 6.5: *Source term in the tangential stress equation for different pressure discretizations. No-model simulations with central scheme.*

the profile is instead better predicted by these schemes can be justified by looking at the resolved tangential stress. Indeed, except for the second order scheme, this appears to be better predicted in the range $0 < y^+ < 100$. This better prediction can, in turn, be motivated by the different pressure behavior which, while being completely erroneous in the channel center, is much closer to the DNS one in the near-wall region. While this can be hardly appreciated in Figure 6.2b, the resulting effect in the $\langle u'v' \rangle^+$ source term, equation (6.33), is evident, as shown in Figure 6.5. Thus, the alternative pressure discretizations, while altering most of the basic flow features, are capable to better represent the near wall pressure behavior which, in turn, is responsible for a better prediction of the tangential stress and, finally, for the near-wall velocity profile. However, no matter how desirable this feature might be, it is obvious from the previous results that such alternative pressure discretizations are certainly not well suited for LES, as their overall behavior produces strongly unphysical results. As a consequence, in all the remaining tests, the PRESTO scheme is confirmed as the default pressure discretization scheme. It is worth highlighting that no particular effort has been put in assessing the dependence of the alternative schemes from the remaining discretization options. Nonetheless, the effective existence of such dependence seems unlikely.

The second basic solver aspect that needs a preliminary investigation is the convective scheme. The three options preliminarily investigated in section 5.5.4, the central scheme, the bounded scheme and the symmetry preserving scheme, are compared in Figure 6.6 for some representative flow statistics. In order to better understand the outcome of the analysis, the addition of the DS model is also investigated for two of the schemes. The main fact emerging from the comparison is that the three schemes

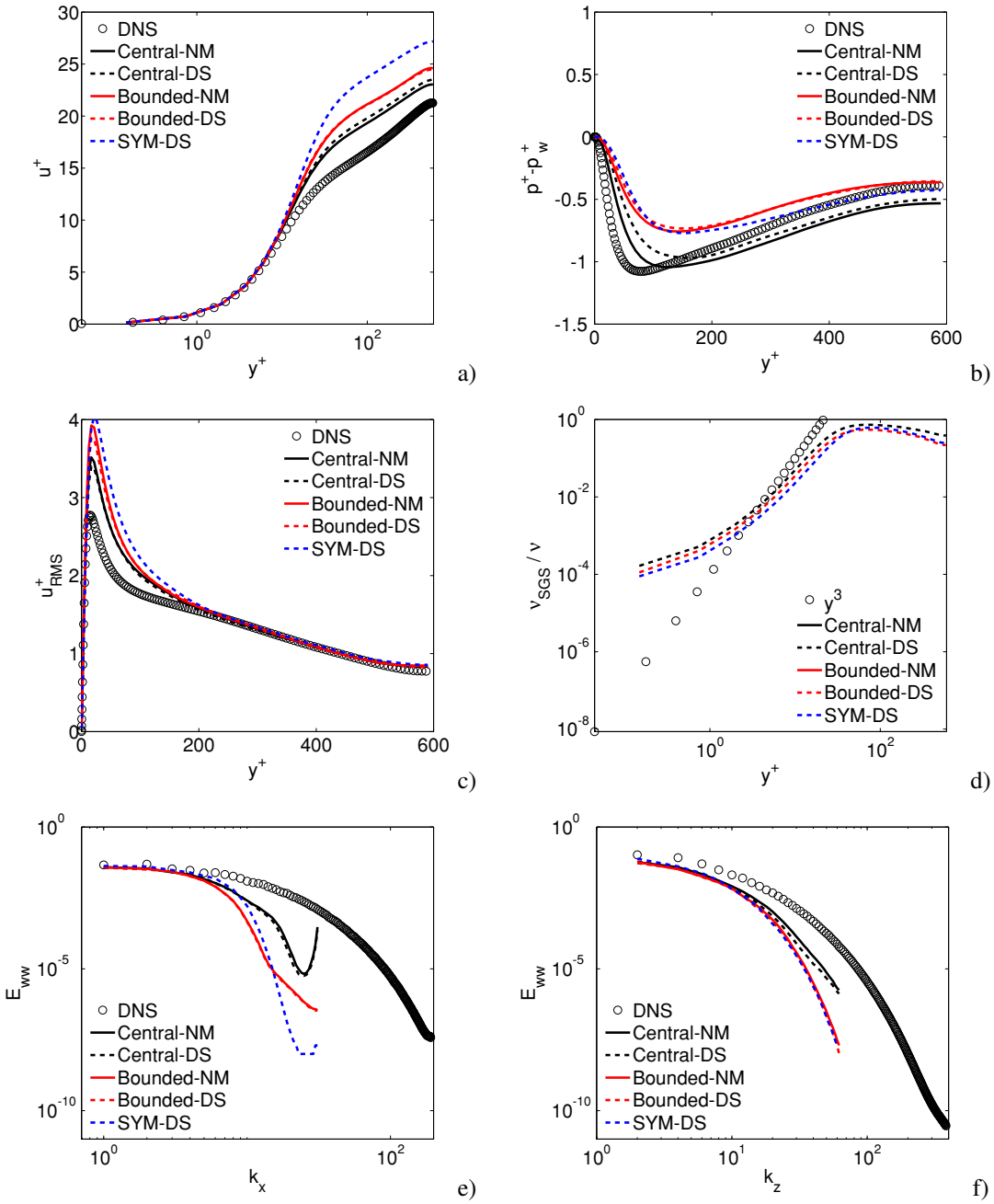

Figure 6.6: *Main flow statistics for the channel flow with different convective schemes. DS vs. NM computations.*

behave very differently and, more specifically, with very different levels of dissipation. This can be appreciated from the spectral results, Figures 6.6e and 6.6f, as most of the differences among the schemes are concentrated at the smallest resolved scales. An interesting feature emerging from these figures is that the addition of a SGS model (DS) has nearly no influence while the dominant dissipation is due to overall numerical setting. In particular, somehow surprisingly, the central scheme is found as the less dissipative while the bounded and the SYM scheme nearly have the same level of

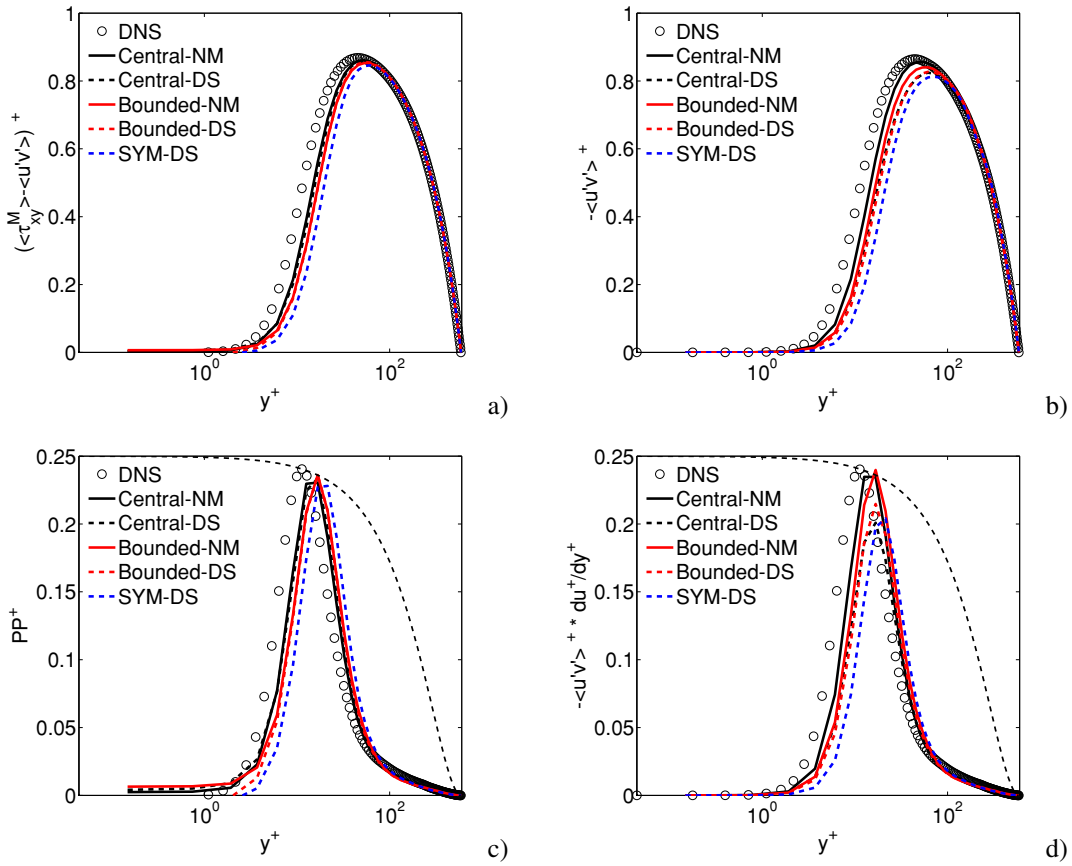

Figure 6.7: *Additional statistics for the channel flow with different convective schemes and SGS modeling options. a) Equivalent tangential stress. b) Resolved tangential stress. c) Pseudo production. d) Resolved production.*

dissipation. This fact, which is in straight contradiction with the assumption regarding the SYM scheme, suggests that there might be solver details preventing the disabled reconstruction to behave as expected. However, it is also true that it might be the implicit treatment of the higher order part in the central scheme which produces unlikely results, for both the bounded and the unbounded schemes. Indeed, while not shown in the tests presented in section 5.5.3, the implicit treatment of this part is responsible for the low energy bump in the spectra at the smallest scales, as a result of a Courant number still not sufficiently low. When the same spectral results are compared in the near wall region (not shown), much similar results are obtained among the different schemes. Still, even in this case, the SYM scheme tend to produce the highest level of dissipation in most of the cases while there is always an appreciable range of resolved scales for which the central scheme better reproduces the energy content. As a consequence, at the moment, no conclusive answer can be given on this matter. Returning back to the main results in Figure 6.6, it can be also seen that there is a net correspondence between a higher dissipation level, as discussed above, and a larger overestimation of both the mean velocity profile and the stream-wise fluctuation, with the pressure in the near-wall zone following the same trend. For the mean velocity profile this can be justified either trough equation (6.40) or by looking at the equiva-

lent stress in Figure 6.7a, which determines the mean velocity trough equation (6.24). Notice, instead, how the same correspondence does not hold with the resolved stress in Figure 6.7b, showing that the LES term is important in determining the overall velocity profile, even without a SGS model on such a relatively fine grid. The analogous trend in the resolved stream-wise velocity fluctuation, Figure 6.6c, can instead be justified by looking at the pseudo-production term in Figure 6.7c or the full resolved production term in Figure 6.7d. These two figures clarify that, independently from the actual level of production, there is a one to one relation between the distance of the production peak from the wall and the overestimation in the stream-wise velocity fluctuation. In practice, the farther is the peak from the wall the higher is the velocity fluctuation, which could be justified by the fact that a peak far from the wall has a less narrow distribution toward the wall, hence it is less affected by the viscous dissipation, which is dominant in this zone. In turn, considering equation (6.32) and comparing Figure 6.7a and 6.7c, it is clear that there is a direct relation between the production peak location and the underestimation of the equivalent tangential stress. In contrast, the addition of a SGS model does not appear as a relevant factor in determining the peak location, but only its magnitude, which is always decreased by the DS model. However, such effect has nearly no influence on the resulting velocity fluctuation. Finally, it is also worth noting that the implementation of the DS model, independently from the convective scheme, nearly reproduces the expected y^3 behavior for the SGS eddy viscosity, Figure 6.6d, even if not exactly.

In conclusion, from the analyses presented above, emerges that the combination PRESTO/Central scheme is optimal for LES computations in Fluent® and the general trend of the results is in complete accordance with the theoretical analysis provided in section 6.1. The overall effect of adding the DS model does not seem especially satisfactory for two reasons. On one side, because of the basic features of the solver without a SGS model, it is apparent that it is not an added dissipation that is needed to improve the results, as the most influencing quantity, the equivalent tangential stress, is already underestimated in the important near wall zone and the DS model does not significantly affects it, due to its correct near-wall limiting behavior. On the other side, the effect of the added viscosity appears as strongly limited, with minimum differences in all the quantities between the NM and the DS cases. From the analysis in section 5.5.3 seems that a possible cause might simply be the low value of the dynamic viscosity predicted by the dynamic procedure implemented in Fluent®, which instead should be higher to produce a net effect on the resulting spectra.

6.3.2 Dynamic Mixed SGS model

The proposed dynamic, mixed SGS model in its default setting (DM) is compared next with alternative SGS modeling options. In particular, the comparison is made with a no model computation (NM), the default Fluent® implementation of the dynamic Smagorinsky model (DS), a novel implementation of the dynamic Smagorinsky model based on the present dynamic procedure developed in the GLES framework (DS-Present) and the dynamic mixed model without the proper scaling based on the squared delta ratio (DM-NDR). The results from the different models are presented in Figures 6.8-6.11.

A general comment that can be made is that, overall, the proposed model provides a

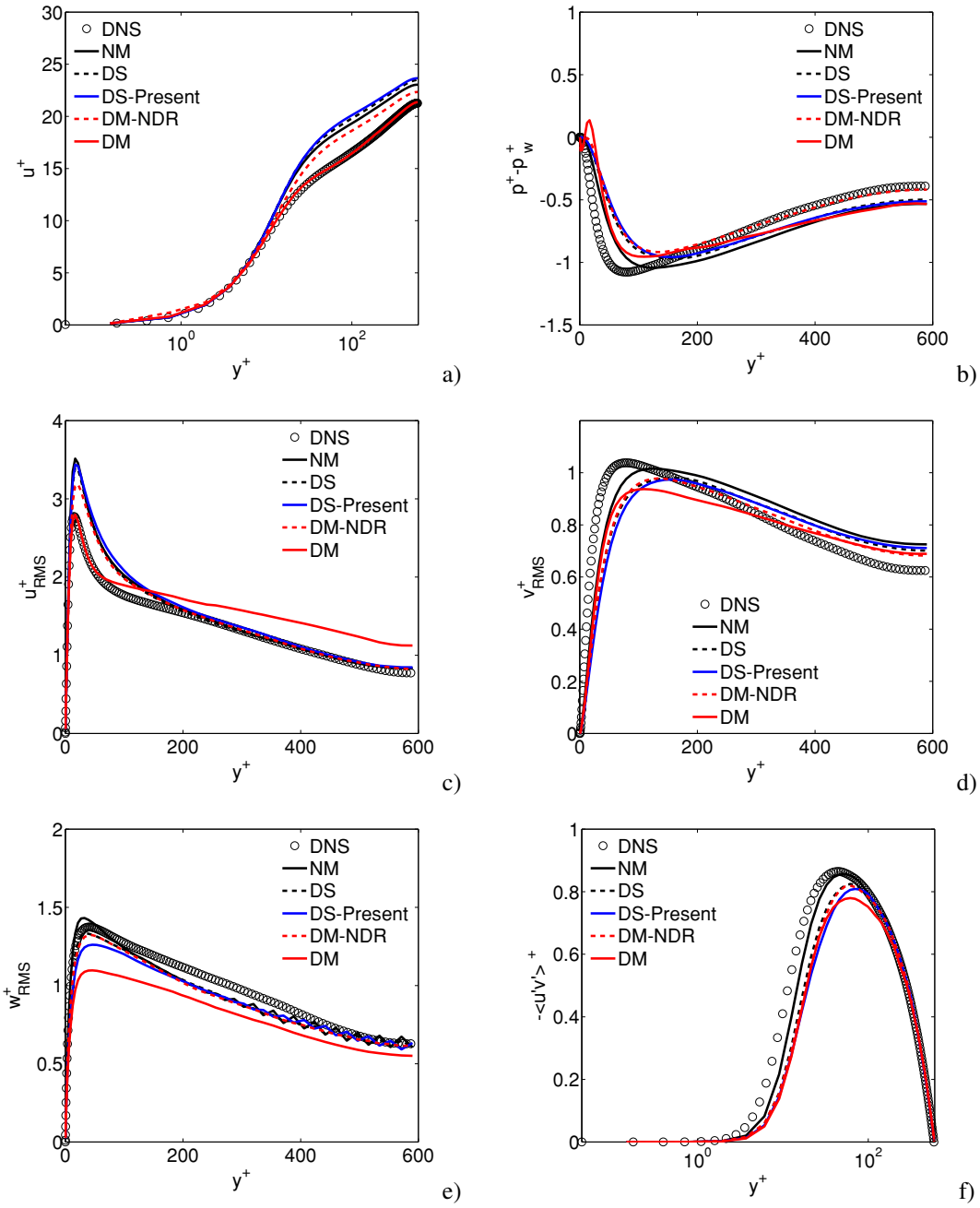

Figure 6.8: *Mean and RMS quantities for the channel flow with different SGS models.*

better, almost perfect, resolution for the mean velocity profile (subfigure 6.8a), the near wall peak in the stream-wise velocity fluctuation (subfigure 6.8c) and the stream-wise spectra at $y/H = 1$ (subfigures 6.9a-c-e). No particular differences are found, with respect to the other models, in the transverse fluctuations (subfigure 6.8d-e), except that, for both, slightly lower values are predicted. The span-wise energy content at $y/H = 1$ (subfigures 6.9b-d-f) is instead overestimated at the smallest scales, where the dissipation levels appear lower than in the remaining models. Wherever necessary, the model is capable to remove the anomalous low energy bump in the stream-wise spectra

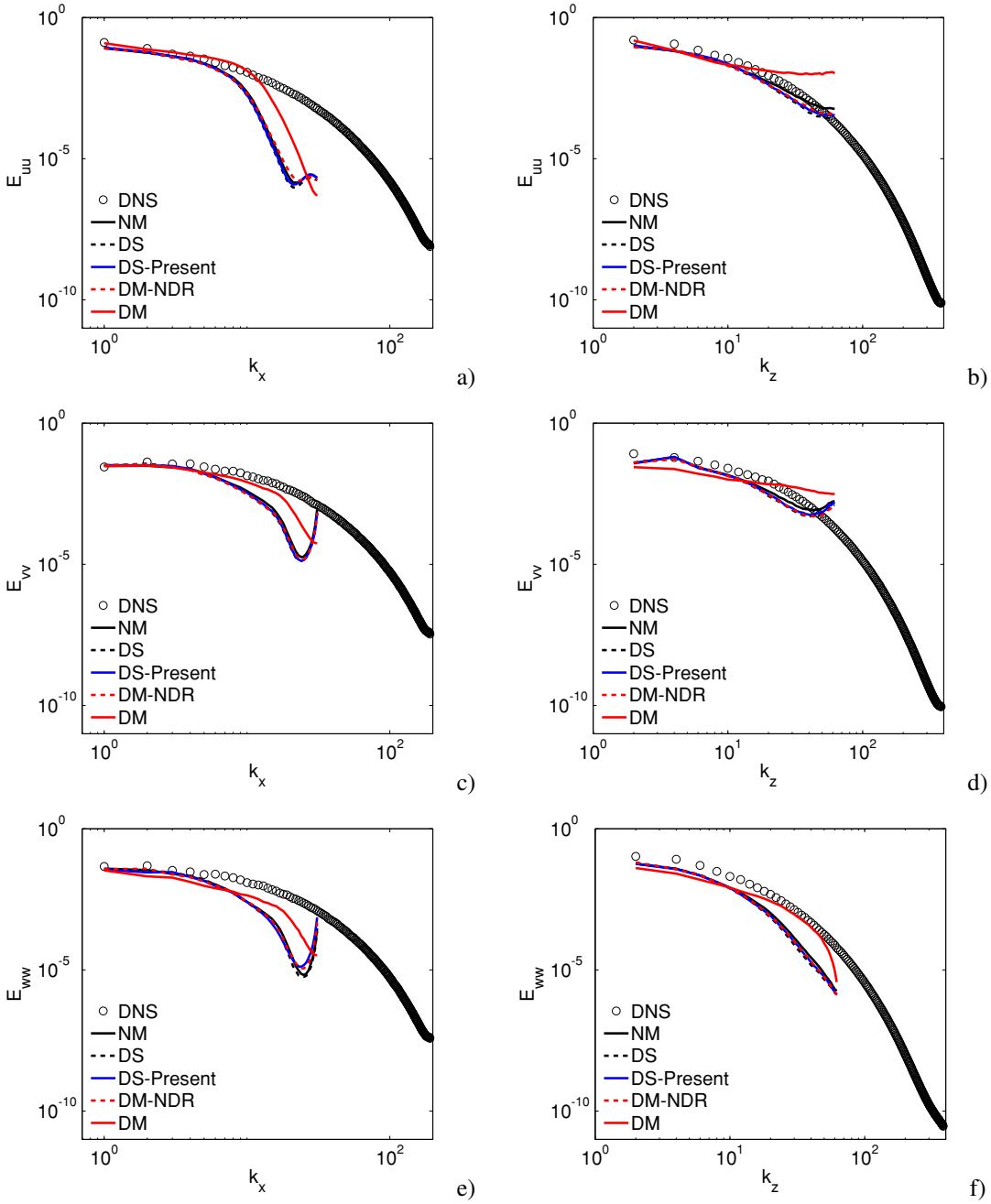

Figure 6.9: *Spectral energy distributions for the channel flow at $y/H = 1$ with different SGS models.*

but, in the near wall region (Figures 6.10 and 6.11) the differences in the spectra are mitigated. Two anomalous results are also found, which are the higher level of streamwise fluctuations in the channel center and a slightly non monotone pressure behavior in the near wall region. However, the overall spectral behavior of the model seems in line with the expectation, producing a recovery of the energy at the intermediate frequencies and, possibly, enhancing the effective dissipation at the smallest scales for $y/H = 1$.

The better prediction in the mean velocity profile can be justified by a general lower

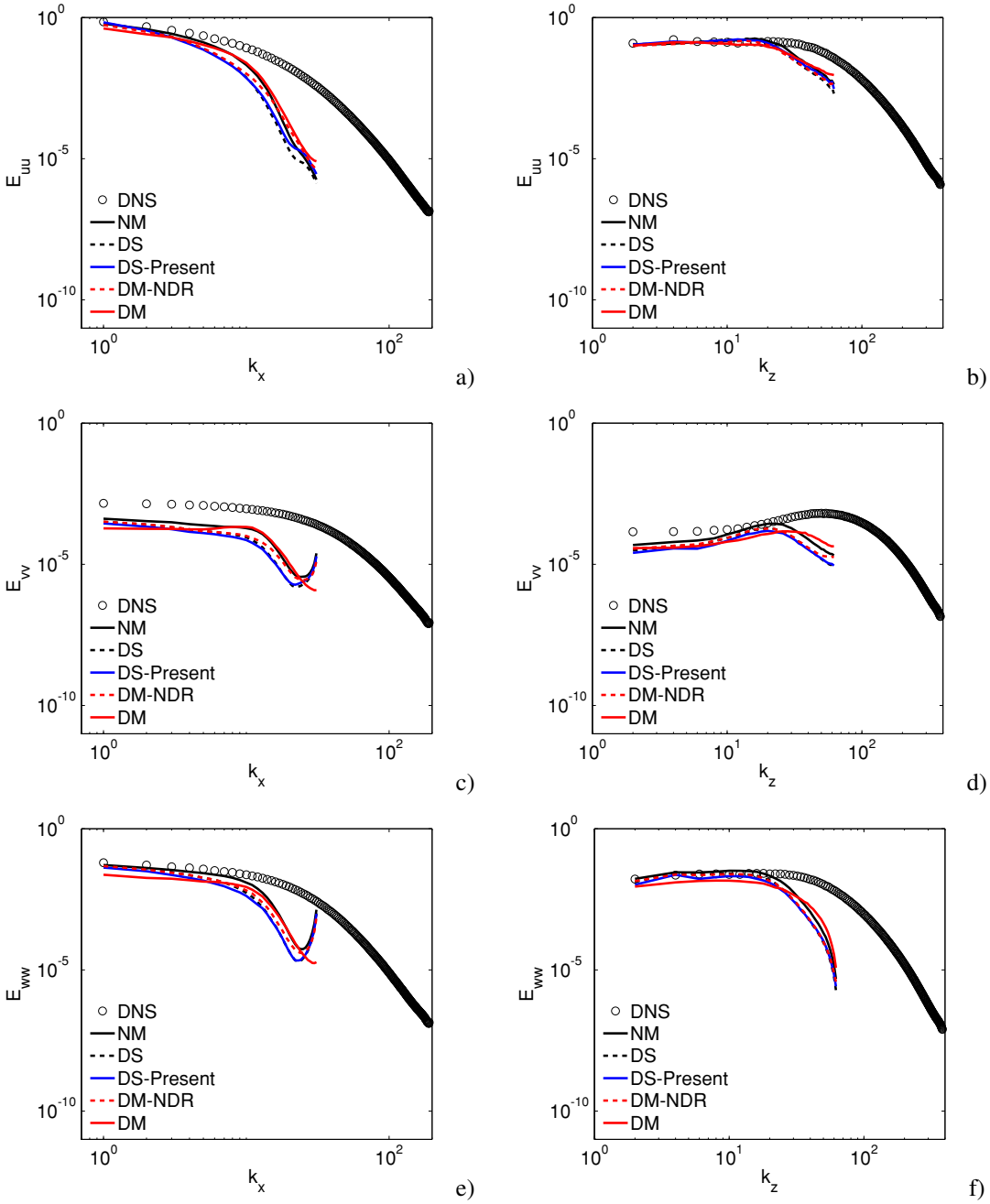

Figure 6.10: *Spectral energy distributions for the channel flow at $y^+ = 5$ with different SGS models.*

dissipation, according to equation (6.40), or, more precisely, by a better reconstruction of the equivalent tangential stress. Indeed, while the resolved tangential stress (subfigure 6.8f) is the lowest among the SGS models, the equivalent one (not shown) is necessarily in accordance with the velocity profile and closely follows the reference DNS. This, in turn, can be associated with higher values of $\langle \tau_{xy}^{LES} \rangle$ in the near wall-region (not shown), which counteract the low values of the resolved tangential stress, limited by the scarce resolution. The observed behavior for the pressure is, instead, solely a consequence of the model acting on the velocity field, as only the traceless part

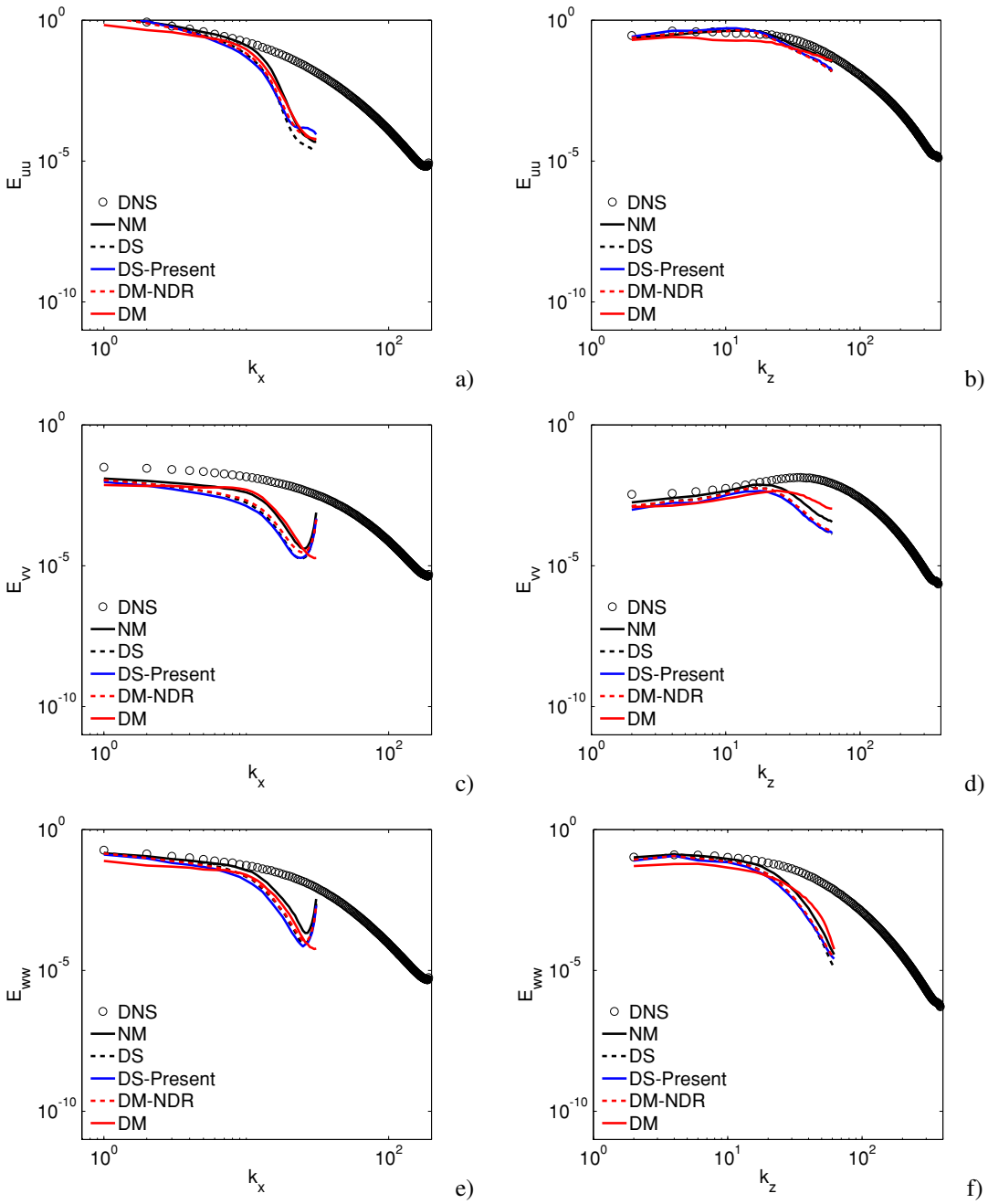

Figure 6.11: *Spectral energy distributions for the channel flow at $y^+ = 19$ with different SGS models.*

of the model has been coherently included in all the tests presented here[15]. More specifically, its behavior implies a negatively divergent mean velocity field which, in turn, is a possible enhancement for the mean velocity profile. The outcome for the streamwise fluctuation is more problematic as, analyzing the pseudo-production (not shown), it appears that it closely follows the DNS production over all the channel height, as implied by the correct velocity profile. However, this nearly perfect behavior turns out

[15] Its inclusion and correct treatment would have probably avoided the observed behavior, due to the purely dissipative features of the pressure part in the model.

to be problematic in the channel center, where it is higher than those relative to the other SGS models. Hence, in practice, transferring the correct amount of energy in the stream-wise fluctuation is negative as then this is not correctly dissipated far from the wall. Comparing the span-wise spectra at $y/H = 1$ (subfigures 6.9b-d-f) with the relative fluctuations (subfigures 6.8c-d-e), readily confirms that the observed behavior is due to the lack of dissipation and the consequent pile-up of the energy at the smallest scales. While merely increasing the maximum allowed value for the eddy viscosity coefficient would certainly serve the scope of increasing the dissipation, it will be shown in the following that a different remedy is indeed necessary, as the problem is in fact related to the way the scale-similarity constant is computed and then applied to the model[16].

A comment on the remaining SGS models is also necessary. In particular, it is evident that the same mixed model without the proper scaling (DM-NDR) is almost useless. In particular, as the model is certainly active in the near wall region, like its correct counterpart, the result on the velocity profile is positive with respect to the NM case, and the same is also true for the stream-wise velocity fluctuation. However, the effect is minimal and, as testified by the spectral results, it is not related to any enhancement of the predicted velocity field, whose spectral content is identical to the NM/DS cases, but just to a mere perturbation of the momentum equation in the right place, the near wall-zone. This seems also confirmed by the fact that the DM-NDR model has a slight overestimate of the velocity in the zone near $y^+ = 1$, where the grid stretching is higher. As a matter of fact, most of the remaining results are practically coincident with the NM case, testifying the fact that the proposed scaling is indeed necessary and correct.

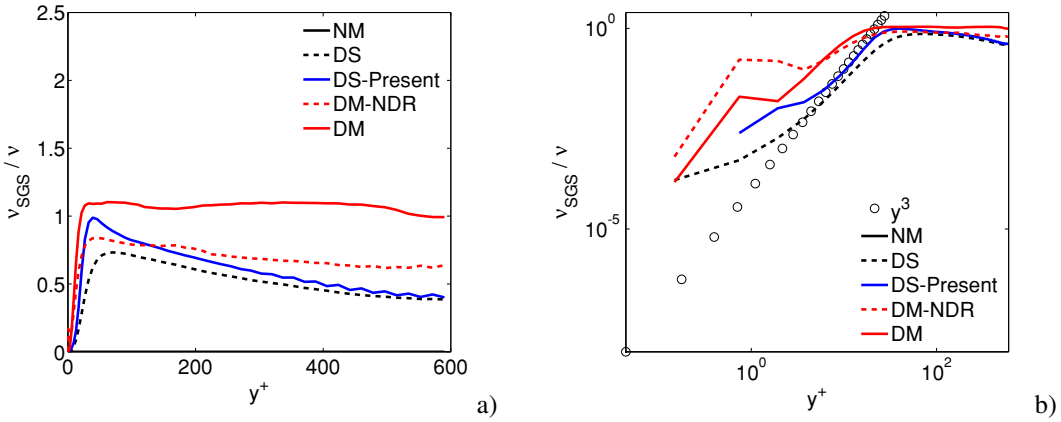

Figure 6.12: *SGS eddy viscosities for different SGS models. a) Linear scale. b) Logarithmic scale.*

Finally, the analysis of the DS model and the present, cheaper, dynamic procedure also evidences that, while not particularly useful for this flow, the latter is slightly more effective than the default DS model. In particular, as shown in Figure 6.12, the proposed dynamic procedure produces a higher eddy viscosity and the required y^3 limiting behavior is more closely respected.

[16]Indeed, no such effect is present in the stream-wise component of the spectra.

6.3.3 Effect of the eddy viscosity formulation on the mixed model

The results from the previous paragraph suggest that changing the eddy viscosity formulation might, maybe, alter the model dissipation and possibly ameliorate some of the critical behaviors observed, like the high energy content in the channel center. This would be also justified by the fact that, among the different options available in the mixed scale formulation adopted here, $\alpha = 0$ is possibly the one with the lowest dissipation, as it is the only one dependent form the small scales only. In order to test these ideas, the basic dynamic, mixed SGS model ($\alpha = 0$) is compared, on the grid F, with three alternative options: one based on the Smagorinsky model ($\alpha = 1$), one based on the original mixed-scale formulation ($\alpha = 0.5$) and one based on the Tsubokura model ($\alpha = -1$). Only few selected results are presented here, in Figure 6.13, as they are sufficient to show that, in practice, no difference exists among the different models and certainly not in the critical behaviors. The formulations based on $\alpha = 1$ and $\alpha = -1$ are effectively found more dissipative, but the resulting effect is only slightly discernible (subfigures 6.13c-f). As a consequence of this comparison, and because it provides a slightly better prediction for both the mean velocity and the stream-wise fluctuation, while having the lowest computational cost, the formulation with $\alpha = 0$ is kept as reference for the DM model.

6.3.4 Effect of the grid resolution

The effect of the grid resolution is, possibly, the most important factor when assessing the performance of a SGS model. Indeed, for LES, it would be desirable to have a model whose accuracy is independent from the filter width, at least when this is in the inertial range (Pope, 2004). However, for most practical cases, and especially the channel flow considered here, such independence might not be really possible and obviously depends from the specific statistical quantity at hand. For example, none of the DNS spectral energy distributions shown in Figures 6.10 and 6.11 has a clear inertial range. Also, the overall flow features are actually dependent from the smallest scales near the wall (see Figure 1.1 and the relative discussion). Hence, irrespective of the specific LES approach, an independence from the filter width cannot be expected. Using an implicit filtering approach, obviously, makes the matter more complicated, as the dependence form the filter width is then explicit in the equations, trough the local truncation errors.

As a consequence, whether or not an independence is effectively achievable[17], studying the influence of the grid resolution on a SGS model allows to understand its effective limits of applicability as, still today, no definite rules for the determination of the proper filter width exist, besides different heuristic estimates for different specific flows.

Two different assessments are proposed in the following, which are based on two groups of simulations compared together. The first one is based on the two grids, C and F, which simply differ by a factor of 3 in their wall normal resolution. On these two grids, which are common to the LESinItaly database, the dynamic mixed model DM is compared with the respective no model (NM) simulations, in order to understand the effective model capability to influence the flow simulations independently from the resolution. The second one is instead based on using the model DM on all the

[17] Besides the formal discussion in Pope (2004), to the best of the author's knowledge, no such independence from the filter width has been ever addressed. Note that this is different from demonstrating independence from the filter to grid width ratio, which instead simply assess the numerical convergence.

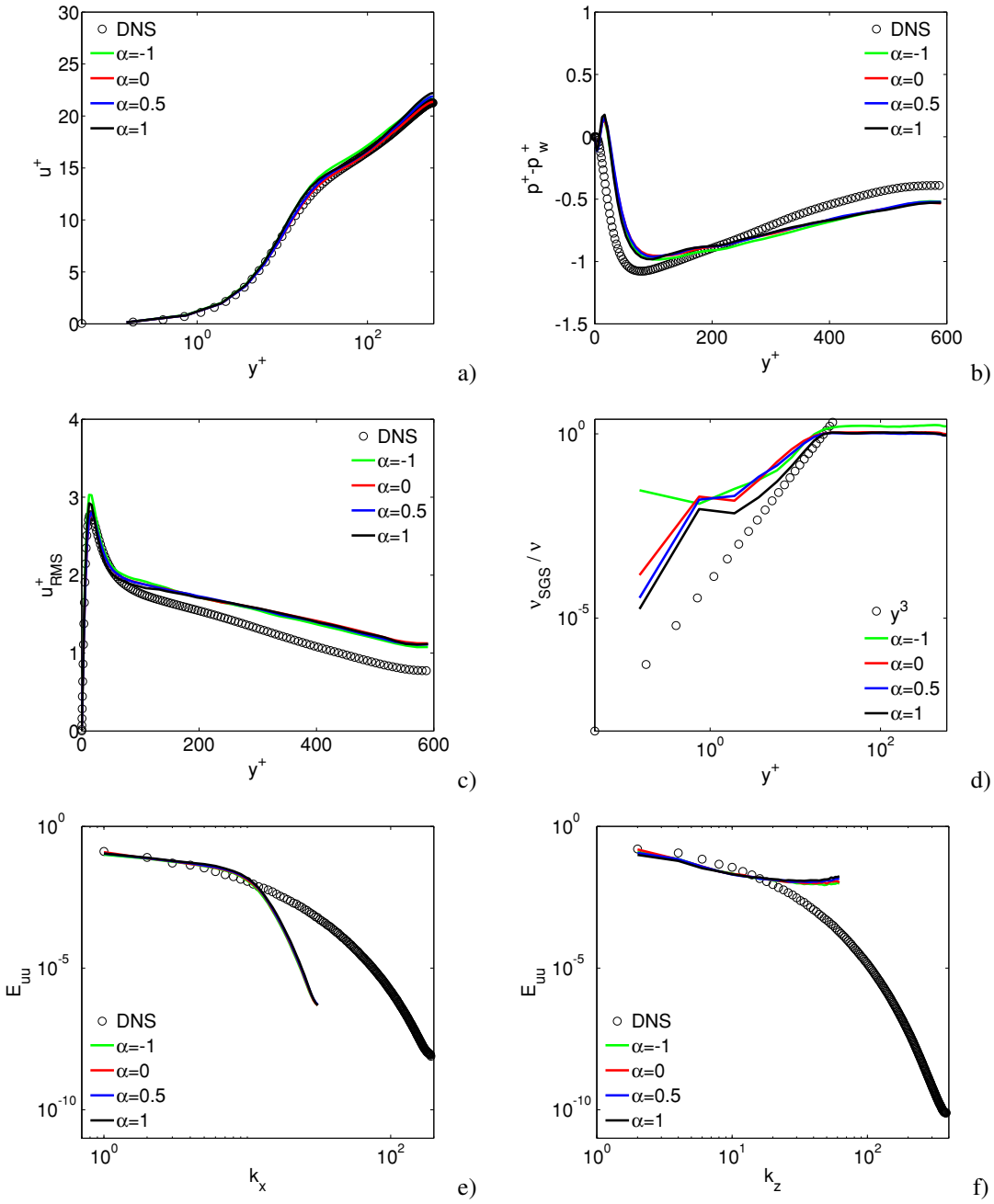

Figure 6.13: *Main flow statistics for the channel flow with the DM model and different eddy viscosity formulations.*

grids in Table 6.1, in order to understand the model dependence from all the resolution parameters.

The first comparison, presented in Figure 6.14, includes the main flow statistics usually used in applications, like the mean velocity profile and the wall-parallel velocity fluctuations. The NM-DM figures (left side) evidence that, while the model effect has the same qualitative behavior, independently from the grid, the model effectiveness is reduced for the grid C. Hence, moving from grid F to grid C, in correspondence of

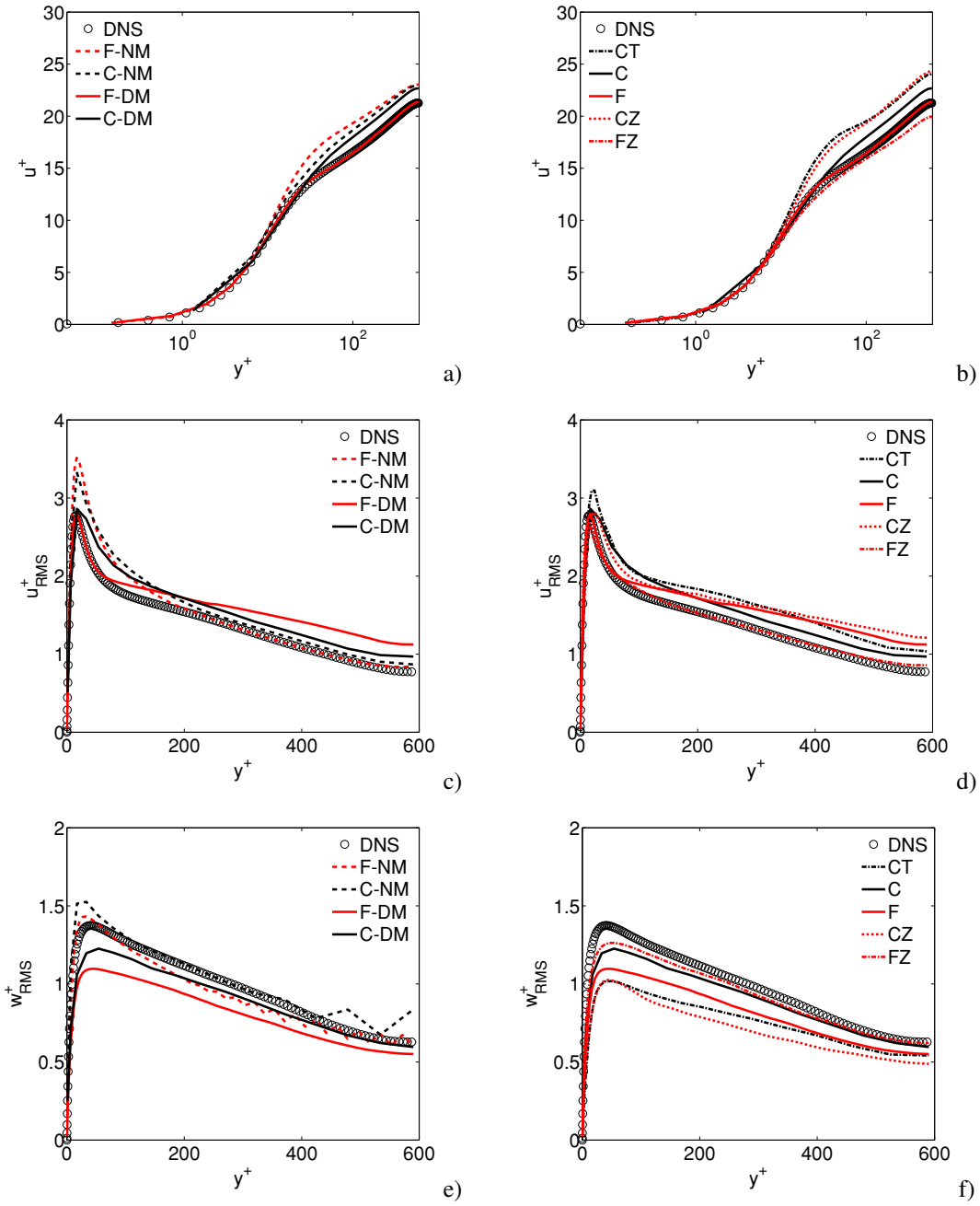

Figure 6.14: *Mean and RMS quantities for the channel flow with different grid resolutions. Left) NM vs. DM on the grids C and F. Right) DM model on the grids of Table 6.1.*

a natural increase of the numerical effects there is also an equivalent decrease in the model effect. While this is an expected feature of an implicit filtering approach, the specific details of the mechanisms at play can be better appreciated in Figure 6.16a, where the mean LES effect $\langle \tau^M_{xy} \rangle^+$ is represented. It is evident that, despite some minor differences in the channel center, to be discussed in the following, the qualitative and quantitative behavior of the DM model is independent from the grid, which is no less than the maximum expectation from a SGS model. However, as a consequence of

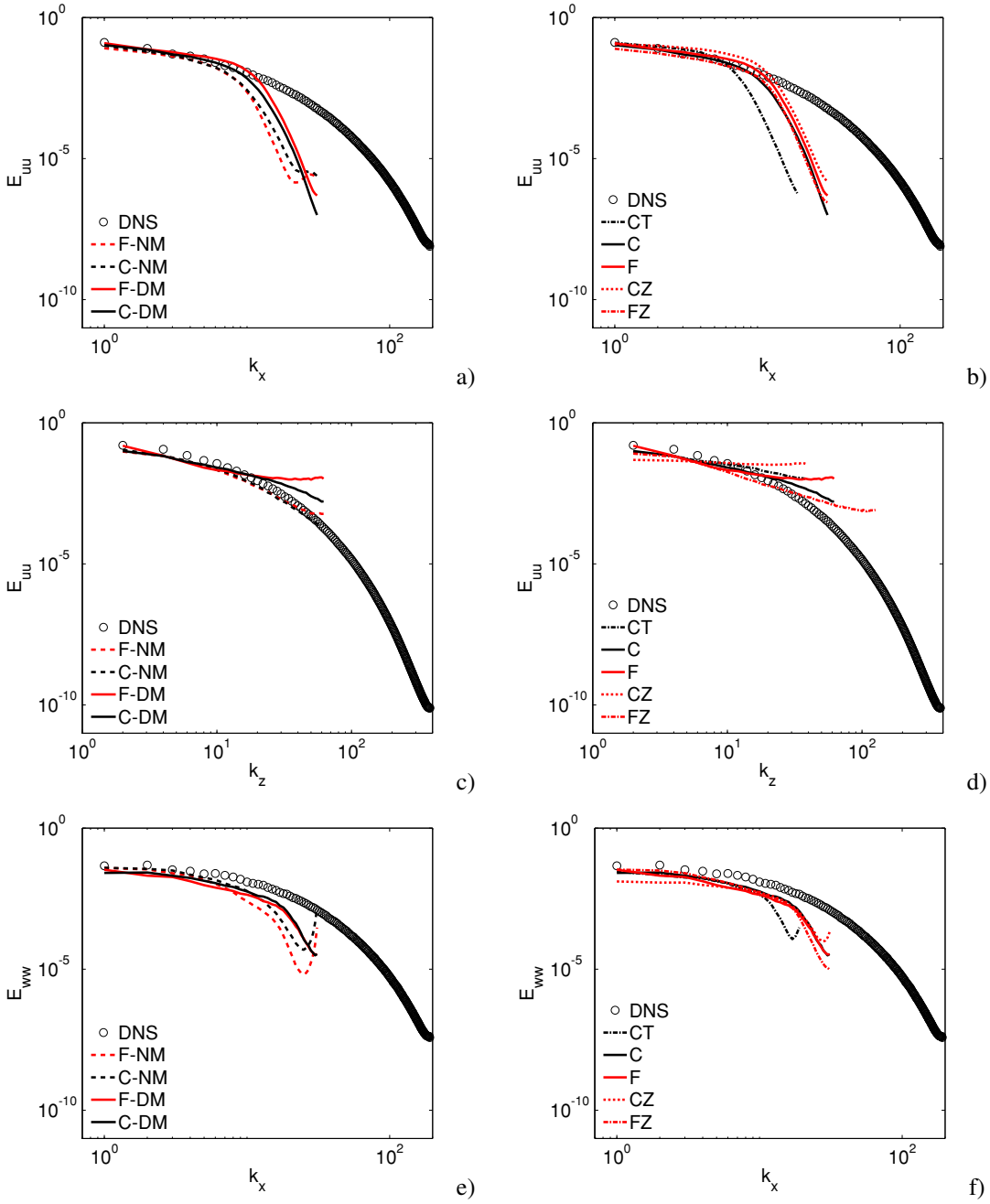

Figure 6.15: *Representative spectral energy distributions at $y/H = 1$ for the channel flow with different grid resolutions. Left) NM vs. DM on the grids C and F. Right) DM model on the grids of Table 6.1.*

the scare resolution on the grid C, the anti-diffusive model effect in the near-wall zone cannot be resolved and the resulting model effectiveness is strongly limited. Paradoxically, the NM simulation on the grid C has a near-wall numerical effect which closely resembles the one of the DM model and, as a consequence, the relative velocity profile improves the NM one on the grid F, where such numerical error is consistently reduced.

In contrast, the model effectiveness is stronger for the stream-wise fluctuation (subfigure 6.14c) as, independently from the grid, the near-wall peak is correctly repro-

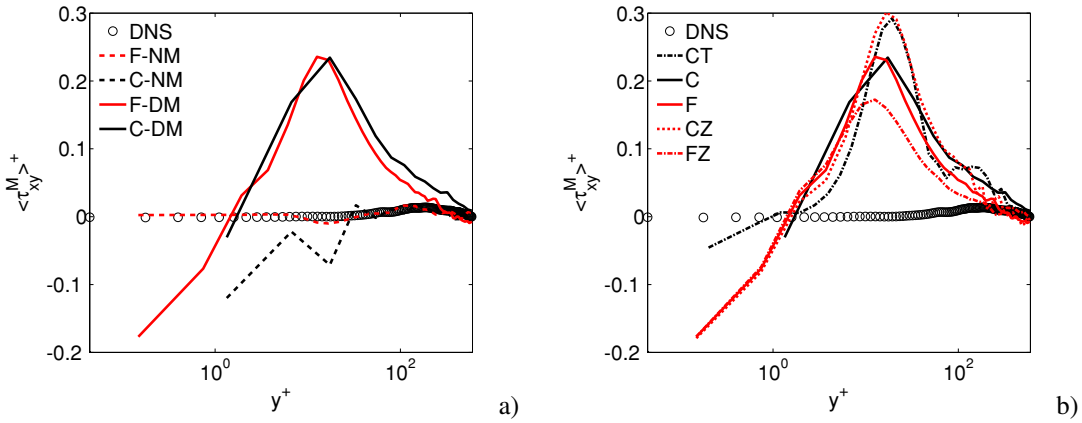

Figure 6.16: *Mean LES effect in the x momentum equation. Left) NM vs. DM on the grids C and F. Right) DM model on the grids of Table 6.1.*

duced. It can be also noted that the simulation on the grid C has a lower overestimation in the channel center, which is a direct effect of the higher $\langle \tau_{xy}^M \rangle^+$ values discussed above. Note, in particular, that these are mostly related to the higher velocity derivative and the higher eddy viscosity resulting from the larger filter width. When the spectral results are analyzed, on the left side of Figure 6.15, it still emerges that the qualitative behavior of the model is not impaired by the grid, especially in relation to the differences between the NM simulations. However, specific quantitative differences emerge for the stream-wise velocity, which confirm the fact that a higher dissipation would improve both the spectra and the fluctuations.

The analysis on the remaining grid parameters, right sides of Figures 6.14, 6.15 and 6.16, reveals an additional effect, typical of wall bounded flows, that the DM model appears to not be able to contrast. Indeed, what these figures show is that the span-wise resolution has a strong influence on the results, while both the wall-normal and the stream-wise resolutions have a relatively lower effect.

In particular, as depicted in Figure 6.16b, the effect of reducing the span-wise resolution (red curves) consistently increases the model effects, but with two issues. On one side, increasing the resolution (e.g., grid FZ) does not deactivate the near wall anti-dissipative effect, hence producing the slight underestimation of the velocity profile (subfigure 6.14b). In contrast, the increase in the model effect in the range $1 < y^+ < 100$, which emerges as function of the span-wise spacing only, is not able to counteract the fact that the flow driving mechanism is not anymore resolved or even represented on the grids with $N_z = 40$ (CT and CZ), as the stream-wise wall streaks have span-wise spacings which are comparable to the span-wise grid step. Hence, a sort of grid independence is achieved and, despite the very different spacings in the remaining directions and the resulting numerical error effects, the two grids CT and CZ provide very similar results. Even in this case, the latter effect is no less than the maximum expectation from a model which is not specifically equipped with wall-functions or alternative eddy viscosity formulations, more suited for a not resolved wall region. A different sensitivity to the span-wise spacing for $0 \leq y^+ \leq 1$ could be desirable but, for the given resolutions, the independence shown by the model should be considered correct and not a deficiency.

Moreover, the analysis of the remaining quantities reveals that some positive effects due to the model are still present. For example, a very low sensitivity is shown in the resolution of the near-wall peak of the stream-wise velocity fluctuation as well as in the channel center. Also, besides the due differences, similar spectral results are also obtained (right sides of Figure 6.15), with the CT and CZ grids being the only ones showing a slight energy pile-up at the smallest resolved scales. In conclusion, while not optimal, the results of this grid sensitivity analysis reveal that the proposed DM model is not affected by particular, grid related, issues and preserves most of its specificities independently from the grid. In practice, the reported differences can be ascribed to the effective capability of the grids in sustaining the flow, more than a possible negative grid effect on the model.

6.3.5 Effect of the filter stencil

A model parameter which deserves attention is the stencil of the test filter, which in the present implementation is the only parameter affecting the test filter width. Indeed, the test filter directly influences the dynamic procedure, the scale similar part and even the eddy viscosity part (for the present mixed scale model). In this section these effects are investigated by changing the number of cell layers N_L in the filter stencil (see section 5.6.2 for more details). In particular, the default setting with $N_L = 1$ and first neighbor cells only involved in the stencil (DM) is compared with an extended stencil formulation with $N_L = 2$ and a no model formulation (NM).

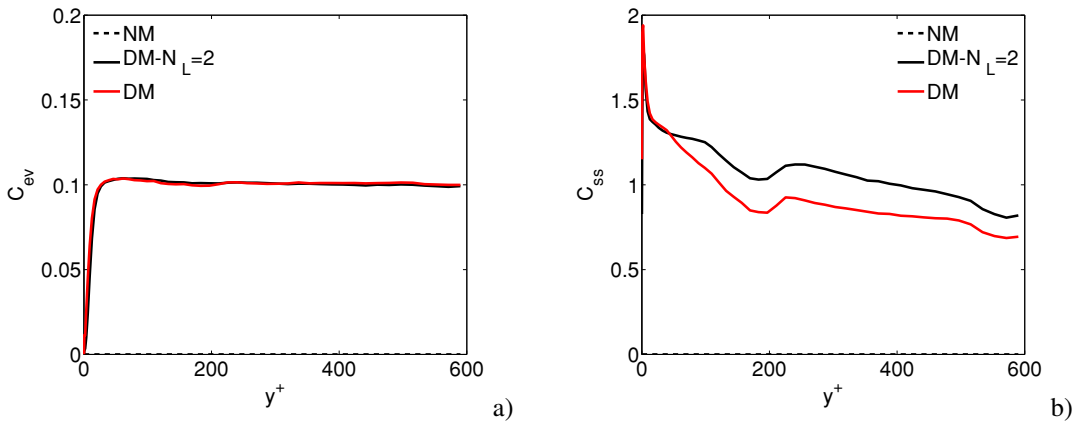

Figure 6.17: *Effect of the filter stencil on the dynamically computed constants.*

The representative set of results presented in Figure 6.18 reveals that two main aspects are involved in the filter extension. On one side, the overall dissipative features of the model are increased in the logarithmic region, as revealed by the subfigures 6.18c-d. This, in turn, has two effects: a slight overestimation of the mean velocity in the same zone and a substantial recovery of the stream-wise velocity fluctuation, which is now correctly predicted over most of the channel height. This behavior seems in accordance with the expected one. Indeed, by construction, the present scale similar term is such that it is always scaled to be representative of the true SGS stresses, independently from the filter width. In contrast, the eddy viscosity part (for $\alpha = 0$ used here) contains a strong connection with the test filter width, because of its functional dependence on

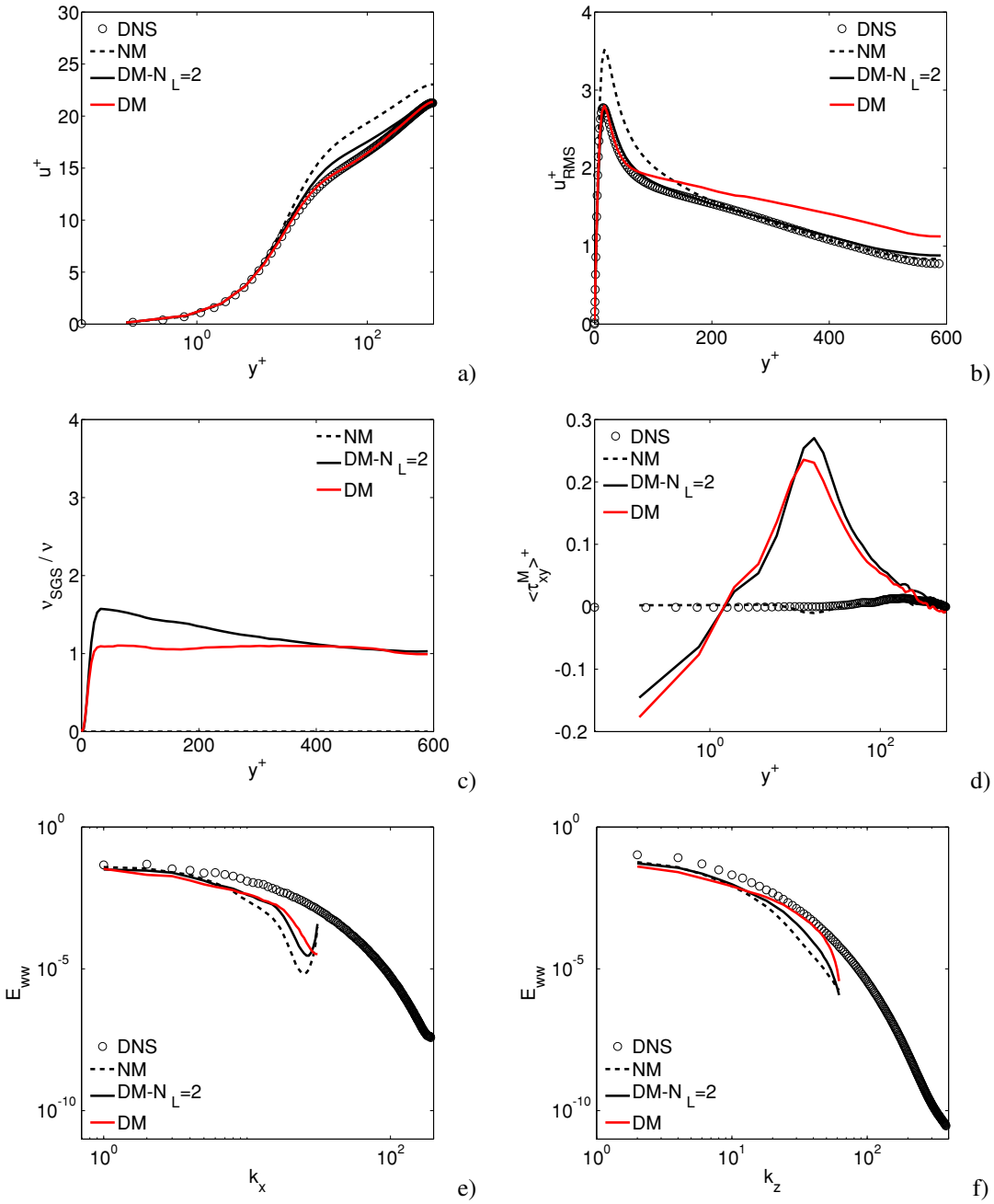

Figure 6.18: *Main flow statistics for the channel flow with different filter stencils.*

the sub-test kinetic energy (see equation (4.26)). However, when the overall model is inserted in the Germano identity (3.15), it is still the scale similar part that plays a dominant role in the dynamic procedure[18], while the eddy viscosity part is usually constrained by its specific formulation. Hence, the dynamic procedure tends to give almost the same results as for the lower filter width, possibly increasing the scale-similar constant but leaving unaltered the eddy viscosity one. This is indeed confirmed in Figure

[18]Remember that the known term in the GGI is equal to the unscaled scale-similar term.

6.17, where the average profiles of the two dynamically computed constants are shown. Thus, with the eddy viscosity constant substantially unaltered, changing the filter width then increases the present eddy viscosity where there is more difference between the resolved kinetic energy and the test filtered one, which is around the production peak.

The second aspect involved in the extension of the filter stencil is that, because of its specific volume average formulation (4.19), the enlarged filter is not able to completely remove the highest spatial frequencies from the current solution. Then, notably, while the augmented dissipation of the model is apparent in the spectra (subfigures 6.18e-f), the stream-wise spectral result also reveals a different trend. Indeed, with the present filter stencil, the same frequency band less affected by the test filter appears also less affected by the overall model and dynamic procedure, while the rest of the spectrum mostly retains its favorable properties. This behavior somehow shows that the dissipation of the energy peak in the largest frequencies is strictly related to the scale similar formulation and its underlying test filter, possibly in connection with the hyper-viscosity effects evidenced for the viscous term (see section 4.7). However, the overall results appear unaffected by this slight pile up of energy and as valid as the ones for the smaller stencil.

6.3.6 Smoothing the constants

A typical approach used in CLES to regularize the dynamically computed constants consists in smoothing them with the test filter before applying the clipping rules. This is usually justified on the basis that the inconsistent extraction of the constant from the test filter (see equation (2.35)) implies that the latter is smooth on the test filter scale. However, the same reasoning does not apply to the GLES framework, because the constants are not extracted from any test filter. In contrast, the clipping is nonetheless necessary in both cases, as the dynamic procedure does not ensures that the resulting constants assume physically sound values.

In order to show that such smoothing is indeed unnecessary, few selected results are presented in Figure 6.19, where the default, not smoothed case (DM) is compared with a simulation whose constants are smoothed (DM-SC) with the default test filter ($N_L = 1$). All the remaining results (not shown) have the same level of agreement, hence smoothing the constants has no actual effect and is not even needed to improve the stability of the computation, which has been already testified by all the previous tests, performed without smoothing.

6.3.7 Galilean and rotation invariance

In this section two tests are performed, which are useful to understand some basic features of the model and of the channel flow computation in general. In particular, these two tests consist in performing the channel flow simulation in two different reference frames: one is fixed, but has its stream-wise axis directed along the direction $(1, 1, 1)$, hence it is rotated with respect to the original reference frame; the second one is instead still aligned with the reference axes, but moving along the x direction with a velocity $c_x = 18.72 m/s$. The former test (DM-RI) is performed by first rotating the domain, running the simulation with a rotated pressure gradient and then rotating back the flow samples before computing the statistics. The second test (DM-GI) is instead simpler as it just requires fixing a slip velocity equal to $-c_x$ for both walls, running the simulation

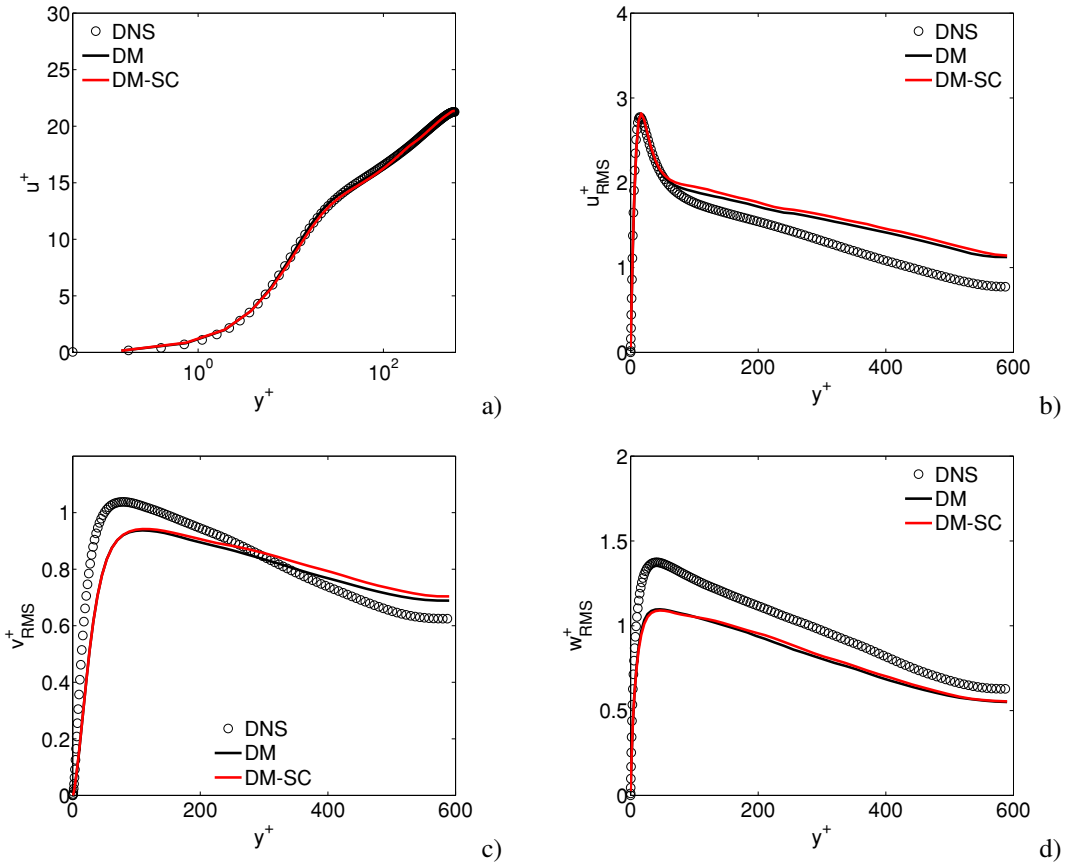

Figure 6.19: *Effect of the constants smoothing on the main flow statistics for the channel flow.*

and then adding c_x back to the flow samples before computing the statistics. In an ideal situation, both tests would give exactly the same results of the previous sections. However, both the numerical method and the SGS model can indeed alter the simulation in several aspects.

These effects are shown in Figure 6.20 and 6.21 where such computations are compared with the default DM one and a NM one. Considering first the effect of the rotation (DM-RI), it appears that most of the flow statistics are, indeed, largely independent from the rotation and, in some aspects, even better for the rotated case. However, two distinctive features are evident for the DM-RI case. The first one is that all the fluctuations and the spectra seem to suggest that the scale-similar part of the model is less active (with respect to the non-rotated case), while from Figure 6.20e clearly appears the contrary (the eddy viscosity part, not shown, has no substantial differences). This behavior reveals a possible drawback of the model which might also explain its too high effect for some quantities in the non rotated case. Indeed, the overall model relies on a single constant, computed from a tensorial identity and then applied again to full scale-similar tensor. However, both the model formulation and its practical application reveal that it is Reynolds number sensitive, and correctly reduces its effect near the walls (see, for example, Figures 6.10 and 6.11 or Figure 6.20e). If then the three velocity components in the channel are considered separately, it is plausible that the value of the dynamic scale-similar constant is dominated by the momentum bal-

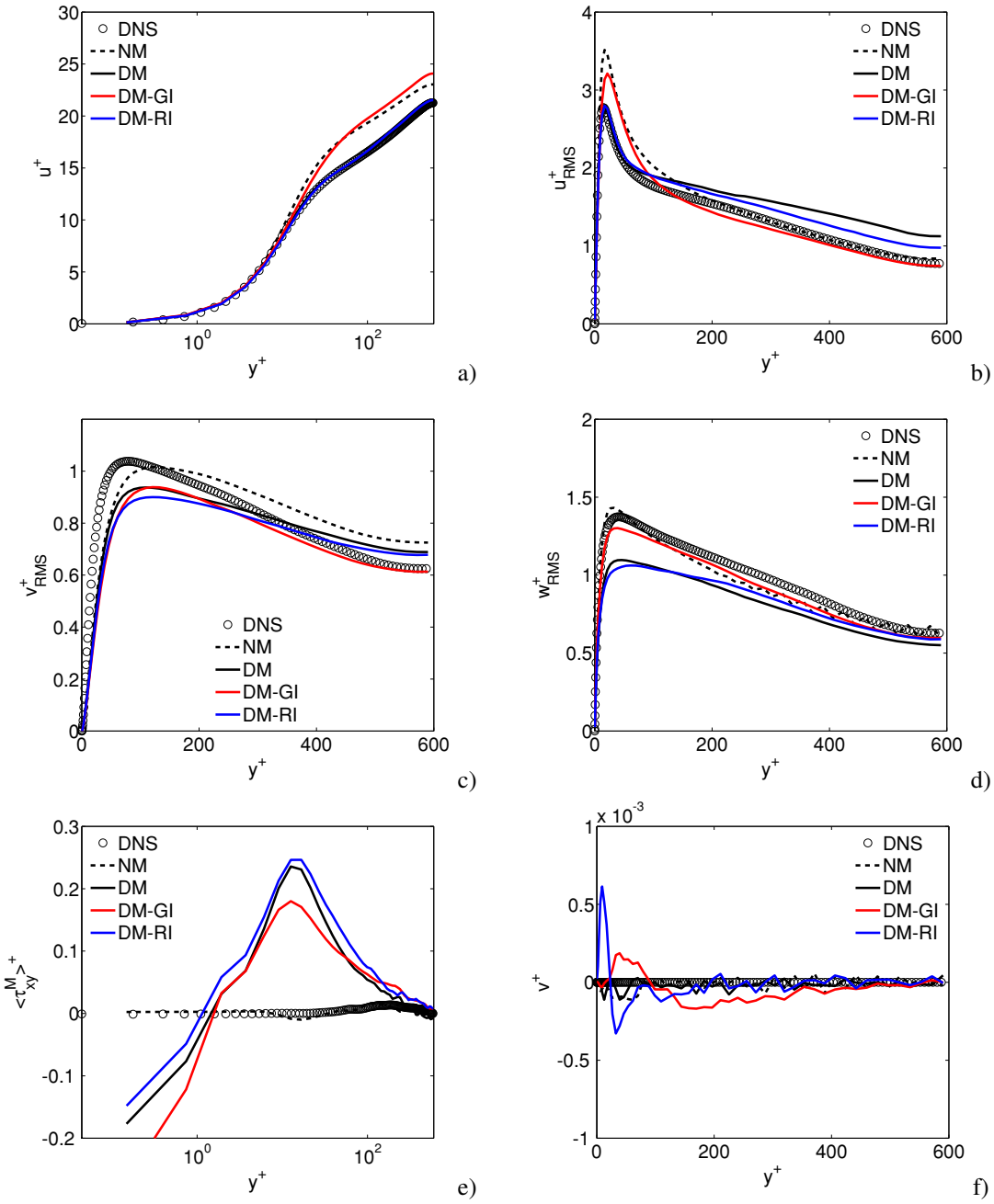

Figure 6.20: *Main flow statistics for the channel flow with different reference frames.*

ance in the stream-wise direction, the remaining ones having a relatively low, possibly null, Reynolds number. Therefore, applying the same single constant also for those scale-similar components acting on the transverse directions would certainly lead to an overestimation of the required energy recovery in those directions, which is indeed what happens in the base DM case. The idea behind this rotation test is indeed that, if the flow is directed in such a way to maximize the Reynolds number in all the directions, then the dynamic procedure as implemented here would lead to better results as the single dynamic constant would be more representative of all the flow directions.

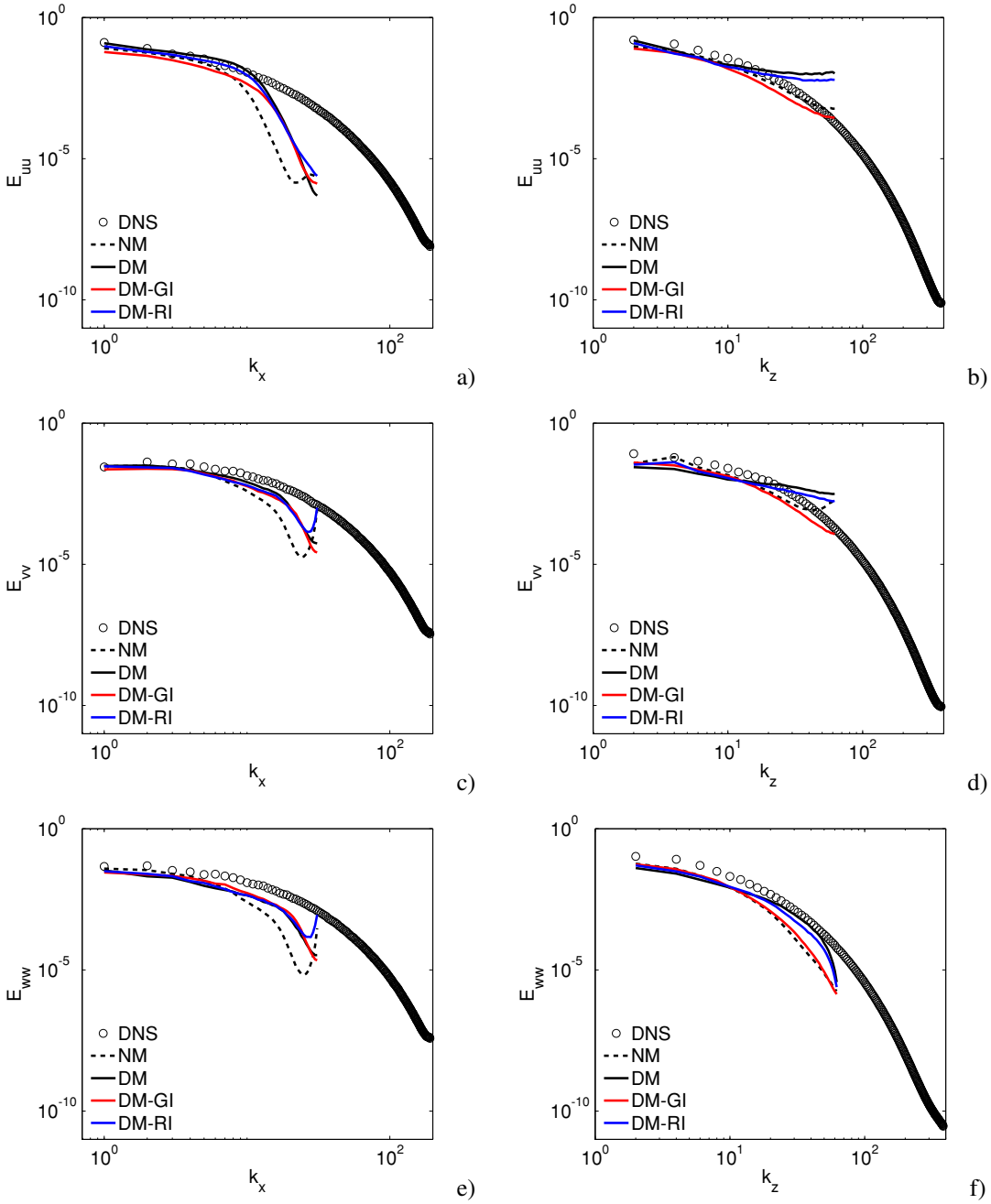

Figure 6.21: *Spectral energy distributions for the channel flow with different reference frames.*

While this immediately introduces a lack of effectiveness in the stream-wise action of the model (e.g., subfigures 6.21c-e), it also reduces the spurious effects in the transverse directions, from which some better results readily follows (e.g., compare Figure 6.20b and the relative span-wise spectra in Figure 6.21b). Obviously, rotating the domain is not an option for more complex flows and a different strategy should be adopted. Among the possible options, relying on a fully tensorial dynamic constant seems the most promising approach, as the increased cost could be easily managed within the low ones of the overall dynamic procedure in GLES. The second distinctive feature of the

DM-RI case is instead represented in Figure 6.20f where, despite the generally good results, it is apparent that a net mean vertical velocity is present, v^+. While no specific efforts have been devoted to find the origin of such spurious velocity (whose effects on the other variables are not clearly evident), it seems plausible that it is a combined effect of two causes: a non perfect alignment between the pressure gradient, fixed by components, and the channel centerline, as the channel is rotated axis by axis; round-off errors in the velocity, caused by the backward rotations before the computation of the statistics. As no secondary effects are evident, the last option is the most plausible.

When the effect of a constant translation velocity is considered (DM-GI), the main conclusion that can be drawn is that the model appears not active for most of the quantities, but also fully operative for the stream-wise spectra (left side of Figure 6.21). A careful analysis of Figure 6.20e and the reconsideration of the rotation effects on the dynamic scale-similar constant, reveal that both things actually happen. Indeed, the overall effect of shifting the reference frame is that the mean velocity is also shifted and, in particular, it is negative in the near wall zone up to the station where, approximately, the DM and the DM-GI curves intersect in Figure 6.20e, slightly below $y^+ = 100$. Hence, there is a substantial region near the wall where the Reynolds number is significantly lower than in the non moving reference frame, the model being thus less active. In particular, it also appears to be less active than the same model on the grid FZ (see Figure 6.16b), which justifies most of the results. In contrast, in the channel center, two things happen. Not only the flow recovers its positive direction but, as the Reynolds numbers in the three coordinate directions are more similar[19], the resulting dynamic constant is much better calibrated for all the three flow directions. As a consequence, the model can exactly recover the stream-wise spectra for the DM case without negatively affecting the span-wise ones.

Obviously, a fundamental problem remains, as the Galilean invariance is certainly not satisfied by the proposed SGS model, as a result of its dependence from the Reynolds number. As explained in section 6.1.1, additional terms are present in the equations which might have impaired the model performances. In particular, the term $\phi_x = -\langle u \rangle \langle v \rangle$ (not shown) has a qualitative behavior that would have exactly determined the same model reduction effects as those previously discussed. In this case the model would have the same behavior observed in the fixed frame, but would result unable to counteract its lack of Galilean invariance. The NM-GI case that would clarify the issue was not initially scheduled among the tests for the model, as well as the case NM-RI, and both will be the object of future investigations.

However, the combined results of the two tests, a direct inspection of the dynamically computed constant (4.28) and the Galilean invariance study in section 4.8, all sustain the fact that the scale-similar constant and the resulting effect of the model might depend from the mean flow direction and intensity. This further sustains the hypothesis that a full tensorial constant might be the proper solution to the above problems.

6.3.8 On the reconstruction and the statistics

All the results presented so far have been obtained by direct application of the formulas (6.43) and (6.44) to the raw computed fields, without any particular concern on the specific meaning of such variables in LES or GLES in general. In fact, the interpretation

[19] The peak velocity in this case reaches approximately $8u_\tau$.

given in this chapter to the LES approach is somehow based on considering as best SGS modeling option available the one that can better balance all the remaining effects, no matter what their specific source is. In contrast, it is known (Sagaut, 2006, p. 305) that, in order to compare such results with the DNS ones, the latter have to be filtered according to the G operator embedded in the simulation or, alternatively, the former have to be augmented by the contribution due to the adopted SGS model. It being understood that both approaches are correct, two problems arise in general applications. On one side, comparing the results with filtered DNS ones gives no reliability, as numerical results are not demanded to satisfy some filtered counterpart of the NSE and providing perfect filtered results is useless if they differ from the unfiltered ones. Also, reference DNS are not usually available, filtered or not. The second, more important, problem is that the LES terms which should be accounted for in reconstructing the statistics might not be available or suitable for the purpose, which is exactly what happens in GLES with an implicitly filtered approach. Indeed, not only the numerical error would not be considered in such reconstruction, but even the adopted SGS model might not be suitable for the purpose as, for example, in GLES it also accounts for pressure and viscous terms.

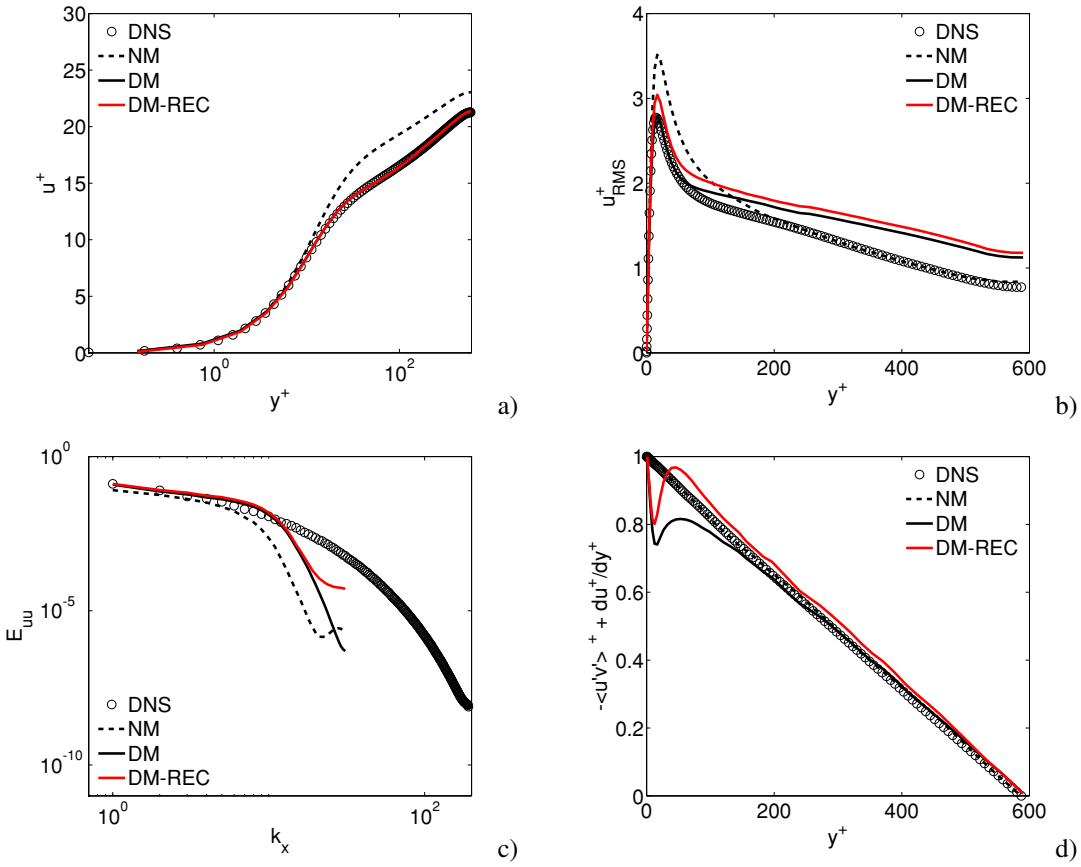

Figure 6.22: *Effect of the reconstruction* (5.63) *on the main flow statistics for the channel flow.*

However, as briefly discussed in section 5.6.4, an alternative option exists for the present GLES approach based on the FV method and the proposed dynamic mixed model. This consists in using the relation (5.63) for each single variable before com-

puting the statistics, instead of adding specific SGS models to the higher order moments. This approach has the advantage of being compatible with the SGS model and the FV part of the implicit filter without requiring any additional effort in selecting specific SGS models for specific statistical moments. The differences which are obtained between the raw approach used up to now and such reconstruction are summarized in Figure 6.22 for the few selected variables which have shown a larger effect. In particular, no explicit effect is apparent on the mean velocity profile[20], while both the effect on the spectrum and the fluctuation are as expected, the reconstruction increases the energy content at the smallest scales which, in turn, increases the level of the RMS fluctuation. However, the most important difference is found in the resolved tangential stress, which is shown in terms of the total linear stress in Figure 6.22d. This specific presentation helps clarifying the main limit in using the approach (5.63), which cannot take into account the effect of the eddy viscosity part of the model. Such limitation, and the additional impossibility to take the numerical error into account, is what partially justified not considering the reconstruction for the presentation of the results[21]. In contrast, Figure 6.23 shows that considering the equivalent tangential stress as most relevant variable avoids such problems ab initio. Obviously, its use is only possible in the present channel flow case, where the total stress is known to vary linearly in the wall normal direction but, nonetheless, this justifies the presentation of the results in the previous paragraphs[22].

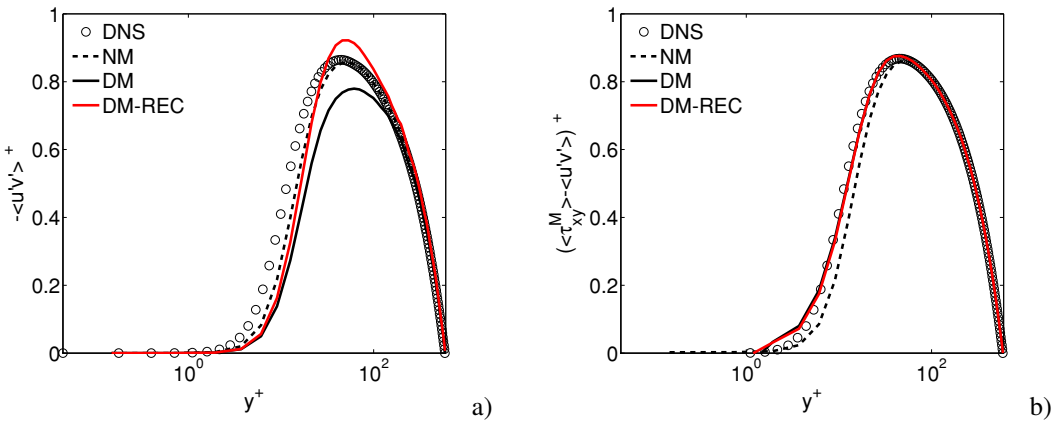

Figure 6.23: *Difference between resolved (a) and equivalent (b) tangential stress in the channel flow with or without reconstruction.*

6.3.9 Comparison with alternative SGS models

As a final test, in view of the forthcoming comparison presented in the next section, it is worth assessing the performance of the proposed SGS model with respect to additional modeling options. In particular, besides the DS model already considered, all the

[20] Note that it is still assumed that the correct friction velocity for the channel flow is the one determined by the pressure gradient in (6.15). Otherwise, differences would arise in the velocity profile too, whose wall derivative is increased by the reconstruction.

[21] Still, according to Winckelmans et al. (2002), this is the only option to partially include the filtering effects in the normal stresses.

[22] Note that such correspondence is not tautological and also holds when the friction velocity u_τ is computed from the velocity profile (not shown).

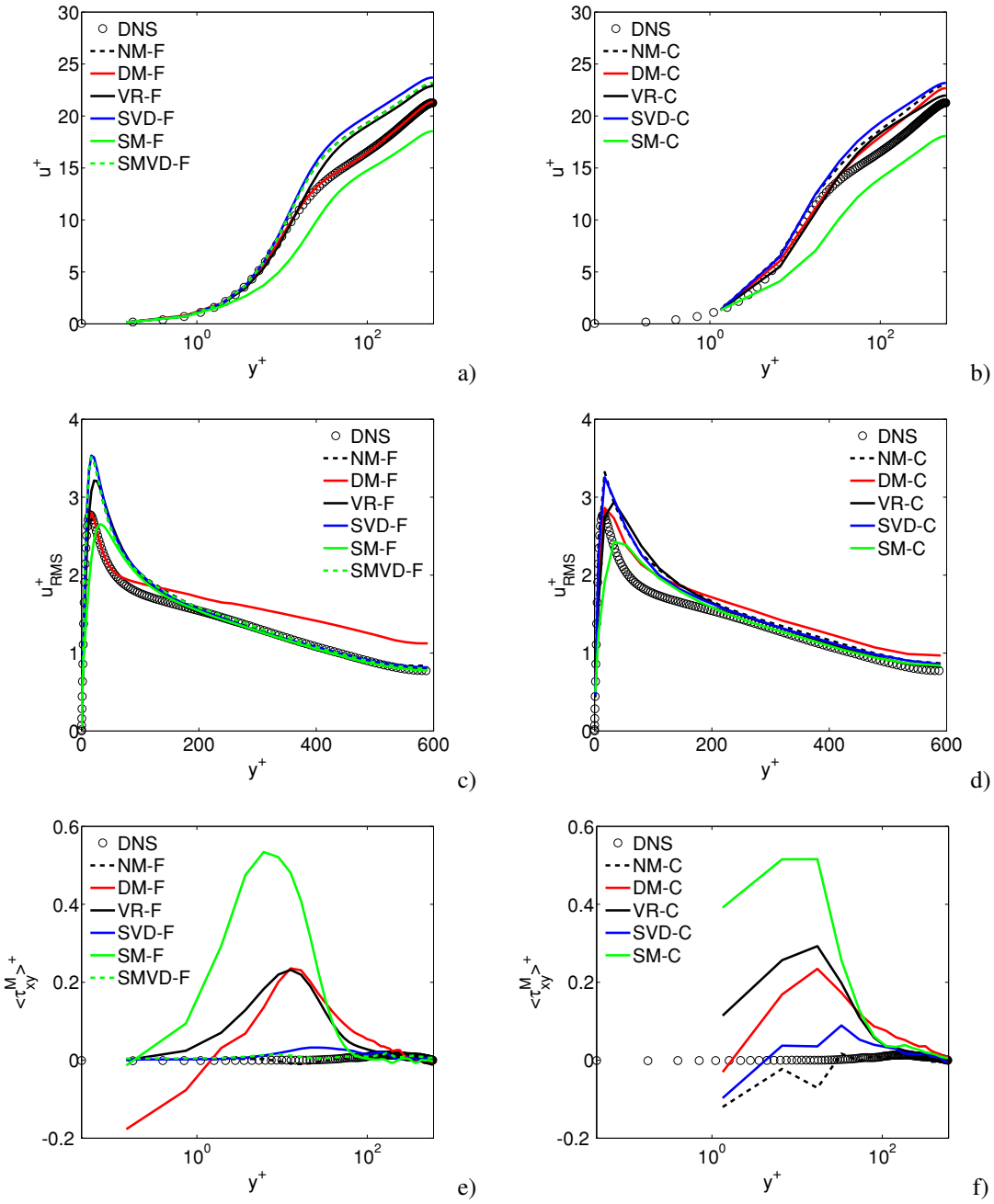

Figure 6.24: *Main flow statistics for the channel flow with different SGS models. Left) Grid F. Right) Grid C.*

remaining models listed in Table 6.2 do not rely on any dynamic procedure and, as a consequence, are much cheaper than the present DM model. It is thus worth evaluating the convenience of the present model with respect to such cheaper alternatives.

The comparison is presented in Figure 6.24 and Figure 6.25 in terms of some representative quantities (see Table 6.2 for the legend). The first thing to note is that, besides slight differences on the grid C, all the spectral results for the static models substantially coincide and do not dissociate from the NM case. This is coherent with the fact that

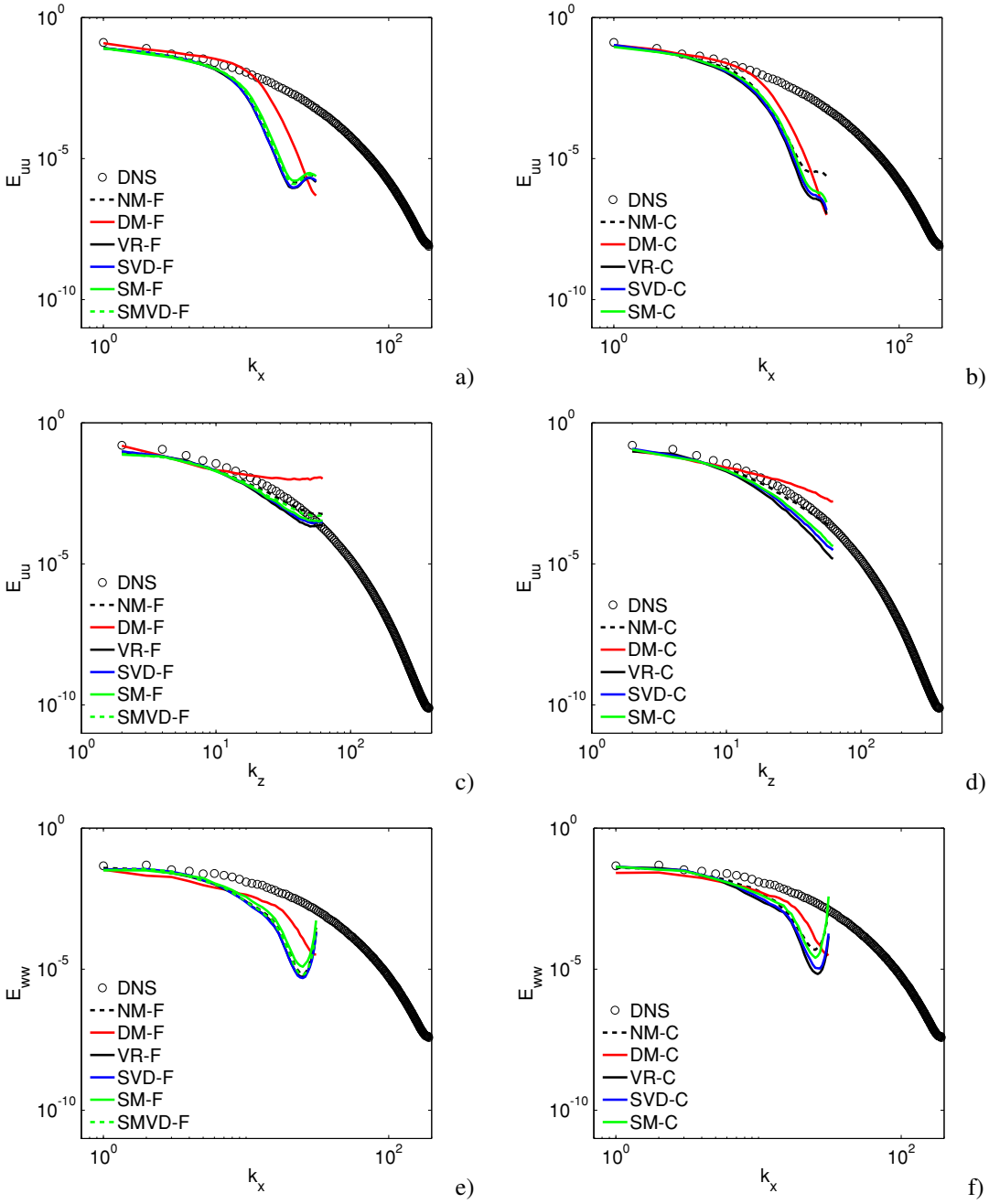

Figure 6.25: *Spectral energy distributions at $y/H = 1$ for the channel flow with different SGS models. Left) Grid F. Right) Grid C.*

the model contribution (subfigures 6.24e-f) for $y/H = 1$ is similar among the different models and essentially null. Nonetheless, the models differ significantly in the near-wall region, producing the differences appearing in the mean velocity profile and RMS stream-wise fluctuation. In particular, from the Figures 6.24e-f, it can be observed that only the present DM model provides a grid independent effect while all the remaining options are sensitive to the details of the grid near the wall. Among the static models, SVD appears to be the most sensitive as its mean contribution is practically null. The

default SM model, in contrast, is only slightly sensitive to the grid, but its contribution is much larger than expected, with the consequence that the near wall velocity derivative is substantially underestimated and the dissipative part in the production term is much more effective and reduces the stream-wise fluctuation near the wall. It is worth noting how such behavior is only due to the wall damping (2.26) used in SM, as the use of the van Driest formulation (SMVD-F) practically annihilates the model contribution, producing results very similar to those for the model SVD. Interestingly, while still having a certain sensitivity to the grid, the VR model has an effect which is similar to the one of the DM model. However, the agreement is essentially due to the eddy viscosity part of the DM model, which shares with the VR one the same linear scaling with the distance from the wall. In contrast, the scale-similar part in DM produces major differences in the two most important regions: the near wall one, where the effect is anti-dissipative, and the logarithmic one (the channel center), where the effect is instead dissipative. Note, in particular, that both effects are fundamental in order to correctly predict the slope of the velocity profile in the two respective regions and the DM model is particularly effective in achieving both. In conclusion, the use of the less cheaper DM model appears justified by the more accurate results and by the fact that all the remaining models do not substantially differ from the NM option. The VR model, nonetheless, represents a potential cheaper alternative.

Another conclusion which is worth stressing again is that, as confirmed by all the results presented in this and the previous sections, the requirement for a SGS model with an y^3 near-wall scaling appears as largely overrated, if not completely wrong. Indeed, not only the results show that, for the present code, a net near-wall contribution is necessary, but also that such contribution should ideally be independent from the grid, in order to correctly recover the mean velocity profile with different near wall resolutions. Both the DM and the VR model are successful in giving a net near-wall contribution, but with important differences. The former has a physically sound independence from the grid, but then fails in actively contributing for coarse wall-normal resolutions. The latter has a near-wall scaling proportional to the linear distance from the wall, y, hence produces better results for coarser grids but inevitably fails when the wall-normal spacing is sufficiently fine[23]. While it is the net contribution, more than the scaling, that gives different results, it is nonetheless evident that an y^3 scaling would prevent any SGS model from actively contributing in the near-wall region. Obviously, as already stated, this is a code dependent issue. Any code whose NM formulation can exactly reproduce the flow in the near wall zone would instead benefit from an y^3 scaling.

6.4 The LESinItaly database

It is instructive to close this chapter by extending the previous comparisons to additional SGS models as implemented in different codes. This not only allows to detect some of the previously described effects independently from the specific solver, but also permits to evaluate the performances of the DM model with respect to additional modeling strategies. The selected codes and SGS models, listed in Table 6.3, are those from the LESinItaly database (Denaro et al., 2011; Abbà et al., 2013).

Most of the codes use a standard second order FV formulation with a DS model. The

[23] A combination of the two is possibly a candidate for better overall performances and is currently under investigation.

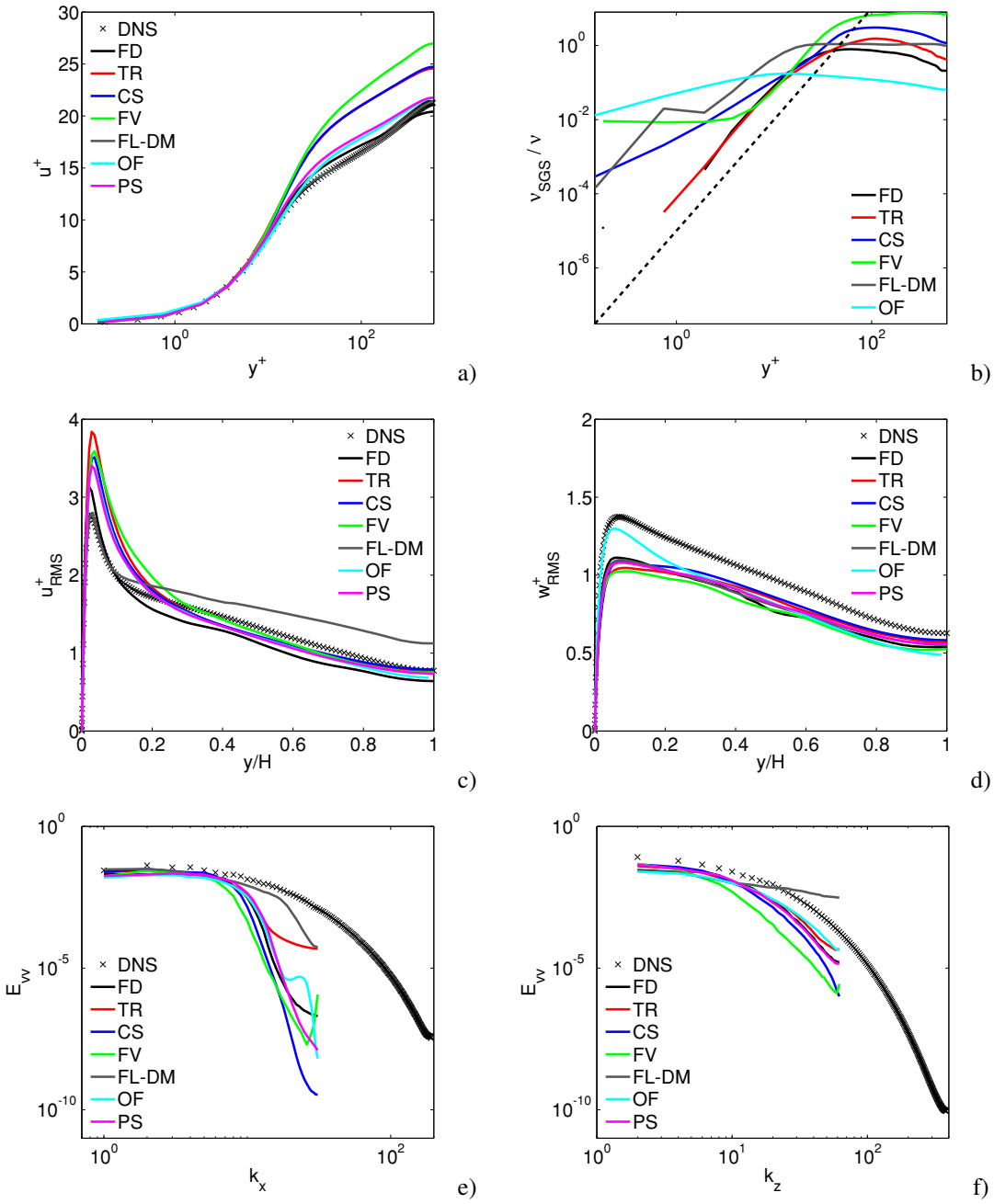

Figure 6.26: *Main flow statistics for the channel flow with different codes and SGS models from the LESinItaly database. Grid F.*

code OF uses a Turbulent Kinetic Energy transport equation with a dynamic coefficient which is averaged over the whole domain. The code FV instead uses the DS model as implemented in the GLES framework and presented here in section 6.3.2; however the details of the implementation are not known and may strongly differ from the present ones. The code FD uses an anisotropic extension of the DS model, whose main advantage is the fact that it does not rely on a single dynamic constant, hence the CGI (2.33) is satisfied exactly and not in a least squares sense. Finally, code PS uses a stan-

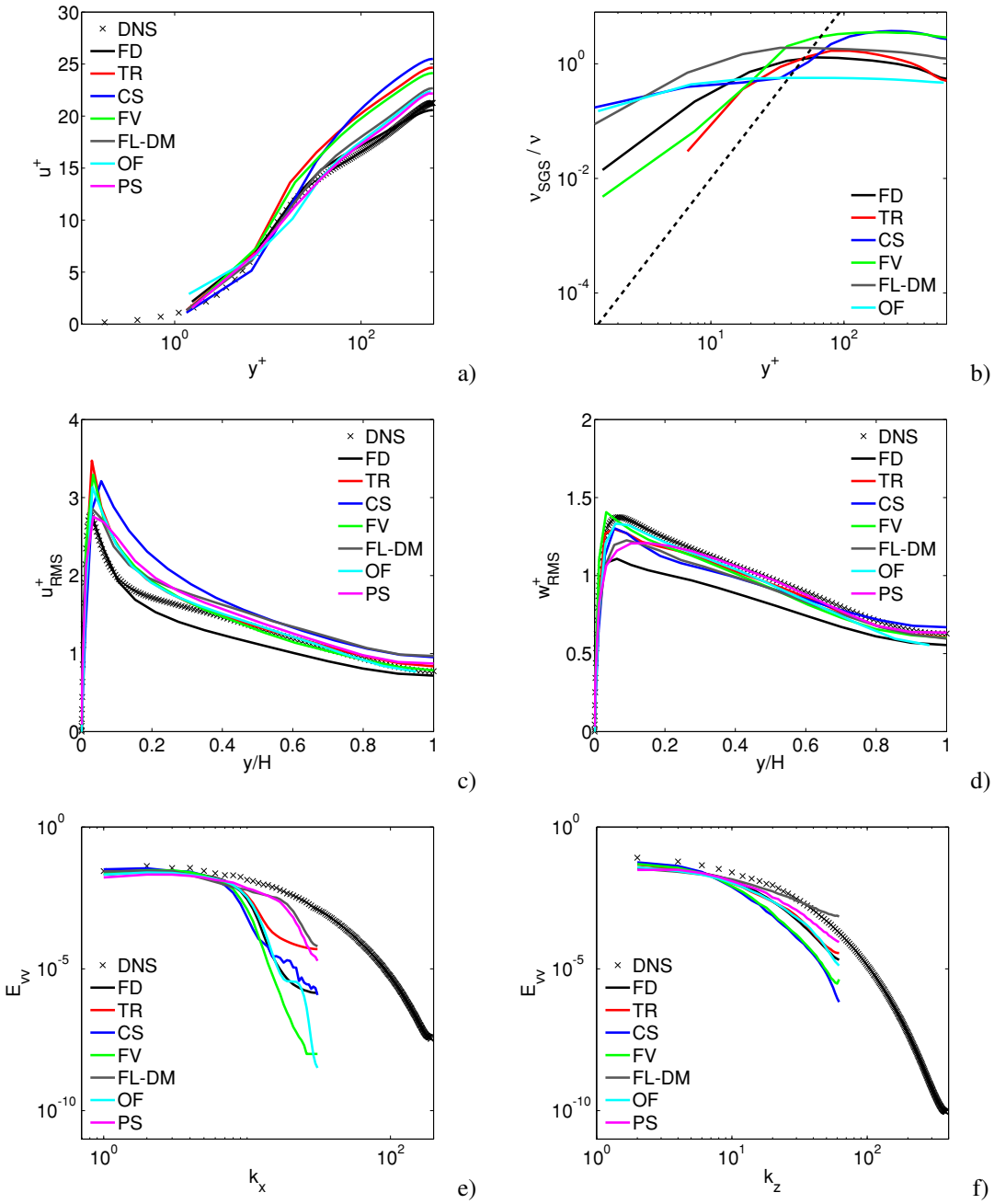

Figure 6.27: *Main flow statistics for the channel flow with different codes and SGS models from the LESinItaly database. Grid C.*

dard SM model with van Driest wall damping and a model for the commutation error, which is reduced to a 4^{th} order term. In practice, as previously mentioned, this commutation error model has strong similarities with the scale-similar model proposed here. Additional details on the codes and the models can be found in the cited references.

The results, presented in Figure 6.26 for the grid F and in Figure 6.27 for the grid C, essentially reveal that, besides the specific differences, most of the FV codes are affected by the same limitations present in Fluent® with the classic DS model, in the

Table 6.3: *Codes and SGS models from the LESinItaly database.*

ID	Code	Formulation	Model	Reference
FD	In-house	Finite difference	Anisotropic DS	Abbà et al., 2003
TR	TransAT®	Finite volume	DS	ASC, 2009
CS	Code_Saturne®	Finite volume	DS	Benhamadouche et al., 2002
FV	In-house	Finite volume	GLES DS	Denaro and De Stefano, 2011
FL-DM	Fluent®	Finite volume	DM	(4.25)
OF	OpenFOAM®	Finite volume	TKE equation	Menon et al., 1996
PS	In-house	Pseudo-spectral	SM + Comm.err.	Iovieno and Tordella, 2003

velocity profile as well as in the remaining quantities. The only exception to this is for code OF, which does not suffer the same problems. This could be explained by the higher eddy viscosity value near the wall (subfigure 6.26b) or, considering the anomalous velocity values in the first cell near the wall (Figures 6.26a and 6.27a), by a non proper nondimensionalization of the velocity. The code FD, possibly because of its specific SGS model, is the only one which is essentially independent from the grid. Finally, while giving different results on the grid F, code PS and the present DM model have striking similarities on the grid C, which is possibly justified by the fact that, for this coarse grid, there is a dominance of the effects related to the wall-normal spacing, hence the correspondence between the two formulations emerges[24].

In conclusion, this brief analysis highlights that, on the grid F, the present DM model is superior to all the alternative codes, as it is the only one correctly predicting the mean velocity profile and the near-wall peak in the stream-wise velocity fluctuation, while not being inferior for the remaining quantities. On the grid C the capability of the the DM model is comparable to the one of the code PS or code FD. Notably, both are in-house research codes with advanced numerical features, while the present DM model has been implemented in a commercial code via User Defined Functions (UDF).

[24]Note, in particular, that code PS uses the commutation error model only in the y direction.

CHAPTER 7

Application to complex flows

In this chapter the proposed dynamic, mixed SGS model is applied to flows of increasing complexities. The first case, considered in section 7.1, is the turbulent flow in a pipe with circular cross section, which allows extending the model testing to unstructured grids and higher Reynolds numbers while retaining the advantages of a fully developed flow. The mapping procedure, presented in section 5.6.3, is also briefly tested on a turbulent pipe flow for two different pipe sections. The second test case is the flow and heat transfer in a matrix of surface mounted cubes, which is investigated in section 7.2. While still retaining the conceptual simplicity of a fully developed flow, this test case introduces both additional physics and strong grid stretching in the flow direction, thus allowing a controlled test of the model in a more realistic scenario. Finally, in section 7.3, the dynamic mixed model is applied to the turbulent cold flow in a swirled combustor. Besides being representative of combustion applications, the flow also has features typical of general engineering applications, ranging from the need of wall functions to strong grid non-uniformity and the specification of inflow/outflow boundary conditions under epistemic uncertainty. Additional complexity is added by the physics of the flow, whose dependence from the swirl is also investigated.

7.1 Turbulent pipe flow

The case considered in this section is represented by the fully developed, turbulent, incompressible, isothermal flow in a straight circular pipe. From the formal point of view, besides geometrical factors, the governing equations for the turbulent pipe flow are identical to the ones for the plane channel described in the previous chapter (Tennekes and Lumley, 1972). As a consequence, most of the ideas already developed for the channel flow apply for this flow as well and are thus not repeated here. Despite the

appearances, both flows have a great practical relevance as most engineering applications have to deal with wall boundaries and, even for very complex domains, inflow sections are usually related to fully developed flows in pipes of circular or rectangular cross section. Hence, in order to correctly predict the flow statistics in the domain, it is fundamental for the incoming flow to be correctly predicted as well. Moreover, as shown in section 5.6.3, the mapping procedure later tested in this section strongly relies on the correct prediction of such flows in order to provide a correct inflow condition.

However, despite these similarities, turbulent pipe flows can still be considered of greater practical relevance as most industrial flows are actually flows in pipes with circular cross section, which essentially motivated this separated test. Also, the domain geometry allows a natural introduction of grids with unstructured topology, which is the next logical step in testing a SGS model for industrial flows. Such switch in grid topology, in turn, also allows extending the range of Reynolds numbers achievable in wall resolved LES, as the grid resolution can be concentrated in the near wall zone without strongly affecting the resolution in the rest of the domain.

7.1.1 Computational setup

The considered domain consists in a straight circular pipe of radius R and length L_z. The mean flow direction is along the z axis, while the r and θ directions define, respectively, the radial and tangential coordinates in planes normal to the mean flow direction. The velocities in the three respective coordinate directions are u_z, u_r and u_θ. Before describing the specific setup for this flow, it is worth addressing the issue of how the mean driving pressure gradient $\partial\langle p\rangle/\partial z$ can be setup for a fully developed flow in a pipe with a generic, constant, cross section. Denoting by P and A, respectively, the perimeter and the area of the pipe cross section, the z momentum balance for the fully developed flow condition in the pipe yields:

$$-\frac{\partial\langle p\rangle}{\partial z}A = \bar{\tau}_w P \qquad \text{with:} \qquad \bar{\tau}_w = \frac{1}{P}\int_P \tau_w dl \tag{7.1}$$

where $\bar{\tau}_w = \rho u_\tau^2$ is the average wall shear stress on the cross section perimeter. Hence, introducing the hydraulic diameter of the section $D_H = 4A/P$ and the relative friction Reynolds number $Re_\tau^D = u_\tau D_H/\nu$, the equation above leads to:

$$\frac{\partial\langle p\rangle}{\partial z} = -\frac{4}{D_H}\rho u_\tau^2 = -4\rho\frac{\left(\nu Re_\tau^D\right)^2}{D_H^3} \tag{7.2}$$

which can be used to drive the flow for a given Re_τ^D. Also, as for the channel flow, this pressure gradient uniquely defines the friction velocity u_τ:

$$u_\tau = \sqrt{-\frac{D_H}{4\rho}\frac{\partial\langle p\rangle}{\partial z}} \tag{7.3}$$

However, with respect to the channel flow, here it is even more important to use equation (7.3). Indeed, not only the computation of the wall shear stress in Fluent®

is affected by a first order error (see equation (6.9)), but even the geometry of the section might not be exactly reproduced by linear FV cells. For the present pipe flow, $D_H = D = 2R$ and the formulas above are more commonly expressed in terms of the pipe radius R:

$$Re_\tau = \frac{u_\tau R}{\nu} \qquad \frac{\partial \langle p \rangle}{\partial z} = -2\rho \frac{\nu^2 Re_\tau^2}{R^3} \qquad u_\tau = \sqrt{-\frac{R}{2\rho}\frac{\partial \langle p \rangle}{\partial z}} \tag{7.4}$$

Two distinct cases at different Reynolds numbers are considered for this test, respectively $Re_\tau = 320$ and $Re_\tau = 1142$, and comparisons are made with the relative reference DNS, Wagner et al. (2001) for the low Reynolds case and Wu and Moin (2008) for the high Reynolds one. In terms of the mean bulk velocity U_b:

$$U_b = \frac{1}{A}\int_A \langle u_z \rangle \, dA \tag{7.5}$$

and pipe diameter D, the respective bulk Reynolds numbers are instead $Re_D = 10,000$ and $Re_D = 44,000$. In both cases, a no-slip boundary condition is applied at the wall and a periodicity condition along the axial direction with L_z selected according to the relative DNS domains, namely $L_z = 10R$ for the low Reynolds case and $L_z = 15R$ for the higher one.

Unstructured hexahedral grids of different resolutions are used, whose topology is sketched in figure 7.1. Note that, despite the prevalent role of tetrahedral grids in general applications, these would severely affect the numerical accuracy of the computation, independently from the SGS model. As such, they are not well suited for LES of wall bounded flows, where the smallest resolved scales are the turbulence driving mechanism and the largest available accuracy is required. For this reason, a fully structured layer of cells has also been used near the walls.

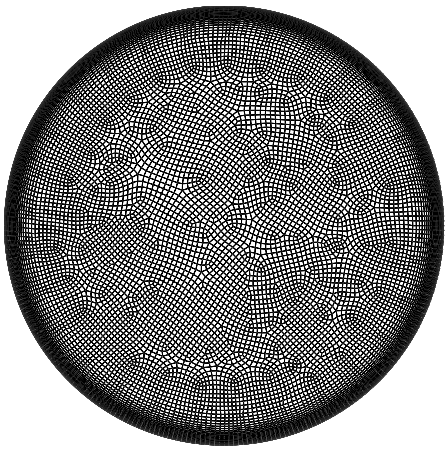

Figure 7.1: *Sketch of the grid topology for the pipe flow computations.*

Table 7.1: *Dimensionless grid parameters for the turbulent pipe flows.*

Case	Δz^+	$R\Delta\theta^+$	Δr^+_{min}	N° DOF
$Re_\tau = 320$ - DNS	6.6	8.4	0.6	$8.2 \cdot 10^6$
$Re_\tau = 320$	50	15	0.1	$0.2 \cdot 10^6$
$Re_\tau = 1142$ - DNS	8.4	7.0	0.4	$6.3 \cdot 10^8$
$Re_\tau = 1142$ - C	60	32	0.1	$2.4 \cdot 10^6$
$Re_\tau = 1142$ - M	57	28	0.1	$3.4 \cdot 10^6$
$Re_\tau = 1142$ - F	54	25	0.1	$5.2 \cdot 10^6$

As summarized in Table 7.1, a single grid resolution is used for the low Reynolds case, while three different grids with increasing resolutions, denoted C, M and F, are tested for the higher Reynolds case. Note that, for all the grids, the maximum radial cell dimension in the channel center is only slightly lower than the span-wise one at the wall, $R\Delta\theta^+$. However, the radial direction is not anymore representative of the grid topology in the channel center, hence it is not reported in Table 7.1. Computational parameters for the reference DNS computations are instead reported to highlight the difference, with respect to the present computations, in terms of total degrees of freedom represented. In particular, due to the single block structured grid topology used in these studies, the near-wall resolution is lower than usual (e.g., compare the DNS grid for the channel flow in Table 6.2) in order to avoid excessive resolution on the pipe axis. Also, it is worth mentioning that the two DNS codes are based on second order finite volumes/differences, in contrast to the fully spectral DNS code used as reference for the channel flow.

The numerical setting is the default one chosen also for the channel flow tests: a Central/PRESTO discretization, FSM for the pressure-velocity coupling and the backward second order scheme for the time advancement, with the time step fixed approximately by $\Delta t = 0.23\nu/u_\tau^2$.

Only two SGS modeling options are tested. One is the default DS model already implemented in the code, which according to the results in section 6.3.2 can also be interpreted as representative of a NM computation. For the high Reynolds case this model is only used on the grid M. The second one, used instead for all the grids listed in Table 7.1, is the present DM model. The model is used with its default setting except for one parameter, the number of layers N_L in the filter stencil, which is set to 2. While the results in section 6.3.5 possibly justify, or even suggest, the use of the enlarged stencil, the only practical reason determining its exclusive use for the present test is the fact that the single layer filter resulted to be problematic, as it either led to instabilities or strongly polluted the solution with unphysical fluctuations. The reason for this behavior has been found in the fact that, for the present unstructured grids, the range of scales affected by the numerical error is larger than for the fully structured grids used in the channel flow tests. As a consequence, in order for the scale similar model and the dynamic procedure to use a physically sound small scale flow sample, the test filter width required to be enlarged. The consequences of this forced choice will be discussed with the presentation of the results.

For all the cases, the mean axial velocity is initialized by using the Reichardt's velocity profile (5.27) with superimposed random fluctuations. After the statistically steady state is reached, flow samples are collected at each time step for a total sampling time of $80R/u_\tau$ or, approximately, $1200R/U_b$ and $1540R/U_b$ for the low and high Reynolds cases respectively. Both are enough to allow a particle to travel more than 100 times trough the pipe axial length at velocity U_b. Flow statistics are computed in time by the means of the algorithm presented in section 5.6.4 and additional spatial averages are performed in the homogeneous direction θ using, for simplicity, only 4 perpendicular radial profile samples. All the presented results, unless otherwise stated, are made non-dimensional by the friction velocity u_τ and the pipe radius R.

7.1.2 Numerical results

The main results for the low Reynolds case are presented in Figure 7.2 and substantially show that no particular difference exists among the two models and both, in practice, correctly predict all the flow statistics. The small specific differences can however be explained by looking at the overall LES effect $\langle \tau_{zr}^M \rangle^+$, in Figure 7.2f, which can be computed as for the channel flow. In particular, by comparison with Figure 6.16b, it emerges that the model activation has the same pattern and maximum value seen for the simulation of the turbulent channel flow on the grid FZ. In contrast, the near-wall behavior appears more resemblant of the one on the grid CT, both being substantially null at the wall. Notably, the present grid shares with the former ones the span-wise resolution and the wall-normal grid stretching respectively. This, in practice, suggests that the range $2 \leq y^+ \leq 100$ is mostly affected by the span-wise resolution and, in both cases (present one and FZ), the model is too active, leading to the slight underestimations observed in the stream-wise profiles (subfigures 7.2a-b). In contrast, it also appears that the present grid stretching (which is very similar to the one used for the grid CT) somehow deactivates the model in the first few cells near the wall. However, the overall model effectiveness remains higher than required as, for such low Reynolds number, the already low model activity near the wall is not substantially altered[1].

The higher Reynolds number case, whose results are presented in Figure 7.3, can help in clarifying the previous issues, due to the larger number of grid resolutions adopted. The first thing to note is that, for this case, more differences among the models arise and the effects of the extended filter stencil in the model DM are also more easily recognizable. In particular, the stream-wise fluctuation is substantially predicted in a correct way by the DM model for all the grids and wall distances, that is, without excessive overestimation in the pipe center. Also, the mean velocity profiles present a slight bump at the beginning of the logarithmic region, which is another feature of the extended filter stencil, as observed in section 6.3.5. However, while most of the remaining quantities are satisfactorily predicted, it is also clear that the model DM does not particularly improve the DS one in the critical mean velocity profile, and for most of the remaining quantities there is a substantial agreement with the model DS, independently from the grid. Slight differences are present in the peak values of the tangential stress and the span-wise fluctuation, but these are in line with the general features of the models as observed in the previous chapters.

[1] Note that such low Reynolds number effect has already been noticed in section 6.3.2 for the near-wall spectra. Moreover, a theoretical analysis as performed in section 5.5.3 also confirms the result.

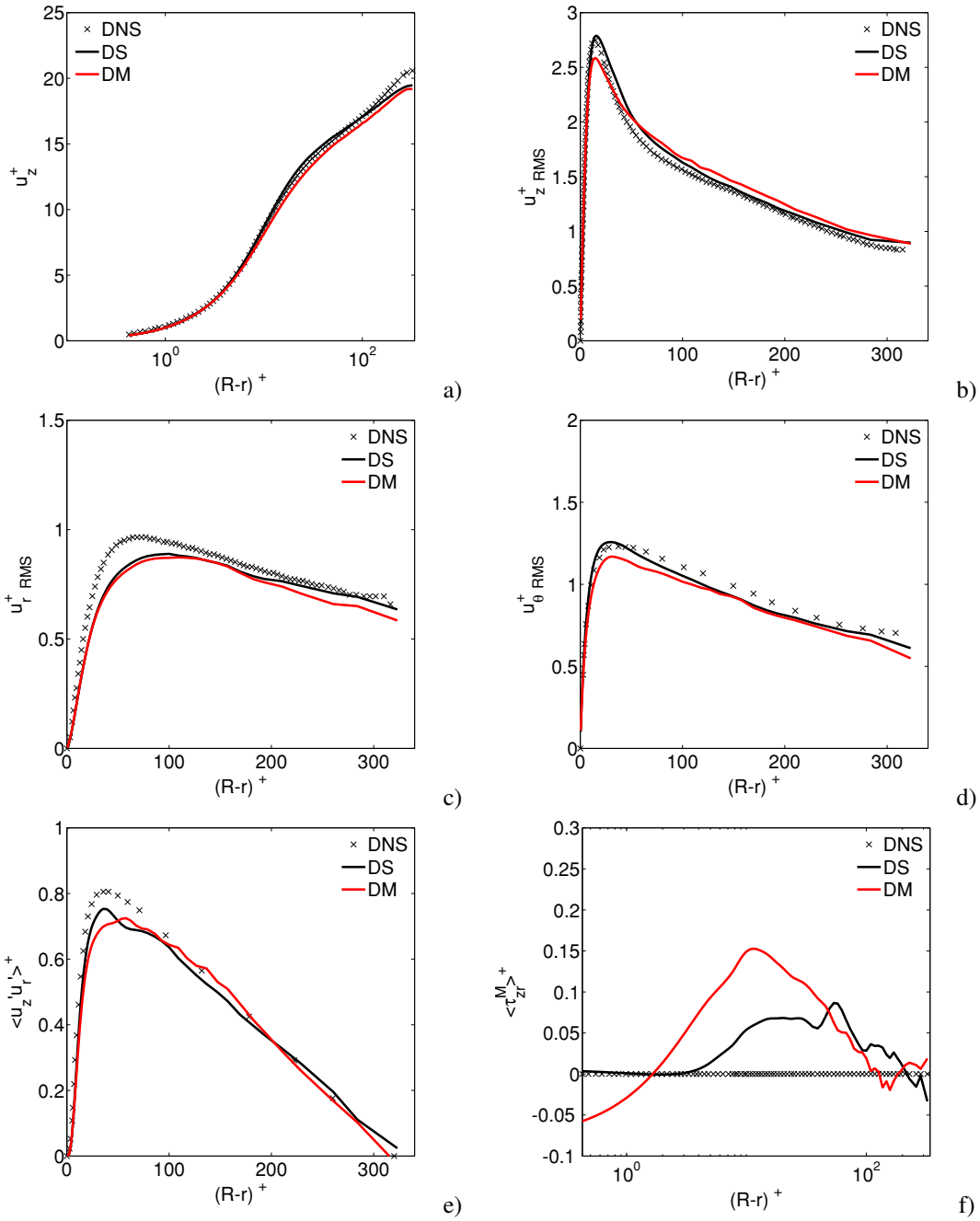

Figure 7.2: *Main flow statistics for the turbulent pipe flow at* $Re_\tau = 320$.

Such perpetual lack of activation for the model DM[2], which is thus confirmed for a higher Reynolds on three additional grids, can again find a justification in $\langle \tau_{zr}^M \rangle^+$, represented in Figure 7.3f. This figure first confirms that the three grids are substantially identical from the point of view of the model, and differences in the results are not to be expected. However, more importantly, the lack of model activation in the near wall zone (approximately for $y^+ \leq 10$) abruptly emerges again for all the three grids. While

[2]With respect to the channel flow results.

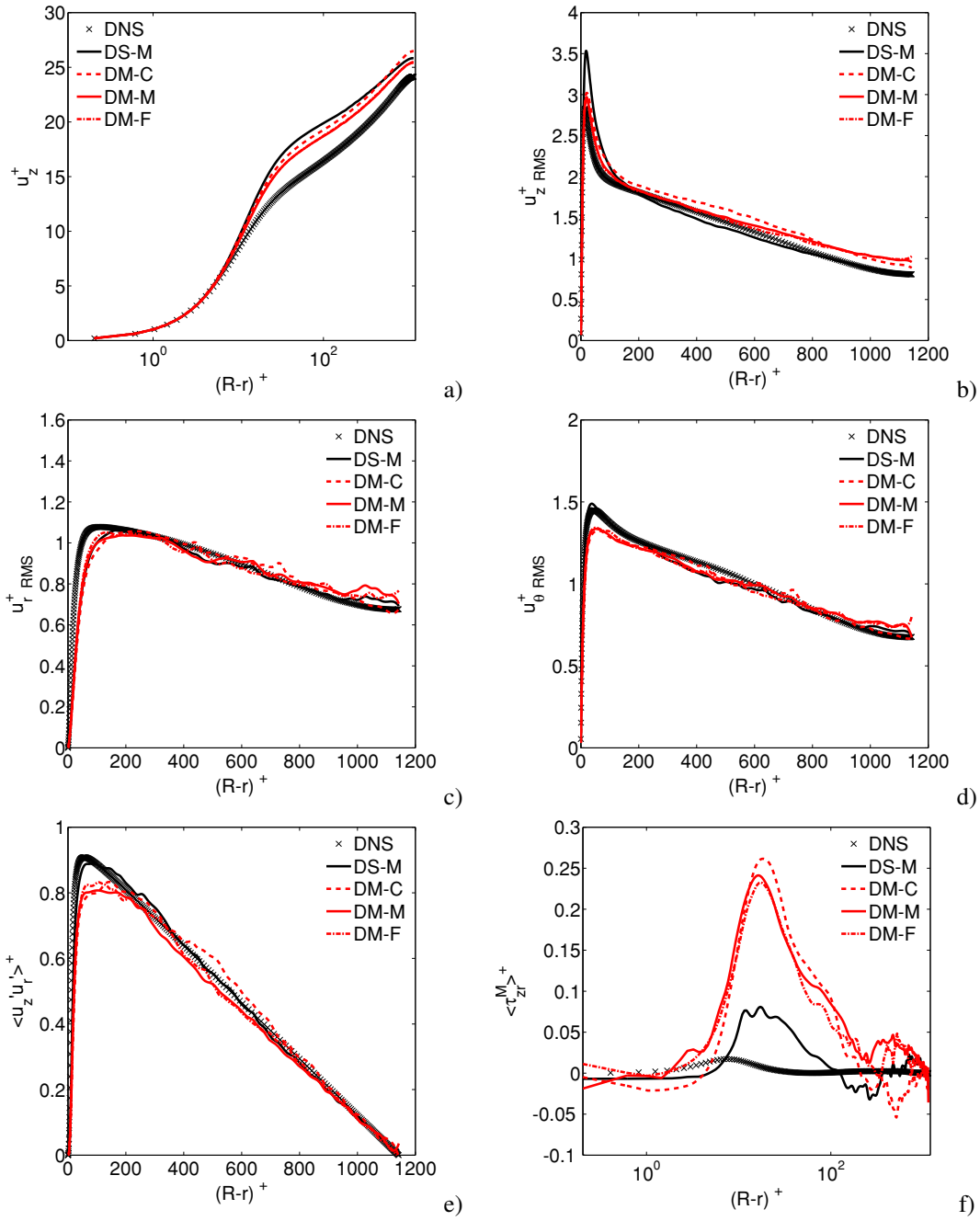

Figure 7.3: *Main flow statistics for the turbulent pipe flow at* $Re_\tau = 1142$.

this could be again explained by the specific grid refinement at the wall, which is still similar to the one used for the grid CT in the channel case, such behavior deserves a more detailed analysis.

Indeed, what emerges from the two Reynolds cases analyzed here and, by extension, also from the channel flow case on the grid CT, is that a specific grid stretching near the wall is capable of completely nullifying the model action in that zone, which is also the most important from the model performance point of view. In particular, such specific grid stretching is characterized by a constant or nearly constant expansion ratio. While

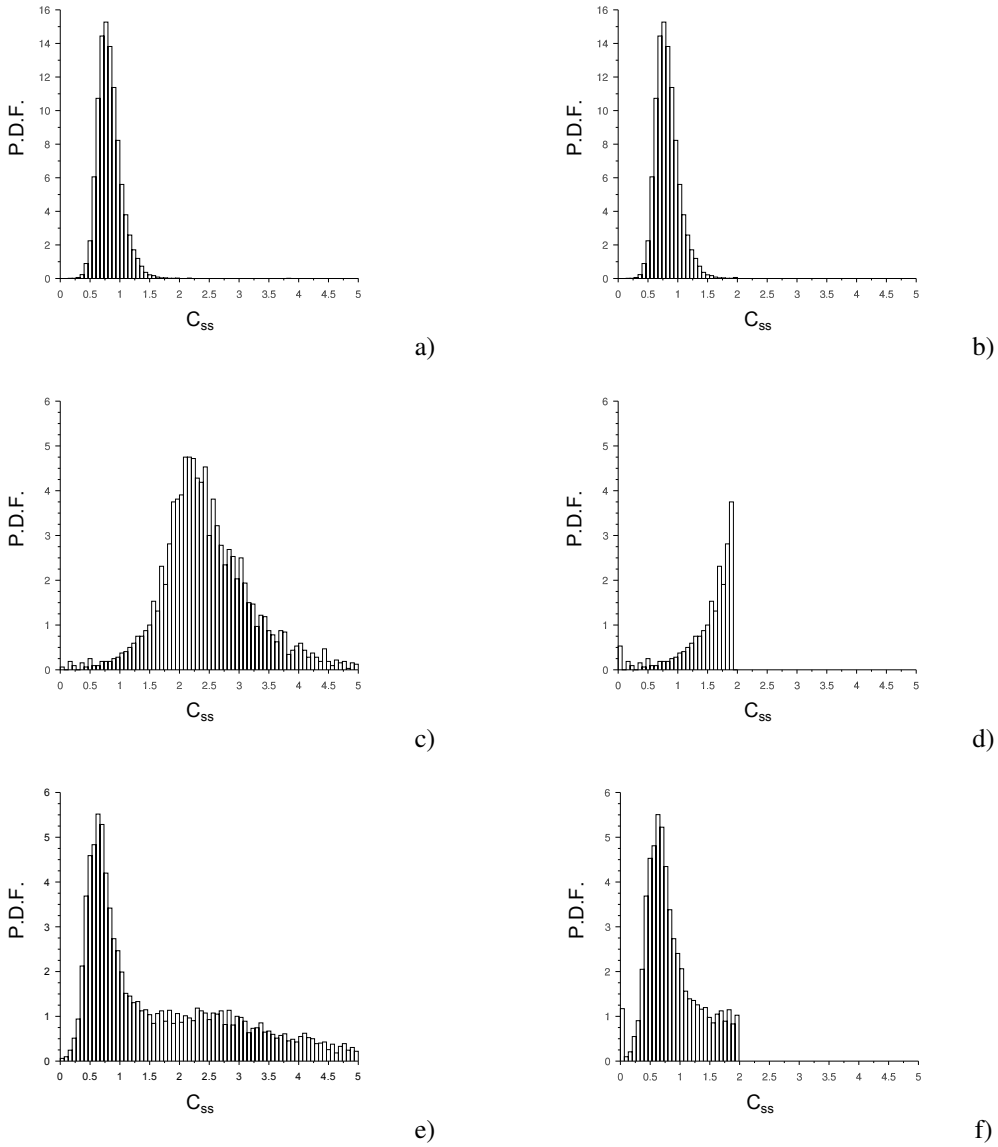

Figure 7.4: *PDF for the dynamic constant C_{ss} at the wall. Top: turbulent channel flow at $Re_\tau = 590$, $N_L = 2$, grid F, DM model. Center: turbulent channel flow at $Re_\tau = 590$, $N_L = 1$, grid CT, DM model. Bottom: turbulent channel flow at $Re_\tau = 590$, $N_L = 1$, grid F, DM-NDR model. Left: raw constant as computed by the dynamic procedure. Right: clipped constant.*

a detailed explanation is hard to find at the moment, a possible heuristic justification can be found by reconsidering the DM model formulation, and more specifically the ratio $\Delta_{n,0}^2/\Delta_{m,n}^2$, which also appears, inverted, in the lowest order error term in equation (4.24). It is easy to show that for a structured grid with stretching in the y direction only, the volume average filter involving the first neighbor cells yields for such term:

$$\left.\frac{\Delta_{m,n}^2}{\Delta_{n,0}^2}\right|_j = \left(\frac{\Delta y_{j-1} + 5\Delta y_j + \Delta y_{j+1}}{\Delta y_j}\right)^{\frac{2}{3}} = \left(7 + \frac{\Delta y_{j-1} - 2\Delta y_j + \Delta y_{j+1}}{\Delta y_j}\right)^{\frac{2}{3}} \quad (7.6)$$

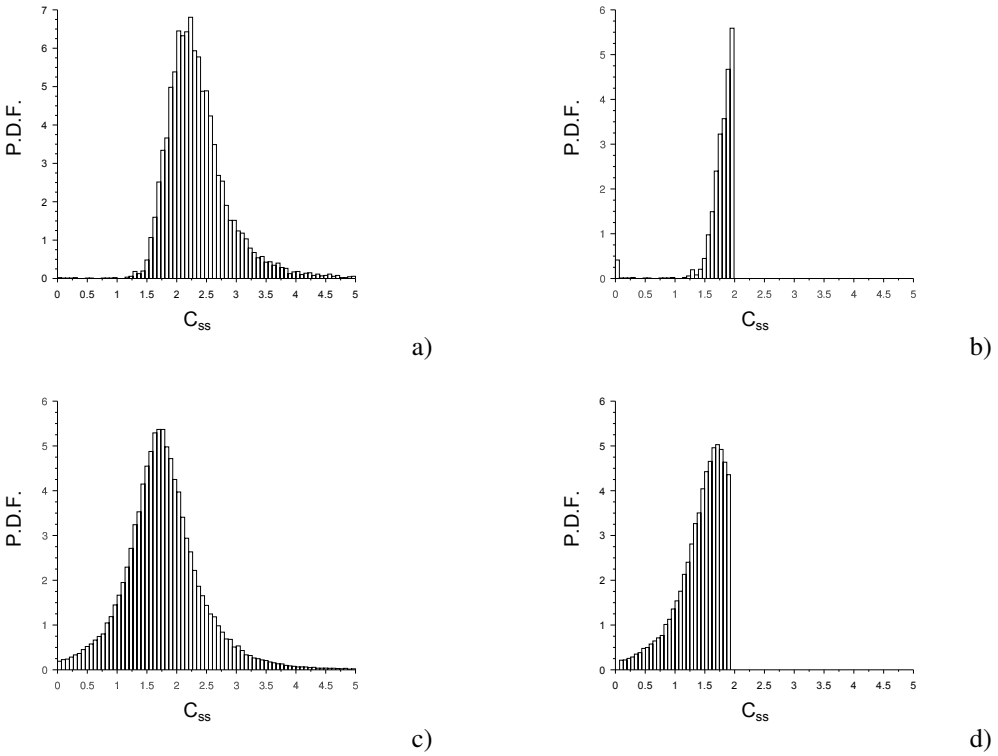

Figure 7.5: *PDF for the dynamic constant C_{ss} at the wall. Top: turbulent pipe flow at $Re_\tau = 320$. Bottom: turbulent pipe flow at $Re_\tau = 1142$, grid M. Left: raw constant as computed by the dynamic procedure. Right: clipped constant.*

where j is the grid index along the y direction and Δy_j denotes the grid spacing for the j^{th} cell. It is thus apparent how such ratio is affected by a term which can be roughly identified with the second derivative of the grid spacing. While for most grids such perturbation is constant (not for the grid CT) and does not alter the 4^{th} order accuracy of the model, it readily assumes different values for different grid stretching functions and differently affects the resulting dynamic procedure. For example, it is positive for both the grid CT (at the wall) and any grid with an expansion ratio $R > 1$, but it is strictly negative for the sine stretching law (6.41) and two orders of magnitude larger, in terms of absolute value. While the overall ratio in equation (7.6) would still differ only slightly for an intermediate cell, it should be noted that higher differences are found in the near wall cells, where the filter stencil necessarily becomes asymmetric, and the larger is the filter stencil the larger is the layer of cells involved. The fact that such ratio strongly affects the resulting model has already been evidenced in section 6.3.2, where the model DM-NDR has been shown to be completely ineffective. Here, such effect is investigated more precisely, by looking at the probability distribution (PDF) of the dynamically computed scale-similar constant, C_{ss}, in the first layer of cells near the walls.

When the analysis is performed for the channel flow, Figure 7.4, it readily emerges that the extended filter stencil is not, by itself, any cause of problems as the relative PDF (subfigures 7.4a-b) has a well defined peak at the wall and the clipping does not affect its distribution. Identical results are also obtained for a single layer filter stencil

($N_L = 1$) on both the grid C and F (not shown). However, the same analysis for the grid CT (subfigures 7.4c-d) and the DM-NDR model (subfigures 7.4e-f) reveals that in both cases the dynamic procedure is instead affected, even if in different ways. In particular, as also predicted in section 4.5.4 (see Figure 4.5), the DM-NDR model would require a wide range of C_{ss} values near the walls and, even if a definite peak is still present, it is much less significant and the scale-similar part of the model mostly works with a saturated value of the constant $C_{ss} = 2$. Such peak has been removed from the figure for the sake of clarity, but it is nonetheless present. The result for the grid CT, notably, shows a very similar behavior, with the PDF preserving its shape but, because of the larger range of the constant values, the main peak is substantially lowered. Moreover, after the clipping the PDF is substantially altered (the peak in $C_{ss} = 2$ has again been removed for the sake of clarity).

With such results at hand, it is easy to recognize the exact same behavior of the grid CT in the turbulent pipe flows, both at low (subfigures 7.5a-b) and high (subfigures 7.5c-d) Reynolds numbers. In particular, the non clipped PDF has a peak location and a shape which are similar in the two cases but the required range for the dynamic constant is substantially larger than assumed and the clipping has a very strong effect on the resulting PDF. However, even not resorting to any clipping, it is apparent that using a constant grid expansion ratio is not beneficial for the dynamic procedure at the wall, whose outcome is much more spread than for a cosine stretching law.

At the moment, the most plausible cause for such behavior seems to be the specific test filter at hand, which is strongly affected by the underlying grid. However, it is not yet clear if it is just the ratio $\Delta^2_{n,0}/\Delta^2_{m,n}$ that is affecting the dynamic procedure[3] or the filter as a whole, when providing the full scale-similar term[4]. Considering the strong difference between the DM-NDR model and the basic DM one, it appears that the former plays a more important role in the dynamic procedure, as also evidenced in section 4.5.4.

However, in conclusion, despite the mentioned flaws, the agreement of the model DM with the DNS data can be considered satisfactory, and certainly better than the one for the DS model. Also, besides a possible lack of convergence for the statistics and the requirement for an extended filter stencil, the use of the model on such unstructured grids has not shown particular issues with respect to the channel case[5].

7.1.3 Test of the mapping procedure

Before switching the attention to more complex flows, the analysis presented in section 7.1.1 allows to briefly introduce the tests performed on the mapping procedure, presented in section 5.6.3. In particular, it has been applied in the generation of the inflow condition for two fully developed turbulent flows in two straight ducts of different cross sections. In the first case the cross section is circular and all the flow parameters are those relative to the $Re_\tau = 320$ case presented in the previous section. The second case is instead based on a square sectioned duct, with a fully structured grid and a friction

[3] This could justified by the fact that the scale-similar term entering the dynamic procedure is always proportional to the Leonard tensor in the relative Germano identity. It is only the proportionality constant which is affected by the filter, trough the ratio $\Delta^2_{n,0}/\Delta^2_{m,n}$.

[4] For example, because of the filter asymmetry, odd error terms not considered in the model derivation might play an important role

[5] Paradoxically, the main problem is in the structured part of the grid.

Reynolds number based on the hydraulic diameter $Re_\tau^D = 600$. In both cases the mapping procedure is compared with the two stochastic inflow generation methods already available in the solver, the VM and the SS, while the reference solution is a periodic computation on a domain with length L_z and equal numerical/physical settings.

These settings, in particular, are identical to those used in the previous tests except for the SGS modeling, which for simplicity is based on the NM approach with the Bounded Central scheme for the convective term. However, all such details are not actually influent as what really matters is that, for a given case, the three methods and the reference solution all have the exact same setting, including the grid in the pipe cross section and the axial spacing of the grid[6]. Thus, for the sake of conciseness, no additional details are provided.

For the methods VM and SS the domain has an overall length $L = 20D_H$, with D_H the hydraulic diameter of the section. The two methods are applied at the inlets with all the required quantities to be prescribed determined by a preliminary RANS computation with a full Reynolds stress model. The details of the model are not influent, it just suffices to mention that, among all the available models in the solver, the selected one provided the most accurate solution for both the cross sections and for all the required quantities. Hence the two methods worked in the best possible condition[7]. An outflow condition is instead applied on the outlet section of the pipe, with the stream-wise viscous derivatives set to zero and the three velocity components extrapolated from the interior with a global mass flux computed in order to satisfy the continuity for the given inlet condition.

For the mapping procedure, the original domain of length L has been split in two parts. The auxiliary one, whose length is selected equal to the one of the reference periodic computation, L_z, and the main one, with length $L - L_z$. So that the overall domain length for the mapping procedure is identical to that for the alternative methods, but the main domain length is smaller. This, in turn, allowed a fair comparison of the computational costs for all the methods and, as shown in the results below, has not impaired the outcome of the test. The computation in the auxiliary domain is setup as an exact replica of the reference periodic one, with the same pressure gradient driving the flow[8]. At each time step, following the procedure described in section 5.6.3, the velocity field is then passed, from a reference surface in the auxiliary domain, to the inlet surface of the main domain, where it is used as inflow condition. The outflow condition is instead used for the outlet surface of the main domain.

All the results presented in the following are made non-dimensional by the friction velocity u_τ, the hydraulic diameter D_H and the kinematic viscosity ν. However, differently from the periodic pipe and channel flows previously analyzed, the use of the pressure gradient for the determination of u_τ is not anymore an option, as no actual pressure gradient is used on the main domain. As a consequence, it is computed trough the wall normal derivative of the mean velocity profile: $u_\tau = \sqrt{\nu \partial \langle u_z \rangle / \partial n}$. In the specific case of the square sectioned duct the profiles, and the friction velocity, are computed in the symmetry plane after averaging on the four quadrants of the section.

The first thing to note from the results, presented in Figures 7.6 and 7.7, is that, on

[6] Obviously, for sufficiently long domains, differences in the domain axial length are not influent.

[7] Still, such one to one correspondence between the better quality of the prescribed quantities at the inlet and the output of the methods has not been assessed.

[8] An alternative control algorithm has also been implemented, which allows fixing any integral quantity on the mapped surface.

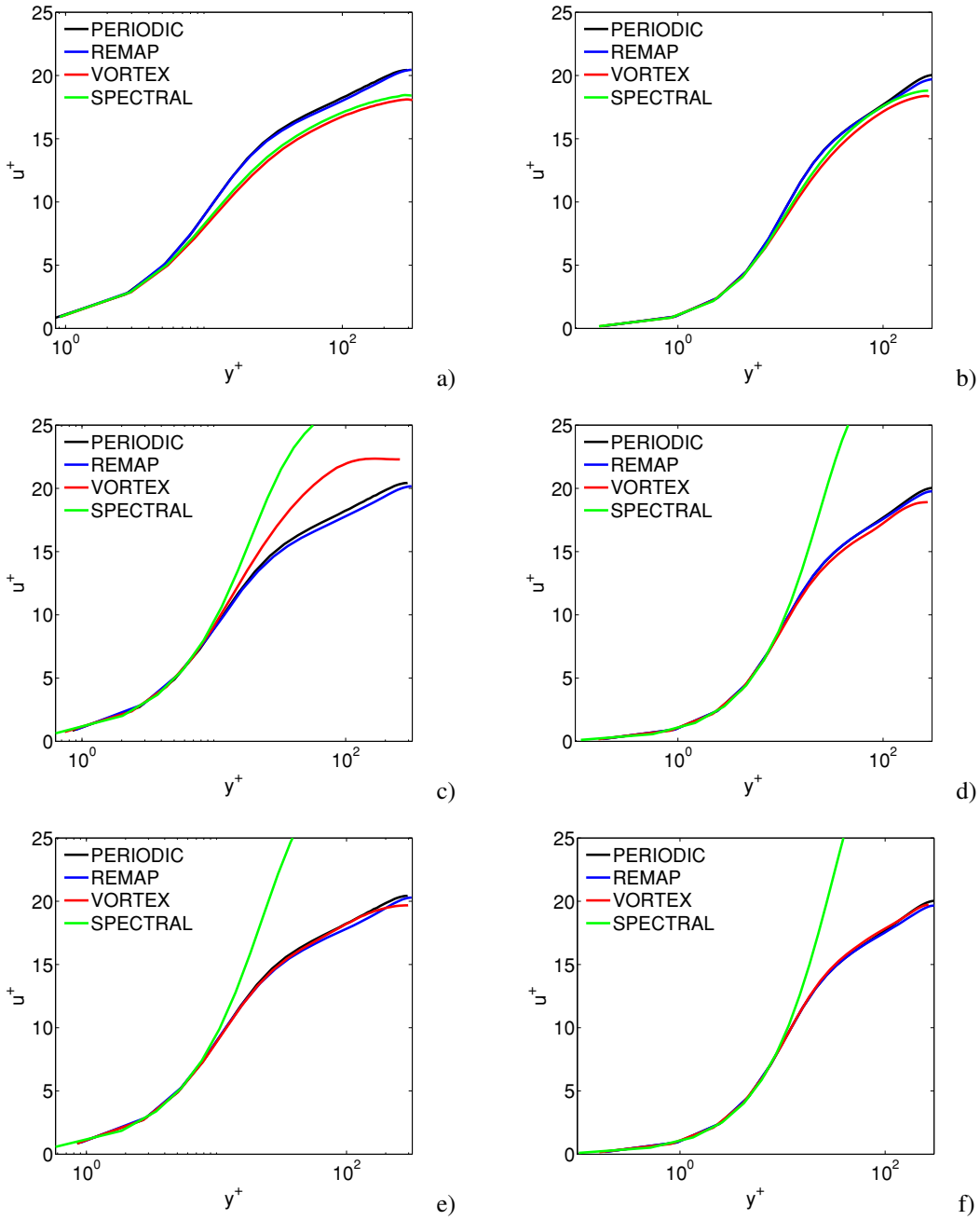

Figure 7.6: *Axial development of the mean velocity profile for the inflow test. Top:* $z/D_H = 0$*. Center:* $z/D_H = 5$*. Bottom:* $z/D_H = 10$*. Left: Circular section. Right: Square section.*

both sections, the mapping procedure can correctly reproduce the mean velocity profile (subfigures 7.6a-b) and the stream-wise fluctuation (subfigures 7.7a-b), hence its effectiveness and correct implementation is readily confirmed. In contrast, what is more interesting to note, is that none of the already available methods is capable to reproduce the correct profiles at inlet. In particular, as the original RANS profiles are not reported (for the sake of clarity), it should be mentioned that the mean velocity profiles correctly reproduce the original RANS prescriptions but, nonetheless, this is not effectively rep-

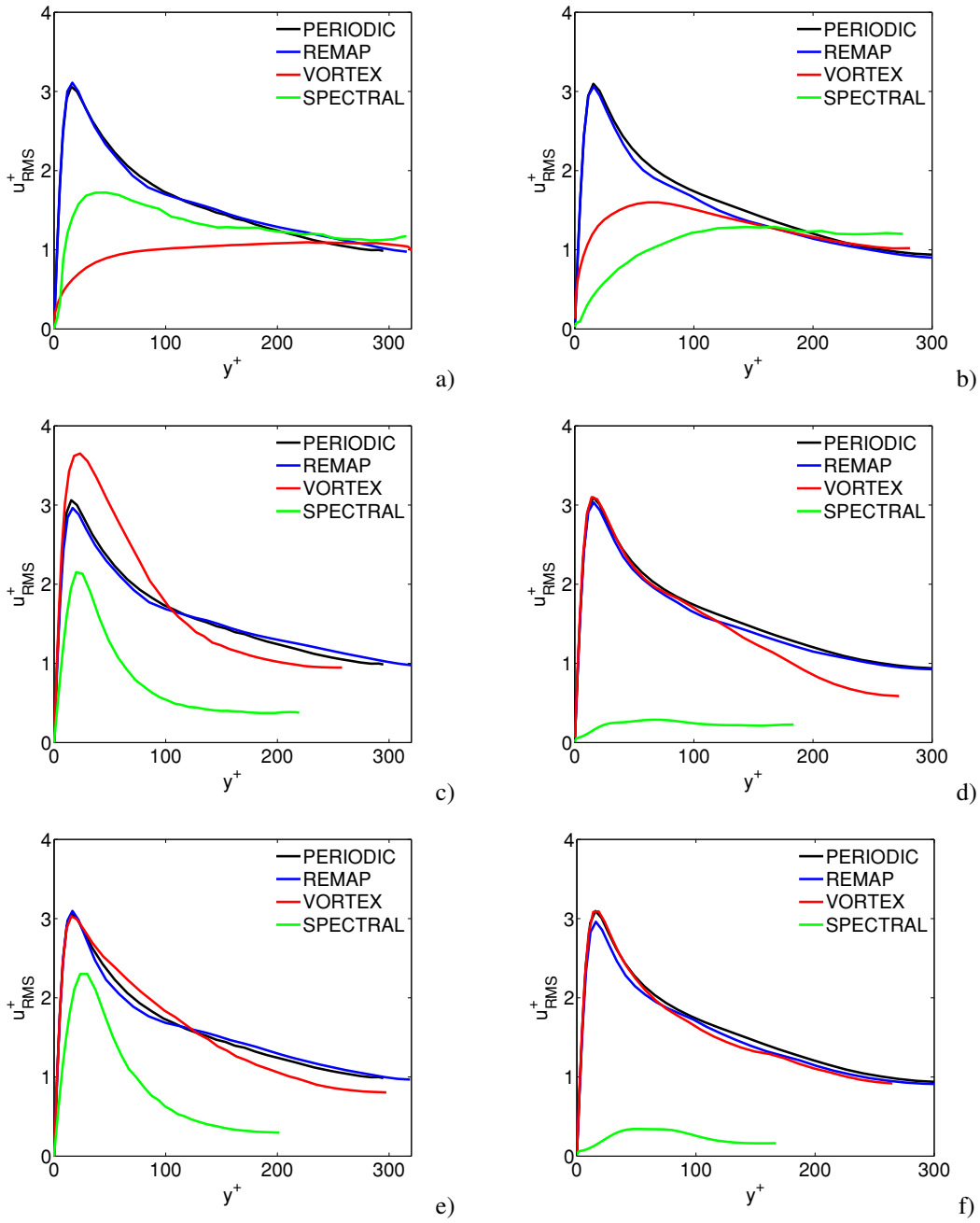

Figure 7.7: *Axial development of the stream-wise velocity fluctuation profile for the inflow test. Top:* $z/D_H = 0$. *Center:* $z/D_H = 5$. *Bottom:* $z/D_H = 10$. *Left: Circular section. Right: Square section.*

resentative of the equilibrium LES solution. In contrast, the reproduced stream-wise fluctuation is far even from the original prescription and strongly underestimated. Following the axial development of the profiles reveals that, still independently from the section shape, the velocity field generated by the mapping procedure preserves its correspondence with the reference periodic one. This thing, while probably obvious from the physical point of view, confirms also that there are no evident implementation errors

in the parallel communication procedure, so that the full spatio/temporal flow dynamics is replicated on the main domain as if it was an actual continuation of the auxiliary domain. In contrast, the two default methods presents strong differences. On one side, the SS method completely fails in providing a sustainable, physical inflow field, and the flow laminarizes independently from the section shape. The analysis of the spectral content for the inflow generated with such method (not shown) has revealed that its main flaw is due to a lack of spatial correlation for the fluctuations in points on the same inlet plane, while no problem exists for the temporal correlation. This suggests that the observed behavior might be due to a wrong parallel implementation[9]. On the other side, the VM is effective in producing a sustainable inflow field but, in order for this to be completely adapted to the overall numerical/physical setting, requires a development region which, for the present cases, is no less than $10D_H$. For the present specific implementation, it has been observed that such behavior is mostly due to the fact that the VM method provides a velocity field with no dissipative range in the spectrum (not shown), thus rendering the adaption sensibly slow.

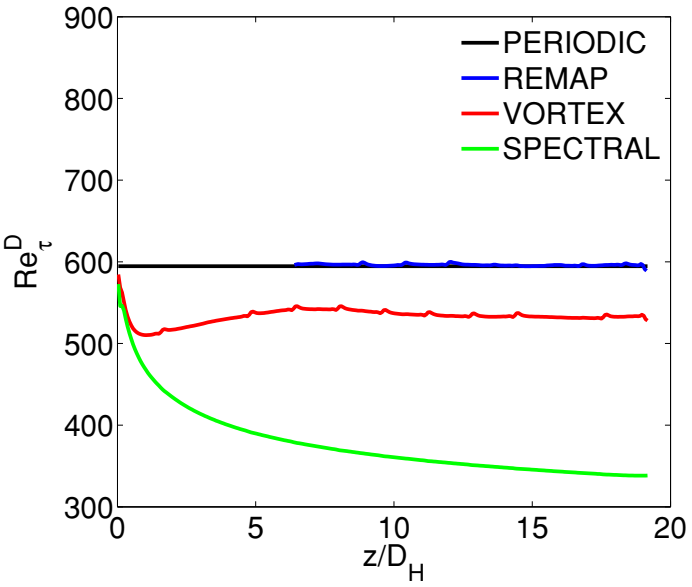

Figure 7.8: *Axial development of the friction Reynolds number for the inflow test on the square sectioned duct.*

However, it is worth noting that, even when the equilibrium is reached, the resulting flow would still be representative of the original RANS prescription and not the desired LES one. In particular, as shown in Figure 7.8 for the square sectioned pipe, while the original prescription is based for all the methods on a friction Reynolds number $Re_\tau^D = 600$, only the mapping procedure is able to sustain it. Note that, to elucidate the fact that the mapping uses a fraction of the domain for a periodic computation, the relative curve in Figure 7.8 has been properly shifted. However, no attempt has been

[9]It is usually reported in the literature, e.g., Castro and Paz (2013), that such spectral like methods are embarassingly parallel. However, a fundamental requirement for such implementation is that all the random part of the method is generated by a single process, or in the same way by all the processes. The present implementation might thus fail because of a not correct management of this aspect.

made here in minimizing such length and the full reference periodic domain is used.

Besides the correctness of the implementation for the mapping procedure, these results also provide a more interesting conclusion. Indeed, from the last figure is evident that the cost for the auxiliary domain in the mapping method is lower than the one for development region in the VM. However, even forcing the hand and assuming that the same fraction of the domain is sufficient for both, the computational costs of the present mapping procedure are the lowest among the two working methods.

Table 7.2: *Normalized computational costs of the tested inflow methods.*

VM	SS	Mapping
1	0.65-1.02	0.77-0.88

These costs, normalized with respect to the relative VM case, are summarized in Table 7.2. In particular, the reported ranges are representative of the maximum and minimum values detected in a group of tests performed on several different machines, various load balances and different partitions of the domain. Even in the worst case, the present mapping is found the 12% cheaper than the VM, while the average saving is around the 18%. Note, also, that these costs refer to time advancement over 100 time steps. Hence, considering the necessary development region for the method VM, the overall cost saving offered by the mapping procedure can be substantial while being also the best inflow prescription.

7.2 Flow and heat transfer in a matrix of surface mounted cubes

The test cases analyzed up to now, despite containing most of the flow physics encountered in more complex applications[10], are somehow limited by the fact that no actual obstacles have been considered and the fluid-solid interaction has been confined to the walls of plane channels or pipes. As a consequence, the previous tests cannot certainly be considered representative of most of the remaining interactions between flows and solid objects, which are clearly the rule in the engineering practice. In order to overcome such deficiency, while still relying on controlled flow conditions, the DM model developed in this work has been used to compute the flow and heat transfer in a matrix of surface mounted cubes.

Indeed, the inclusion of the heat transfer, and more specifically with a bluff body, can be considered one of the most common fluid-solid interaction found in applications. A typical example is the cooling of electronic parts and devices, which mostly resemble bluff bodies. Also, cooling strategies for turbine blades are usually based on protruding ribs in internal passages, which again involve a classical bluff body transferring heat to the surrounding fluid. Such flows are characterized by recirculation regions as well as shear layers, separations and vortex shedding, with the overall flow having strong three-dimensionality and unsteadiness which, in turn, strongly influence the heat transfer characteristics. Thus, even from the pure testing point of view, these flows can be considered a representative benchmark for more challenging applications.

[10]The reluctant reader can convince himself by reanalyzing the channel flow test performed in a moving reference frame and noting the concomitant presence of near wall structures and a mixing layer.

Moreover, for the particular flow configuration analyzed here, as well as for similar ones, RANS/URANS methods have shown to be strongly inadequate (Hellsten and Rautaheimo, 1999), either because of the overlapping between modeled and geometry dependent scales or because of the difference in Reynolds number between typical applications and the range of validity of these models. Thus, from this point of view, the present test is also well suited for LES.

However, on the other side, this class of flows is also known to be particularly insensitive to the details of the SGS model (Mathey et al., 1999b; Krajnović and Davidson, 2002; Krajnović, 2009), which certainly promotes a lack of attractiveness for further studies in LES. Nonetheless, when considering the development of new SGS models, it is certainly important to also assess that such limiting behaviors are correctly represented. In this sense, with respect to the previous test cases, bluff body flows would represent the opposite extreme in the scale of sensitivities to the SGS details.

Something that instead goes usually unnoticed, or not sufficiently stressed, is that a lack of sensitivity in the SGS model necessarily denotes a much stronger sensitivity on the resolved scales. This, in turn, implies that, among all the parameters, the computational grid assumes a fundamental role. In particular, while the flow details can somehow be predicted accurately by a sufficient resolution of the geometry dependent scales, which are large, the prediction of the heat transfer characteristics can easily escape this line of reasoning. Indeed, on average, the heat transfer from a body to a surrounding fluid is proportional to the local average fluid velocity and the mean temperature difference between the solid and the fluid. However, the local heat transfer characteristics strongly depend on the flow around the body, due to its influence on the relative temperature distribution and the capability of the resolved flow structures to enhance or impede the replacement of heated fluid parcels near the body surface. Typical examples of such influence are the decrease of heat transfer in strong recirculation zones, where the fluid is trapped, as well as increased heat transfer in attachment/separation zones, due to the high local turbulence intensity. Thus, in practice, the overall heat transfer can be easily dominated by small scale features, which in turn are still influenced by the SGS model and its interaction with the grid. Moreover, from the conceptual point of view, the effective transfer of heat between a solid and a fluid still necessarily happens at the molecular level as no equivalent of the pressure drag exists for the energy. Hence, again, the details of smallest resolved scales near the solid can affect the mean heat transfer and the influence of the SGS model on such mechanism needs to be properly assessed.

7.2.1 Flow description and computational setup

The flow considered in this test has been investigated experimentally by Meinders and Hanjalić (Meinders, 1998; Meinders and Hanjalić, 1999), whose data served as reference for the 6$^{\text{th}}$ and 8$^{\text{th}}$ ERCOFTAC workshops on refined flow and turbulence modeling (Hellsten and Rautaheimo, 1999) and are used here with the same purpose. The experimental setup consists of a matrix of 25×10 equally spaced cubes, as sketched in Figure 7.9. The cubes, whose sides have a length $H = 0.015m$, are placed in a channel of depth $D = 3.4H$ and their face to face distances are $S_x = S_y = 3H$, with x and y denoting the stream-wise and span-wise directions respectively. Flow and heat transfer measurements are performed around the 18$^{\text{th}}$ cube row in the stream-wise

direction, where a single internally heated cube is placed. The heated cube consists of a copper core at fixed temperature $T_c = 348.15K$, covered by an epoxy mantle of thickness $0.1H$. The working fluid is air, with bulk temperature and velocity equal to $T_i = 293.15K$ and $U_b = 3.86m/s$ respectively. At these conditions, the Reynolds number based on the cube height is $Re_H = HU_b/\nu = 3854$ and the flow at the investigated cube row is fully developed.

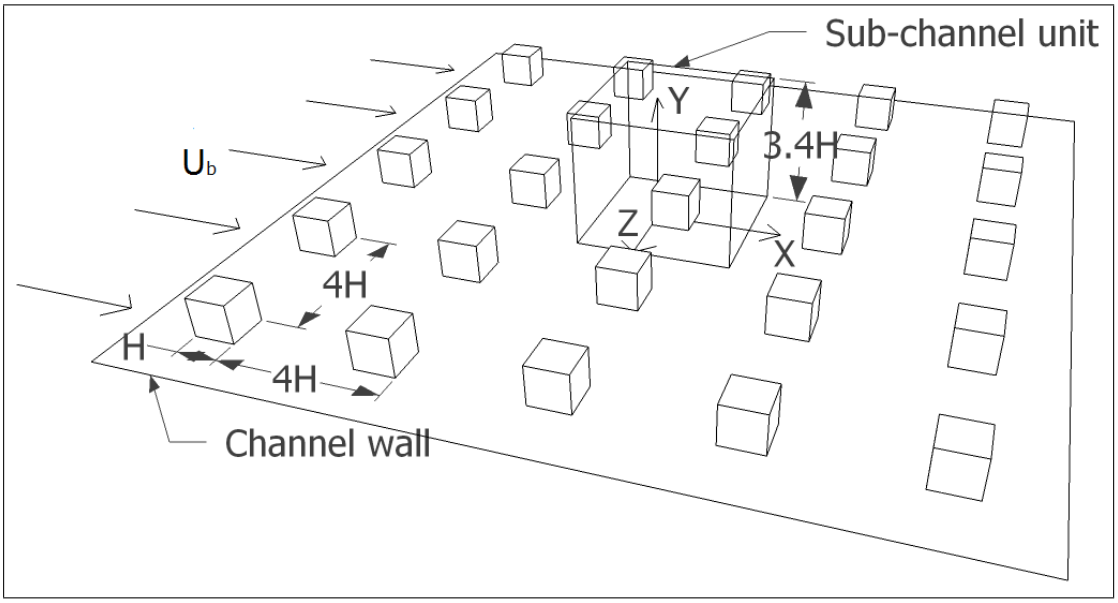

Figure 7.9: *Sketch of the flow under investigation. Opposite channel wall not shown.*

The flow and heat transfer under these conditions are simulated by the means of three SGS modeling options. One is the present dynamic mixed model (DM) in its default setting with the turbulent heat flux modeled according to equation (4.30). The second option investigated is the default DS model implemented in the solver, with the turbulent heat flux modeled according to equation (2.19). For both the previous models, a constant SGS Prandtl number $Pr_{sgs} = 0.85$ is used, as typically done in this kind of flows (Tyacke and Tucker, 2012). Finally, the third option considered is based on the ILES approach, namely, a Bounded Central scheme for the convective terms and no SGS model. All the remaining numerical settings are the default ones already established in the previous chapter. The only exception to this is the convective term in the temperature/energy equation, which is discretized with the bounded central scheme for all the modeling options, including those relying on an explicit SGS heat flux model. This choice has been motivated by the need of ensuring the proper physical boundedness for the temperature and the fact that, especially for the DS model, the effectiveness of the eddy viscosity appeared very limited (see section 6.3.2). Hence, in order to have a fair comparison, the same bounded scheme has been used for all the modeling options.

The computational domain is based on a sub-channel unit with dimensions $4H \times 3.4H \times 4H$ in the x, y and z directions respectively (see Figure 7.9). The coupling of the conduction in the heated cube with the convection in the outer flow is taken into account by simultaneously solving the energy equation in the fluid domain and in the

solid epoxy layer, whose internal surface temperature is fixed equal to T_c. As the flow is fully developed, periodic boundary conditions apply for the stream-wise and span-wise directions. However, to properly take into account the fact that only one cube was heated in the experiment, a buffer constant temperature zone is defined adjacent to the inlet of the domain, to force the recycled flow temperature to be uniform and equal to T_i. No-slip velocity conditions are applied at all the solid walls and adiabatic conditions for the temperature on the channel walls. Relevant physical properties for the fluid and the solid epoxy mantle are summarized in Table 7.3. According to Meinders and Hanjalić (1999), buoyancy effects are neglected as well as the variation of the molecular coefficients with the temperature, leaving the energy equation uncoupled with respect to the momentum equations.

Table 7.3: *Material properties for the surface mounted cubes case.*

Property	Fluid (Air)	Solid (Epoxy)
$\rho\,[\mathrm{kg/m^3}]$	1.16	1150
$\lambda\,[\mathrm{W/mK}]$	0.0246	0.236
$C_p\,[\mathrm{J/kgK}]$	1007	1668.5
$\mu\,[\mathrm{kg/ms}]$	$1.743{\cdot}10^{-5}$	

The flow has been initialized with a RANS solution on a coarse grid (see next section) and then further advanced in time with superimposed random fluctuations and the ILES approach. The resolved kinetic energy in the fluid and the temperature in the solid have been monitored and this coarse simulation has been advanced in time until a statistically steady state has been reached. This preliminary flow field has then been used to initialize all the remaining cases, which are advanced to the statistically steady state before collecting the statistics, computed with the single-pass algorithm developed in this thesis. The flow is driven by a constant pressure gradient in the stream-wise direction, $\partial p/\partial x = -7\mathrm{kg/m^2s^2}$, with a maximum difference in all the predicted mass flow rates within the 4% of the experimental value. This has been assumed acceptable, considering the lack of sensitivity shown by the experimental results in this specific range of Reynolds numbers (Meinders and Hanjalić, 1999), and allowed a strong reduction of the computational costs as fixing the mass flow rate would have required abandoning the FSM for the pressure-velocity coupling[11].

The time step is fixed equal to $\Delta t = 1 \cdot 10^{-5} s$, which ensured a maximum Courant number below 0.5 for all the simulations. Time statistics are collected over $5 \cdot 10^5$ time steps, which approximately amounts to $1290 H/U_b$. With respect to the main shedding frequency of the cubes' wake, determined by the experiments, this time represents approximately 135 shedding cycles. While being a relatively limited time with respect to the one used in the experimental campaign, it appears to be sufficient for the purposes of the present comparison and no significant differences have been appreciated by extending it over additional shedding cycles.

[11] This is a specific solver feature that, obviously, has nothing to do with the FSM itself.

7.2.2 Computational grids

Besides assessing the DM model capabilities, the specific aim of the present test is to also evaluate, for this class of flows, the effective degree of independence of the LES predictions from the grid, in terms of both flow and thermal quantities. In order to do so, three fully structured grids are used, whose representative topology is sketched in Figure 7.10 for a cross section in the flow symmetry plane (e.g., flow from left to right).

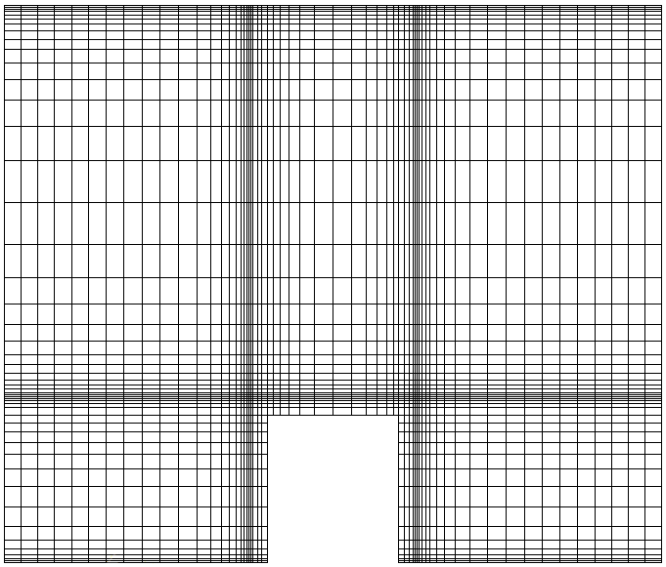

Figure 7.10: *Representative grid topology for the surface mounted cubes case.*

In practice, in order to understand the effective resolution capabilities in terms of the total number of cells invested in the computation, the classical grid refinement approach used up to now is not especially suitable in this case, as most cells would be used where not specifically required, i.e., away from the cube and its wake. Instead, it is known (Mathey et al., 1999b) that the correct prediction of this flow requires correctly capturing the flow separations from the sharp edges and their dynamical behavior. Also, the mean heat transfer characteristics are expected to depend on the proper representation of the stresses at the walls of the cube (Mathey et al., 1999a). In contrast, the stresses at the walls of the channel do not directly influence any of the heat transfer mechanisms at play and, with respect to the overall drag generated by the cube, their influence is certainly negligible.

For these reasons, the computational grids used here have all been designed to achieve the maximum possible resolution near the cube surface with all the remaining grid aspects determined solely by prefixed limits on the total cell count for the given grid. The only exception to this has been determined by a specific solver feature, which automatically enables the wall function (5.25) whenever the local wall-normal spacing is not within the viscous sub-layer. Hence, in order to prevent a spurious switch in the boundary conditions at the channel walls, a fixed spacing in wall-normal direction, $\Delta y_{min} = 0.01H$, has been used, for all the grids, in the cells next to the channel walls. Note that, according to the channel height D, the fluid properties and the driving pressure gradient, this value would give approximately $\Delta y^+_{min} = 5.5$ for a pure channel flow. However, it has been verified a posteriori that such value represents only an up-

per limit and is never effectively reached. The remaining relevant grid parameters are instead summarized in Table 7.4. In particular, N_s denotes the number of cells along the cube sides, while Δx denotes the grid spacing in both the wall-parallel directions, x and z, which are kept equal in their extreme values but with different expansion ratios in stream-wise and span-wise directions.

Table 7.4: *Main grid parameters for the surface mounted cubes case.*

Grid	N° Cells	N_s	Δx_{min}	Δx_{max}	Δy_{max}
C	$6.7{\cdot}10^5$	35	$0.02H$	$0.13H$	$0.11H$
M	$1.3{\cdot}10^6$	50	$0.01H$	$0.14H$	$0.10H$
F	$2.3{\cdot}10^6$	60	$0.01H$	$0.09H$	$0.10H$

Among the different features of the grids, it is worth highlighting that the coarse grid has just a slight increase in the grid spacing near the cube faces ($0.02H$ vs. $0.01H$ for the remaining cases) but this inevitably led to a more uniform grid in the wall-parallel planes and a maximum spacing Δx_{max} which is lower than the one relative to the medium grid. As a result, the three grids strongly differ also in the ratio $\Delta x_{max}/\Delta x_{min}$, whose variation is not monotone with the total cell count.

It is worth mentioning that, from the modeling point of view, these grids represent a challenging benchmark because, as both Figure 7.10 and Table 7.4 indicate, strong positive/negative grid stretching exists in the mean flow direction and this could impair the stability of a non-dissipative SGS model. Still, the present DM model has already shown to have embedded hyper-viscous effects which should prevent such instability and the present grids are a perfect benchmark for this feature.

7.2.3 Numerical results

Selected statistical results are presented on the paths depicted in Figure 7.11, which include four vertical paths at different stream-wise stations in the symmetry plane of the flow and two paths approximately on the symmetry planes of the cube. Unless otherwise stated, all the quantities are nondimensionalized by the bulk velocity U_b and the cube height H. For the thermal analysis, the nondimensional temperature θ and the Nusselt number Nu are evaluated on the cube's surface as follows:

$$\begin{aligned} \theta &= \frac{T(\xi,\eta) - T_i}{T_c - T_i} \\ Nu &= \frac{\lambda_s H}{\lambda_f \left[T(\xi,\eta) - T_i\right]} \frac{\partial T(\xi,\eta)}{\partial n} \end{aligned} \tag{7.7}$$

where λ_f and λ_s denote the thermal conductivities of the fluid and the solid, $T(\xi,\eta)$ is the local temperature on the surface of the cube, expressed in a local coordinate system, and the temperature derivative is evaluated on the solid side of the cube surface, along the normal direction n. This overall evaluation procedure exactly follows the experimental one (Meinders, 1998), and has been found fundamental in order to correctly compare the numerical results with the experimental ones.

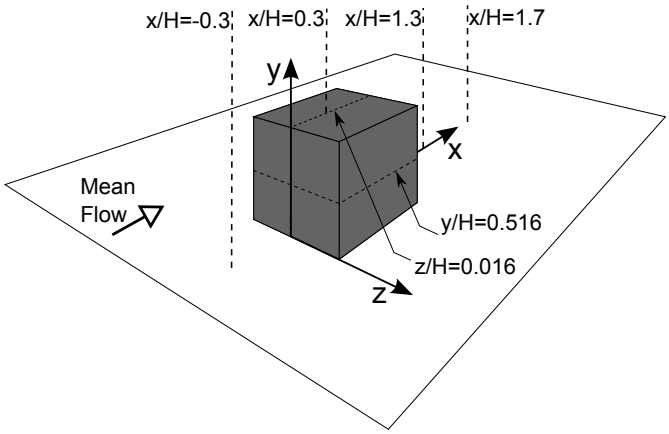

Figure 7.11: *Location of the paths for the comparison of the results in the surface mounted cubes case.*

Flow analysis

The effect of the grid resolution and the SGS model is investigated first, in Figure 7.12, for the representative section at $x/H = 1.3$. Indeed, it suffices to show that, independently from the resolution, all the SGS models investigated can correctly represent the overall fluid dynamic behavior. This essentially confirms the expected low influence of the SGS model. Specific differences among the models are found only for the velocity fluctuations in the core of the channel, but these are reduced by increasing the resolution. Note, however, how the distinctive features of the present DM model are still evident. Namely, it is the only one correctly predicting all the local fluctuation peaks, independently from the resolution. Also, as a single layer of cells is involved in the test filter (e.g., $N_L = 1$), it tends to overestimate the fluctuations in the channel center for all the resolutions. The results obtained for the channel flow suggest that, in this case, the simulations would have benefited from the filter stencil extension as the predicted mean velocity profile seems roughly independent from both the resolution and the SGS model. Still, a resolution limit is also present as none of the models can correctly predict the fluctuation in the channel center.

A less marked, but nonetheless present, defect is also present, for all the grids, on the mean velocity profile near the top wall. This behavior essentially replicates the one for low resolutions in the channel flow and, remarkably, is still present in this case. The fact that the model DM is not capable of reducing this effect is due to a combination of the used grid stretching, already discussed in section 7.1.2, and of the generally low span-wise resolution, which on the grid F still reaches $\Delta z^+_{max} = 50$. However, the relative fluctuation in the same zone is instead better predicted by the model and, in any case, the flow near the cube essentially behaves independently from the upper wall zone.

The general trends observed here are essentially replicated for all the remaining quantities and axial stations, they are thus not reported for the sake of convenience. A notable exception is only present in the transverse velocity fluctuations (not shown), which are underestimated in the wake of the cube, independently from the SGS model and the grid resolution. This fact has been observed in most of the scale-resolving simulations performed on this flow (Mathey et al., 1999b; Ničeno et al., 2002) and seems

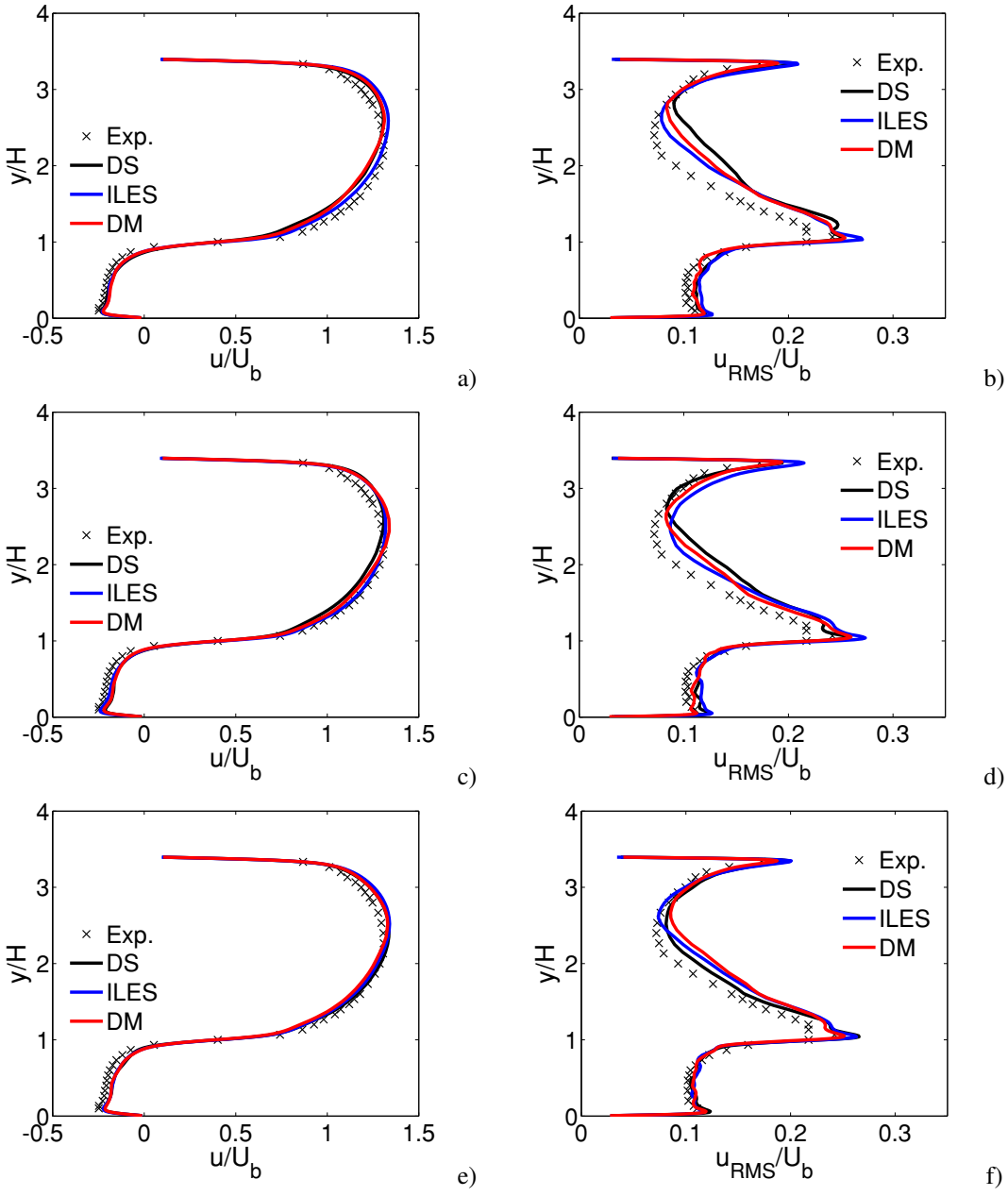

Figure 7.12: *Axial profiles for the surface mounted cubes at $x/H = 1.3$. Left) Mean velocity. Right) RMS fluctuation of the stream-wise velocity. Top) Grid C. Center) Grid M. Bottom) Grid F.*

to suggest that much higher resolutions are required to properly capture the anisotropy features of the wake. A general overview of the overall accuracy achievable on the coarse grid is instead given in Figure 7.13, where the profiles for the stream-wise velocity and its RMS fluctuation are compared on the remaining sections depicted in Figure 7.11. Again, no difference appears among the SGS models, but sufficient accuracy is achieved at all the stations.

Overall, these results evidence two aspects. On one side, it is readily confirmed that the prediction of this flow is mostly independent from the SGS details and sufficient

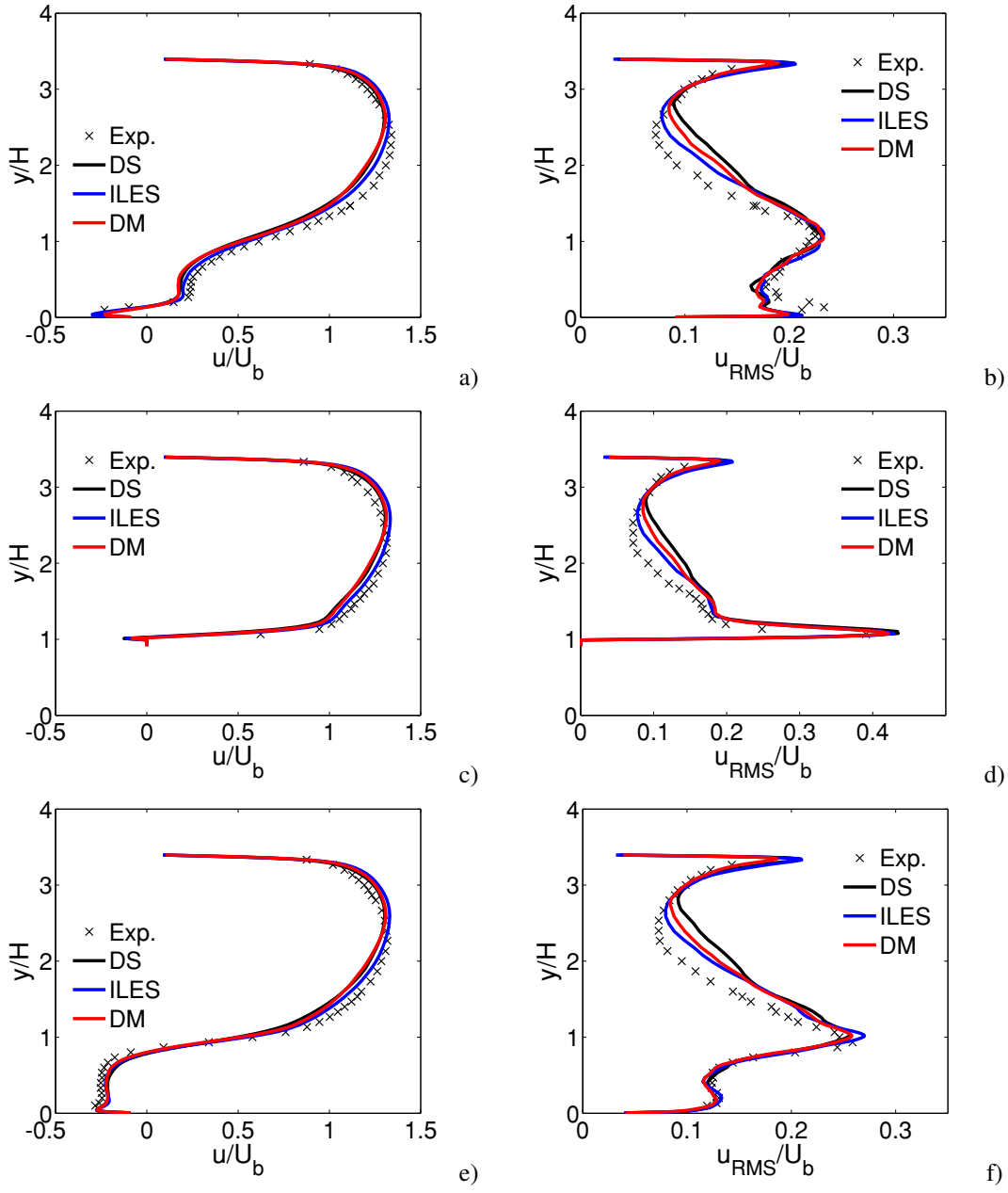

Figure 7.13: *Axial profiles for the surface mounted cubes on the grid C. Left) Mean velocity. Right) RMS fluctuation of the stream-wise velocity. Top)* $x/H = -0.3$*. Center)* $x/H = 0.3$*. Bottom)* $x/H = 1.7$*.*

accuracy is recoverable on relatively coarse grids (e.g., grid C). On the other side, while not particularly effective, the model DM has shown no stability issues on any of the grids. In this regard, it has to be mentioned that, differently from the previous test cases, the scale-similar part of the model tended to be relatively active in most of the domain zones for all the grids. While the details of such activation have not been investigated and certainly produced few overall effects, this seems to confirm that the scale-similar part of the model has embedded dissipative features which prevent instabilities even when the model is strongly active in the whole domain. Also, the resulting general

lower effectiveness could then be explained by the relatively low Reynolds number, not producing a sufficient scale separation between the enhanced spectral zone and the one affected by the model dissipative effects.

Thermal analysis

More interesting results are instead observed for the thermal quantities, illustrated in Figures 7.14 and 7.15 as a function of the curvilinear coordinate s/H. Indeed, in contrast to the flow predictions, two main distinctive features are now present which evidence the complexity of the thermal predictions for bluff body flows.

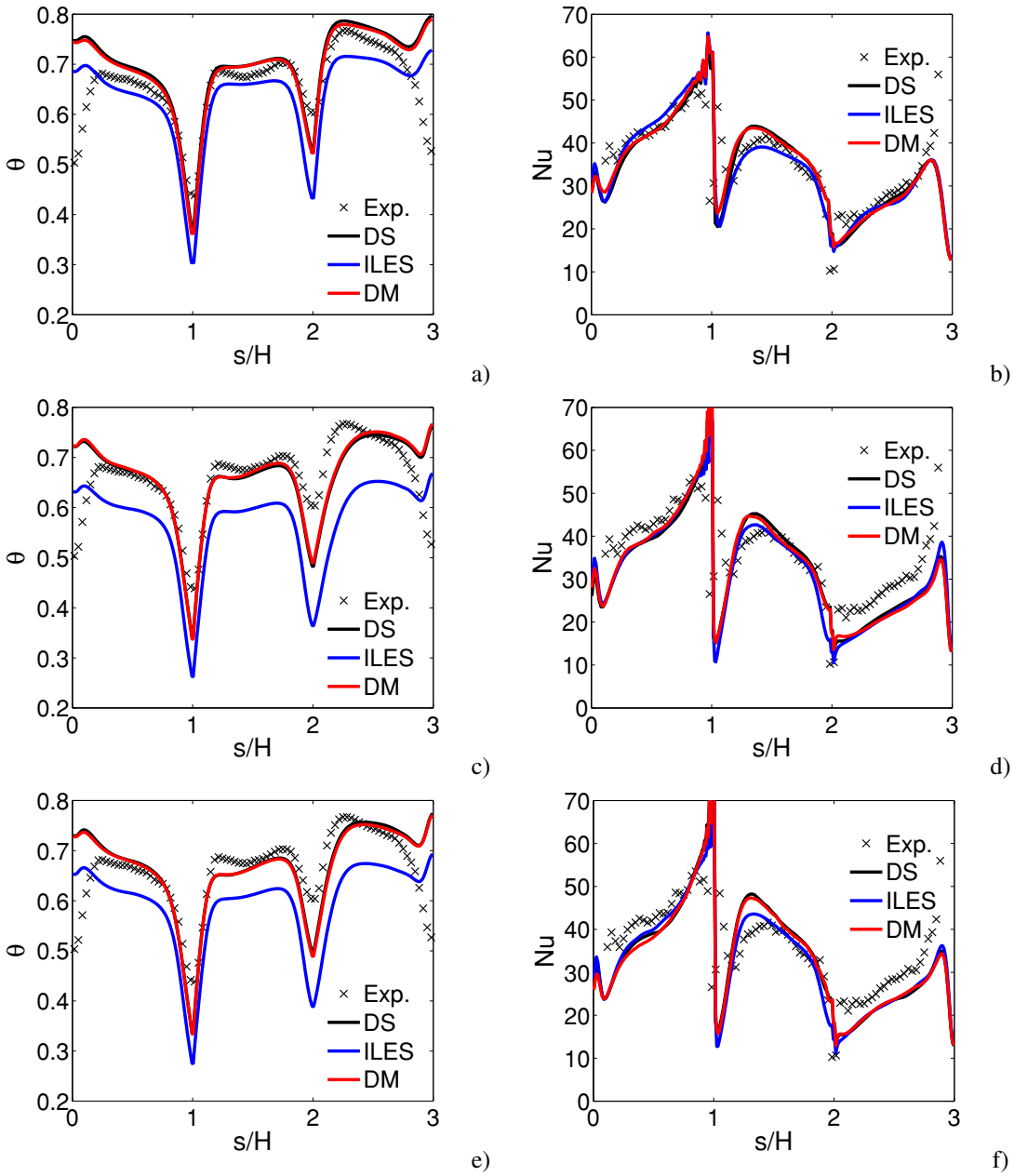

Figure 7.14: *Temperature (left) and Nusselt (right) profiles on the surface of the cube for* $z/H = 0.016$. *Top) Grid C. Center) Grid M. Bottom) Grid F.*

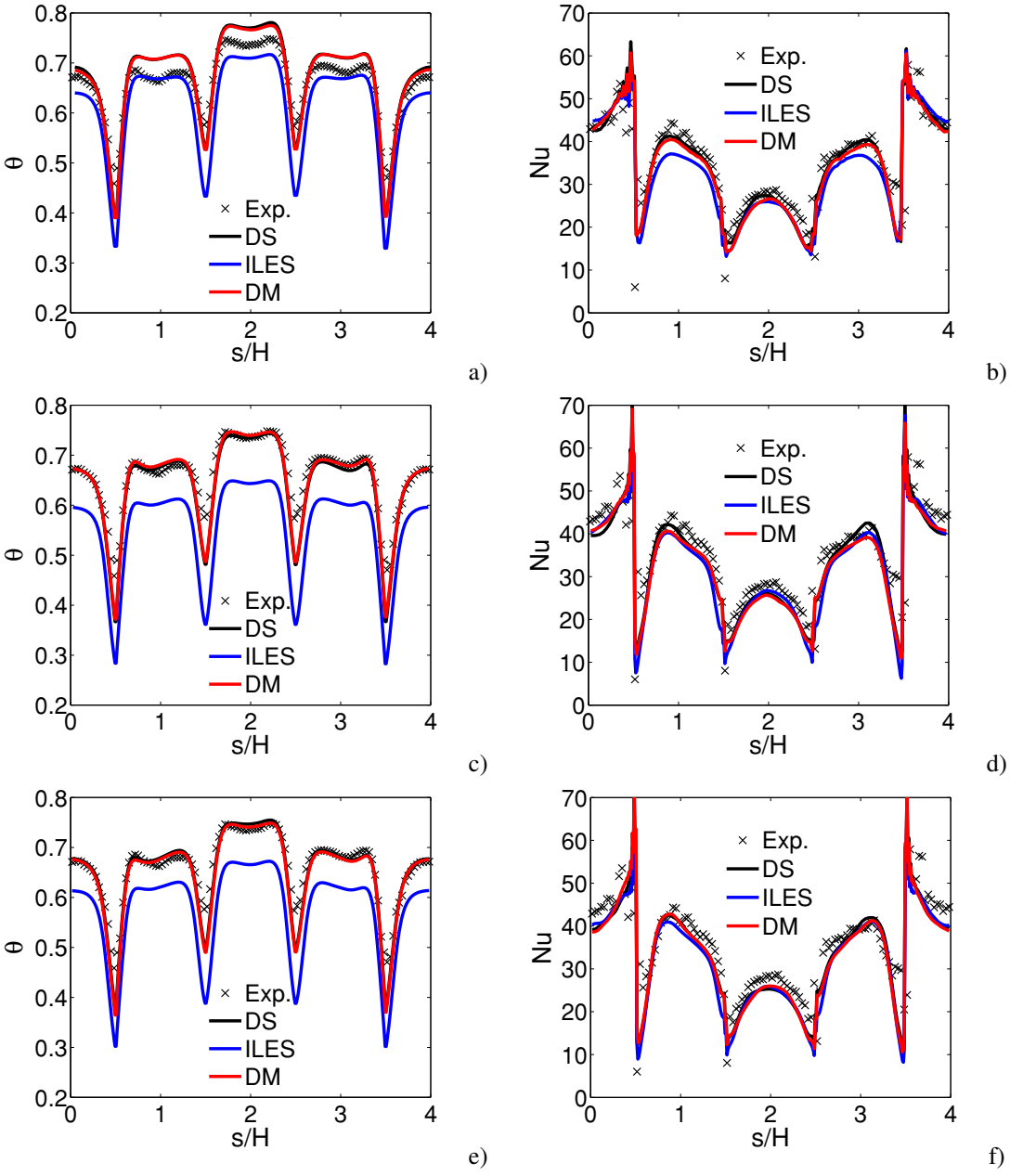

Figure 7.15: *Temperature (left) and Nusselt (right) profiles on the surface of the cube for* $y/H = 0.516$*. Top) Grid C. Center) Grid M. Bottom) Grid F.*

The first of such features is that the two investigated quantities, the temperature and the heat flux at the wall, both have a strong sensitivity to the grid and the SGS model. The second feature is instead a remarkable difference between the ILES approach and the explicit SGS modeling options, both being also sensitive to the grid. This is especially evident in Figure 7.14, but somehow masked in Figure 7.15, whose fortuitous vertical position tends to show contrasting trends.

Considering the general agreement found in all the flow results, a detailed explanation of such differences is hard to find. However, few details seem important in order to clarify the matter. Indeed, two different regions can be clearly identified, one being the

top and lateral faces of the cube, the other one being the front-rear ones. For the former ones an increased resolution always tends to increase the predicted heat flux, but mostly near the edges of the cube. This shows that the small scale details are indeed important as they regulate the correct representation of the small separation regions along the cube edges. These, in turn, are responsible for a larger fraction of the heat transfer on such faces and tend to influence most of the relative temperature distribution. In particular, the lower is the resolution the larger are the dimensions of such separation regions and, as a consequence, the lower is the effectiveness in the heat transfer. While this is only slightly appreciable for the explicit SGS modeling options, it is more evident for the ILES approach, whose strong dependence on the grid resolution tends to produce the largest variations in the Nusselt and temperature profiles.

In contrast, both the rear and front faces exhibit an inverse behavior, with both the predicted Nusselt and temperature decreasing with increasing resolution, but with a decreased sensitivity to the grid (with respect to the remaining faces). When the relatively lower differences among the SGS models are also considered (still with respect to the remaining faces), it becomes evident that on these two faces the heat transfer mechanisms at play are substantially independent from the small scales, to the extent that increasing the resolution does not improve the results[12].

However, even for such faces, a small scale influence seems to be nonetheless present. Indeed, assuming that the SGS heat flux model has a negligible influence with respect to the bounded central scheme used for the temperature convection, the large difference in the results, and their sensitivity, among the models can be only determined by the mass fluxes predicted by the relative momentum equations. As even for similar Nusselt profiles the resulting temperature distributions on all the faces tend to be lower for the ILES approach, this suggests that the relative velocity field tends to diffuse the temperature in a stronger, incorrect, way. In particular, this mechanism appears to be active independently from the grid resolution or the specific face of the cube.

A different possible explanation for the present temperature results, which however has not been investigated, is that, given the rough correctness for the different Nusselt profiles and flow statistics, the mean surface temperature might actually depend on higher order flow statistics not considered in the comparison. However, once again this would confirm the fact that the resolution of the small scales is actually important for the correct prediction of the heat transfer with bluff bodies.

In either case, when the DM and DS models are considered separately, the strong agreement in their thermal results suggests that the DM model has, on this specific flow, a practically null effect at all the resolved scales.

7.3 Cold flow in a swirled combustor

The last case considered in this thesis for the testing of the dynamic mixed model is the turbulent cold flow in a swirled, lab scale, combustor. Besides the direct availability of experimental data, this choice is essentially motivated by two factors. One is its representativity of modern LES applications (Mahesh et al., 2004; Poinsot and Veynante,

[12]This conclusion might be somehow impaired by the possibly incorrect adiabatic condition at the wall, but the described effect seems independent from the wall distance, hence largely negligible.

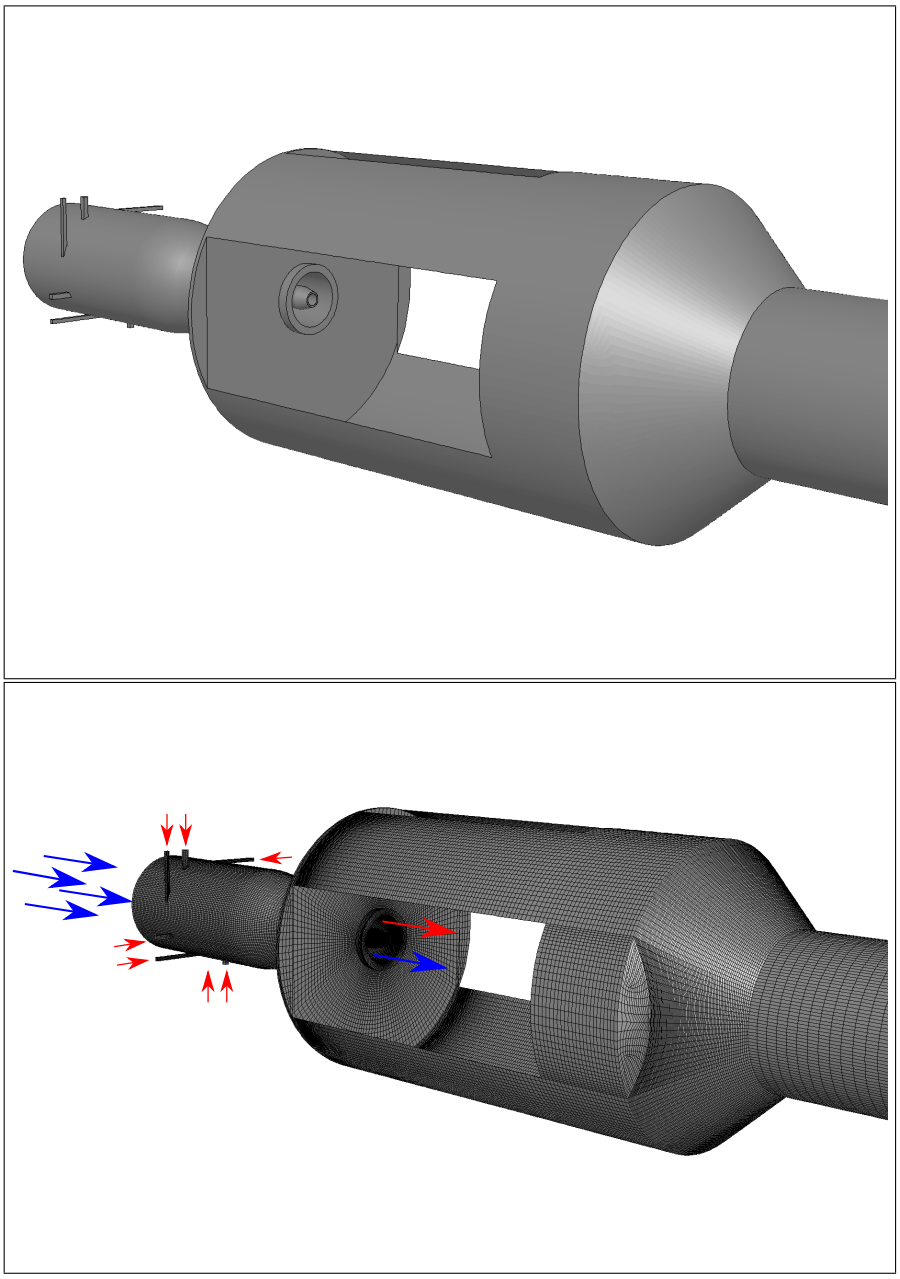

Figure 7.16: *Geometry and computational grid for the combustor test case. Top view. Red arrows: tangential inlet. Blue arrows: axial inlet.*

2005), LES being, for example, the only practical available tool to investigate combustion instabilities. Moreover, the presence of the swirl, which in practical applications is used, for example, to stabilize a non-premixed flame at high Reynolds numbers, also introduces several fluid dynamical instabilities (Lucca-Negro and O'Doherty, 2001), like precessing vortexes, and multiple recirculating regions, making the test a severe one. In addition to this, the specific flow considered here also has features requiring additional modeling efforts, thus making the overall test more representative of real engineering applications. While no actual combustion is involved in the present analysis, this test

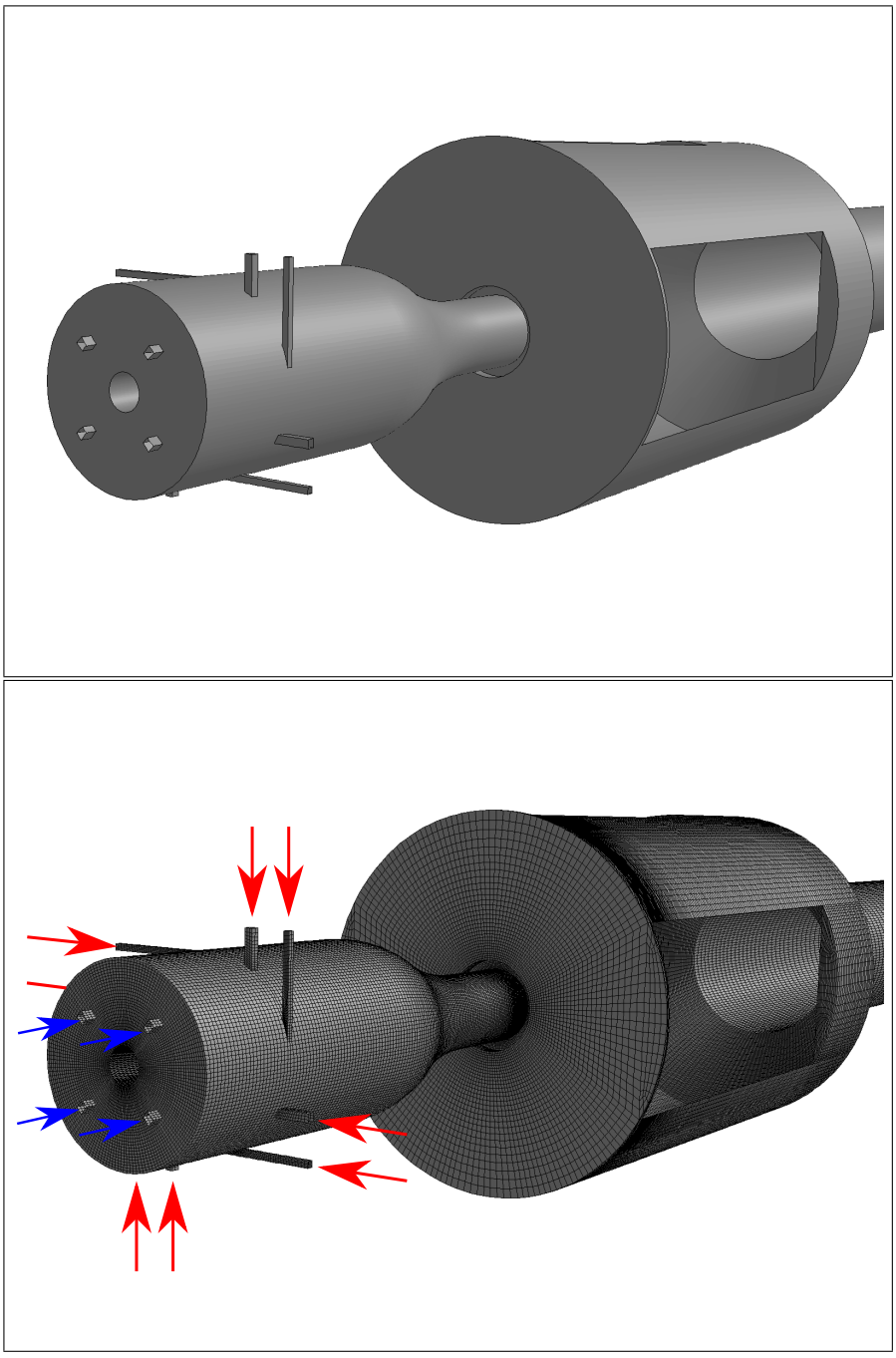

Figure 7.17: *Geometry and computational grid for the combustor test case. Bottom view. Red arrows: tangential inlet. Blue arrows: axial inlet.*

still represents a necessary step before additional physics is added to the simulation.

7.3.1 Flow description and computational setup

The investigated flow domain consists in a full, lab-scale, combustor composed by three parts, as depicted in Figures 7.16 and 7.17. In the first part, the swirl generator, the air flow enters the domain trough 8 separate tangential (red arrows in the figures) and 4

axial (blue arrows in the figures) inlets. The swirler essentially consists of a hollow cylinder whose external diameter is reduced toward the injection section, its overall shape being resemblant of a bottle. The internal cylindrical core of the swirler accomodates an additional axial inlet directly entering the combustion chamber, as clarified in Figure 7.18. This cylindrical pipe is typically used for the fuel gas in combustion studies and, for the present cold flow case, was closed and only partly considered in the computation.

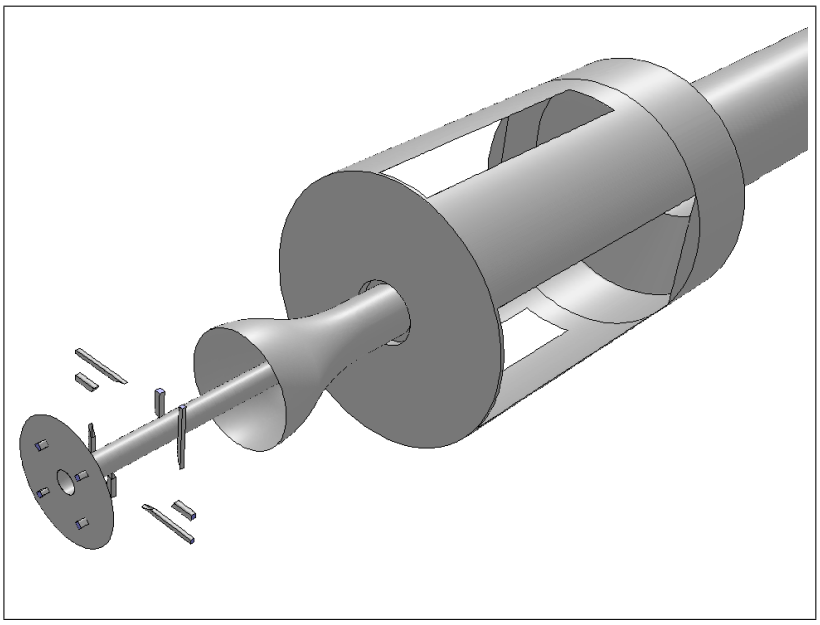

Figure 7.18: *Internal details of the swirler.*

The air injection in the combustion chamber is trough a slightly divergent section which precedes an abrupt expansion, as shown in Figure 7.19. The combustion chamber, which is essentially cylindrical, has four plane windows, used as visual access during the experiments[13], and is connected with the final, cylindrical, exhaust trough a convergent conical section. The main geometrical dimensions of the combustor are summarized in Table 7.5 for reference.

Table 7.5: *Lengths and diameters for the main parts of the combustor.*

Part	Length (mm)	External Diameter (mm)	Internal Diameter (mm)
Swirler	265	80	15
Injector		36	10
Combustion chamber	297	194	
Conical section	55	194	98
Exhaust	299	98	

[13] Such visual access has been replicated in the geometry images reported here but, nonetheless, the relative surfaces are solid and the lateral surface of the chamber is fully closed.

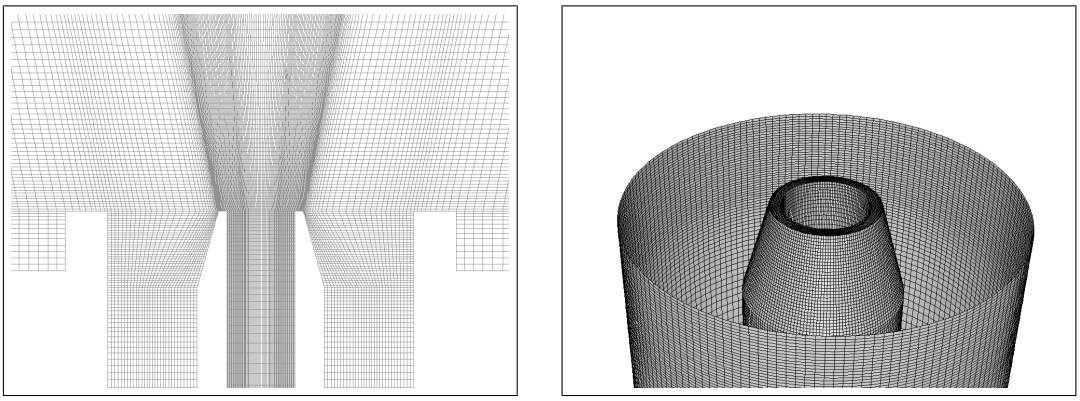

Figure 7.19: *Geometry and computational grid for the combustor test case. Details of the injector section.*

The role of the different tangential and axial inlets is to produce different degrees of swirl by splitting the overall air mass flow rate entering the domain. Such degree of swirl can be classified in different ways. One simple possibility is the geometric swirl number S_g (Claypole and Syred, 1980):

$$S_g = \frac{\pi D_e D_s}{4 A_{TG}} SR^2 \tag{7.8}$$

where D_e is the external diameter at the injector (efflux) section, D_s is the swirler diameter at the section of the tangential inlets and A_{TG} is the total area of the tangential inlets. The parameter $SR = \dot{m}_{TG}/(\dot{m}_{TG} + \dot{m}_{AX})$ denotes instead the ratio between the tangential mass flow rate and the total mass flow rate entering the swirler (tangential + axial). Alternatively, a more detailed characterization of the swirl can be obtained by the swirl number S (Gupta et al., 1984):

$$S = \frac{\int_{D_i/2}^{D_e/2} \langle u_z \rangle \langle u_\theta \rangle r^2 dr}{\frac{D_e}{2} \int_{D_i/2}^{D_e/2} \langle u_z \rangle^2 r dr} \tag{7.9}$$

where $\langle u_z \rangle$ and $\langle u_\theta \rangle$ denote, respectively, the mean axial and tangential velocities at the injector section, expressed in the local cylindrical coordinate system (z, r, θ), and D_i is the injector internal diameter. In the following analysis two different swirl conditions are considered, whose classification trough the parameters introduced above is reported in Table 7.6.

In the original, tentative, approach to this simulation the swirler was not actually included in the computational domain and the generation of the inflow field was expected to be produced by the mapping procedure tested in section 7.1.3, fixing the swirl number according to the work of Pierce and Moin (1998). Also, the outlet section was placed just at the end of the exhaust. However, this approach determined two problems. From the conceptual point of view, while suitable for general studies, fixing the swirl number is not actually representative of the computational practice, as such flow characterization is usually asked as output from the simulation. The second, more subtle,

Table 7.6: *Swirl numbers investigated for the combustor test case.*

Case	S_1	S_2
$\dot{m}_{TG}$ [kg/s]	$4.31 \cdot 10^{-3}$	$8.40 \cdot 10^{-3}$
$\dot{m}_{AX}$ [kg/s]	$5.17 \cdot 10^{-3}$	$1.08 \cdot 10^{-3}$
SR	0.45	0.89
S_g	5.95	22.63
S	2.05	3.13

aspect is related to the effect of the boundary conditions in this kind of internal flows. Indeed, on one side, placing the outflow section just at the end of the exhaust, produced essentially wrong results due to a coupling between the flow in the domain and the boundary condition. On the other side, a preliminary computation has also shown that the same coupling would exists upstream, toward the inlet section. This is shown in Figure 7.20, where the main fluid dynamic instability affecting this flow, the Precessing Vortex Core (PVC), is seen to influence the flow in the swirler.

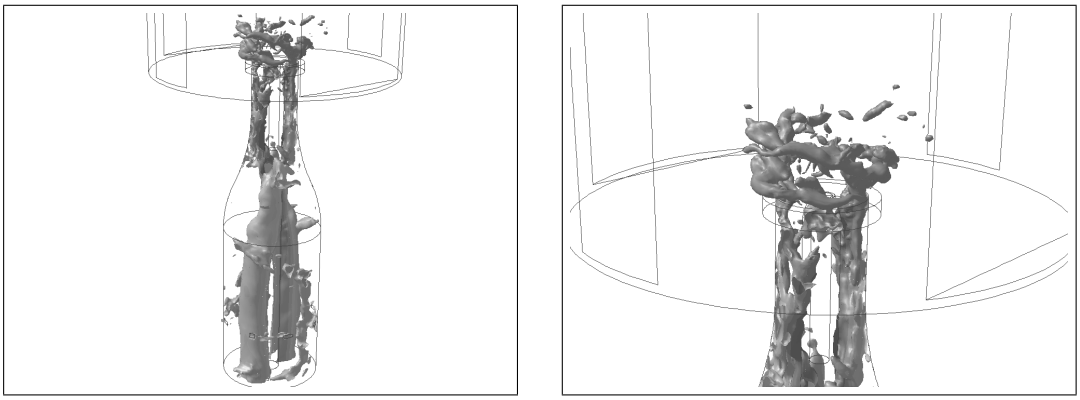

Figure 7.20: *Fluid dynamic coupling of the flow in the combustor visualized by an iso-surface of the instantaneous pressure fluctuation. Left) Global view. Right) Enlargement on the PVC.*

As a consequence, the original approach has been definitely abandoned and the final computational domain extended. In particular, the inflow section has been placed more correctly where the actual boundary condition is known, in the tangential and axial pipes supplying the mass flow in the swirler. The outlet section, not shown in the previous images, has instead been moved in the quiescent air surrounding the experimental testbed (an additional cylindrical volume with a 200mm length and a 300mm diameter). The latter choice required no particular efforts and fixing the average pressure on the new outlet section equal to the ambient pressure resolved the problem.

However, moving the inlet section upstream in the tangential and axial inflow ducts determined a drastic change in the overall approach. First of all, the actual mass flow rates in the experiments were only known globally and in terms of the split ratio SR, but not for each single duct feeding the swirler. Hence, a preliminary 1D computation has been used to estimate how the mass flow should be split among the single ducts,

considering their lengths and the pressure losses in the various junctions of the feeding network. As a consequence of this approach, specific flow details at the inlet sections were also unknown, and only the single mass flow rates have been assigned, without any fluctuation or variation over the section. Finally, the inclusion of the whole swirler also determined an enormous increase of the overall estimated cell count. This was not only the straight consequence of the additional fluid volume but, more importantly, was determined by the required resolution at the swirler walls. Indeed, the already high resolution which would be required at the wall is made even higher by the swirl, which tends to enhance the near wall effects. In practice, for the higher swirl number case S_2, a grid resolution estimated trough the actual flow parameters, listed in Table 7.7, and considering the flow in the swirler as a straight flow in a straight duct, would have required a factor 10 increase in resolution for each spatial direction because of the swirl, making the computation largely unfeasible.

Table 7.7: *Flow conditions for the combustor test case.*

Property	Symbol	Value
Mean velocity at the injector section	V_b [m/s]	9.2
Density	ρ [kg/m^3]	1.225
Dynamic viscosity	μ [kg/ms]	1.7894·10^{-5}

In order to solve the problem, a different approach has instead been followed, using the wall function boundary condition (5.25) for all the internal swirler walls, which justifies some of the disturbing grid details emerging from the Figures 7.17 and 7.19. Note, however, that this allowed to keep the overall cell count around $4.5 \cdot 10^6$, but the swirler still required about $1/3$ of the cells. For all the remaining boundaries classical no-slip conditions have been applied, including the inlet of the central fuel gas duct, which is truncated ten diameters below the injector section.

As for the previous test case, three modeling options are investigated here. Namely, the ILES approach, a standard DS model and the present dynamic mixed model (DM) with an extended filter stencil ($N_L = 2$). A single computational grid has been used for both the flow conditions S_1 and S_2, which is the one presented in the previous figures, and the default computational settings are used.

The computations are started with quiescent air and advanced in time with a time step approximately equal to $7.72\nu/V_b$, which determined a maximum Courant number below one in most of the domain and a value around two for few single cells per time step near the injector section. Once the statistically steady state is reached, flow statistics are computed over $1 \cdot 10^5$ time steps, which has been verified to be sufficient for all the reported quantities.

7.3.2 Numerical results

The experimental data for the comparison have been produced by both Laser Doppler Velocimetry (LDV) and Particle Image Velocimetry (PIV), in two separate experimental campaigns realized at the Department of Energy of Politecnico di Milano. Radial,

tangential and axial mean velocity and fluctuation profiles are available at different axial stations in a symmetry plane of the combustion chamber but, for the present comparison, only few selected paths are considered, whose location is sketched in Figure 7.21. Note, however, that not all the data are available at all the locations while both LDV and PIV data are available for some others. Also, among the several available swirl conditions, the cases S_1 and S_2 (see Table 7.6) have been selected as representative, respectively, of low and high swirl conditions. In both cases, the nominal Reynolds number based on the external diameter of the injector section, D_e, and the mean bulk velocity at the same section (i.e., $z = -19mm$), V_b, is $Re = 22674$. Unless otherwise stated, the results are nondimensionalized by these same quantities, D_e and V_b.

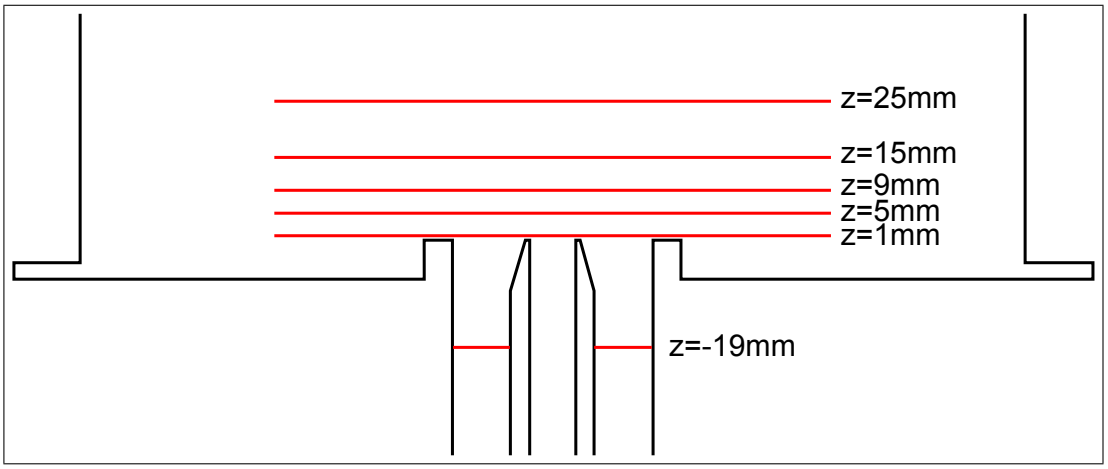

Figure 7.21: *Location of the paths for the comparison of the results in the swirled combustor case. Reference $z = 0$ on the injector section.*

The first comparison is presented for the section $z = -19mm$, which is inside the injector, to analyze the correctness of the present approach in prescribing the boundary conditions. For the S_2 condition, Figure 7.22, this is actually the case (considering the approximations adopted) and no specific differences arise among the models except, possibly, for the fluctuations, whose axial component is better predicted by the DS/ILES models while the tangential one is better predicted by the DM model. Except for the mean tangential profile, the agreement of the DM model is less satisfactory for the S_1 case, Figure 7.23, while the other models maintain their level of agreement. While an explanation is hard for this complex flow, it is notable that strong differences exist among the models.

The anomaly in the mean velocity profile (subfigure 7.23a) can instead by justified by the fact that for such intermediate swirl number there is a delicate balance of axial and tangential momentum fluxes and the axial velocity profile results to be relatively susceptible to small changes of the swirl number in this specific range. This can be also understood by the fact that the differences among the models are mostly related to the fact that the DM model predicts a different tangential velocity profile.

Overall, this comparison confirms that, as expected, for high swirl numbers the inflow procedure adopted is robust and can be used efficiently in the computational practice. In contrast, at low swirl numbers the flow is more susceptible to additional details, to the extent that cannot be even excluded that the experimental data might have been af-

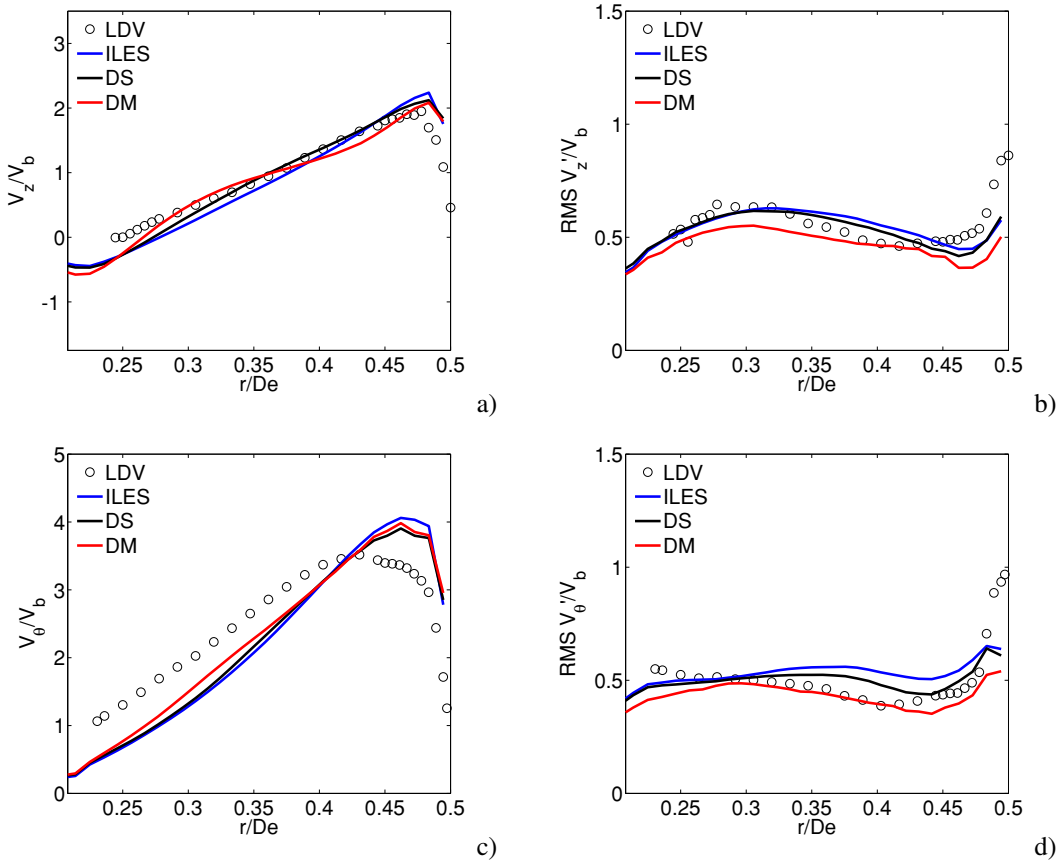

Figure 7.22: *Mean and fluctuation profiles at z=-19mm for the S_2 case. Left) Mean velocities. Right) RMS fluctuations. Top) Axial component. Bottom) Tangential component.*

fected as well. Note, however, that the adoption of the wall function approach revealed to be fundamental in order to obtain this level of agreement as completely incorrect results have been obtained when a tentative wall resolving grid has been used[14].

When the analysis is extended to the first section in the combustion chamber, Figures 7.24 and 7.25, the same trend in the results is replicated. For the S_2 case no specific difference arises among the models except for the fluctuations, whose predicted values are higher for the ILES approach. While this is in accordance with the results in all the preceding tests, it should be mentioned that all the data, experimental and numerical, necessarily suffer a slight asymmetry due to the non perfect statistical convergence. As a consequence, a quantitative agreement on the peak values of higher order statistics is likely to be subject to a higher uncertainty. Notably, the DM model more closely describes the details of the tangential velocity component due to the separation on the outer edge of the injector, which is possibly due to the better prediction of the RMS tangential velocity fluctuation at $z = -19mm$ (subfigure 7.22d).

For the S_1 case the differences are higher as expected, but only affect the fluctuations. However, these can be all explained by the higher level of swirl predicted by the DM model with respect to the alternative ones.

[14]Obviously, the motivation of the incorrect results resides in the wrong estimation of the required resolution, as explained in the text.

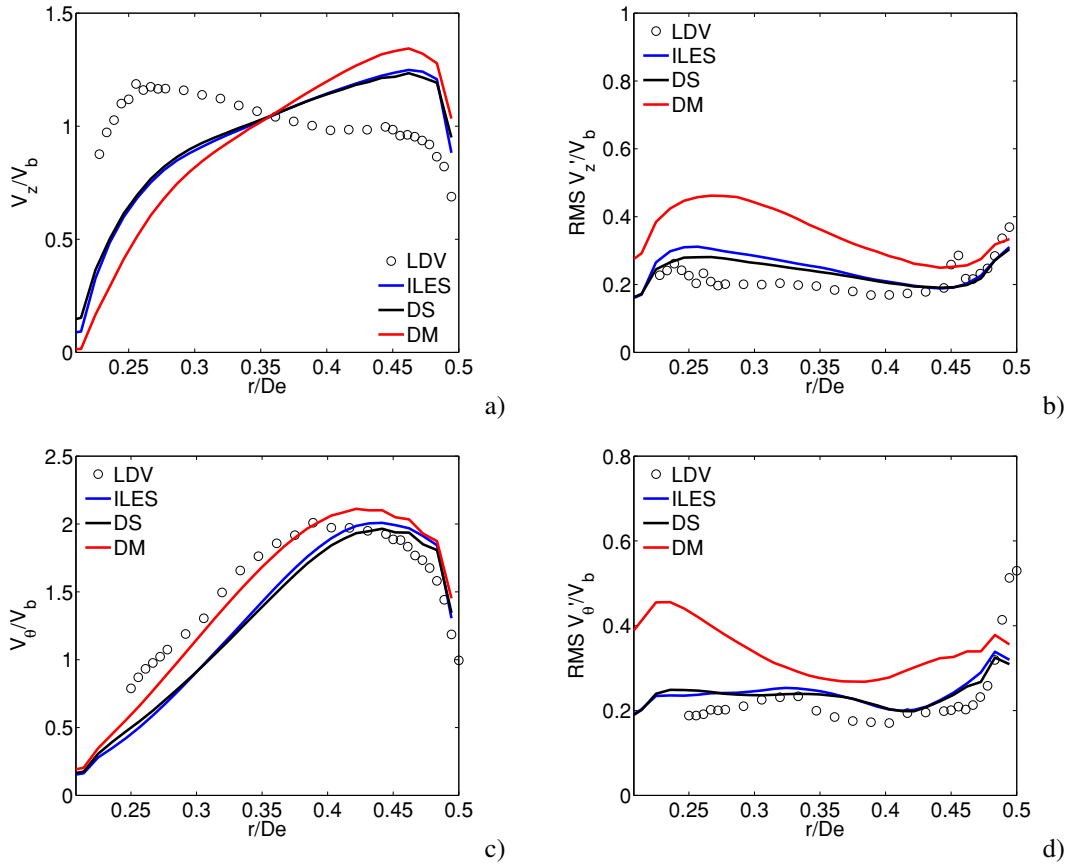

Figure 7.23: *Mean and fluctuation profiles at z=-19mm for the S_1 case. Left) Mean velocities. Right) RMS fluctuations. Top) Axial component. Bottom) Tangential component.*

When the remaining axial stations are considered, the overall picture is somehow changed. For what concerns the high swirl case S_2, Figures 7.26 and 7.27, the agreement in all the mean velocity components is replicated at all the considered stations, confirming the substantial correctness of the present approach for high swirl numbers, whose effects tend to dominate most of the differences among the models, except maybe for few details of the ILES one, which predicts a relatively weaker reverse flow on the axis.

The relative fluctuations, Figure 7.27, confirm the trend with only minor differences. However, it can be readily appreciated that the DM model tends to produce slightly narrower, lower peaks in the fluctuations (with respect to the DS model), which is possibly a consequence of the extended filter stencil and/or the already confirmed embedded dissipative features of the scale similar part of the model[15].

The analysis for the lower swirl number case S_1 is however more interesting. Indeed, as shown in Figures 7.28 and 7.29, while a substantially good agreement with the experimental data is found for all the models at all the stations, the DM model clearly outperforms the remaining one. This can be appreciated for the mean velocities as, besides some anomalous asymmetries in the experimental data, the DM model constantly predicts better all the peak values, especially notable being the reverse flow intensity

[15] According to the lack of sensitivity to the eddy viscosity part shown in the channel test.

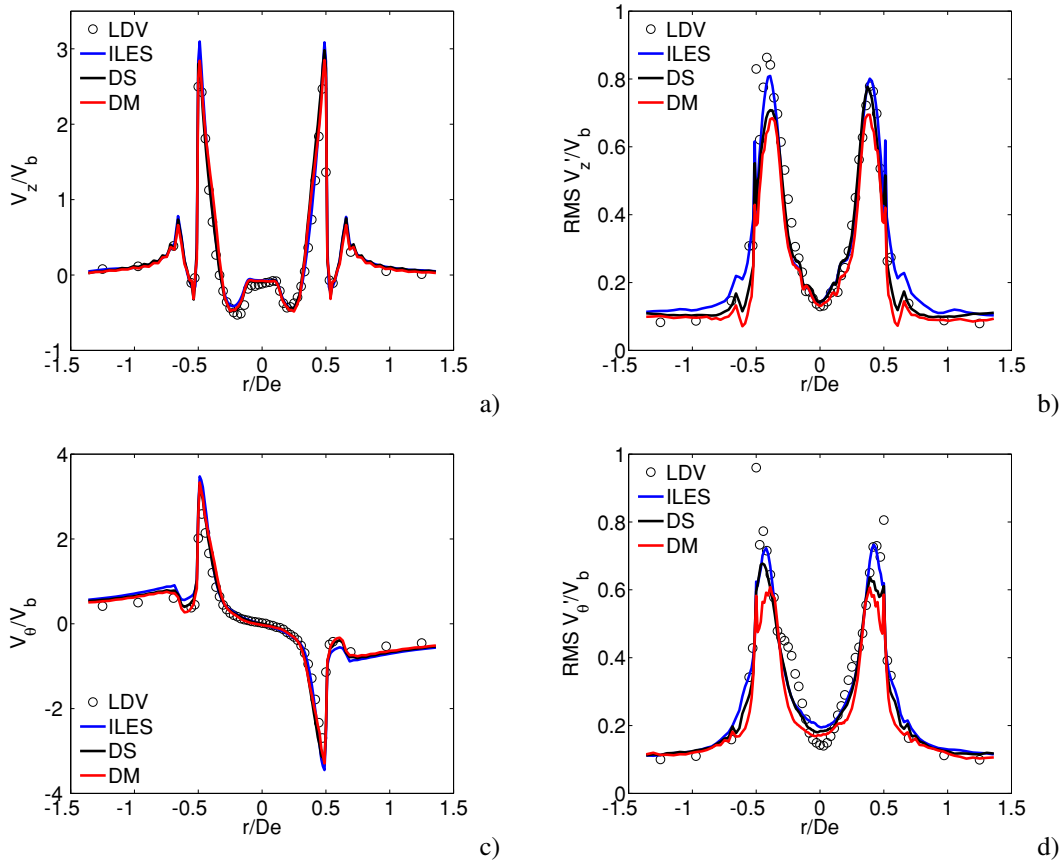

Figure 7.24: *Mean and fluctuation profiles at z=1mm for the S_2 case. Left) Mean velocities. Right) RMS fluctuations. Top) Axial component. Bottom) Tangential component.*

on the axis and the maximum radial velocities.

The same effect is more evident for the fluctuations, in Figure 7.29, as again the DM model appears to be the only one correctly predicting all the peak values independently from the location. For selected locations (subfigures 7.29b-d) the DM model produces larger differences with respect to the experimental data, but these seem related to the grid resolution. In practice, in such locations the DM model predicts qualitative features of the radial velocity fluctuation which are missed by the remaining models, but in doing so the local quantitative agreement is lost.

The previous analysis for the low swirl number reveals two interesting aspects. From one side, as the overall results have confirmed, the prediction in the combustion chamber mostly depends from the prediction at the injector section (e.g., $z = -19mm$), with the models producing only slight differences in the axial evolution. As such, the better results of the DM model in the S_1 case can only be related to the better representation of the flow features at the injector, especially its swirl number. This is also substantiated by the fact that all the features better predicted by the model DM are relative to a higher swirl number, as effectively observed in Figure 7.23. Thus, the aspect highlighted here is that the DM model possibly produced a better representation of the flow in the swirler and, as a consequence, produced a more correct flow evolution in the combustion chamber.

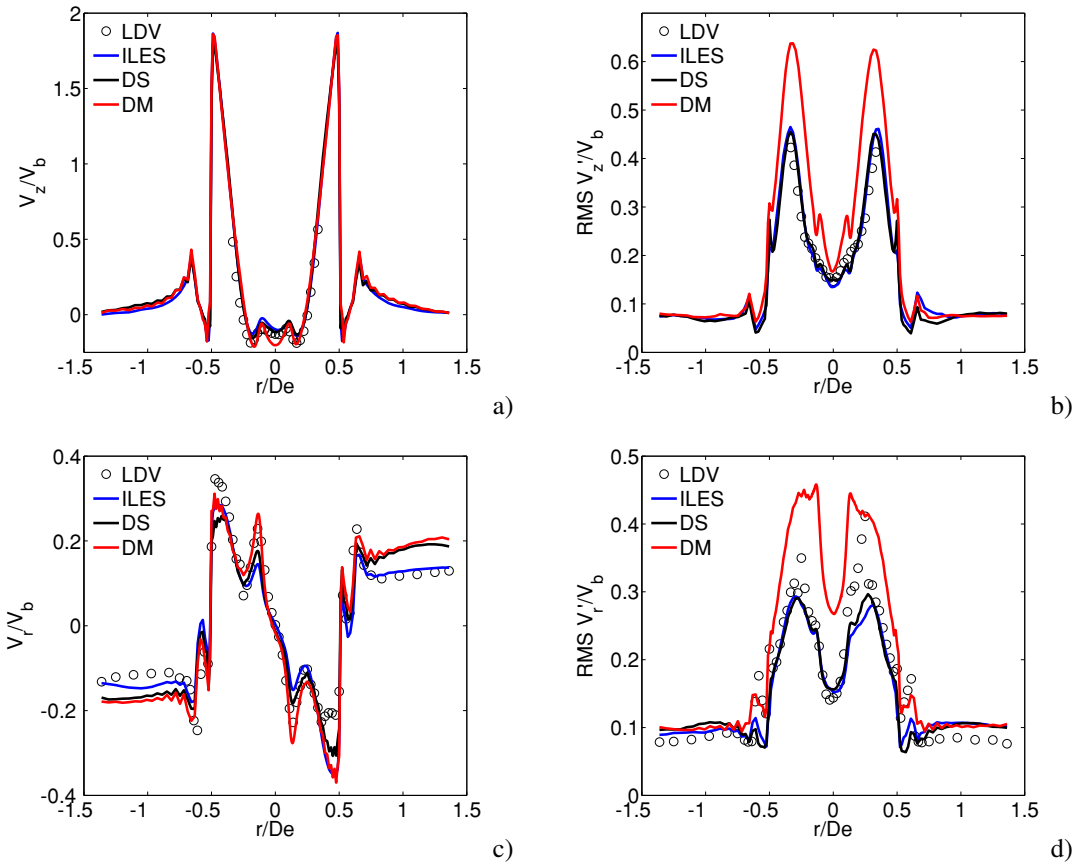

Figure 7.25: *Mean and fluctuation profiles at z=1mm for the S_1 case. Left) Mean velocities. Right) RMS fluctuations. Top) Axial component. Bottom) Radial component.*

This conclusion obviously contrasts with the experimental data used as reference. However, and this is the second interesting aspect emerged from the analysis, there are sufficient elements to, at least, doubt the experimental data for the injector section in the case S_1. Indeed, in general, it readily emerges here that the two techniques, PIV and LDV, provided different results. While both are formally correct and there is no specific clue suggesting the correctness of one over the other[16], it is important to highlight that only the PIV data are spatially coherent, in the sense that all the PIV data in the Figures 7.26, 7.27, 7.28 and 7.29 are taken from a single experiment as done for the simulations. In contrast, the LDV data were not only the object of a different campaign, but also taken in different moments for each flow variable and for each of the two stations at $z = -19mm$ and $z = 1mm$. As a consequence, considering the large sensitivity of the flow at this swirl number (as also testified by the larger differences among the SGS models), it is possible that there is a lack of coherence between the nominal flow condition and the two conditions relative to the PIV and LDV data. Obviously, none of these arguments sustains one data set over the other and the wrong flow condition might actually be the one represented in the PIV dataset. However, on repetition of the PIV campaign, its results have been confirmed, which thus sustains the initial hypothesis

[16]The author is perfectly aware of the connection between PIV and LES (Sheng et al., 2000) and of the resolution limits of both PIV and LDV. However, all such issues have been nominally resolved in the postprocessing phase.

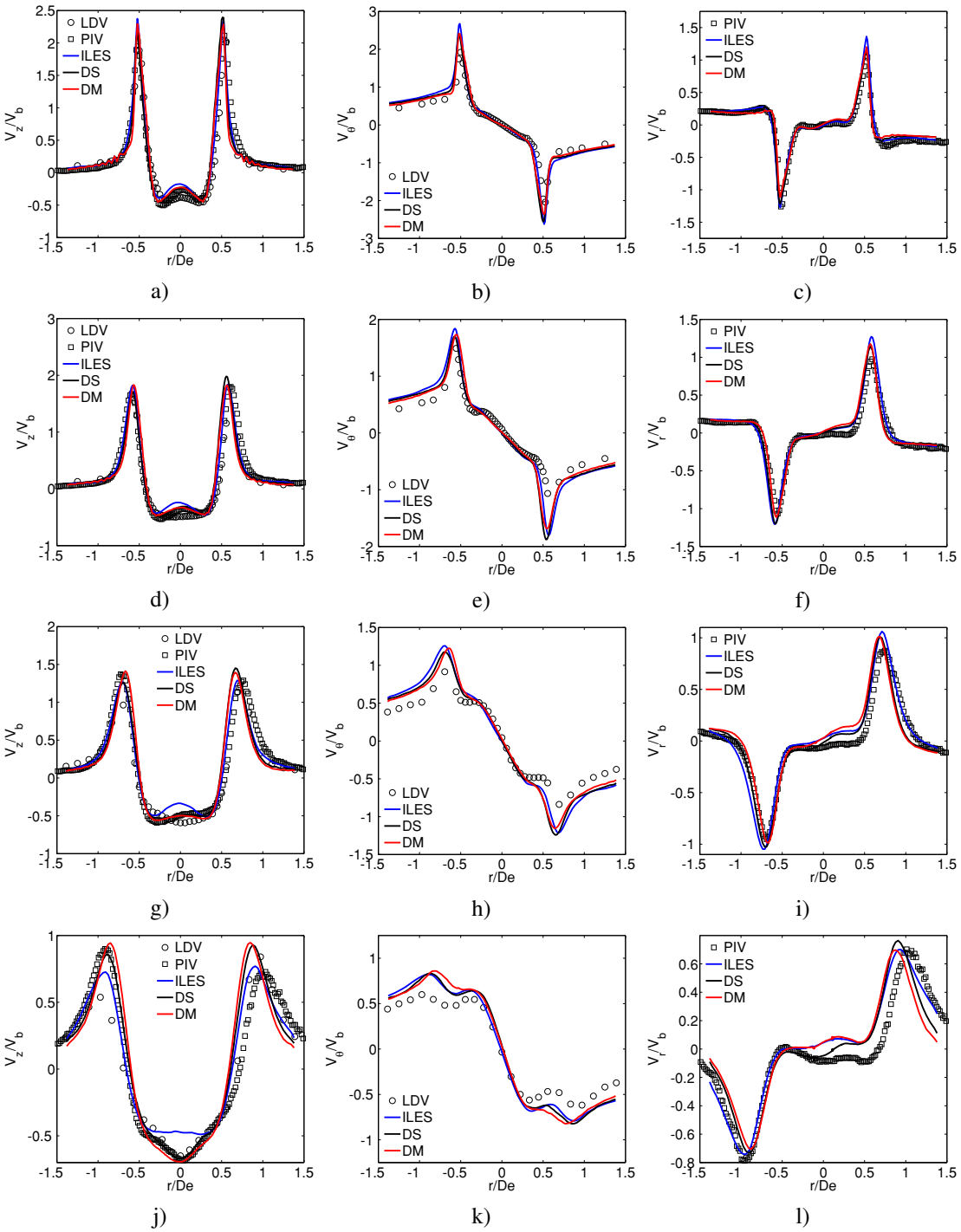

Figure 7.26: *Mean velocity profiles for the S_2 case. Left) Axial component. Center) Tangential component. Right) Radial component. From top to bottom: $z = 5mm$, $z = 9mm$, $z = 15mm$, $z = 25mm$.*

on the LDV data. In conclusion, what emerged from this test case is that the present approach in providing the inflow condition is affordable and provides reliable results at both low and high swirl numbers. For high swirl numbers, besides few effects related to the use of a bounded scheme, SGS models have no appreciable effect and the overall

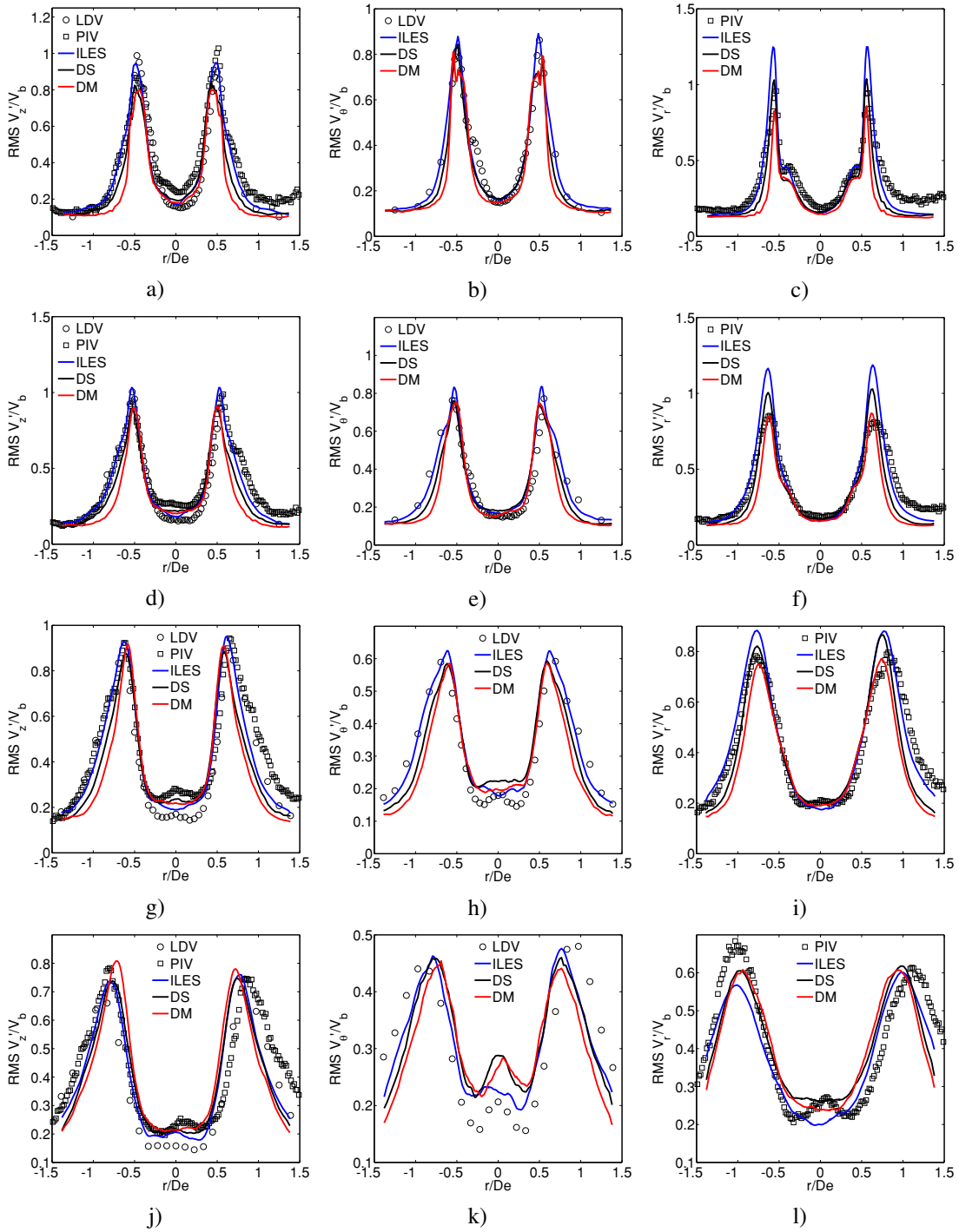

Figure 7.27: *Mean RMS fluctuation profiles for the S_2 case. Left) Axial component. Center) Tangential component. Right) Radial component. From top to bottom: $z = 5mm$, $z = 9mm$, $z = 15mm$, $z = 25mm$.*

flow prediction is somehow saturated by the high swirl. LDV data for different swirl numbers (not reported here) confirm this saturation effect. For lower swirl numbers and, more specifically, for split ratios SR around 0.5, the flow exhibited a larger sensitivity

to the inflow and the fluid dynamics in the swirler. Notably, for this more difficult case, there is sufficient experimental evidence to sustain that the present DM model provided a better prediction of all the flow quantities. More generally, the proposed model has shown no sign of instability and correctly interacted with all the features of this complex application, including the strong grid stretching in all the flow directions, the use of wall functions and the very coarse resolution used in several, non primary, parts of the flow domain. Considering the generally better results obtained with the DM model, for this as well as the previous tests, the model has certainly shown its full potential for complex engineering applications.

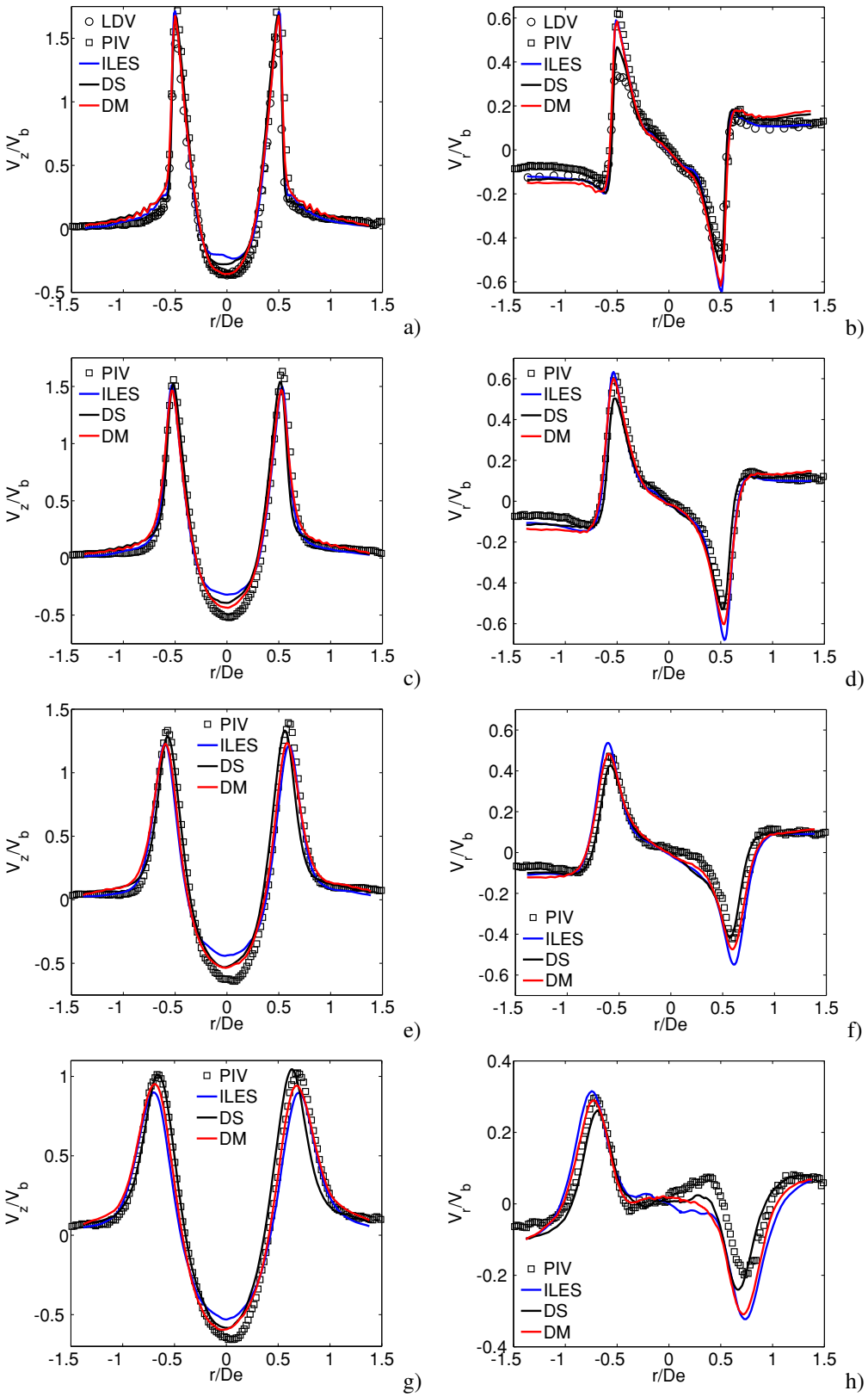

Figure 7.28: *Mean velocity profiles for the S_1 case. Left) Axial component. Right) Radial component. From top to bottom: $z = 5mm$, $z = 9mm$, $z = 15mm$, $z = 25mm$.*

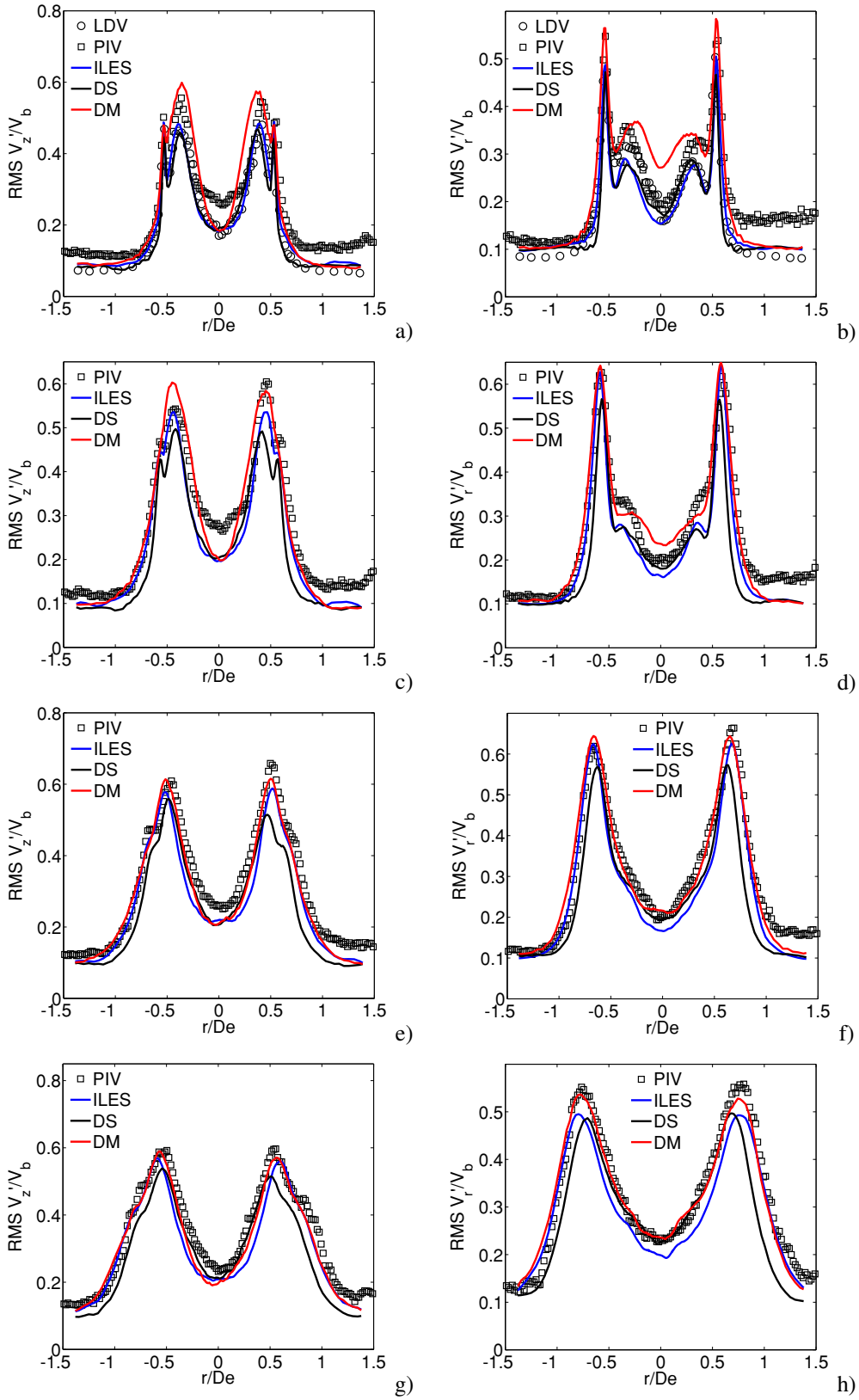

Figure 7.29: *Mean RMS fluctuation profiles for the S_1 case. Left) Axial component. Right) Radial component. From top to bottom: $z = 5mm$, $z = 9mm$, $z = 15mm$, $z = 25mm$.*

CHAPTER 8

Conclusions

The present thesis has been developed with the aim of applying the Large Eddy Simulation (LES) approach to complex industrial flows. This aim has been pursued by analyzing and extending the LES theoretical foundation and by systematically analyzing its results from increasingly complex applications.

The theoretical developments have been motivated and generated by a careful analysis of the Classical LES (CLES) framework, realized with specific attention on its main hypotheses and working paradigms. The analysis, in turn, revealed that, in CLES, a strong limiting role is played by the formal commutation hypothesis for the underlying implicit or explicit filter. Indeed, this classical assumption, while usually overlooked, is shown to influence the form of the unknown subgrid-scale (SGS) stresses as well as more practical aspects of LES computations, like the form and the consistency of the Germano Identity or the cost of the resulting Dynamic Procedure.

As a consequence of this analysis, the overall LES framework has been redefined by simply avoiding the commutation requirement *ab initio* and by introducing a general multi-level notation. These two simple modifications have produced, in turn, important results. On one hand, simply removing the commutation requirement has modified the actual form of the equations and of the SGS terms requiring a model, with the main consequence of producing a fully consistent formulation (i.e., without any approximation besides the SGS model) and a different Germano Identity whose associated Dynamic Procedure has much lower costs than in CLES. On the other hand, both the modifications have allowed sufficient flexibility to adapt the new LES formulation to most of the known LES approaches. In particular, by further analysis of sampling operators and of the formalism of the weighted residuals method, the proposed LES framework is shown to provide exact model equations for most of the known numerical approaches (e.g., finite differences, finite volumes, spectral elements) to the resolution of LES equations.

This result, in particular, is in strong contrast with CLES, where a wrong toy model equation is usually used as theoretical reference. This fact has been highlighted by naming the proposed LES framework GLES (Generalized LES).

Because of this exact correspondence between GLES and the numerical practice, the GLES framework is here elected as the best option for further developments toward the LES application in complex industrial flows. In particular, the finite volume (FV) method is further analyzed as representative of a large class of industrial applications. With the GLES theoretical basis at hand, the FV method is bring back to its basic operator form, which is a combination of a top-hat filter and a sampling operator. The framework, however, also allowed a formal justification for separating the effects of the two and only focusing on the top-hat part. More specifically, this focus consisted in looking for the most suitable form of structural SGS model for a practical application in an unstructured FV solver. The use of such form of model in a general low order code has also been motivated, by alluding at the qualitatively different roles of the top-hat filter and the sampling operator determining the numerical error.

Such structural model is identified with a specific form of scale-similar term, which is properly scaled to account for the specificities of the approach. A dynamic mixed version of the model is also presented as most suitable option, because of the possible lack of stability and to counteract possible misalignments with the underlying model assumptions. Specific theoretical and numerical aspects of the model are also briefly analyzed.

With the model at hand, the flexibility of the GLES framework is shown by its implementation in a commercial unstructured FV solver, which in the present case simply required the use of a single external subroutine (UDF). However, in doing so, a general attention is also given to the several aspects affecting the practical LES approach, and two additional modifications are inserted in the solver. One is relatively new and consisted in a novel algorithm for the efficient computation of arbitrary order, weighted, central moments and co-moments. The second one is instead a simple inflow generation method based on the mapping of the velocity field, but its implementation is shown to be largely superior, in terms of costs and performances, to the default methods implemented in the solver.

The applications and tests of the proposed SGS model/LES framework have been organized in terms of flows with increasing complexity, with a specific attention given to the turbulent channel flow case, because of the relative importance of the test. In particular, the analysis is enriched by considering in more detail the equations governing the mean LES solution and providing tentative explanations for some of the common effects usually encountered in LES. The specific form of the equations is also used to identify the actual effect of an LES model in the overall computation, allowing a simple, effective, assessment also of the proposed one. Different tests have been performed, in order to assess the most relevant aspects of the model and define its most suitable default settings. The channel test case reveals that the model not only provides an improvement over the general solver capabilities, but also over the different codes and SGS models participating the LESinItaly database.

The feasibility of the model for real complex applications is shown in the last chapter, where the model performances are found, at worst, equal to the no-model case, and always better than the default modeling options when such differences are observed,

without ever showing sign of instability, possibly because of its embedded hyper-viscous effects. In the most complex scenario analyzed, the cold turbulent swirling flow in a model combustor, the model is found compatible with all the typical assumptions and working hypotheses used in complex engineering flows, being at the same time the most accurate tested model over a range of swirl conditions.

8.1 Future work

Specific critical points and not originally envisaged research directions have also emerged during the development and testing phases of the present work. In particular:

- An important part of the developed SGS model is dependent from a numerical test filter which, for ease of implementation and practical relevance, has been chosen as a simple volume weighted average. However, while no result has evidenced specific problems, such filter is possibly incongruent with the basic assumptions underlying the model. As consistent test filters, possibly based on a differential formulation, would not be difficult to implement in general, their use should be strongly considered in further uses of the model.

- A specific possible inconsistency of the model is related to the possible presence of spurious first order terms in its Taylor series development and the misrepresentation of the second order moment of the basic FV cell filter. These two aspects could be easily assessed by changing, respectively, the exponent in the delta ratio factor of the model and excluding the central cell from the filter stencil (which in a simplified 1D framework showed to better represent the second order moment of a top-hat filter). Both tests should be also considered in the future.

- Besides the possible incongruence with the hypotheses underlying the model, the adopted test filter has also shown to be sensitive to the specific details of the underlying grid, influencing in turn the dynamic procedure and the activation of the model in critical zones. However, the numerical evidence suggests that this specific aspect could be somehow modified by simply acting on the expression of the filter width without necessarily affecting the whole filtering procedure. Such modification should be easy to perform and is strongly suggested before further applications of the proposed model.

- An additional drawback of the model has been certainly found in the adoption of a single model constant for the full scale-similar tensor of the model. In particular, while very common in the LES community, such approach has shown here to produce dynamic constants which are strongly dependent form the main flow direction and how it is aligned with the reference frame. Modifying this model aspect with a full tensorial constant would probably improve the model performances while still being largely within the costs of a classical dynamic procedure. Still, the model complexity would certainly rise and such a kind of modification should be considered carefully.

- More generally, a detailed investigation on the results of the present dynamic procedure has not been originally considered, but would certainly clarify additional

aspects of the overall model, possibly indicating the better route for additional improvements. Possible aspects to investigate in a more systematic way would be: the correlation between the dynamically computed constants and specific flow details, like main flow direction and magnitude; extension of the clipping ranges and the dependence of the suitable ranges from the Reynolds number/spatial location; the dependence of the dynamic constants from the specific filter and the underlying grid. Some of these aspects have been preliminarily analyzed but further investigations are required.

- The single more interesting aspect emerged from the present work, but whose investigation has been avoided, is the role of the model in the pressure equation. It clearly emerged from the present work that the inclusion of the pressure part of the model in the relative pressure equation could be a physically sound alternative to the more common Rhie-Chow approach for cell centered FV codes. However, this would have been a research topic in its own and a detailed investigation would have necessarily required a different software platform, possibly developed ad hoc. As such, and because of the lack of practical relevance that this would have created for more general solvers, this topic has not been further investigated.

- As a side note, the whole testing part in this thesis failed in clarifying some disturbing aspects which would need running additional tests. These, in particular, include assessing the code dependence from the reference frame, in order to clarify if the observed behaviors are due to the specific model adopted, and further tests on the symmetry preserving scheme as obtainable in the code (Disable Reconstruction Option), in order to clarify its effective resolution capabilities.

More attention to these aspects, as well as a more detailed investigation of the fluid dynamic aspects involved in the prediction of the more complex flows analyzed here, would have certainly improved the present work.

APPENDIX $\mathcal{A}$

On scale-similarity models in CLES of compressible flows

While not specifically relevant for the present work, it is important to emphasize how different approaches can be used in proposing scale-similar terms for compressible CLES. Considering first the IFCLES case, the main SGS term in the momentum equation reads (a similar reasoning follows for the other terms):

$$\tau_{ij} = -\bar{\rho}\left(\widetilde{u_i u_j} - \tilde{u}_i \tilde{u}_j\right) \tag{A.1}$$

The basic idea behind scale-similarity modeling is to assume that the SGS stresses are scale invariant and can be well approximated by an upward shift in the filtering level, so that any unclosed term is expressed in terms of resolvable quantities and their explicitly filtered counterparts. The basic approach used in IFCLES, as presented in section 2.4.2, is to directly consider as unclosed, in equation (A.1), the terms in parentheses, replace the velocities with the resolved ones and the Favre filter with an explicit one based on the resolved density. The outcome of such an approach is the following scale-similar model:

$$\tau_{ij} = -\frac{\bar{\rho}}{\hat{\bar{\rho}}}\left(\widehat{\bar{\rho}\tilde{u}_i\tilde{u}_j} - \frac{\widehat{\bar{\rho}\tilde{u}_i}\,\widehat{\bar{\rho}\tilde{u}_j}}{\hat{\bar{\rho}}}\right) \tag{A.2}$$

While completely valid and consistent, this is not the only possible approach in IFCLES. Indeed, a possible route is to consider instead the density as well and rearrange

equation (A.1) as follows:

$$\tau_{ij} = -\left(\overline{\rho u_i u_j} - \bar{\rho}\frac{\overline{\rho u_i}}{\bar{\rho}}\frac{\overline{\rho u_j}}{\bar{\rho}}\right) \tag{A.3}$$

At this point, a shift in the filter is introduced (a hat instead of a bar) and the unfiltered variables replaced with the known one, leading to:

$$\tau_{ij} = -\left(\widehat{\bar{\rho}\tilde{u}_i\tilde{u}_j} - \frac{\widehat{\bar{\rho}\tilde{u}_i}\widehat{\bar{\rho}\tilde{u}_j}}{\hat{\bar{\rho}}}\right) \tag{A.4}$$

which exactly fits the known term in the CGI (2.33), as for incompressible flows. Of course, the difference is subtle and only apparent for variable density flows. For what concerns EFCLES, the SGS term is:

$$\tau_{ij} = -\left(\widehat{\rho u_i u_j} - \widehat{\bar{\rho}\tilde{u}_i\tilde{u}_j}\right) \tag{A.5}$$

In this case, it is the treatment of the density in the second term that matters. However, the approach proposed by Radhakrishnan and Bellan (2012) and reported in section 2.4.4:

$$\tau_{ij} = -\left[\bar{\rho}\left(\tilde{u}_i\tilde{u}_j - \frac{\widehat{\bar{\rho}\tilde{u}_i}}{\hat{\bar{\rho}}}\frac{\widehat{\bar{\rho}\tilde{u}_j}}{\hat{\bar{\rho}}}\right)\right]^{\wedge} \tag{A.6}$$

appears as largely inconsistent as, now, the EFCLES SGS term explicitly involves the density at two distinct filter levels. If, instead, the second term in (A.5) is first expressed with bar variables only:

$$\tau_{ij} = -\left(\rho u_i u_j - \bar{\rho}\frac{\overline{\rho u_i}}{\bar{\rho}}\frac{\overline{\rho u_j}}{\bar{\rho}}\right)^{\wedge} \tag{A.7}$$

then the bar filter is substituted with the hat one and resolved variables are used instead of the basic unknown ones, the following form is obtained:

$$\tau_{ij} = -\left(\bar{\rho}\tilde{u}_i\tilde{u}_j - \frac{\widehat{\bar{\rho}\tilde{u}_i}\widehat{\bar{\rho}\tilde{u}_j}}{\hat{\bar{\rho}}}\right)^{\wedge} \tag{A.8}$$

which again, besides the difference between the basic and test filter operations, is the form which fits the known term in the EFCGI (2.44). This difference, however, is simply dependent from the fact that in EFCLES an explicit filter is available for the scale-similar term but nothing prohibits using the test filter itself, in which case the exact equality would be restored.

APPENDIX $\mathcal{B}$

Derivation of the kinetic energy equations in the GLES framework

The peculiarities of the GLES framework are such that an equation for the resolved kinetic energy cannot be simply obtained by a scalar product of the momentum equation in (3.9) with $\tilde{u}_i^n$, but further manipulations are required to circumvent the non commutation property. In order to proceed, it is useful to first express the momentum equation of the basic NSE in the following form:

$$\frac{\partial\left(\bar{\rho}^n\tilde{u}_i^n\right)}{\partial t}+\frac{\partial}{\partial x_j}\left(\bar{\rho}^n\tilde{u}_i^n\tilde{u}_j^n+\bar{p}^n\delta_{ij}+\tilde{\Sigma}_{ij}^n-\tau_{ij}^{n-0}\right)=\frac{\partial\chi_i^{n-0}}{\partial t} \tag{B.1}$$

With such equation, and nothing that:

$$\frac{\partial\left(\bar{\rho}^n\tilde{u}_i^n\tilde{u}_j^n\right)}{\partial t}=\tilde{u}_i^n\frac{\partial\left(\bar{\rho}^n\tilde{u}_j^n\right)}{\partial t}+\tilde{u}_j^n\frac{\partial\left(\bar{\rho}^n\tilde{u}_i^n\right)}{\partial t}-\tilde{u}_i^n\tilde{u}_j^n\frac{\partial\bar{\rho}^n}{\partial t} \tag{B.2}$$

an evolution equation can be written for $\bar{\rho}^n\tilde{u}_i^n\tilde{u}_j^n$:

$$\begin{aligned}\frac{\partial\left(\bar{\rho}^n\tilde{u}_i^n\tilde{u}_j^n\right)}{\partial t}=&\tilde{u}_i^n\frac{\partial\chi_j^{n-0}}{\partial t}+\tilde{u}_j^n\frac{\partial\chi_i^{n-0}}{\partial t}-\tilde{u}_i^n\tilde{u}_j^n\frac{\partial\bar{\rho}^n}{\partial t}\\&-\tilde{u}_i^n\frac{\partial}{\partial x_k}\left(\bar{\rho}^n\tilde{u}_j^n\tilde{u}_k^n+\bar{p}^n\delta_{jk}+\tilde{\Sigma}_{jk}^n-\tau_{jk}^{n-0}\right)\\&-\tilde{u}_j^n\frac{\partial}{\partial x_k}\left(\bar{\rho}^n\tilde{u}_i^n\tilde{u}_k^n+\bar{p}^n\delta_{ik}+\tilde{\Sigma}_{ik}^n-\tau_{ik}^{n-0}\right)\end{aligned} \tag{B.3}$$

This equation can be further rearranged as follows:

$$\begin{aligned}\frac{\partial\left(\bar{\rho}^n\tilde{u}_i^n\tilde{u}_j^n\right)}{\partial t} =&\tilde{u}_i^n\frac{\partial\chi_j^{n-0}}{\partial t}+\tilde{u}_j^n\frac{\partial\chi_i^{n-0}}{\partial t}-\tilde{u}_i^n\tilde{u}_j^n\frac{\partial\bar{\rho}^n}{\partial t}\\ &-\frac{\partial}{\partial x_k}\left(\bar{\rho}^n\tilde{u}_i^n\tilde{u}_j^n\tilde{u}_k^n+\bar{p}^n\tilde{u}_i^n\delta_{jk}+\tilde{u}_i^n\tilde{\Sigma}_{jk}^n-\tilde{u}_i^n\tau_{jk}^{n-0}\right)\\ &-\frac{\partial}{\partial x_k}\left(\bar{\rho}^n\tilde{u}_i^n\tilde{u}_j^n\tilde{u}_k^n+\bar{p}^n\tilde{u}_j^n\delta_{ik}+\tilde{u}_j^n\tilde{\Sigma}_{ik}^n-\tilde{u}_j^n\tau_{ik}^{n-0}\right)\\ &+\frac{\partial\tilde{u}_i^n}{\partial x_k}\left(\bar{\rho}^n\tilde{u}_j^n\tilde{u}_k^n+\bar{p}^n\delta_{jk}+\tilde{\Sigma}_{jk}^n-\tau_{jk}^{n-0}\right)\\ &+\frac{\partial\tilde{u}_j^n}{\partial x_k}\left(\bar{\rho}^n\tilde{u}_i^n\tilde{u}_k^n+\bar{p}^n\delta_{ik}+\tilde{\Sigma}_{ik}^n-\tau_{ik}^{n-0}\right)\end{aligned} \tag{B.4}$$

Finally, nothing that:

$$\bar{\rho}^n\tilde{u}_j^n\tilde{u}_k^n\frac{\partial\tilde{u}_i^n}{\partial x_k}+\bar{\rho}^n\tilde{u}_i^n\tilde{u}_k^n\frac{\partial\tilde{u}_j^n}{\partial x_k}=\frac{\partial}{\partial x_k}\left(\bar{\rho}^n\tilde{u}_i^n\tilde{u}_j^n\tilde{u}_k^n\right)-\tilde{u}_i^n\tilde{u}_j^n\frac{\partial\left(\bar{\rho}^n\tilde{u}_k^n\right)}{\partial x_k} \tag{B.5}$$

the following form is obtained:

$$\begin{aligned}\frac{\partial\left(\bar{\rho}^n\tilde{u}_i^n\tilde{u}_j^n\right)}{\partial t} =&-\frac{\partial}{\partial x_k}\left[\bar{\rho}^n\tilde{u}_i^n\tilde{u}_j^n\tilde{u}_k^n+\bar{p}^n\left(\tilde{u}_i^n\delta_{jk}+\tilde{u}_j^n\delta_{ik}\right)+\left(\tilde{u}_i^n\tilde{\Sigma}_{jk}^n+\tilde{u}_j^n\tilde{\Sigma}_{ik}^n\right)\right]\\ &+\bar{p}^n\left(\frac{\partial\tilde{u}_i^n}{\partial x_k}\delta_{jk}+\frac{\partial\tilde{u}_j^n}{\partial x_k}\delta_{ik}\right)+\tilde{\Sigma}_{jk}^n\frac{\partial\tilde{u}_i^n}{\partial x_k}+\tilde{\Sigma}_{ik}^n\frac{\partial\tilde{u}_j^n}{\partial x_k}\\ &+\frac{\partial}{\partial x_k}\left(\tilde{u}_i^n\tau_{jk}^{n-0}+\tilde{u}_j^n\tau_{ik}^{n-0}\right)-\tau_{jk}^{n-0}\frac{\partial\tilde{u}_i^n}{\partial x_k}-\tau_{ik}^{n-0}\frac{\partial\tilde{u}_j^n}{\partial x_k}\\ &+\tilde{u}_i^n\frac{\partial\chi_j^{n-0}}{\partial t}+\tilde{u}_j^n\frac{\partial\chi_i^{n-0}}{\partial t}-\tilde{u}_i^n\tilde{u}_j^n\left[\frac{\partial\bar{\rho}^n}{\partial t}+\frac{\partial\left(\bar{\rho}^n\tilde{u}_k^n\right)}{\partial x_k}\right]\end{aligned} \tag{B.6}$$

At this point, to obtain the equation for the resolved kinetic energy $\tilde{q}_r^n=\bar{\rho}^n\tilde{u}_j^n\tilde{u}_j^n/2$ just requires multiplying equation (B.6) by $\delta_{ij}/2$:

$$\begin{aligned}\frac{\partial\left(\tilde{q}_r^n\right)}{\partial t} =&-\frac{\partial}{\partial x_k}\left[\tilde{q}_r^n\tilde{u}_k^n+\bar{p}^n\tilde{u}_k^n+\tilde{u}_j^n\left(\tilde{\Sigma}_{jk}^n-\tau_{jk}^{n-0}\right)\right]+\bar{p}^n\frac{\partial\tilde{u}_k^n}{\partial x_k}+\tilde{\Sigma}_{jk}^n\frac{\partial\tilde{u}_j^n}{\partial x_k}\\ &-\tau_{jk}^{n-0}\frac{\partial\tilde{u}_j^n}{\partial x_k}+\tilde{u}_j^n\frac{\partial\chi_j^{n-0}}{\partial t}-\frac{\tilde{q}_r^n}{\bar{\rho}^n}\left[\frac{\partial\bar{\rho}^n}{\partial t}+\frac{\partial\left(\bar{\rho}^n\tilde{u}_k^n\right)}{\partial x_k}\right]\end{aligned} \tag{B.7}$$

The equation for the SGS kinetic energy $q_{sgs}^n=\tilde{q}_r^0-\tilde{q}_r^n$ is then easily obtained by subtraction of the equation (B.7) from the equation for $\tilde{q}_r^0=\rho u_j u_j/2$, obtained by

setting $n = 0$ in equation (B.7) itself. This finally leads to:

$$\begin{aligned}\frac{\partial\left(\tilde{q}_{sgs}^{n}\right)}{\partial t} = &-\frac{\partial}{\partial x_k}\left[\tilde{q}_{sgs}^{n}\tilde{u}_k^n + \left(pu_k - \bar{p}^n\tilde{u}_k^n\right) + \left(u_j\Sigma_{jk} - \tilde{u}_j^n\tilde{\Sigma}_{jk}^n\right) + \tilde{q}_r^0\left(u_k - \tilde{u}_k^n\right)\right] \\ &-\frac{\partial}{\partial x_k}\left(\tilde{u}_j^n\tau_{jk}^{n-0}\right) + \left(p\frac{\partial u_k}{\partial x_k} - \bar{p}^n\frac{\partial\tilde{u}_k^n}{\partial x_k}\right) + \left(\Sigma_{jk}\frac{\partial u_j}{\partial x_k} - \tilde{\Sigma}_{jk}^n\frac{\partial\tilde{u}_j^n}{\partial x_k}\right) \\ &+\tau_{jk}^{n-0}\frac{\partial\tilde{u}_j^n}{\partial x_k} - \tilde{u}_j^n\frac{\partial\chi_j^{n-0}}{\partial t} + \frac{\tilde{q}_r^n}{\bar{\rho}^n}\left[\frac{\partial\bar{\rho}^n}{\partial t} + \frac{\partial\left(\bar{\rho}^n\tilde{u}_k^n\right)}{\partial x_k}\right]\end{aligned} \tag{B.8}$$

APPENDIX C

Approximation of the FV operator in GLES

It is shown in section 4.2 that the unique operator G affecting the governing equations in the FV approach can be assumed to be a top-hat filter:

$$G * \phi = \frac{1}{V_i} \int_{\Omega_i} \phi\left(\boldsymbol{\xi}, t\right) d\boldsymbol{\xi} = \bar{\phi}_{FV}\left(\mathbf{x}_i, t\right) \tag{C.1}$$

A classical way to understand how this operator affects the continuous solution ϕ is by expanding it in a Taylor series around $\mathbf{x}_i$, the centroid of the volume Ω_i:

$$\phi\left(\boldsymbol{\xi}, t\right) = \sum_{q,r,s=0}^{\infty} \frac{\left(\xi - x_i\right)^q \left(\eta - y_i\right)^r \left(\zeta - z_i\right)^s}{q!r!s!} \left. \frac{\partial^{q+r+s}\phi}{\partial x^q \partial y^r \partial z^s} \right|_{\mathbf{x}_i} \tag{C.2}$$

and then to substitute it in the definition (C.1). The resulting expression would then be of the form:

$$\bar{\phi}_{FV}\left(\mathbf{x}_i, t\right) = \sum_{q,r,s=0}^{\infty} V_i^{\frac{q+r+s}{3}} M_{qrs} \left. \frac{\partial^{q+r+s}\phi}{\partial x^q \partial y^r \partial z^s} \right|_{\mathbf{x}_i} \tag{C.3}$$

with the moments M_{qrs} defined as:

$$M_{qrs} = \frac{1}{V_i^{\frac{q+r+s+3}{3}}} \int_{\Omega_i} \frac{\left(\xi - x_i\right)^q \left(\eta - y_i\right)^r \left(\zeta - z_i\right)^s}{q!r!s!} d\xi d\eta d\zeta \tag{C.4}$$

While relation (C.3) provides a sufficient description of the effect of G on the original variable ϕ, it is however in a form still not amenable for analysis. A further, common, simplification is then introduced, which consists in assuming the volume Ω_i sufficiently small that terms of second order in $V_i^{1/3}$ are sufficient in describing the effect of G and, moreover, that the topology of Ω_i allows the separation of the integrals (C.4) in the three coordinate directions. As a result of these assumptions, the following final estimate is then obtained:

$$\bar{\phi}_{FV}\left(\mathbf{x}_i,t\right)=\phi\left(\mathbf{x}_i,t\right)+V_i^{\frac{2}{3}}\left[M_{200}\frac{\partial^2\phi}{\partial x^2}+M_{020}\frac{\partial^2\phi}{\partial y^2}+M_{002}\frac{\partial^2\phi}{\partial z^2}\right]\Bigg|_{\mathbf{x}_i}+O\left(V_i^{\frac{4}{3}}\right) \quad \text{(C.5)}$$

It is worth mentioning that, while first order terms are always zero by definition of centroid, the mixed second order terms neglected here are in general non null, not only for polyhedral cells, but also for fully structured grids not aligned with the reference axes. However, these hypotheses are only functional to part of the theoretical developments presented here and in Appendix D. It is shown, in chapter 4, that they have no specific influence on the main results of the analysis.

In order to streamline the notation and bring it back to the more general terms developed within the GLES framework, the relation (C.5) can also be expressed between two contiguous generic levels, n and $n-1$, as:

$$\bar{\phi}^n=\bar{\phi}^{n-1}+\left(\Delta^n\right)^2 M_k\frac{\partial^2\bar{\phi}^{n-1}}{\partial x_k^2}+O\left(\left(\Delta^n\right)^4\right);\Delta^n=V_i^{\frac{1}{3}};M_k=\begin{cases}M_{200} & \text{for} \quad k=1\\ M_{020} & \text{for} \quad k=2\\ M_{002} & \text{for} \quad k=3\end{cases} \quad \text{(C.6)}$$

where the intended mean of Δ^n is that of the cubic root of the volume which defines the FV variable $\bar{\phi}^n$. However, the advantage of all the previous simplifications and generalizations is that the relation in (C.6) can now be used in its own as a model for the operator G in (C.1).

A further possible generalization, useful for the multilevel formalization used in GLES, is the extension of relation (C.6) to two generic levels m and n. This is easily accomplished by noting that, for sufficiently smooth variations of Δ^n and within the $O((\Delta^n)^4)$ approximation:

$$\begin{aligned}\bar{\phi}^n=&\bar{\phi}^{n-1}+\left(\Delta^n\right)^2 M_k\frac{\partial^2\bar{\phi}^{n-1}}{\partial x_k^2}\\ =&\bar{\phi}^{n-2}+\left(\Delta^{n-1}\right)^2 M_k\frac{\partial^2\bar{\phi}^{n-2}}{\partial x_k^2}+\left(\Delta^n\right)^2 M_k\frac{\partial^2\bar{\phi}^{n-2}}{\partial x_k^2}\\ =&\bar{\phi}^{n-3}+\left(\Delta^{n-2}\right)^2 M_k\frac{\partial^2\bar{\phi}^{n-3}}{\partial x_k^2}+\left(\Delta^{n-1}\right)^2 M_k\frac{\partial^2\bar{\phi}^{n-3}}{\partial x_k^2}+\left(\Delta^n\right)^2 M_k\frac{\partial^2\bar{\phi}^{n-3}}{\partial x_k^2}\\ =&\bar{\phi}^{n-q}+\Delta_{n,n-q}^2 M_k\frac{\partial^2\bar{\phi}^{n-q}}{\partial x_k^2}\qquad \Delta_{n,n-q}^2=\sum_{j=0}^{q-1}\left(\Delta^{n-j}\right)^2\end{aligned} \quad \text{(C.7)}$$

Thus, with the present notation and within the previous hypotheses, the resolved variables at two generic levels m and $n > m$ are related by:

$$\bar{\phi}^n = \bar{\phi}^m + \Delta^2_{n,m} M_k \frac{\partial^2 \bar{\phi}^m}{\partial x_k^2} + O\left(\Delta^4_{n,m}\right) \qquad \Delta^2_{n,m} = \sum_{j=1}^{n-m} \left(\Delta^{m+j}\right)^2 \tag{C.8}$$

An additional relation, that is useful in the derivations of Appendix D, is the inverse of the previous one:

$$\frac{1}{\bar{\phi}^m \pm \Delta^2_{n,m} M_k \frac{\partial^2 \bar{\phi}^m}{\partial x_k^2} + O\left(\Delta^4_{n,m}\right)} = \frac{1}{\bar{\phi}^m} \mp \frac{\Delta^2_{n,m} M_k}{\left(\bar{\phi}^m\right)^2} \frac{\partial^2 \bar{\phi}^m}{\partial x_k^2} + O\left(\Delta^4_{n,m}\right) \tag{C.9}$$

which is obtained by equating the equal order coefficients in the following relation:

$$\frac{a_0 + a_1 \Delta_{n,m} + a_2 \Delta^2_{n,m} + O\left(\Delta^3_{n,m}\right)}{b_0 + b_1 \Delta_{n,m} + b_2 \Delta^2_{n,m} + O\left(\Delta^3_{n,m}\right)} = c_0 + c_1 \Delta_{n,m} + c_2 \Delta^2_{n,m} + O\left(\Delta^3_{n,m}\right) \tag{C.10}$$

and solving the resulting linear system for the c_j:

$$a_i = \sum_{j=0}^{i} c_j b_{i-j} \tag{C.11}$$

APPENDIX $\mathcal{D}$

FV approximation for τ_{ij}^{n-m} in GLES

Within the approximations determined, for FV operators, by the relations (C.8) and (C.9), it is possible to analyze, at the lowest order, the term τ_{ij}^{n-m} in the GLES framework, which is reported here for clarity:

$$\tau_{ij}^{n-m} = \overbrace{\left(\bar{\rho}^n \tilde{u}_i^n \tilde{u}_j^n - \bar{\rho}^m \tilde{u}_i^m \tilde{u}_j^m\right)}^{\text{I}} + \overbrace{\left(\bar{p}^n - \bar{p}^m\right)}^{\text{II}} \delta_{ij} - 2\mu \overbrace{\left(\tilde{S}_{ij}^n - \tilde{S}_{ij}^m\right)}^{\text{III}} + \frac{2\mu}{3}\delta_{ij} \overbrace{\left(\tilde{S}_{qq}^n - \tilde{S}_{qq}^m\right)}^{\text{IV}} \tag{D.1}$$

For the sake of simplicity, it is assumed in (D.1) and the following that μ is constant which, for the high Reynolds numbers typical of applications, can be considered an acceptable approximation. The four parts I-IV are analyzed separately in the following. Whenever necessary, use is made of the relations (3.4) and (3.7).

I - Convective term

Term I in (D.1) can be first rearranged as follows:

$$\begin{aligned}\left(\bar{\rho}^n \tilde{u}_i^n \tilde{u}_j^n - \bar{\rho}^m \tilde{u}_i^m \tilde{u}_j^m\right) =& \frac{\overline{\rho u_i}^n \overline{\rho u_j}^n}{\bar{\rho}^n} - \bar{\rho}^m \tilde{u}_i^m \tilde{u}_j^m \\ =& \frac{\overline{\bar{\rho}^m \tilde{u}_i^m}^{+(n-m)} \overline{\bar{\rho}^m \tilde{u}_j^m}^{+(n-m)}}{\overline{\bar{\rho}^m}^{+(n-m)}} - \bar{\rho}^m \tilde{u}_i^m \tilde{u}_j^m\end{aligned} \tag{D.2}$$

Then the first term can be approximated as:

$$\frac{\overline{\bar{\rho}^m \tilde{u}_i^m}^{+(n-m)} \overline{\bar{\rho}^m \tilde{u}_j^m}^{+(n-m)}}{\overline{\bar{\rho}^m}^{+(n-m)}} = \\ = \frac{\left[\bar{\rho}^m \tilde{u}_i^m + \Delta_{n,m}^2 M_k \frac{\partial^2 \bar{\rho}^m \tilde{u}_i^m}{\partial x_k^2} + O\left(\Delta_{n,m}^4\right)\right]\left[\bar{\rho}^m \tilde{u}_j^m + \Delta_{n,m}^2 M_k \frac{\partial^2 \bar{\rho}^m \tilde{u}_j^m}{\partial x_k^2} + O\left(\Delta_{n,m}^4\right)\right]}{\bar{\rho}^m + \Delta_{n,m}^2 M_k \frac{\partial^2 \bar{\rho}^m}{\partial x_k^2} + O\left(\Delta_{n,m}^4\right)} \tag{D.3}$$

So that, considering equation (C.9), the overall approximation becomes:

$$\left(\bar{\rho}^n \tilde{u}_i^n \tilde{u}_j^n - \bar{\rho}^m \tilde{u}_i^m \tilde{u}_j^m\right) = \Delta_{n,m}^2 M_k \left(\tilde{u}_i^m \frac{\partial^2 \bar{\rho}^m \tilde{u}_j^m}{\partial x_k^2} + \tilde{u}_j^m \frac{\partial^2 \bar{\rho}^m \tilde{u}_i^m}{\partial x_k^2} - \tilde{u}_i^m \tilde{u}_j^m \frac{\partial^2 \bar{\rho}^m}{\partial x_k^2}\right) \\ + O\left(\Delta_{n,m}^4\right) \tag{D.4}$$

This can be further rearranged by noting that:

$$\tilde{u}_i^m \frac{\partial^2 \bar{\rho}^m \tilde{u}_j^m}{\partial x_k^2} + \tilde{u}_j^m \frac{\partial^2 \bar{\rho}^m \tilde{u}_i^m}{\partial x_k^2} = \\ = 2\tilde{u}_i^m \tilde{u}_j^m \frac{\partial^2 \bar{\rho}^m}{\partial x_k^2} + \bar{\rho}^m \left(\tilde{u}_i^m \frac{\partial^2 \tilde{u}_j^m}{\partial x_k^2} + \tilde{u}_j^m \frac{\partial^2 \tilde{u}_i^m}{\partial x_k^2}\right) + 2\frac{\partial \bar{\rho}^m}{\partial x_k}\left(\tilde{u}_i^m \frac{\partial \tilde{u}_j^m}{\partial x_k} + \tilde{u}_j^m \frac{\partial \tilde{u}_i^m}{\partial x_k}\right) \tag{D.5}$$

Finally, by further expanding $\partial^2 \bar{\rho}^m \tilde{u}_i^m \tilde{u}_j^m / \partial x_k^2$ (see equations (E.4) and (E.5)), one can readily show that the approximation (D.4) can be put in the more convenient form:

$$\left(\bar{\rho}^n \tilde{u}_i^n \tilde{u}_j^n - \bar{\rho}^m \tilde{u}_i^m \tilde{u}_j^m\right) = \Delta_{n,m}^2 M_k \left(\frac{\partial^2 \bar{\rho}^m \tilde{u}_i^m \tilde{u}_j^m}{\partial x_k^2} - 2\bar{\rho}^m \frac{\partial \tilde{u}_i^m}{\partial x_k} \frac{\partial \tilde{u}_j^m}{\partial x_k}\right) + O\left(\Delta_{n,m}^4\right) \tag{D.6}$$

II - Pressure term

The treatment of the pressure term is immediate as its approximation directly follows from equation (C.8):

$$\bar{p}^n - \bar{p}^m = \Delta_{n,m}^2 M_k \frac{\partial^2 \bar{p}^m}{\partial x_k^2} + O\left(\Delta_{n,m}^4\right) \tag{D.7}$$

III/IV - Viscous term and its trace

To analyze the viscous terms, it is first necessary to approximate the following term (notice the tilde instead of the bar operator):

$$\begin{aligned}
\tilde{u}_i^n &= \frac{\overline{\bar{\rho}^m \tilde{u}_i^m}^{+(n-m)}}{\overline{\bar{\rho}^m}^{+(n-m)}} \\
&= \left[\bar{\rho}^m \tilde{u}_i^m + \Delta_{n,m}^2 M_k \frac{\partial^2 \bar{\rho}^m \tilde{u}_i^m}{\partial x_k^2} + O\left(\Delta_{n,m}^4\right)\right] \left[\frac{1}{\bar{\rho}^m} - \frac{\Delta_{n,m}^2 M_k}{\left(\bar{\rho}^m\right)^2} \frac{\partial^2 \bar{\rho}^m}{\partial x_k^2} + O\left(\Delta_{n,m}^4\right)\right] \\
&= \tilde{u}_i^m + \frac{\Delta_{n,m}^2 M_k}{\bar{\rho}^m} \left(\frac{\partial^2 \bar{\rho}^m \tilde{u}_i^m}{\partial x_k^2} - \tilde{u}_i^m \frac{\partial^2 \bar{\rho}^m}{\partial x_k^2}\right) + O\left(\Delta_{n,m}^4\right) \\
&= \tilde{u}_i^m + \Delta_{n,m}^2 M_k \left(\frac{\partial^2 \tilde{u}_i^m}{\partial x_k^2} + \frac{2}{\bar{\rho}^m} \frac{\partial \bar{\rho}^m}{\partial x_k} \frac{\partial \tilde{u}_i^m}{\partial x_k}\right) + O\left(\Delta_{n,m}^4\right)
\end{aligned} \tag{D.8}$$

From which the approximation for the viscous term III easily follows:

$$\begin{aligned}
\tilde{S}_{ij}^n - \tilde{S}_{ij}^m = &\frac{1}{2}\left[\frac{\partial}{\partial x_j}\left(\Delta_{n,m}^2 M_k \frac{\partial^2 \tilde{u}_i^m}{\partial x_k^2}\right) + \frac{\partial}{\partial x_i}\left(\Delta_{n,m}^2 M_k \frac{\partial^2 \tilde{u}_j^m}{\partial x_k^2}\right)\right] \\
&+\frac{1}{2}\left[\frac{\partial}{\partial x_j}\left(\frac{2\Delta_{n,m}^2 M_k}{\bar{\rho}^m} \frac{\partial \bar{\rho}^m}{\partial x_k} \frac{\partial \tilde{u}_i^m}{\partial x_k}\right) + \frac{\partial}{\partial x_i}\left(\frac{2\Delta_{n,m}^2 M_k}{\bar{\rho}^m} \frac{\partial \bar{\rho}^m}{\partial x_k} \frac{\partial \tilde{u}_j^m}{\partial x_k}\right)\right] \\
&+O\left(\Delta_{n,m}^4\right)
\end{aligned} \tag{D.9}$$

Term IV is then simply obtained as the trace of the previous one:

$$\tilde{S}_{qq}^n - \tilde{S}_{qq}^m = \frac{\partial}{\partial x_q}\left(\Delta_{n,m}^2 M_k \frac{\partial^2 \tilde{u}_q^m}{\partial x_k^2} + \frac{2\Delta_{n,m}^2 M_k}{\bar{\rho}^m} \frac{\partial \bar{\rho}^m}{\partial x_k} \frac{\partial \tilde{u}_q^m}{\partial x_k}\right) + O\left(\Delta_{n,m}^4\right) \tag{D.10}$$

APPENDIX $\mathcal{E}$

Additional FV approximations in GLES

Following the same approach delineated in Appendix D, it is possible to derive two additional relations which are useful to show the connection between GLES and ADM (Stolz and Adams, 1999). To this end, let us denote by a superscript asterisk the following approximation:

$$\phi^* = \bar{\phi}^n - \Delta_{n,0}^2 M_k \frac{\partial^2 \bar{\phi}^n}{\partial x_k^2} + O\left(\Delta_{n,0}^4\right) \qquad \Delta_{n,m}^2 = \sum_{j=1}^{n-m} \left(\Delta^{m+j}\right)^2 \tag{E.1}$$

The first approximation is needed for $(\rho u_i)^*(\rho u_j)^*/\rho^*$. This can be obtained by the same passages between equations (D.3) and (D.4) with inverted signs:

$$\begin{aligned} &\frac{\left(\rho u_i\right)^* \left(\rho u_j\right)^*}{\rho^*} = \\ &= \frac{\left[\bar{\rho}^n \tilde{u}_i^n - \Delta_{n,0}^2 M_k \frac{\partial^2 \bar{\rho}^n \tilde{u}_i^n}{\partial x_k^2} + O\left(\Delta_{n,0}^4\right)\right]\left[\bar{\rho}^n \tilde{u}_j^n - \Delta_{n,0}^2 M_k \frac{\partial^2 \bar{\rho}^n \tilde{u}_j^n}{\partial x_k^2} + O\left(\Delta_{n,0}^4\right)\right]}{\bar{\rho}^n - \Delta_{n,0}^2 M_k \frac{\partial^2 \bar{\rho}^n}{\partial x_k^2} + O\left(\Delta_{n,0}^4\right)} \end{aligned} \tag{E.2}$$

and, considering equation (C.9), leads to:

$$\begin{aligned} \frac{\left(\rho u_i\right)^* \left(\rho u_j\right)^*}{\rho^*} =& \bar{\rho}^n \tilde{u}_i^n \tilde{u}_j^n \\ & - \Delta_{n,0}^2 M_k \left(\tilde{u}_i^n \frac{\partial^2 \bar{\rho}^n \tilde{u}_j^n}{\partial x_k^2} + \tilde{u}_j^n \frac{\partial^2 \bar{\rho}^n \tilde{u}_i^n}{\partial x_k^2} - \tilde{u}_i^n \tilde{u}_j^n \frac{\partial^2 \bar{\rho}^n}{\partial x_k^2} \right) + O\left(\Delta_{n,0}^4\right) \end{aligned} \tag{E.3}$$

By using equation (D.5), this can be further rearranged as:

$$\begin{aligned}
&\frac{(\rho u_i)^* (\rho u_j)^*}{\rho^*} = \bar{\rho}^n \tilde{u}_i^n \tilde{u}_j^n \\
&- \Delta_{n,0}^2 M_k \left[\tilde{u}_i^n \tilde{u}_j^n \frac{\partial^2 \bar{\rho}^n}{\partial x_k^2} + \bar{\rho}^n \left(\tilde{u}_i^n \frac{\partial^2 \tilde{u}_j^n}{\partial x_k^2} + \tilde{u}_j^n \frac{\partial^2 \tilde{u}_i^n}{\partial x_k^2} \right) + 2 \frac{\partial \bar{\rho}^n}{\partial x_k} \left(\tilde{u}_i^n \frac{\partial \tilde{u}_j^n}{\partial x_k} + \tilde{u}_j^n \frac{\partial \tilde{u}_i^n}{\partial x_k} \right) \right] \\
&+ O\left(\Delta_{n,0}^4\right)
\end{aligned} \tag{E.4}$$

Finally, by the identities:

$$\begin{aligned}
\tilde{u}_i^n \frac{\partial^2 \tilde{u}_j^n}{\partial x_k^2} + \tilde{u}_j^n \frac{\partial^2 \tilde{u}_i^n}{\partial x_k^2} &= \frac{\partial^2 \tilde{u}_i^n \tilde{u}_j^n}{\partial x_k^2} - 2 \frac{\partial \tilde{u}_i^n}{\partial x_k} \frac{\partial \tilde{u}_j^n}{\partial x_k} \\
\tilde{u}_i^n \frac{\partial \tilde{u}_j^n}{\partial x_k} + \tilde{u}_j^n \frac{\partial \tilde{u}_i^n}{\partial x_k} &= \frac{\partial \tilde{u}_i^n \tilde{u}_j^n}{\partial x_k} \\
\tilde{u}_i^n \tilde{u}_j^n \frac{\partial^2 \bar{\rho}^n}{\partial x_k^2} + \bar{\rho}^n \frac{\partial^2 \tilde{u}_i^n \tilde{u}_j^n}{\partial x_k^2} + 2 \frac{\partial \bar{\rho}^n}{\partial x_k} \frac{\partial \tilde{u}_i^n \tilde{u}_j^n}{\partial x_k} &= \frac{\partial^2 \bar{\rho}^n \tilde{u}_i^n \tilde{u}_j^n}{\partial x_k^2}
\end{aligned} \tag{E.5}$$

the following final approximation is obtained:

$$\frac{(\rho u_i)^* (\rho u_j)^*}{\rho^*} = \bar{\rho}^n \tilde{u}_i^n \tilde{u}_j^n - \Delta_{n,0}^2 M_k \left(\frac{\partial^2 \bar{\rho}^n \tilde{u}_i^n \tilde{u}_j^n}{\partial x_k^2} - 2 \bar{\rho}^n \frac{\partial \tilde{u}_i^n}{\partial x_k} \frac{\partial \tilde{u}_j^n}{\partial x_k} \right) + O\left(\Delta_{n,0}^4\right) \tag{E.6}$$

The second approximation is needed for $(\rho u_i)^*/\rho^*$, which is obtained as:

$$\begin{aligned}
\frac{(\rho u_i)^*}{\rho^*} &= \left[\bar{\rho}^n \tilde{u}_i^n - \Delta_{n,0}^2 M_k \frac{\partial^2 \bar{\rho}^n \tilde{u}_i^n}{\partial x_k^2} + O\left(\Delta_{n,0}^4\right) \right] \left[\frac{1}{\bar{\rho}^n} + \frac{\Delta_{n,0}^2 M_k}{\left(\bar{\rho}^n\right)^2} \frac{\partial^2 \bar{\rho}^n}{\partial x_k^2} + O\left(\Delta_{n,0}^4\right) \right] \\
&= \tilde{u}_i^n + \frac{\Delta_{n,0}^2 M_k}{\bar{\rho}^n} \left(\tilde{u}_i^n \frac{\partial^2 \bar{\rho}^n}{\partial x_k^2} - \frac{\partial^2 \bar{\rho}^n \tilde{u}_i^n}{\partial x_k^2} \right) + O\left(\Delta_{n,0}^4\right) \\
&= \tilde{u}_i^n - \frac{\Delta_{n,0}^2 M_k}{\bar{\rho}^n} \left(\bar{\rho}^n \frac{\partial^2 \tilde{u}_i^n}{\partial x_k^2} + 2 \frac{\partial \bar{\rho}^n}{\partial x_k} \frac{\partial \tilde{u}_i^n}{\partial x_k} \right) + O\left(\Delta_{n,0}^4\right) \\
&= \tilde{u}_i^n - \Delta_{n,0}^2 M_k \frac{\partial^2 \tilde{u}_i^n}{\partial x_k^2} - \frac{2 \Delta_{n,0}^2 M_k}{\bar{\rho}^n} \frac{\partial \bar{\rho}^n}{\partial x_k} \frac{\partial \tilde{u}_i^n}{\partial x_k} + O\left(\Delta_{n,0}^4\right)
\end{aligned} \tag{E.7}$$

APPENDIX $\mathcal{F}$

Single-pass, parallel computation of arbitrary-order, weighted, moments

Given two sets of N data samples, $x_1, x_2, \ldots, x_N$ and $y_1, y_2, \ldots, y_N$, and the corresponding weights, $w_1, w_2, \ldots, w_N$, the weighted means $\overline{x}_N$ and $\overline{y}_N$, and the generic, weighted, multivariate, central moment $C_{k,q}^N$ are defined by:

$$\begin{aligned} \overline{x}_N &= \frac{\sum_{i=1}^{N} w_i x_i}{\sum_{i=1}^{N} w_i} \qquad \overline{y}_N = \frac{\sum_{i=1}^{N} w_i y_i}{\sum_{i=1}^{N} w_i} \\ C_{k,q}^N &= \frac{\sum_{i=1}^{N} w_i \left(x_i - \overline{x}_N\right)^k \left(y_i - \overline{y}_N\right)^q}{\sum_{i=1}^{N} w_i} \end{aligned} \tag{F.1}$$

Let us assume that the original data couples and weights are available as two separate data sets of respective cardinality M and $N - M$, with $0 < M < N$. Also, weighted means and moments are available for both the subsets: $\overline{x}_M$, $\overline{x}_{N-M}$, $\overline{y}_M$, $\overline{y}_{N-M}$, $C_{r,s}^M$ and $C_{r,s}^{N-M}$, with $(0,0) \leq (r,s) \leq (k,q)$. The relations derived in the following are intended to express the equations (F.1) only in terms of these quantities and the weights of the two data sets.

Recurrence formulas for the weighted means can be easily developed and are not the subject of the present discussion. However, they are useful to introduce further nomenclature conventions and for reference in the following manipulations; limiting

the discussion to the variables x_i:

$$\overline{x}_N = \frac{\sum_{i=1}^{N} w_i x_i}{\sum_{i=1}^{N} w_i} = \frac{\sum_{i=1}^{M} w_i x_i + \sum_{i=M+1}^{N} w_i x_i}{\sum_{i=1}^{N} w_i} = \underbrace{\left(\frac{\sum_{i=1}^{M} w_i}{\sum_{i=1}^{N} w_i} \right)}_{w^M/w^N} \overline{x}_M + \underbrace{\left(\frac{\sum_{i=M+1}^{N} w_i}{\sum_{i=1}^{N} w_i} \right)}_{w^{N-M}/w^N} \overline{x}_{N-M} \tag{F.2}$$

Noting that $w^M + w^{N-M} = w^N$, equation (F.2) can be also expressed in the two following forms:

$$\begin{aligned} \overline{x}_N &= \overline{x}_M + \frac{w^{N-M}}{w^N} \left(\overline{x}_{N-M} - \overline{x}_M \right) \\ \overline{x}_N &= \overline{x}_{N-M} - \frac{w^M}{w^N} \left(\overline{x}_{N-M} - \overline{x}_M \right) \end{aligned} \tag{F.3}$$

To obtain a recurrence formula for $C_{k,q}^N$, it is first multiplied by w^N and then the sum is split over the two separate sets:

$$\begin{aligned} & w^N C_{k,q}^N = \sum_{i=1}^{N} w_i \left(x_i - \overline{x}_N \right)^k \left(y_i - \overline{y}_N \right)^q = \\ & \sum_{i=1}^{M} w_i \left[(x_i - \overline{x}_M) + (\overline{x}_M - \overline{x}_N) \right]^k \left[(y_i - \overline{y}_M) + (\overline{y}_M - \overline{y}_N) \right]^q + \\ & \sum_{i=M+1}^{N} w_i \left[(x_i - \overline{x}_{N-M}) + (\overline{x}_{N-M} - \overline{x}_N) \right]^k \left[\left(y_i - \overline{y}_{N-M} \right) + \left(\overline{y}_{N-M} - \overline{y}_N \right) \right]^q \end{aligned} \tag{F.4}$$

Then, by introducing the binomial expansion formula:

$$(a+b)^p = \sum_{j=0}^{p} \frac{p! a^{p-j} b^j}{(p-j)! j!} = \sum_{j=0}^{p} \binom{p}{j} a^{p-j} b^j \tag{F.5}$$

equation (F.4) can be rewritten as:

$$\begin{aligned} & w^N C_{k,q}^N = \sum_{i=1}^{M} w_i \sum_{r=0}^{k} \sum_{s=0}^{q} \binom{k}{r} \binom{q}{s} \left(x_i - \overline{x}_M \right)^{k-r} \alpha_{x,M}^r \left(y_i - \overline{y}_M \right)^{q-s} \alpha_{y,M}^s + \\ & \sum_{i=M+1}^{N} w_i \sum_{r=0}^{k} \sum_{s=0}^{q} \binom{k}{r} \binom{q}{s} \left(x_i - \overline{x}_{N-M} \right)^{k-r} \alpha_{x,N-M}^r \left(y_i - \overline{y}_{N-M} \right)^{q-s} \alpha_{y,N-M}^s \end{aligned} \tag{F.6}$$

where:

$$\begin{aligned}
\alpha_{x,M}^{r} &= \left(\overline{x}_M - \overline{x}_N\right)^r \\
\alpha_{y,M}^{s} &= \left(\overline{y}_M - \overline{y}_N\right)^s \\
\alpha_{x,N-M}^{r} &= \left(\overline{x}_{N-M} - \overline{x}_N\right)^r \\
\alpha_{y,N-M}^{s} &= \left(\overline{y}_{N-M} - \overline{y}_N\right)^s
\end{aligned} \tag{F.7}$$

Finally, like in Pébay (2008), the commutativity of the addition over finite sets can be used to exchange the summation order, obtaining the following expression:

$$\begin{aligned}
& w^N C_{k,q}^N = \\
& \sum_{r=0}^{k}\sum_{s=0}^{q}\binom{k}{r}\binom{q}{s}\left[w^M C_{k-r,q-s}^M \left(\overline{x}_M - \overline{x}_N\right)^r \left(\overline{y}_M - \overline{y}_N\right)^s + \right. \\
& \left. w^{N-M} C_{k-r,q-s}^{N-M} \left(\overline{x}_{N-M} - \overline{x}_N\right)^r \left(\overline{y}_{N-M} - \overline{y}_N\right)^s\right]
\end{aligned} \tag{F.8}$$

Equation (F.8) is already in a recurrence form however, by using the relations (F.3), it can be further simplified to obtain the following one:

$$\begin{aligned}
C_{k,q}^N &= \sum_{r=0}^{k}\sum_{s=0}^{q}\binom{k}{r}\binom{q}{s}\frac{\left(\overline{x}_{N-M} - \overline{x}_M\right)^r \left(\overline{y}_{N-M} - \overline{y}_M\right)^s}{\left(w^N\right)^{r+s+1}} A_{k-r,q-s}^{N,M} \\
A_{k-r,q-s}^{N,M} &= w^{N-M}\left(w^M\right)^{r+s} C_{k-r,q-s}^{N-M} + w^M\left(-w^{N-M}\right)^{r+s} C_{k-r,q-s}^{M}
\end{aligned} \tag{F.9}$$

which is the final recurrence formula presented in section 5.6.4.

Bibliography

A. Abbà, C. Cercignani, and L. Valdettaro. Analysis of subgrid scale models. *Comput. Math. Appl.*, 46:521–535, 2003.

A. Abbà, A. Aprovitola, E. Colombo, F.M. Denaro, M. Germano, M. Icardi, F. Inzoli, M. Iovieno, P. Lampitella, D. Marchisio, F.S. Marra, S. Rolfo, and D. Tordella. A comparative test of large-eddy simulation codes. *Meccanica*, 2013. Under Review.

V. Adumitroaie, J.R. Ristorcelli, and D.B. Taulbee. Progress in Favré-Reynolds stress closures for compressible flows. *Phys. Fluids*, 11(9):2696–2719, 1999.

R. Anderson and C. Meneveau. Effects of the similarity model in finite-difference LES of isotropic turbulence using a Lagrangian dynamic mixed model. *Flow, Turbulence and Combustion*, 62:201–225, 1999.

ANSYS® Fluent®, Release 13.0 Theory guide. ANSYS, Inc., Canonsburg, PA, USA, 2010.

A. Aprovitola and F.M. Denaro. On the application of congruent upwind discretizations for large eddy simulations. *J. Comp. Phys.*, 194:329–343, 2004.

MultiFluid NavierStokes Solver TransAT User Manual. ASCOMP, GmbH, 2009.

A. Ashrafizadeh, M Rezvani, and B. Bakhtiari. Pressure-velocity coupling on co-located grids using the method of proper closure equations. *Numer. Heat Transf. B*, 56:259–273, 2009.

A. Ashrafizadeh, M Rezvani, and B. Alinia. Use of proper closure equations in finite volume discretization schemes. In R. Petrova, editor, *Finite Volume Method - Powerful Means of Engineering Design*, chapter 3, pages 61–82. InTech, 2012.

M.H. Baba-Ahmadi and G.R. Tabor. Inlet conditions for LES using mapping and feedback control. *Comput. Fluids*, 38:1299–1311, 2009.

S. Banerjee, R. Krahl, F. Durst, and Ch. Zenger. Presentation of anisotropy properties of turbulence, invariants versus eigenvalue approaches. *J. Turbulence*, 8(32):1–27, 2007.

J. Bardina, J.H. Ferziger, and W.C. Reynolds. Improved subgrid scale models for large eddy simulation. *AIAA Paper*, (80-1357), 1980.

J. Bardina, J.H. Ferziger, and W.C. Reynolds. Improved turbulence models based on large eddy simulation of homogeneous, incompressible, turbulent flows. Report TF-19, Thermosciences Division, Dept. of Mechanical Engineering, Stanford University, 1983.

T. J. Barth. A 3-D upwind Euler solver for unstructured meshes. *AIAA Paper*, (91-1548), 1991.

T. J. Barth and D. C. Jespersen. The design and application of upwind schemes on unstructured meshes. *AIAA Paper*, (89-0366), 1989.

P. Batten, C. Lambert, and D.M. Causon. Positively conservative high-resolution convection schemes for unstructured elements. *Int. J. Numer. Meth. Engng.*, 39:1821–1838, 1996.

H. Baya Toda, K. Truffin, and F. Nicoud. Is the dynamic procedure appropriate for all SGS models? In J.C.F. Pereira and A. Sequeira, editors, *V European Conference on Computational Fluid Dynamics*. ECCOMAS, 2010.

H. Baya Toda, O. Cabrit, K. Truffin, B. Gilles, and F. Nicoud. A dynamic procedure for advanced subgrid-scale models and wall-bounded flows. In *7th International Symposium on Turbulence and Shear Flow Phenomena*, 2011.

S. Benhamadouche, K. Mahesh, and G. Costantinescu. Colocated finite-volume schemes for large-eddy simulation on unstructured meshes. Proceedings of the Summer Program 8, Center for Turbulence Research, 2002.

M. Bernardini, S. Pirozzoli, M. Quadrio, and P. Orlandi. Turbulent channel flow simulations in convecting reference frames. *J. Comp. Phys.*, 232:1–6, 2013.

L. Biferale. Shell models of energy cascade in turbulence. *Annu. Rev. Fluid Mech.*, 35: 441–468, 2003.

J. Blazek. *Computational Fluid Dynamics: Principles and Applications*. Elsevier, 2nd edition, 2005.

J.P. Boris, F.F. Grinstein, E.S. Oran, and R.L. Kolbe. New insights into large eddy simulation. *Fluid Dyn. Res.*, 10:199–228, 1992.

S.T. Bose, P. Moin, and D. You. Grid-independent large-eddy simulation using explicit filtering. *Phys. Fluids*, 22(105103), 2010.

R. Bouffanais. Advances and challenges of applied large-eddy simulation. *Comput. Fluids*, 39:735–738, 2010.

J.W. Brooke and T.J. Hanratty. Origin of turbulence-producing eddies in a channel flow. *Phys. Fluids A*, 5(4):1011–1022, 1993.

D. Carati, G.S. Winckelmans, and H. Jeanmart. On the modelling of the subgrid-scale and filtered-scale stress tensors in large-eddy simulation. *J. Fluid Mech.*, 441:119–138, 2001.

H.G. Castro and R.R. Paz. A time and space correlated turbulence synthesis method for large eddy simulations. *J. Comp. Phys.*, 235:742–763, 2013.

T.F. Chan, G.H. Golub, and R.J. LeVeque. Updating formulae and a pairwise algorithm for computing sample variances. Report STAN-CS-79-773, Dept. of Computer Science, Stanford University, 1979.

T.F. Chan, G.H. Golub, and R.J. LeVeque. Algorithms for computing the sample variance: Analysis and recommendations. *The American Statistician*, 37(3):242–247, 1983.

S. Chester, F. Charlette, and C. Meneveau. Dynamic model for LES without test filtering: Quantifying the accuracy of Taylor series approximations. *Theoret. Comp. Fluid Dyn.*, 15:165–181, 2001.

H. Choi and P. Moin. Grid-point requirements for large eddy simulation: Chapman's estimates revisited. *Phys. Fluids*, 24(011702), 2012.

M. Choi and B. Sweetman. Efficient calculation of statistical moments for structural health monitoring. *Structural Health Monitoring*, 9:13–24, 2010.

A.J. Chorin. Numerical solution of the Navier-Stokes equations. *Math. Comp.*, 22 (104):745–762, 1968.

A.J. Chorin and J.E. Marsden. *A Mathematical Introduction to Fluid Mechanics*. Springer, 3rd edition, 1997.

F.K. Chow and P. Moin. A further study of numerical errors in large-eddy simulations. *J. Comp. Phys.*, 184:366–380, 2003.

S.G. Chumakov. Statistics of subgrid-scale stresses states in homogeneous isotropic turbulence. *J. Fluid Mech.*, 562:405–414, 2006.

R.A. Clark, J.H. Ferziger, and W.C. Reynolds. Evaluation of subgrid-scale models using an accurately simulated turbulent flow. *J. Fluid Mech.*, 91(1):1–16, 1979.

T. C. Claypole and N. Syred. Coherent structures in swirl generators and combustors. In W. L. Swift, P. S. Barna, and C. Dalton, editors, *Vortex Flows*, pages 47–56, 1980.

B. Cockburn and C.-W. Shu. TVB Runge-Kutta local projection discontinuous Galerkin finite element method for conservation laws II: General framework. *Math. Comp.*, 52: 411–435, 1989.

J. Crank and P. Nicolson. A practical method for numerical evaluation of solutions of partial differential equations of the heat-conduction type. *Proc. Camb. Phil. Soc.*, 43: 50–67, 1947.

A.W. Date. Solution of Navier-Stokes equations on non-staggered grid. *Int. J. Heat Mass Transfer*, 36(7):1913–1922, 1993.

A.W. Date. Fluid dynamical view of pressure checkerboarding problem and smoothing pressure correction on meshes with colocated variables. *Int. J. Heat Mass Transfer*, 46:4885–4898, 2003.

G. De Stefano and O.V. Vasilyev. "Perfect" modeling framework for dynamic SGS model testing in large eddy simulation. *Theoret. Comp. Fluid Dyn.*, 18:27–41, 2004.

G. de With and A.E. Holdø. The use of turbulent inflow conditions for the modelling of a high aspect ratio jet. *Fluid Dyn. Res.*, 37:443–461, 2005.

J.W. Deardorff. A numerical study of three-dimensional turbulent channel flow at large Reynolds numbers. *J. Fluid Mech.*, 41:453–480, 1970.

J.W. Deardorff. On the magnitude of the subgrid scale eddy coefficient. *J. Comp. Phys.*, 7:120–133, 1971.

O. Debliquy, B. Knaepen, D. Carati, and A.A. Wray. Sampling versus filtering in large-eddy simulations. Proceedings of the Summer Program 10, Center for Turbulence Research, 2004.

J.C. del Alamo and J. Jiménez. Spectra of the very large anisotropic scales in turbulent channels. *Phys. Fluids*, 15(6):L41–L44, 2003.

J.C. del Alamo, J. Jiménez, P. Zandonade, and R.D. Moser. Scaling of the energy spectra of turbulent channels. *J. Fluid Mech*, 500:135–144, 2004.

F.M. Denaro. On the application of the Helmholtz-Hodge decomposition in projection methods for incompressible flows with general boundary conditions. *Int. J. Numer. Meth. Fluids*, 43:43–69, 2003.

F.M. Denaro. What does finite volume-based implicit filtering really resolve in large-eddy simulations? *J. Comp. Phys.*, 230:3849–3883, 2011.

F.M. Denaro. A new integral-based two-coefficients mixed model for LES. In *9th European Fluid Mechanics Conference*, Rome, Italy, 2012.

F.M. Denaro. On the relevance of the type of contraction of the Germano identity in the new integral-based dynamic Smagorinsky model. *Comput. Fluids*, 72:30–45, 2013.

F.M. Denaro and G. De Stefano. A new development of the dynamic procedure in large-eddy simulation based on a Finite Volume integral approach. Application to stratified turbulence. *Theor. Comput. Fluid Dyn.*, 25:315–355, 2011.

F.M. Denaro, G. De Stefano, D. Iudicone, and V. Botte. A finite volume dynamic large-eddy simulation method for buoyancy driven turbulent geophysical flows. *Ocean Modelling*, 17:199–218, 2007.

F.M. Denaro, A. Abbà, M. Germano, M. Icardi, D. Marchisio, S. Rolfo, P. Lampitella, E. Colombo, F. Inzoli, A. Aprovitola, F.S. Marra, M. Iovieno, and D. Tordella. A comparative test for assessing the performances of large-eddy simulation codes. In *Proc. XX AIMETA Conference*, 2011.

G.B. Deng, J. Piquet, P. Queutey, and M. Visonneau. Incompressible flow calculations with a consistent physical interpolation finite volume approach. *Comput. Fluids*, 23 (8):1029–1047, 1994.

A.R. Dobrovolskis. Inertia of any polyhedron. *Icarus*, 124(243):698–704, 1996.

E. Dormy. An accurate compact treatment of pressure for colocated variables. *J. Comp. Phys.*, 151:676–683, 1999.

J.K. Dukowicz and A.S. Dvinsky. Approximate factorization as a high order splitting for the implicit incompressible flow equations. *J. Comp. Phys.*, 102:336–347, 1992.

T.M. Eidson. Numerical simulation of the turbulent Rayleigh-Bénard problem using subgrid modelling. *J. Fluid Mech.*, 158:245–268, 1985.

G. Erlebacher, M.Y. Hussaini, C.G. Speziale, and T.A. Zang. Toward the large-eddy simulation of compressible turbulent flows. *J. Fluid Mech.*, 238:155–185, 1992.

G.L. Eyink. Turbulent flow in pipes and channels as cross-stream "inverse cascades" of vorticity. *Phys. Fluids*, 20(125101), 2008.

D. Fauconnier and E. Dick. On the spectral and conservation properties of nonlinear discretization operators. *J. Comp. Phys.*, 230:4488–4518, 2011.

D. Fauconnier, C. De Langhe, and E. Dick. The dynamic procedure for accuracy improvement of numerical discretizations in fluid mechanics. *J. Comp. Phys.*, 224: 1095–1123, 2007.

D. Fauconnier, C. De Langhe, and E. Dick. The sampling-based dynamic procedure as tool for higher-order discretization. *Int. J. Numer. Meth. Fluids*, 56:1241–1247, 2008.

D. Fauconnier, C. De Langhe, and E. Dick. A family of finite difference schemes for large-eddy simulation. *J. Comp. Phys.*, 228:1830–1861, 2009.

A. Favre. Turbulence: space-time statistical properties and behavior in supersonic flows. *Phys. Fluids*, 26(10):2851–2863, 1983.

I. Fedioun, N. Lardjane, and I. Gökalp. Revisiting numerical errors in direct and large eddy simulations of turbulence: Physical and spectral spaces analysis. *J. Comp. Phys.*, 174:816–851, 2001.

F.N. Felten and T. Lund. Kinetic energy conservation issues associated with the collocated mesh scheme for incompressible flow. *J. Comp. Phys.*, 215:465–484, 2006.

J.H. Ferziger and D.C. Leslie. Large eddy simulation - A predictive approach to turbulent flow computation. In *4th Computational Fluid Dynamics Conference*, AIAA, pages 234–246, 1979.

J.H. Ferziger and M. Perić. *Computational Methods for Fluid Dynamics*. Springer, 3rd edition, 2002.

B.A. Finlayson. *The Method of Weighted Residuals and Variational Principles*. Academic Press, 1972.

B.A. Finlayson and L.E. Scriven. The method of weighted residuals–A review. *Appl. Mech. Rev.*, 19(9):735–748, 1966.

U. Frisch. *Turbulence, the Legacy of A.N. Kolmogorov*. Cambridge University Press, 1995.

K. Fukagata, K. Iwamoto, and N. Kasagi. Contribution of Reynolds stress distribution to the skin friction in wall-bounded flows. *Phys. Fluids*, 14(11):L73–L76, 2002.

C. Fureby. Towards the use of large eddy simulation in engineering. *Prog. Aerospace Sci.*, 44:381–396, 2008.

C. Fureby and G. Tabor. Mathematical and physical constraints on large-eddy simulations. *Theoret. Comp. Fluid Dyn.*, 9:85–102, 1997.

R. García-Mayoral and J. Jiménez. Drag reduction by riblets. *Phil. Trans. R. Soc. A*, 369:1412–1427, 2011.

R. García-Mayoral and J. Jiménez. Scaling of turbulent structures in riblet channels up to $Re_\tau \approx 550$. *Phys. Fluids*, 24(105101), 2012.

E. Garnier, N. Adams, and P. Sagaut. *Large Eddy Simulation for Compressible Flows*. Springer, 2009.

P.H. Gaskell and A.K.C. Lau. Curvature-compensated convective transport: SMART, a new boundedness-preserving transport algorithm. *Int. J. Numer. Meth. Fluids*, 8: 617–641, 1988.

C.W. Gear. *Numerical Initial Value Problems in Ordinary Differential Equations*. Prentice-Hall, 1971.

M. Germano. Turbulence: the filtering approach. *J. Fluid Mech.*, 238:325–336, 1992.

M. Germano, U. Piomelli, P. Moin, and W.H. Cabot. A dynamic subgrid-scale eddy viscosity model. *Phys. Fluids A*, 3(7):1760–1765, 1991.

B. Geurts, B. Vreman, H. Kuerten, and R. Van Buuren. Noncommuting filters and dynamic modelling for LES of turbulent compressible flow in 3D shear layers. In J.-P. Chollet, P.R. Voke, and L. Kleiser, editors, *Direct and Large Eddy Simulation II*, volume 5 of *ERCOFTAC Series*, pages 47–56, Grenoble, France, 1997. Springer.

B.J. Geurts and D.D. Holm. Regularization modeling for large-eddy simulation. *Phys. Fluids*, 15(1):L13–L16, 2003.

S. Ghosal. An analysis of numerical errors in large-eddy simulations of turbulence. *J. Comp. Phys.*, 125:187–206, 1996.

S. Ghosal and P. Moin. The basic equations for the large eddy simulation of turbulent flows in complex geometry. *J. Comp. Phys.*, 118:24–37, 1995.

S. Ghosal, T.S. Lund, P. Moin, and K. Aksevoll. A dynamic localization model for large-eddy simulation of turbulent flows. *J. Fluid Mech.*, 286:229–255, 1995.

T. Gomez, V. Flutet, and P. Sagaut. Contribution of Reynolds stress distribution to the skin friction in compressible turbulent channel flows. *Phys. Rev. E*, 79(3):035301, 2009.

F. Griman, M. Terracol, and P. Sagaut. An explicit filtering method for Large Eddy Simulation. *AIAA Paper*, (2010-5025), 2010.

F.F. Grinstein. On integrating numerical and laboratory turbulent flow experiments. *AIAA Paper*, (2006-3048), 2006.

F.F. Grinstein. On integrating large eddy simulation and laboratory turbulent flow experiments. *Phil. Trans. R. Soc. A*, 367:2931–2945, 2009.

F.F. Grinstein, C. Fureby, and C.R. DeVore. On MILES based on flux-limiting algorithms. *Int. J. Numer. Meth. Fluids*, 47:1043–1051, 2005.

J.-L. Guermond, J.T. Oden, and S. Prudhomme. Mathematical perspectives on large eddy simulation models for turbulent flows. *J. Math. Fluid Mech.*, 6:194–248, 2004.

J.L. Guermond, P Minev, and J. Shen. An overview of projection methods for incompressible flows. *Comput. Methods Appl. Mech. Engrg.*, 195:6011–6045, 2006.

J. Gullbrand and F.K. Chow. The effect of numerical errors and turbulence models in large-eddy simulations of channel flow, with and without explicit filtering. *J. Fluid Mech.*, 495:323–341, 2003.

A.K. Gupta, D.G. Lilley, and N. Syred. *Swirl Flows*. Abacus Press, 1984.

S. Hammarling. An introduction to the quality of computed solutions. In B. Einarsson, editor, *Accuracy and Reliability in Scientific Computing*, chapter 4, pages 43–76. SIAM, 2005.

A. Haselbacher and O.V. Vasilyev. Commutative discrete filtering on unstructured grids based on least-squares techniques. *J. Comp. Phys.*, 187:197–211, 2003.

A. Hellsten and P. Rautaheimo, editors. *8th ERCOFTAC/IAHR/COST Workshop on Refined Turbulence Modelling*, Espoo, Finland, June 1999. Helsinky University of Technology.

N.J. Higham. *Accuracy and Stability of Numerical Algorithms*. SIAM, 2nd edition, 2002.

K. Horiuti. A new dynamic two-parameter mixed model for large-eddy simulation. *Phys. Fluids*, 9(11):3443–3464, 1997.

K. Horiuti. Roles of non-aligned eigenvectors of strain-rate and subgrid-scale stress tensors in turbulence generation. *J. Fluid Mech.*, 491:65–100, 2003.

S. Hoyas and J. Jiménez. Scaling of the velocity fluctuations in turbulent channels up to $Re_\tau = 2003$. *Phys. Fluids*, 18(011702), 2006.

S.H. Huang, Q.S. Li, and J.R. Wu. A general inflow turbulence generator for large eddy simulation. *J. Wind. Eng. Ind. Aerodyn.*, 98:600–617, 2010.

X. Huang. *Volume average technique for turbulent flow simulation and its application to room airflow prediction*. PhD thesis, University of Saskathcewan, September 1997.

T.J.R. Hughes, L. Mazzei, and K.E. Jansen. Large eddy simulation and the variational multiscale method. *Comput. Visual. Sci*, 3:47–59, 2000.

P. Iannelli, F.M. Denaro, and G. De Stefano. A deconvolution-based fourth-order finite volume method for incompressible flows on non-uniform grids. *Int. J. Numer. Meth. Fluids*, 43:431–462, 2003.

M. Iovieno and D. Tordella. Variable scale filtered Navier-Stokes equations: A new procedure to deal with the associated commutation error. *Phys. Fluids*, 15(7):1926–1936, 2003.

K. Iwamoto, K. Fukagata, N. Kasagi, and Y. Suzuki. Friction drag reduction achievable by near-wall turbulence manipulation at high Reynolds numbers. *Phys. Fluids*, 17 (011702), 2005.

H. Jasak. *Error Analysis and Estimation for the Finite Volume Method with Applications to Fluid Flows*. PhD thesis, Department of Mechanical Engineering, University of London, June 1996.

H. Jasak, H.G. Weller, and A.D. Gosman. High resolution NVD differencing scheme for arbitrarily unstructured meshes. *Int. J. Numer. Meth. Fluids*, 31:431–449, 1999.

J. Jiménez. Turbulent flows over rough walls. *Annu. Rev. Fluid Mech.*, 36:173–196, 2004.

J. Jiménez and A. Pinelli. The autonomous cycle of near-wall turbulence. *J. Fluid Mech*, 389:335–359, 1999.

L. Jofre, O. Lehmkuhl, J. Ventosa, F.X. Trias, and A. Oliva. Conservation properties of unstructured finite-volume mesh schemes for the Navier-Stokes equations. *Numer. Heat Transf. B*, 65:53–79, 2014.

B.A. Kader. Temperature and concentration profiles in fully turbulent boundary layers. *Int. J. Heat Mass Transfer*, 24(9):1541–1544, 1981.

G.E. Karniadakis and S.J. Sherwin. *Spectral/hp Element Methods for CFD*. Oxford University Press, 1999.

A. Keating, U. Piomelli, and E. Balaras. A priori and a posteriori tests of inflow conditions for large-eddy simulation. *Phys. Fluids*, 16(12):4696–4712, 2004.

P.K. Khosla and S.G. Rubin. A diagonally dominant second-order accurate implicit scheme. *Comput. Fluids*, 2(2):207–209, 1974.

J. Kim. The 14th biennial Center for Turbulence Research Summer Program. *Phys. Fluids*, 24(100501), 2012a. Previous editions available as *Studying Turbulence Using Numerical Simulation Databases* at `http://nix.nasa.gov/search.jsp`.

J. Kim. Progress in pipe and channel flow turbulence. *J. Turbulence.*, 13(45):1–19, 2012b.

J. Kim, P. Moin, and R.D. Moser. Turbulence statistics in fully developed channel flow at low Reynolds number. *J. Fluid Mech.*, 177:133–166, 1987.

S.-E. Kim. Large eddy simulation using an unstrcutured mesh based finite-volume solver. *AIAA Paper*, (2004-2548), 2004.

S.-E. Kim and B. Makarov. An implicit fractional-step method for efficient transient simulation of incompressible flows. *AIAA Paper*, (2005-5253), 2005.

S.-E. Kim, S.R. Mathur, J.Y. Murthy, and D. Choudhury. A Reynolds-Averaged Navier-Stokes solver using unstructured mesh-based finite-volume scheme. *AIAA Paper*, (98-0231), 1998.

S.-E. Kim, B. Makarov, and D. Caraeni. A multi-dimensional linear reconstruction scheme for arbitrary unstructured grids. *AIAA Paper*, (2003-3990), 2003.

W.W. Kim and S. Menon. Application of the localized dynamic subgrid-scale model to turbulent wall-bounded flows. *AIAA Paper*, (97-0210), 1997.

B. Knaepen, O. Debliquy, and D. Carati. Subgrid-scale energy and pseudo pressure in large-eddy simulation. *Phys. Fluids*, 14(12):4235–4241, 2002.

B. Knaepen, O. Debliquy, and D. Carati. Large-eddy simulation without filter. *J. Comp. Phys.*, 205:98–107, 2005.

D. Knight, G. Zhou, N. Okong'O, and V. Shukla. Compressible large eddy simulation using unstructured grids. *AIAA Paper*, (98-0535), 1998.

A.N. Kolmogorov. The local structure of turbulence in incompressible viscous fluid for very large Reynolds numbers. *Proc. R. Soc. Lond. A*, 434(1890):9–13, 1991. First published in Russian in *Dokl. Akad. Nauk SSSR* (1941) **30**(4).

B. Kosovic, D.I. Pullin, and R. Samtaney. Subgrid-scale modeling for large-eddy simulations of compressible turbulence. *Phys. Fluids*, 14(4):1511–1522, 2002.

S. Krajnović. Large eddy simulation of flows around ground vehicles and other bluff bodies. *Phil. Trans. R. Soc. A*, 367:2917–2930, 2009.

S. Krajnović and L. Davidson. Large-eddy simulation of the flow around a bluff body. *AIAA J.*, 40(5):927–936, 2002.

A.G. Kravchenko and P. Moin. On the effect of numerical errors in large eddy simulation. *J. Comp. Phys.*, 131:310–322, 1997.

F. Laadhari. On the evolution of maximum turbulent kinetic energy production in a channel flow. *Phys. Fluids*, 14(10):L65–L68, 2002.

S. Laizet and E. Lamballais. High-order compact schemes for incompressible flows: A simple and efficient method with quasi-spectral accuracy. *J. Comp. Phys.*, 228: 5989–6015, 2009.

P. Lampitella, R. Mereu, F. Inzoli, and E. Colombo. Implementation of a remap boundary condition for LES applications in Fluent. In *28th Enginsoft International CAE Conference*, 2012. URL `http://proceedings2012.caeconference.com/papers/065/PolitecnicoMilano.html`.

B.E. Launder, G.J. Reece, and W. Rodi. Progress in the development of a Reynolds-stress turbulence closure. *J. Fluid Mech.*, 68(3):537–566, 1975.

W.J Layton and L. Rebholz. *Approximate Deconvolution Models of Turbulence. Analysis, Phenomenology and Numerical Analysis.* Springer, 2012.

O. Lehmkuhl, R. Borrell, I. Rodriguez, C.D. Perez-Segarra, and A. Oliva. Assessment of the symmetry-preserving regularization model on complex flows using unstructured grids. *Comput. Fluids*, 60:108–116, 2012.

A. Leonard. Energy cascade in large-eddy simulations of turbulent fluid flows. *Adv. in Geophys. A*, 18:237–248, 1974.

B.P. Leonard. Simple high-accuracy resolution program for convective modeling of discontinuities. *Int. J. Numer. Meth. Fluids*, 8:1291–1318, 1988.

B.P. Leonard. The ULTIMATE conservative difference scheme applied to unsteady one-dimensional advection. *Comp. Meth. Appl. Mech. Eng.*, 88:17–74, 1991.

S. Leonard, M. Terracol, and P. Sagaut. Commutation error in LES with time-dependent filter width. *Comput. Fluids*, 36:513–519, 2007.

S. Lien and J.T. Kajiya. A symbolic method for calculating the integral properties of arbitrary nonconvex polyhedra. *IEEE CG&A*, 4(10):35–42, 1984.

D.K. Lilly. The representation of small scale turbulence in numerical simulation experiments. In *IBM Scientific Computing Symposium on Environmental Sciences*, pages 195–210, 1967.

D.K. Lilly. A proposed modification of the Germano subgrid-scale closure method. *Phys. Fluids A*, 4(3):633–635, 1992.

S. Liu, C. Meneveau, and J. Katz. On the properties of similarity subgrid-scale models as deduced from measurements in a turbulent jet. *J. Fluid Mech.*, 275:83–119, 1994.

Y. Liu, M. Vinokur, and Z.J. Wang. Spectral difference method for unstructured grids I: Basic formulation. *J. Comp. Phys.*, 216:780–801, 2006.

O. Lucca-Negro and T. O'Doherty. Vortex breakdown: a review. *Progr. Energy Comb. Sci.*, 27:431–481, 2001.

T.S. Lund. The use of explicit filters in large eddy simulation. *Comput. Math. Appl.*, 46:603–616, 2003.

J.-C. Magnient, P. Sagaut, and M. Deville. A study of built-in filter for some eddy viscosity models in large-eddy simulation. *Phys. Fluids*, 13(5):1440–1449, 2001.

K. Mahesh, G. Costantinescu, and P. Moin. A numerical method for large-eddy simulation in complex geometries. *J. Comp. Phys.*, 197:215–240, 2004.

P. Majander and T. Siikonen. Evaluation of Smagorinsky-based subgrid-scale models in a finite-volume computation. *Int. J. Numer. Meth. Fluids*, 40:735–774, 2002.

L.G. Margolin. Finite-scale equations for compressible fluid flow. *Phil. Trans. R. Soc. A*, 367:2861–2871, 2009.

A.L. Marsden, O.V. Vasilyev, and P. Moin. Construction of commutative filters for LES on unstructured meshes. *J. Comp. Phys.*, 175:584–603, 2002.

P.J. Mason and N.S. Callen. On the magnitude of the subgrid-scale eddy coefficient in large-eddy simulations of turbulent channel flow. *J. Fluid Mech.*, 162:439–462, 1986.

J. Mathew, R. Lechner, H. Foysi, J. Sesterhenn, and R. Friedrich. An explicit filtering method for large eddy simulation of compressible flows. *Phys. Fluids*, 15(8):2279–2289, 2003.

F. Mathey, J. Fröhlich, and W. Rodi. LES of heat transfer in turbulent flow over a wall-mounted matrix of cubes. In P.R. Voke, N.D. Sandham, and L. Kleiser, editors, *Direct and Large-Eddy Simulation III*, volume 7 of *ERCOFTAC Series*, pages 51–62. Springer, 1999a.

F. Mathey, J. Frölich, and W. Rodi. Large-eddy simulation of the flow over a matrix of surface-mounted cubes. In S. Biringen, H. Örs, A. Tezel, and J.H. Ferziger, editors, *Industrial and Environmental Applications of Direct and Large-Eddy Simulation*, volume 529 of *Lecture Notes in Physics*, pages 153–163. Springer, 1999b.

F. Mathey, D. Cokljat, J.P. Bertoglio, and E. Sergent. Specification of LES inlet boundary condition using vortex method. In K. Hanjalić, Y. Nagano, and M. Tummers, editors, *4th International Symposium on Turbulence, Heat and Mass Transfer*, Antalya, Turkey, 2003.

F. Mathey, D. Cokljat, J.P. Bertoglio, and E. Sergent. Assessment of the vortex method for large eddy simulation inlet conditions. *Progress in Computational Fluid Dynamics, An International Journal*, 6(1):58–67, 2006.

J. Mathieu and J. Scott. *An Introduction to Turbulent Flow*. Cambridge, 2000.

S.R. Mathur and J.Y. Murthy. A pressure-based method for unstructured meshes. *Numer. Heat Transf. B*, (31):195–215, 1997.

E.R. Meinders. *Experimental study of heat transfer in turbulent flows over wall-mounted cubes*. PhD thesis, Technische Universiteit Delft, November 1998.

E.R. Meinders and K. Hanjalić. Vortex structure and heat transfer in turbulent flow over a wall-mounted matrix of cubes. *Int. J. Heat Fluid Flow*, 20:255–267, 1999.

M. Meldi, D. Lucor, and P. Sagaut. Is the Smagorinsky coefficient sensitive to uncertainty in the form of the energy spectrum? *Phys. Fluids*, 23(125109), 2011.

J. Mencinger. An alternative finite volume discretization of body force field on collocated grid. In R. Petrova, editor, *Finite Volume Method - Powerful Means of Engineering Design*, chapter 5, pages 101–116. InTech, 2012.

C. Meneveau. Statistics of turbulence subgrid-scale stresses: Necessary conditions and experimental tests. *Phys. Fluids*, 6(2):815–833, 1994.

C. Meneveau and J. Katz. Scale invariance and turbulence models for large-eddy simulation. *Annu. Rev. Fluid Mech.*, 32:1–32, 2000.

C. Meneveau, T.S. Lund, and W.H. Cabot. A lagrangian dynamic subgrid-scale model of turbulence. *J. Fluid Mech.*, 319:353–385, 1996.

S. Menon, P.-K. Yeung, and W.-W. Kim. Effect of subgrid models on the computed interscale energy transfer in isotropic turbulence. *Comput. Fluids*, 25(2), 1996.

J. Meyers and P. Sagaut. On the model coefficients for the standard and the variational multi-scale Smagorinsky model. *J. Fluid Mech.*, 569:287–319, 2006.

J. Meyers and P. Sagaut. Is plane channel flow a friendly case for the testing of the large-eddy simulation subgrid-scale models? *Phys. Fluids*, 19(048105), 2007.

J. Meyers, C. Lacor, and M. Baelmans. On the use of high-order finite-difference discretization for LES with double decomposition of the subgrid-scale stresses. *Int. J. Numer. Meth. Fluids*, 56:383–400, 2008.

P. Moin and K. Mahesh. Direct numerical simulation: A tool in turbulence research. *Annu. Rev. Fluid Mech.*, 30:539–578, 1998.

P. Moin, K. Squires, W. Cabot, and S. Lee. A dynamic subgrid-scale model for compressible turbulence and scalar transport. *Phys. Fluids A*, 3(8):2746–2757, 1991.

A.S. Monin and A.M. Yaglom. *Statistical Fluid Mechanics. Mechanics of Turbulence*, volume 1. Dover, 1971.

Y. Morinishi and O.V. Vasilyev. Vector level identity for dynamic subgrid scale modeling in large eddy simulation. *Phys. Fluids*, 14(10):3616–3623, 2002.

R.D. Moser, J. Kim, and N. Mansour. Direct numerical simulation of turbulent channel flow up to $Re_\tau = 590$. *Phys. Fluids*, 11(4):943–945, 1999.

F. Moukalled and M. Darwish. Pressure-based algorithms for single-fluid and multi-fluid flows. In W.J. Minkowycz, E.M. Sparrow, and J.Y. Murthy, editors, *Handbook of Numerical Heat Transfer*, chapter 10, pages 325–367. Wiley, 2nd edition, 2006.

A. Muschinski. A similarity theory of locally homogeneous and isotropic turbulence generated by a Smagorinsky-type LES. *J. Fluid Mech.*, 325:239–260, 1996.

Nek5000. Subroutine "avg_all", 2013. URL `http://trac.mcs.anl.gov/projects/nek5/browser/trunk/nek/navier5.f`.

F. Nicoud and F. Ducros. Subgrid-scale stress modelling based on the square of the velocity gradient tensor. *Flow, Turbulence and Combustion*, 62:183–200, 1999.

F. Nicoud, H. Baya Toda, O. Cabrit, S. Bose, and J. Lee. Using singular values to build a subgrid-scale model for large eddy simulations. *Phys. Fluids*, 23(085106), 2011.

B. Ničeno, A.D.T. Dronkers, and K. Hanjalić. Turbulent heat transfer from a multi-layered wall-mounted cube matrix: a large eddy simulation. *Int. J. Heat Fluid Flow*, 23:173–185, 2002.

A.A. Oberai and J. Wanderer. Variational formulation of the Germano identity for the Navier-Stokes equations. *J. Turbulence.*, 6(7):1–17, 2005a.

A.A. Oberai and J. Wanderer. A dynamic approach for evaluating parameters in a numerical method. *Int. J. Numer. Meth. Engng.*, 62:50–71, 2005b.

M. Oberlack. A unified approach for symmetries in plane parallel turbulent shear flows. *J. Fluid Mech.*, 427:299–328, 2001.

OpenFOAM Foundation. fvcReconstruct.C, 2013. URL `http://foam.sourceforge.net/docs/cpp/a05291_source.html`.

S.A. Orszag and G.S. Patterson. Numerical simulation of three-dimensional homogeneous isotropic turbulence. *Phys. Rev. Lett.*, 28:76–79, 1972.

N. Park and K. Mahesh. Analysis of numerical errors in large eddy simulation using statistical closure theory. *J. Comp. Phys.*, 222:194–216, 2007a.

N. Park and K. Mahesh. Numerical and modeling issues in LES of compressible turbulence on unstructured grids. *AIAA Paper*, (2007-722), 2007b.

N. Park, J.Y. Yoo, and H. Choi. Discretization errors in large eddy simulation: on the suitability of centered and upwind-biased compact difference schemes. *J. Comp. Phys.*, 198:580–616, 2004.

A.T. Patera. A spectral element method for fluid dynamics: laminar flow in a channel expansion. *J. Comp. Phys.*, 54:468–488, 1984.

P. Pébay. Formulas for robust, one-pass parallel computation of covariances and arbitrary-order statistical moments. Report SAND2008-6212, Sandia National Laboratories, 2008.

B. Perot. Conservation properties of unstructured staggered mesh schemes. *J. Comp. Phys.*, 159:58–89, 2000.

J.B. Perot. An analysis of the fractional step method. *J. Comp. Phys.*, 108:51–58, 1993.

C.D. Pierce and P. Moin. Method for generating equilibrium swirling inflow conditions. *AIAA J.*, 36(7):1325–1327, 1998.

U. Piomelli. Large-eddy simulation: achievements and challenges. *Prog. Aerospace Sci.*, 35:335–362, 1999.

U. Piomelli and E. Balaras. Wall-layer models for large-eddy simulations. *Annu. Rev. Fluid Mech.*, 34:349–374, 2002.

T. Poinsot and D. Veynante. *Theoretical and Numerical Combustion*. R.T. Edwards, 2nd edition, 2005.

S.B. Pope. *Turbulent Flows*. Cambridge University Press, 2000.

S.B. Pope. Large-eddy simulation using projection onto local basis functions. In J.L. Lumley, editor, *Fluid Mechanics and the Environment: Dynamical Approaches*, volume 566 of *Lecture Notes in Physics*, pages 239–265. Springer, 2001.

S.B. Pope. Ten questions concerning the large-eddy simulation of turbulent flows. *New J. Phys.*, 6(35):1–24, 2004.

C. Pruett. Temporal large-eddy simulation: theory and implementation. *Theor. Comput. Fluid Dyn.*, 22:275–304, 2008.

C.D. Pruett. Toward simplification of dynamic subgrid-scale models. In C. Liu and Z. Liu, editors, *Proc. of the First AFOSR International Conference on DNS/LES*, Advances in DNS/LES, pages 291–298, Ruston, Louisiana, 1997.

C.D. Pruett. Eulerian time-domain filtering for spatial large-eddy simulation. *AIAA J.*, 38(9):1634–1642, 2000.

C.D. Pruett, J.S. Sochacki, and N.A. Adams. On taylor-series expansions of residual stress. *Phys. Fluids*, 13(9):2578–2589, 2001.

A. Quarteroni, F. Saleri, and A. Veneziani. Factorization methods for the numerical approximation of Navier-Stokes equations. *Comput. Methods Appl. Mech. Engrg.*, 188:505–526, 2000.

S. Radhakrishnan and J. Bellan. Explicit filtering to obtain grid-spacing-independent and discretization-order-independent large-eddy simulation of compressible single-phase flow. *J. Fluid Mech.*, 697:399–435, 2012.

H. Reichardt. Vollständige darstellung der turbulenten geschwindigkeitsverteilung in glatten leitungen. *Z. angew. Math. Mech.*, 31(7):208–219, 1951.

O. Reynolds. An experimental investigation of the circumstances which determine whether the motion of water shall be direct or sinuous, and of the law of resistance in parallel channels. *Phil. Trans. R. Soc. Lond.*, 174:935–982, 1883.

O. Reynolds. On the dynamical theory of incompressible viscous fluids and the determination of the criterion. *Phil. Trans. R. Soc. Lond. A*, 186:123–164, 1895.

W.C. Reynolds. The potential and limitations of direct and large eddy simulations. In J.L. Lumley, editor, *Whither Turbulence? Turbulence at the Crossroads*, volume 357 of *Lecture Notes in Physics*, pages 313–343. Springer, 1990.

C. M. Rhie. A numerical study of the turbulent flow past an isolated airfoil with trailing edge separation. *AIAA Paper*, (82-0998), 1982.

C. M. Rhie and W. L. Chow. Numerical study of the turbulent flow past an airfoil with trailing edge separation. *AIAA J.*, 21(11):1525–1532, 1983.

L.F. Richardson. *Weather prediction by numerical process*. Cambridge University Press, 1922.

S.K. Robinson. Coherent motions in the turbulent boundary layer. *Annu. Rev. Fluid Mech.*, 23:601–639, 1991.

M.O. Rodrigues. Des lois géométriques qui régissent les déplacements d'un systéme solide dans l'espace, et de la variation des coordonnées provenant de ces déplacements considérés indépendamment des causes qui peuvent les produire. *Journal de Mathématiques Pures et Appliquées*, 5:380–440, 1840.

R.S. Rogallo. Numerical experiments in homogeneous turbulence. Technical Memorandum 81315, NASA, 1981.

R. Rossi. Direct numerical simulation of scalar transport using unstructured finite-volume schemes. *J. Comp. Phys.*, 228:1639–1657, 2009.

P. Sagaut. Numerical simulations of separated flows with subgrid models. *Rech. Aéro.*, 1:51–63, 1996.

P. Sagaut. *Large Eddy Simulation for Incompressible Flows. An Introduction*. Springer, 3rd edition, 2006.

P. Sagaut and R. Grohens. Discrete filters for large eddy simulation. *Int. J. Numer. Meth. Fluids*, 31:1195–1220, 1999.

P. Sagaut, B. Troff, T.H. Lê, and Ta Phuoc Loc. Large eddy simulation of turbulent flow past a backward facing step with a new mixed scale SGS model. In M. Deville, S. Gavrilakis, and I.L. Rhyming, editors, *Computation of Three-Dimensional Complex Flows*, volume 49 of *Notes on Numerical Fluid Mechanics (NNFM)*, pages 271–277. Springer, 1996.

P. Sagaut, E. Garnier, E. Tromeur, L. Larchevêque, and E. Labourasse. Turbulent inflow conditions for large-eddy simulation of compressible wall-bounded flows. *AIAA J.*, 42(3):469–477, 2004.

M.V. Salvetti and S. Banerjee. A priori tests of a new dynamic subgrid-scale model for finite-difference large eddy simulations. *Phys. Fluids*, 7(11):2831–2847, 1995.

F. Sarghini, U. Piomelli, and E. Balaras. Scale-similar models for large-eddy simulations. *Phys. Fluids*, 11(6):1596–1607, 1999.

J.U. Schlüter, H. Pitsch, and P. Moin. Large eddy simulation inflow conditions for coupling with Reynolds-Averaged flow solvers. *AIAA J.*, 42(3):478–484, 2004.

U. Schumann. Subgrid scale model for finite difference simulations of turbulent flows in plane channels and annuli. *J. Comp. Phys.*, 18:376–404, 1975.

E. Sergent. *Vers une méthodologie de couplage entre la Simulation des Grandes Echelles et les modéles statistiques*. PhD thesis, Ecole Centrale de Lyon, September 2002.

J. Sheng, H. Meng, and R.O. Fox. A large eddy PIV method for turbulence dissipation rate estimation. *Chem. Eng. Science*, 55:4423–4434, 2000.

S. Singh, D. You, and S.T. Bose. Large-eddy simulation of turbulent channel flow using explicit filtering and dynamic mixed models. *Phys. Fluids*, 24(085105), 2012.

J. Smagorinsky. General circulation experiments with the primitive equations I. the basic experiment. *Mon. Wea. Rev.*, 91:99–164, 1963.

A. Smirnov, S. Shi, and I. Celik. Random flow generation technique for large eddy simulations and particle-dynamics modeling. *J. Fluids Eng.*, 123:359–371, 2001.

C.G. Speziale. Galilean invariance of subgrid-scale stress models in the large-eddy simulation of turbulence. *J. Fluid Mech.*, 156:55–62, 1985.

S. Stolz and N.A. Adams. An approximate deconvolution procedure for large-eddy simulation. *Phys. Fluids*, 11(7):1699–1701, 1999.

S. Stolz, N.A. Adams, and L. Kleiser. The approximate deconvolution model for large-eddy simulations of compressible flows and its application to shock-turbulent-boundary-layer interaction. *Phys. Fluids*, 13(10):2985–3001, 2001a.

S. Stolz, N.A. Adams, and L. Kleiser. An approximate deconvolution model for large-eddy simulation with application to incompressible wall-bounded flows. *Phys. Fluids*, 13(4):997–1015, 2001b.

G.R. Tabor and M.H. Baba-Ahmadi. Inlet conditions for large eddy simulation: A review. *Comput. Fluids*, 39:553–567, 2010.

B. Tao, J. Katz, and C. Meneveau. Statistical geometry of subgrid-scale stresses determined from holographic particle image velocimetry measurements. *J. Fluid Mech.*, 457:35–78, 2002.

G.I. Taylor. LXXV. On the decay of vortices in a viscous fluid. *Philos. Mag. Series 6*, 46(274):671–674, 1923.

H. Tennekes and J.L. Lumley. *A First Course in Turbulence*. MIT Press, 1972.

T.B. Terriberry. Computing higher-order moments online, 2008. URL `http://people.xiph.org/~tterribe/notes/homs.html`.

E. Toro. *Riemann Solvers and Numerical Methods for Fluid Dynamics. A Practical Introduction*. Springer, 3rd edition, 2009.

F.X. Trias, R.W.C.P. Verstappen, A. Gorobets, M. Soria, and A. Oliva. Parameter-free symmetry-preserving regularization modeling of a turbulent differentially heated cavity. *Comput. Fluids*, 39:1815–1831, 2010.

F.X. Trias, O. Lehmkuhl, A. Oliva, C.D. Pérez-Segarra, and R.W.C.P. Verstappen. Symmetry-preserving discretization of Navier-Stokes equations on collocated unstructured grids. *J. Comp. Phys.*, 258:246–267, 2014.

M. Tsubokura. Proper representation of the subgrid-scale eddy viscosity for the dynamic procedure in large eddy simulation using finite difference method. *Phys. Fluids*, 13(2):500–504, 2001.

P.G. Tucker and S. Lardeau. Applied large eddy simulation. *Phil. Trans. R. Soc. A*, 367:2809–2818, 2009.

J. Tyacke and P. Tucker. LES of heat transfer in electronics. *App. Math. Mod.*, 36: 3112–3133, 2012.

F. van der Bos and B.J. Geurts. Commutator errors in the filtering approach to large-eddy simulation. *Phys. Fluids*, 17(035108), 2005.

J.P. Van Doormaal and G.D. Raithby. Enhancements of the SIMPLE method for predicting incompressible fluid flows. *Numer. Heat Transf.*, 7(2):147–163, 1984.

E.R. van Driest. On turbulent flow near a wall. *J. Aeronaut. Sci.*, 23(11):1007–1011, 1956.

J. van Kan. A second-order accurate pressure-correction scheme for viscous incompressible flow. *SIAM J. Sci. and Stat. Comput.*, 7(3):870–891, 1986.

O.V. Vasilyev. Computational constrains on large eddy simulation of inhomogeneous turbulent complex geometry flows. In C. Liu, L. Sakell, and T. Beutner, editors, *Proc. of the Third AFOSR International Conference on DNS/LES*, DNS/LES Progress and Challenges, pages 93–104, Arlington, Texas, 2001.

O.V. Vasilyev, T.S. Lund, and P. Moin. A general class of commutative filters for LES in complex geometries. *J. Comp. Phys.*, 146:82–104, 1998.

R. Verstappen. On restraining the production of small scales of motion in a turbulent channel flow. *Comput. Fluids*, 37:887–897, 2008.

R.W.C.P. Verstappen and R.M. Van Der Velde. Symmetry-preserving discretization of heat transfer in a complex turbulent flow. *J. Engng. Math.*, 54:299–318, 2006.

R.W.C.P. Verstappen and A.E.P. Veldman. Spectro-consistent discretization of Navier-Stokes: a challenge to RANS and LES. *J. Engng. Math.*, 34:163–179, 1998.

R.W.C.P. Verstappen and A.E.P. Veldman. Symmetry-preserving discretization of turbulent flow. *J. Comp. Phys.*, 187:343–368, 2003.

S. Viaro, P. Lampitella, R. Mereu, E. Colombo, and F. Inzoli. Large eddy simulation of a turbulent pipe flow: a sensitivity analysis on computational parameters. In *Proc. XXX UIT Heat Transfer Conference*, 2012.

D. Vidović. Polynomial reconstruction of staggered unstructured vector fields. *Theoret. Appl. Mech.*, 36(2):85–99, 2009.

A. Viré and B. Knaepen. On discretization errors and subgrid scale model implementations in large eddy simulations. *J. Comp. Phys.*, 228:8203–8213, 2009.

J. VonNeumann and R.D. Richtmyer. A method for the numerical calculation of hydrodynamic shocks. *J. Appl. Phys.*, 21:232–237, 1950.

A.W. Vreman. The filtering analog of the variational multiscale method in large-eddy simulation. *Phys. Fluids*, 15(8):L61–L64, 2003.

A.W. Vreman. An eddy-viscosity subgrid-scale model for turbulent shear flow: Algebraic theory and applications. *Phys. Fluids*, 16(10):3670–3681, 2004a.

A.W. Vreman. The adjoint filter operator in large-eddy simulation of turbulent flow. *Phys. Fluids*, 16(6):2012–2022, 2004b.

A.W. Vreman. Subgrid modeling in large-eddy simulation of complex flows. In M. Oberlack, G. Khujadze, S. Günther, T. Weller, M. Frewer, J. Peinke, and S. Barth, editors, *Progress in Turbulence II*, volume 109 of *Proceedings in Physics*, pages 301–304. Springer, 2007.

A.W. Vreman and B.J. Geurts. A new treatment of commutation errors in large-eddy simulation. In I.P. Castro, P.E. Hancock, and T.G. Thomas, editors, *Advances in Turbulence IX*, pages 199–202, CIMNE, Barcelona, Spain, 2002.

B. Vreman, B. Geurts, and H. Kuerten. Realizability conditions for the turbulent stress tensor in large-eddy simulation. *J. Fluid Mech.*, 278:351–362, 1994.

B. Vreman, B. Geurts, and H. Kuerten. Subgrid-modelling in LES of compressible flow. *App. Sci. Res.*, 54:191–203, 1995a.

B. Vreman, B. Geurts, and H. Kuerten. A priori tests of large eddy simulation of the compressible plane mixing layer. *J. Eng. Math.*, 29:299–327, 1995b.

B. Vreman, B. Geurts, and H. Kuerten. Large-eddy simulation of the temporal mixing layer using the Clark model. *Theoret. Comp. Fluid Dyn.*, 8:309–324, 1996.

B. Vreman, B. Geurts, and H. Kuerten. Large-eddy simulation of the turbulent mixing layer. *J. Fluid Mech.*, 339:357–390, 1997.

C. Wagner, T.J. Hüttl, and R. Friedrich. Low-Reynolds-number effects derived from direct numerical simulations of turbulent pipe flow. *Comput. Fluids*, 30(5):581–590, 2001.

C. Wagner, T. Hüttl, and P. Sagaut. *Large-Eddy Simulation for Acoustics*. Cambridge University Press, 2007.

Z.J. Wang. Spectral (finite) volume method for conservation laws on unstructured grids. Basic formulation. *J. Comp. Phys.*, 178:210–251, 2002.

B.P. Weldford. Note on a method for calculating corrected sums of squares and products. *Technometrics*, 4(3):419–420, 1962.

D.H.D. West. Updating mean and variance estimates: An improved method. *Communications of the ACM*, 22(9):532–535, 1979.

G.S. Winckelmans, A.A. Wray, O.V. Vasilyev, and H. Jeanmart. Explicit-filtering large-eddy simulation using the tensor-diffusivity model supplemented by a dynamic Smagorinsky term. *Phys. Fluids*, 13(5):1385–1403, 2001.

G.S. Winckelmans, H. Jeanmart, and D. Carati. On the comparison of turbulence intensities from large-eddy simulation with those from experiment or direct numerical simulation. *Phys. Fluids*, 14(5):1809–1811, 2002.

P. Wu and J. Meyers. A constraint for the subgrid-scale stresses in the logarithmic region of high Reynolds number turbulent boundary layers: A solution to the log-layer mismatch problem. *Phys. Fluids*, 25(015104), 2013.

X. Wu and P Moin. A direct numerical simulation study on the mean velocity characteristics in turbulent pipe flow. *J. Fluid Mech*, 608:81–112, 2008.

V. Yakhot and K.R. Sreenivasan. Anomalous scaling of structure functions and dynamic constraints on turbulence simulations. *J. Stat. Phys.*, 121:823–841, 2005.

V. Yakhot and J. Wanderer. Anomalous scaling of structure functions and sub-grid models for large eddy simulations of strong turbulence. `http://arxiv.org/abs/1109.6188`, 2011. [Last accessed on December 28, 2013].

A. Yoshizawa. Statistical theory for compressible turbulent shear flows, with the application to subgrid modeling. *Phys. Fluids*, 29(7):2152–2164, 1986.

A. Yoshizawa. Subgrid-scale modeling with a variable length scale. *Phys. Fluids A*, 1 (7):1293–1295, 1989.

A. Yoshizawa, M. Tsubokura, T. Kobayashi, and N. Taniguchi. Modeling of the dynamic subgrid-scale viscosity in large eddy simulation. *Phys. Fluids*, 8(8):2254–2256, 1996.

A. Yoshizawa, K. Kobayashi, T. Kobayashi, and N. Taniguchi. A nonequilibrium fixed-parameter subgrid-scale model obeying the near-wall asymptotic constraint. *Phys. Fluids*, 12(9):2338–2344, 2000.